# Combined climate-ice flow modelling of the Alpine Ice Field during the Last Glacial Maximum

Versuchsanstalt für Wasserbau
Hydrologie und Glaziologie
der Eidgenössischen
Technischen Hochschule Zürich

**Mitteilungen** **260**

# Combined climate-ice flow modelling of the Alpine Ice Field during the Last Glacial Maximum

Michael Andreas Imhof

Zürich, 2021

Herausgeber: Prof. Dr. Fabian Walter

ETH zürich

*Zitiervorschlag für VAW-Mitteilungen:*

Michael Andreas Imhof (2021).
Combined climate-ice flow modelling of the Alpine Ice Field during the Last Glacial Maximum

*VAW-Mitteilungen* 260, Versuchsanstalt für Wasserbau, Hydrologie und Glaziologie (VAW), (F. Walter, ed.), ETH Zürich, Schweiz.

Im Eigenverlag der
Versuchsanstalt für Wasserbau,
Hydrologie und Glaziologie
ETH Zürich
CH-8093 Zürich

Tel.: +41 - 44 - 632 40 91
Fax: +41 - 44 - 632 40 92
e-mail: info@vaw.baug.ethz.ch

Zürich, 2021

ISSN 0374-0056

DOI 10.3929/ethz-b-000483937

# P R E F A C E

Dr. Michael Imhof's dissertation focuses on numerical modelling of the Alpine ice field during the Last Glacial Maximum about 24,000 BP. Accurate modelling of such ice fields is subject to ongoing research, because ice flow and glacier geometries are tightly constrained by mountain topography. This calls into question the applicability of simplified ice sheet models whereas the time scales needed for modelling ice field and ice sheet evolution are too large to allow for application of full Stokes models solving mass and momentum conservation equations together with ice rheology without approximations. A second reason why modelling the Alpine ice field constitutes a research gap is that paleo climate data needed to force ice sheet models are only now becoming available with accurate temporal and spatial resolution. Geomorphological evidence for ice field and glacier extent or flow directions is not sufficient to reproduce highly dynamic ice flow.

The present thesis aims to fill these research gaps in two regards: First, the suitability of approximations for ice sheet modelling is investigated. Particular attention is paid to a flux limiting scheme to provide numerical stability to ice sheet models, in particular hybrid combinations of shallow ice and shallow shelf approximations (SIA and SSA). These approaches assume predominant horizontal shear deformation and basal sliding, respectively. The flux limitation was introduced to the SIA to handle complex and steep bedrock topography where the conditions of a shallow ice cover are difficult to define, which causes numerical instabilities and spurious violation of mass conservation. The physical consequences and thus the justification for using such a flux limiting scheme are not well understood, a shortcoming, which the present thesis investigates in detail. The second contribution to fill the described research gaps is a detailed modelling exercise of the Alpine ice field using newly available constraints from regional climate models. This allows going beyond geomorphological constraints of ice field extent and ice flow directions and forces the hybrid ice sheet model with spatial and temporal climate patterns, which prevailed during the Last Glacial Maximum.

Chapter 2 compares the hybrid ice sheet model to a previously published full Stokes study of the European Rhine Glacier during the Last Glacial Maximum. Model results describing ice flow, ice extent, thermal regime and ice thickness are compared for the two approaches. A major finding is that the ice flux limitation suppresses shearing speeds leading to overestimated ice thicknesses, which have been observed in previously published modelling studies. This problem may be mitigated by weakening the flux limitation scheme via a smaller kernel for bed topography smoothing. When this kernel is equal to the resolution of the ice sheet model, ice sheet extent, sliding speeds and basal temperatures of the full Stokes model are reproduced. Although this comes at a higher computational cost, it underlines the importance of using flux limiting schemes that are geared towards

the topography of the target ice sheet rather than using a generic bedrock smoothing approach.

In Chapter 3, Michael Imhof applies the hybrid ice sheet model with the weakened flux limitation to the Alpine ice field. Eight different climate conditions extracted by downscaling output of a global climate model to regional scales are used to force the hybrid ice sheet model. The modelling exercise finds that the sizes of the Laurentide and Eurasian ice sheets influenced spatial climate patterns in the Alps. Geomorphological constraints and climate forcing cannot be brought in complete agreement with ice field model output. However, the model runs support an enhanced moisture advection from the West during the Last Glacial Maximum. This study thus underlines the value of regional climate models in paleo ice sheet reconstruction motivating further investigations as presented in the following chapter.

Chapter 4 is another application of the hybrid ice sheet model forced with regional climate model output. The regional climate models provide a spatial distribution of temperature and precipitation for the Last Glacial Maximum and present-day conditions. These spatial distributions can be combined with ice core data, empirical temperature offsets and lapse rates (elevation dependence) to yield time and space dependent temperature and precipitation fields. The ensuing models then focus on the temperature and precipitation fields for the Last Glacial Maximum and quasi-paleo fields derived from spatial distribution of present-day climate paired with temperature and precipitation offset to approximate conditions during the Last Glacial Maximum. The model runs focus on Rhone Glacier and the trajectory of erratic boulders, which were transported via ice flow to the foothills of the Jurassic mountain range. Such glacial deposits are an important piece of geomorphological evidence and show that ice flow was diverted during specific times around the Last Glacial Maximum. One key finding of this chapter is that the simulated climate pattern during the Last Glacial Maximum yields observed boulder diversion, whereas the modifications of the present-day climate do not.

Accurate ice sheet modelling remains a challenge, especially when small-scale variations in bedrock topography are relevant, which is the case for the European ice field during present and paleo conditions. The work by Michael Imhof makes important advances with respect to numerical feasibility and the incorporation of regional climate conditions as given by state-of-the-art climate models. Both factors are shown to be essential for ice sheet modelling (see also elaboration in the appendices). This PhD study thus has important implications not only for the scientific domain but also for various social issues like sea level rise and radioactive waste disposal which heavily rely on the accuracy of predictive ice sheet models.

Dedicated to the vanishing glaciers of our planet

## ABSTRACT

Our knowledge of the European Alpine Ice Field during the Last Glacial Maximum (LGM, 24,000 years ago) mostly relies on sparse geological evidence and is therefore very fragmentary. While ice flow modelling permitted us to complete the picture in recent years, the lack of paleo climate data severely hampered the interpretation of modelling results. In this thesis, I employ novel, high-resolution LGM climate data generated with a regional climate model to force an ice flow model. The aim is to assess the added value of this approach and if it allows to reconstruct the LGM Alpine Ice Field with a higher degree of confidence than previous studies. To facilitate large-scale ice field simulations over relatively long time scales, I use a model with simplified ice dynamics; the Parallel Ice Sheet Model (PISM).

I assess the impact of PISM's ice dynamical simplifications and its capability to reproduce flow velocities, ice extents, and thermal regimes of glaciers in the Alpine Ice Field. For this purpose, I model only a part of the Alpine Ice Field and compare the output to results obtained with an ice flow model employing non-simplified ice dynamics. As a result, I find that the flux limitation typically used in PISM to improve computational time and mass conservation yields significantly reduced shearing speeds and overestimated ice thicknesses. However, reducing the ice flux limitation allows PISM to minimize this mismatch and simulate sliding speeds, ice thicknesses, ice extents and basal temperatures that are in good agreement with those obtained with non-simplified ice dynamics. Using a reduced ice flux limitation, I simulate the entire Alpine Ice Field and compare this to the geologically reconstructed maximum ice extent. I evaluate the benefit of using modelled LGM climate data instead of artificially cooled present-day climate data. The LGM climate model data requires little adjustment to yield a modelled ice extent consistent with the reconstructed extent of the Alpine Ice Field. A detailed study of the LGM Rhone Glacier shows that the modelled flow velocity field results in a boulder deposition matching the present-day distribution. This cannot be achieved using cooled present-day climate data. This thesis demonstrates that combining high-resolution climate and ice flow modelling is a promising approach to remedy the lack of paleo climate data, and permits to expand our knowledge of the Alpine Ice Field during the LGM.

# ZUSAMMENFASSUNG

Unser Wissen bezüglich des Alpinen Eisfeldes des Letzten Glazialen Maximums (LGM, vor ca. 24'000 Jahren) baut grösstenteils auf spärliche geologische Zeugnisse und ist deshalb äusserst lückenhaft. Eisflussmodellierungen jüngeren Datums erlaubten, die geologischen Zeugnisse zu ergänzen, jedoch erschwerte der Mangel an klimatischen Daten für das LGM die Deutung der Modellierungen massgeblich. In dieser Doktorarbeit benutze ich neuartige, hochaufgelöste Klimadatensätze für das LGM, welche mit einem Regionalen Klimamodell angefertigt wurden, um ein Eisflussmodell anzutreiben. Das Ziel ist es, die Vorteile dieser Herangehensweise zu ergründen und das Alpine Eisfeld des LGMs mit grösserer Sicherheit als zuvor zu rekonstruieren. Um grossflächige Eisfeldsimulierungen über relativ grosse Zeiträume durchzuführen, verwende ich ein Eisflussmodell, das auf eine vereinfachte eisdynamische Beschreibung zurückgreift: das Parallel Ice Sheet Model (PISM).

Ich untersuche die Fähigkeit der eisdynamischen Vereinfachungen von PISM, um Fliessgeschwindigkeiten, Eisausdehnung und Temperatur von Gletschern des Alpinen Eisfeldes abzubilden. Hierfür modelliere ich nur einen Teil des Alpinen Eisfeldes und vergleiche die Resultate mit jenen eines Modells, das auf eine nicht vereinfachte Beschreibung der Eisdynamik aufbaut. Das Experiment zeigt, dass der Grad an Eisflusslimitierung, der üblicherweise in PISM gebraucht wird um Rechenzeit und Massenerhaltung zu verbessern, zu stark reduzierten Schergeschwindigkeiten und überschätzten Dicken der Gletschern führt. Eine Reduzierung der Eisflusslimitierung erlaubt es jedoch, diese Diskrepanz zum Modell mit nicht vereinfachter Eisdynamik zu beheben und Gleitgeschwindigkeiten, Eisdicke, Eisausdehnung und basale Temperaturen in guter Übereinstimmung wiederzugeben. Unter Verwendung reduzierter Eisflusslimitierung simuliere ich das gesamte Alpine Eisfeld und vergleiche es mit der rekonstruierten maximalen Eisausdehnung. So schätze ich den Nutzen ab, der mit modellierten LGM Klimadaten gegenüber künstlich gekühlten Varianten des heutigen Klimas erreicht werden kann. Es zeigt sich, dass die modellierten LGM Klimadaten wenig Adaptierung benötigen, um eine modellierte maximale Eisausdehung zu generieren, welche konsistent ist mit der rekonstruierten Ausdehnung des Alpinen Eisfeldes. Eine Detailstudie des eiszeitlichen Rhonegletschers zeigt, dass das modellierte Fliessgeschwindigkeitsfeld zu einer Findlingsverteilung führt, die mit der heute beobachteten Verteilung übereinstimmt. Dies lässt sich mit gekühlten Varianten des heutigen Klimas nicht erreichen. Diese Doktorarbeit demonstriert daher, dass die Kombination aus hochaufgelösten Klimadatensätzen und Eisflussmodellierungen einerseits einen vielversprechenden Ansatz darstellt, um dem Mangel an Paläoklimadaten beizukommen, und es uns andererseits ermöglicht unser Wissen über das Alpine Eisfeld des LGMs zu erweitern.

# ZÄMEFASSIG

Üses Wüsse über z Aupine Yschfäud fom Letschde Glaziale Maximum (LGM, for öppe 24'000 Jahr) chunt forauem fo geologische Spure u isch wäge däm zimmli lückehaft. Yschflussmodelierige us de letschde Jahr hei di geologische Spure chönne ergänze, aber dr Mangu a klimatische Date fom LGM het d Interpretazion fo dene Modelierige starch beyträchtiget. I dere Diss hie tueni es Yschflussmodäu mit nöiartige u hochufglöste LGM Klimadatesätz aatribe wome mitemne Regionale Klimamodäu gmacht het. Z Ziu isch, dr Nuze fo dere Heragehenswys abzschetze u z luege iwifern z Aupine Yschfäud fom LGM gnauer cha rekonstriert wärde im verglych zu früechere Studie. Für so grossflächigi Yschflussmodeliereige über rächd grossi Zytrüm müglech z mache, brucheni äs Yschflussmodäu wo d Yschdynamik vereifacht berächnet: z Parallel Ice Sheet Model (PISM).

Zersch ungersuecheni dr Yfluss fode yschdynamische Vereifachige fo PISM u dene iri Fähigkeit Fliessgschwindikeite, Yschusdehning u Temperatur fode Gletscher fom Aupine Yschfäud z simuliere. Für das modeliereni nume ä Teu fom Aupine Yschfäud u verglyche d Resutat mit dene fomne Modäu wo kener yschdynamische Vereifachige brucht het. Z Experimänt zeigt, das dr Grad for Yschflusslimitierig, wome aube i PISM brucht für Rächnigszyt ud Masseerhautig z verbessere, starch reduzierti Schärgschwindikeite u verdickti Gletscher verursacht. Weme aber d Yschflusslimitierig abschwecht, wärde d Ungerschide zum unvereifachte Modäu chlyner ud Gleitgschwindigkeite, Yschdicki, Yschusdehnig u di basale Temperature chöme ähnlech use. Mit abgschwechter Yschflusslimitierig modeliereni när z ganze Aupine Yschfäud u vergliches mit dr rekonstruerte maximale Yschusdehnig. Uf die Art u Wis schezeni dr Nutze ab wo di modelierte LGM Klimadate hei gägenüber künschdlech gchüute Variantene vom hütige Klima. Di modelierte LGM Klimadate bruche weniger Nachejustierig für das z Yschflussmodäu ä Yschusdehnig liferet wo mit dr rekonstruerte Usdehnig öppe überystimmt. Ä gnaueri Studie fom yschzytleche Rhonegletscher zeigt, das z modelierte Fliessgschwindiketisfäud zure Findlingverteilig füert wo mit dr hüt beobachtete Verteilig überystimmt. Das gyget nid weme anstatdessi ä gchüuti Variante fom hütige Klima brucht. Fo däm här demonstriert di Diss, das d Kombinazion us hochufglöste Klimadatesätz u Yschflussmodelierige einersyz ä fiuversprächende Asatz isch für am Mangu a Paläoklimadate z bcho u s üs angerersyz müglech macht üses Wüsse über z Aupine Yschfäud fom LGM z erwytere.

# CONTENTS

# 1

# INTRODUCTION

*"Halt die Füsse still Onkelchen, alles klar. Die Sache läuft!*
*Morgen früh steche ich in See." - "Stich nicht daneben."*
— Zwei Asse trumpfen auf (1981)

## 1.1 CONTEXT

The Earth's climate has been characterized by oscillations between mild and cool conditions for the last 2.6 million years (Lisiecki and Raymo, 2005). These climatic oscillations are called ice age cycles and have had a length of ≈100 ka (kilo annum) during the last one million years (Clark et al., 2006). A cycle is characterized by a gradual cooling that culminates after ≈90 ka, which is called 'glacial'. The glacial is then followed by a sudden temperature raise and a period of mild temperatures lasting ≈10 ka, the so-called 'interglacial'. The most recent glacial cycle started ≈115 ka BP (Before Present, Dahl-Jensen et al., 2013) and reached its globally coldest period during the Last Glacial Maximum (LGM) ≈21 ka BP (Hughes and Gibbard, 2015), with global mean air temperatures 5.7–6.5 °C lower than today (Tierney et al., 2020). After the LGM, temperatures rose and heralded the current warm period, the Holocene, which started ≈11.7 ka BP (Walker et al., 2009).

Of all glacial periods, the LGM is best documented. Due to its young age and the fact that traces have not been erased by successive glaciations, glacial evidence from the LGM is well preserved. The most prominent features of the LGM, and the last glacial cycle in general, were the large ice sheets that formed in North America and Eurasia. The Laurentide Ice Sheet covered most of what is known today as Canada and parts of the United States (Kleman et al., 2010). In Eurasia, one ice sheet stretched from Ireland, over Great Britain eastwards to Scandinavia and the Baltics, and northwards to Svalbard and northern Russia (Hughes et al., 2016). Besides these vast ice sheets, there were also smaller glaciations in mountain ranges such as the Pyrenees (Palacios et al., 2015) and the European Alps (Wirsig et al., 2016). The research presented in this thesis aims to improve our understanding of the LGM glaciation in the European Alps.

## 1.2 GEOLOGICAL EVIDENCE FROM THE LAST GLACIAL MAXIMUM IN THE ALPS

Research on past glaciations in the Alps goes back more that 200 years (Agassiz, 1840; Charpentier, 1841; Saussure, 1779; Venetz, 1833; Windham and Martel, 1744). Today, we know that the LGM in the European Alps was characterized by an extensive glaciation (formerly also known as "Würm" glaciation, Fig. 1.1). A large part of our knowledge concerning the past glaciations of the Alps is based on geomorphological

evidence that was left by the glaciers such as moraines, erratic boulders, striae, and trimlines:

- Moraines are common in the plains surrounding the Alps. They consist of glacier sediments and rocks piled up to a ridge by an advancing glacier snout (Ivy-Ochs et al., 2004). Thus, moraines indicate the maximum extension of a glacier advance.
- Erratic boulders are rocks from the Alps that were transported to the lowlands by glacier flow. For some boulders it is possible to identify their location of origin based on their lithology. Hence, erratic boulders can indicate from which sources an area was fed (Coutterand et al., 2009).
- Striae are scars on rock surfaces that were eroded by glacier ice and indicate the former ice flow direction (Kelly et al., 2004).
- Trimlines are the transition between glacially eroded rock faces and frost weathered rock on top. In the Alps, they are interpreted as the maximum elevation reached by the glaciers (Kelly et al., 2004). They are only preserved in areas with erosion resistant lithologies.

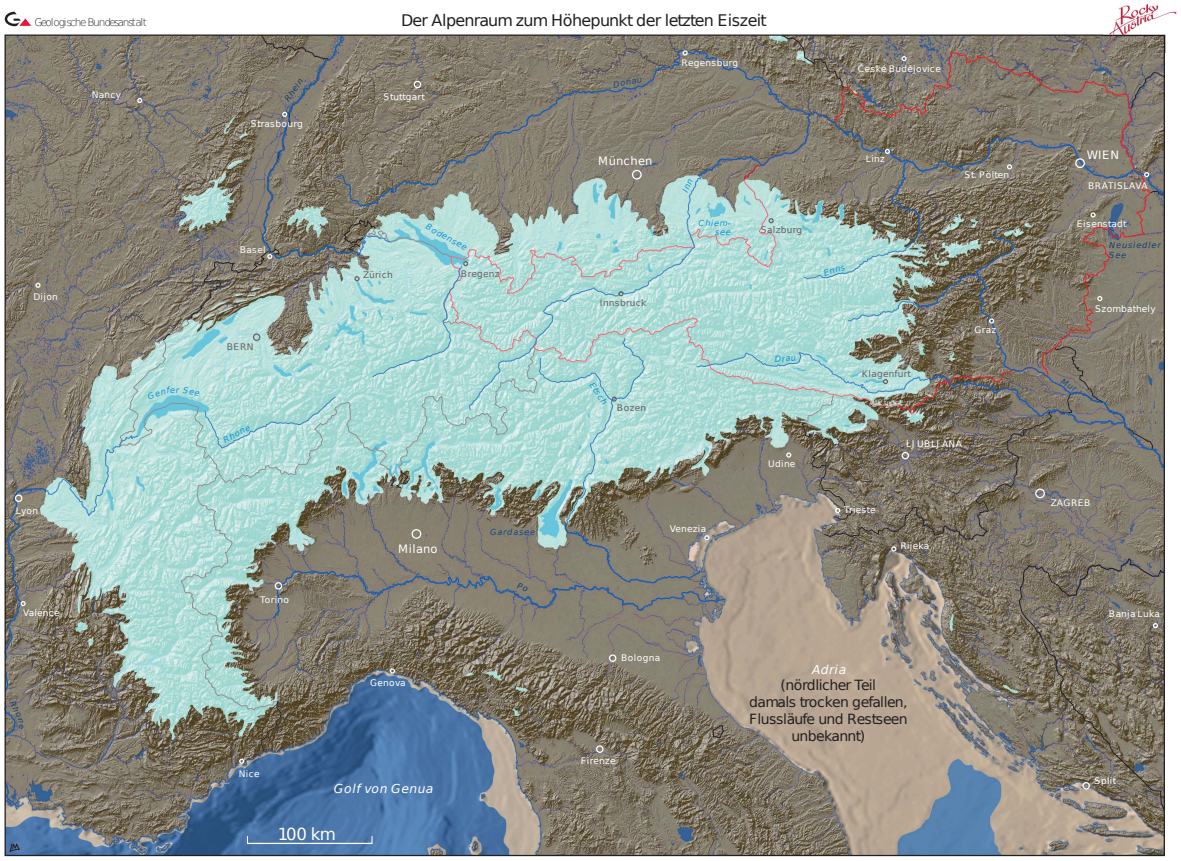


**Figure 1.1:** Ice extent reconstruction of the Alpine Ice Field during the LGM (modified from Geologische Bundesanstalt, 2013).

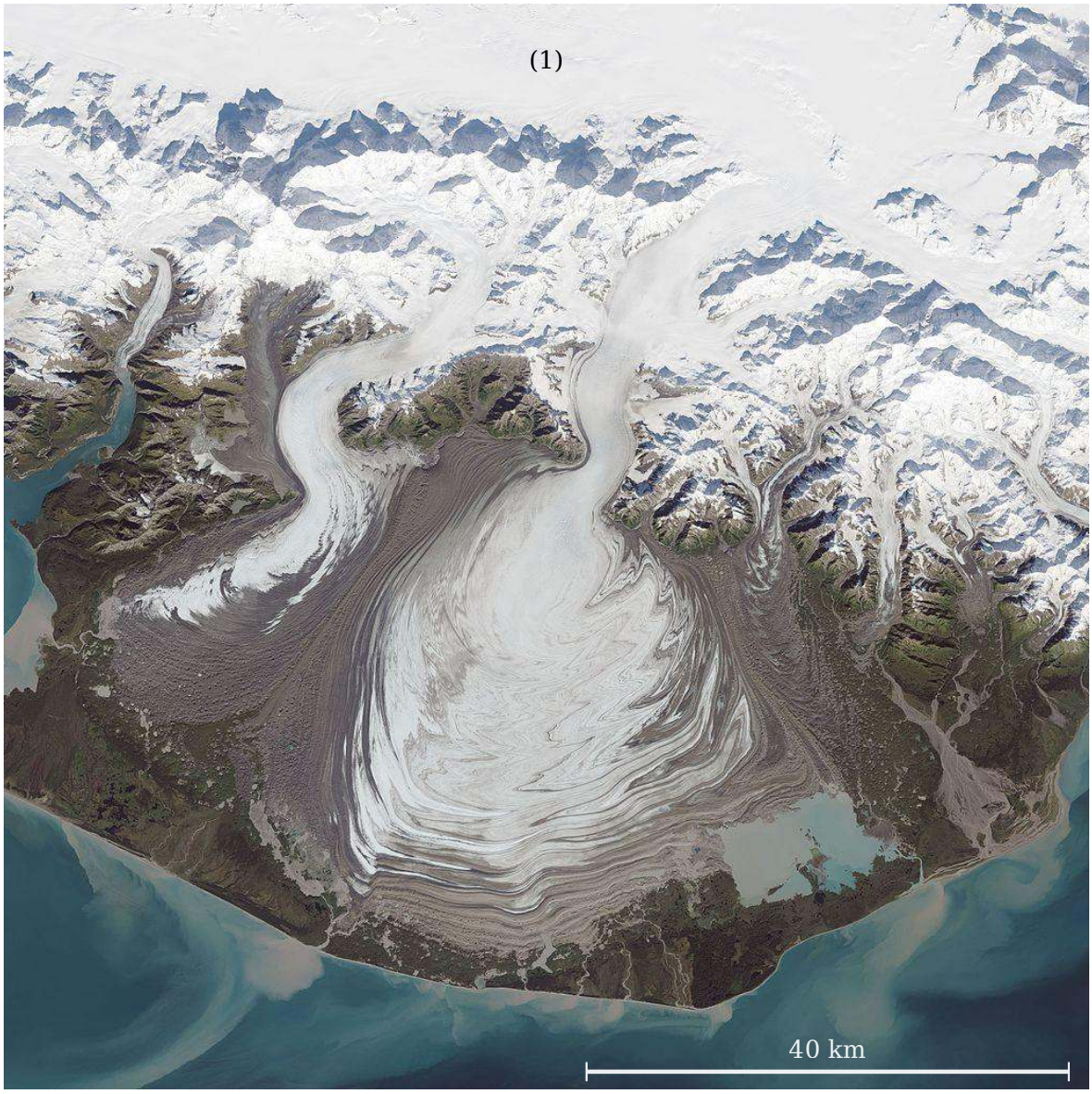


**Figure 1.2:** Satellite image of the St. Elias Range in Alaska, USA and Yukon, Canada by the NASA Earth Observatory (`https://www.flickr.com/photos/gsfc/22800052331/`). The white area at the top centre of the photograph (1) is Seward Glacier that flows through a valley towards the bottom of the image. There, the ice forms a vast piedmont lobe on the plain which is called Malaspina Glacier.

Thanks to this evidence, the maximum ice extent of the glaciation during the LGM is fairly well known (Fig. 1.1). Striae suggest that the ice flow was constrained by the alpine topography which indicates an ice field/valley glacier network. Hence, I will refer to the glaciation in the Alps as the Alpine Ice Field in the following. The Alpine Ice Field was characterized by large piedmont lobes that formed on the forelands north of the Alps, similar to the St. Elias Range in Alaska today (Fig. 1.2). Some of these piedmont lobes such as the one of Rhone Glacier in the western Alps deposited numerous boulders from the Alps on the lowlands. The deposition pattern at Rhone Glacier implies that boulders from different source areas crossed

each others paths, and along the Jura several boulder fields consist of boulders from various origin valleys (Burkhard and Spring, 2004). The observed distribution of erratic boulders and the ice dynamics that caused it remain poorly understood and will be addressed in Research Question 3.

## 1.3 THE LAST GLACIAL MAXIMUM CLIMATE IN EUROPE

In general, the climate during the LGM is incompletely understood and evidence is scarce. The current knowledge on the LGM climate is built on climate proxy reconstructions and climate modelling, which both imply that the climate during the LGM must have been dramatically different from today's climate.

Climate proxy archives from the LGM in central Europe indicate a climate much cooler than that of today. Pollen analysis suggested summer temperatures 6–12 °C cooler than today and 10–17 °C for winter (Wu et al., 2007). Reconstructed precipitation rates indicate that it was probably dryer than today, although uncertainties are extremely large and encompass present day rates. Using accumulation area estimations of ice caps in the periphery of the Alpine Ice Field, Heyman et al. (2013) estimated temperatures north of the Alps between 8.7 °C and 14.8 °C lower than today. The atmospheric circulation over Europe might have been different as well. Luetscher et al. (2015) analysed $\delta^{18}$O records from speleothemes north of the Alps and concluded that the preferential advection of moisture was from south during the LGM. This represents a marked change to today's western advection regime.

Climate models simulate various components of the climate system such as atmosphere, ocean, and land surface and the interactions between them. Such simulations give insight into how the LGM climate was different from today and complement proxy reconstructions (e.g. Hofer et al., 2012b; Löfverström and Lora, 2017). Besides lower mean air temperatures and precipitation rates, these simulations also implied changes in the atmospheric dynamics. For example, the North Atlantic storm track, which today advects humidity from the Atlantic to the north of Great Britain and Norway, arrived more to the south during the LGM (Löfverström and Lora, 2017). This might also have played an important role for the glaciation in the Alps (Višnjević et al., 2020).

## 1.4 MODELLING THE ALPINE ICE FIELD

Over the recent decades, our knowledge from geological evidence has been complemented with ice sheet models that simulated the ice flow during the LGM. Ice sheet or glacier models are computer programs that calculate displacement of glacier ice due to viscous deformation, thermodynamics, and surface mass balance of ice sheets, glaciers and ice shelves. They require at least a bed topography, a mass balance parametrization, and a rheology. Modelling the glaciers of the Alpine Ice Field permitted to analyse the interactions between climate, ice flow, and ice thickness (e.g. Jouvet et al., 2017; Seguinot et al., 2018; Višnjević et al., 2020).

The lack of viable mass balance input climate data representative for the LGM, or the last glacial cycle in general, is a substantial restriction for using ice flow models. Climate models that were applied to the European Alps for the LGM period have so far used a fairly coarse horizontal resolution such the climate could not be resolved at the scale of individual valleys of the Alps. Therefore, climate model data were not sufficiently resolved to be used for paleo ice flow modelling in the Alps. Instead, former ice flow modelling studies relied either on artificially cooled present-day climate data (e.g. Becker et al., 2016) or on an elevation dependent mass balance (e.g. Cohen et al., 2018). A major finding of such studies is that the east-west precipitation distribution must have been different from today during the LGM (Seguinot et al., 2018; Višnjević et al., 2020). Modelling boulder trajectories in the western Alps suggested that changes in the precipitation distribution was even relevant at the scale of neighbouring glacier catchments (Jouvet et al., 2017). This situation was remedied by Velasquez et al. (2020), Velasquez and Raible (in prep), and Velasquez (in prep) who recently applied a regional climate model to the European Alps for LGM conditions. These simulations resolved the climate within individual alpine valleys. Regional climate models are able to do so because they only model a small part of the globe and in return can afford using high spatial resolution. The LGM climate datasets of Velasquez et al. (2020) and Velasquez and Raible (in prep) provide new perspectives for modelling the glaciation in the Alps during the LGM and are exploited in this thesis. The added value of this dataset for modelling the Alpine Ice Field during the LGM will be addressed in Research Question 2.

While the reconstructed maximum extent could be matched with local discrepancies, the reconstructed maximum ice surface elevation inferred from trimlines could not be reproduced by ice flow models (Becker et al., 2016; Becker et al., 2017; Seguinot et al., 2018). The modelled ice surface elevation lay several hundred meters above the trimlines. I will address this discrepancy in Research Question 3.

## 1.5 DESCRIPTION OF THE ICE DYNAMICS

This section provides an elementary introduction into how the ice dynamics are commonly modelled. After describing the characteristics of ice deformation, I introduce two commonly used simplified ice flow descriptions. Last, I introduce the ice flow model that is used throughout this thesis. It is the same model already used in earlier paleo ice flow modelling in the Alps.

Ice is commonly described as an isotropic, incompressible, slow-moving, and nonlinear viscous fluid governed by the Stokes equations, meaning stresses are governed solely by force of gravitay and internal friction. Stresses and strain rates are related with Glen's flow law (Glen, 1952), which is an empirical flow law based on laboratory experiments. Solving the resulting system of equations yields pressure and a three dimensional velocity field. This velocity field is then used to calculate the displacement of ice, i.e. the ice flow. Ice flow models that calculate the ice flow considering all stress components are called Stokes models. Stokes models are com-

putationally very demanding and thus hardly affordable for simulating long time periods or large ice bodies such as proposed in this thesis. Therefore, simplifications are made on the stress balance resulting in less accurate but computationally cheaper ice flow models. The most broadly used ice flow approximations are the Shallow Ice Approximation and the Shallow Shelf Approximation.

*Shallow Ice Approximation*

The Shallow Ice Approximation (SIA, Hutter, 1983) treats an ice body that sits on a flat bed with an ice thickness much smaller than its lateral extent. Basal friction is assumed to be large such that the ice does to not slide over the ground. Further, longitudinal and transverse stresses are neglected. The SIA best describes the ice flow in the interior of an ice sheet in absence of high ice surface gradients. However, its accuracy decreases where basal velocities become larger or where lateral stresses are strong.

*Shallow Shelf Approximation*

Analogous to the SIA, the Shallow Shelf Approximation (SSA, Weis et al., 1999) describes an ice body on a flat base with an ice thickness much smaller than its lateral extent. Basal friction is assumed to be very low such that sliding velocities are high resulting in vertically constant ice velocities (plug flow). In contrast to the SIA, longitudinal and transverse stresses are not neglected. The basal shear stress is connected to basal velocities using a sliding law. The SSA performs best at describing floating ice shelves or areas where the ice dynamics are dominated by basal motion (ice streams).

*The hybrid ice flow model PISM*

Most of the ice flow modelling performed in this thesis employs the Parallel Ice Sheet Model (PISM, PISM authors, 2019; Winkelmann et al., 2011) which is a so-called hybrid ice flow model. It employs a superposition of the SIA and the SSA by summing up the two velocity fields to calculate the ice flow (Bueler and Brown, 2009). The SIA and the SSA are used to account for horizontal shearing and sliding velocities respectively. The dominant ice flux contribution of the two approximations is often disjunct in ice sheets and therefore the superposition justified in most areas. However, the superposition of the velocities is heuristic in the areas where both, horizontal shearing and sliding, contribute to the ice flux. Hybrid ice flow models are designed for modelling large ice sheets such as the Greenland Ice Sheet (e.g. Aschwanden et al., 2016) or the Antarctic Ice Sheets (e.g. Sutter et al., 2019). Recently, they have gained popularity also for modelling glaciers and ice fields (Becker et al., 2016; Golledge et al., 2012; Ziemen et al., 2016). This type of model is very attractive for such applications due to its compromise of computational speed

and ice mechanical accuracy. However, little is known about potential shortcomings of the hybrid formulation if applied to glaciers and ice fields which typically have more complex catchment topographies than ice sheets. This issue will be addressed in Research Question 1.

## 1.6 RESEARCH QUESTIONS AND OUTLINE OF THE THESIS

This thesis addresses three main research questions (RQ):

1. **RQ1: Is a hybrid ice flow model like PISM an adequate model choice to simulate ice fields such as the Alpine Ice Field?**
2. **RQ2: What is the added value of using regional climate model data instead of cooled present-day climate data for modelling the Alpine Ice Field during the LGM?**
3. **RQ3: How thick was Rhone Glacier during the LGM? And how did the ice flow of Rhone Glacier evolve over the LGM?**

This monograph thesis is structured in three self contained chapters which address the above research questions. In **Chapter 2**, a detailed comparison is performed between model results obtained with the hybrid model PISM and the Stokes model Elmer/Ice in order to answer RQ1. The study is performed at the Rhine Glacier of the Alpine Ice Field in order to assess shortcomings of the hybrid ice dynamics of PISM. I compare modelled shear and sliding speeds, basal temperatures, and ice thicknesses of Rhine Glacier during the LGM. This chapter was published as Imhof et al. (2019). **Chapter 3** addresses RQ2 by modelling the Alpine Ice Field using regional climate model data for present-day and LGM conditions. The chapter also investigates how precipitation changes induced by uncertainties in ice surface elevation of the Laurentide Ice Sheet (North America), Eurasian Ice Sheet (Northern Europe), and within the Alps affect the Alpine Ice Field. In **Chapter 4**, RQ3 is investigated by modelling Rhone Glacier in greater detail using the LGM regional climate model data used in Chapter 3. I assess how the transient evolution of the climate and ice dynamical parametrizations affect the Rhone Glacier ice thickness and ice dynamics. The validation of the modelled Rhone Glacier also considers simulated trajectories of erratic boulders from the Valais and field data such as trimline elevation and erratic boulder deposition locations. This allows also to elaborate RQ2 in more detail. In **Chapter 5**, I summarize the outcome of this work and also provide a selection of topics that I consider worth investigating in more detail in the future.

**Appendix C** addresses a common mass conservation problem in SIA-based ice flow models. In Chapter 2 and 4, PISM's routine for improving computational time and mass conservation introduced an ice thickness bias when applied to ice fields. Here, I propose a scheme to calculate the ice surface gradient in such a way that mass is conserved without introducing a bias in ice thicknesses. This appendix provides a prove of concept, demonstrates the scheme's capabilities at a benchmark

test, and compares its performance on an alpine topography with another scheme derived for the same purpose.

## 1.7 SCIENTIFIC, SOCIAL AND ECONOMIC RELEVANCE

The research conducted in this work aims to improve our understanding of the glaciation in the Alps during the last glacial cycle and how the Alpine Ice Field was shaped by the prevailing climate at that time. A better understanding of past climatic conditions and glaciations helps us to put today's climate change into context and to better understand the future climate. Improving our understanding of past glaciations in the Alps is not only of interest for the scientific community but also for the National Cooperative for the Disposal of Radioactive Waste (*Nationale Genossenschaft für die Lagerung radioaktiver Abfälle*, NAGRA). NAGRA considers three sites in northern Switzerland for long-term storage of nuclear waste in deep geological repositories. All three sites have been covered at least once by alpine glaciers. The main concern is that future glaciations may erode and excavate these deep geological repositories and expose the nuclear waste to the environment. While the research in this thesis is not trying to assess this danger, it may contribute to a better basis for future studies that estimate the resilience towards glacial erosion of these sites.

# 2

# MODELLING A PALEO VALLEY GLACIER NETWORK USING A HYBRID MODEL: AN ASSESSMENT WITH A STOKES ICE FLOW MODEL

*"Aber ich kann gar nicht schwimmen!" - "Macht nichts, hier wimmelt's von Krokodilen und Haien."*
— Das Krokodil und sein Nilpferd (1979)

This chapter is published as *Imhof Michael A., Cohen Denis, Seguinot Julien, Aschwanden Andy, Funk Martin, and Jouvet Guillaume (2019). "Modelling a paleo valley glacier network using a hybrid model: an assessment with a Stokes ice flow model". In:* ***Journal of Glaciology*** *65.254, 1000–1010. DOI:10.1017/jog.2019.77*. The version here is slightly reformatted and includes minor orthographic corrections. The footnotes are not present in the original published manuscript and were added here on request of a co-examiner.

## 2.1 INTRODUCTION

During the last glacial cycle the European Alps were covered by a large glacier network with the ice flow direction confined by the underlying topography, a so-called ice field. The glacier extent during this cycle is best known at the Last Glacial Maximum (LGM), 24,000 years before present (Ivy-Ochs et al., 2008; Preusser et al., 2011). Based on terminal moraines and erratic boulders it was possible to reconstruct the former ice extent reached by the Alpine Ice Field (AlpIF) at the LGM (Benz-Meier, 2003; Bini et al., 2009; Coutterand, 2010; Ehlers et al., 2011). Further, trimlines were interpreted as the maximum ice surface elevation reached during the LGM (Benz-Meier, 2003; Bini et al., 2009; Coutterand, 2010; Florineth, 1998; Florineth and Schlüchter, 1998; Kelly et al., 2004). Current geomorphological reconstructions portray the AlpIF as a vast ice field with several large piedmont lobes, abundant nunataks, and ice flow directions predominantly constrained by the bedrock topography (Benz-Meier, 2003; Bini et al., 2009; Coutterand, 2010; Florineth, 1998; Florineth and Schlüchter, 1998; Kelly et al., 2004).

By contrast, recent ice flow modelling studies depict the AlpIF at the LGM as a thick ice cap/ice sheet (Becker et al., 2016; Becker et al., 2017; Cohen et al., 2018; Seguinot et al., 2018). While the reconstructed maximum ice extent can be matched fairly well, the models produce ice thicknesses much greater than suggested by geomorphological evidence, about 500 m thicker in the valley part of Rhine Glacier (Becker et al., 2016), and 800 to 861 m thicker in the valley part of Rhone Glacier (Becker et al., 2017; Seguinot et al., 2018). Only the modelling study by Cohen et al. (2018) is able to match the reconstructed ice surface elevation[1]. The maximum ice

1 Cohen et al. (2018) was able to do so by using extremely low accumulation rates.

thickness reconstructions in the European Alps are mainly inferred from trimline reconstructions which are known within 100 m and only exist at few mountainsides in the valley part of the AlpIF (Florineth, 1998; Florineth and Schlüchter, 1998). This range of uncertainty is much smaller than the ice thickness overestimations found by ice flow modelling, making the overestimated ice thicknesses significant. Therefore, the interpretation of trimlines as a former maximum ice surface elevation has been questioned and it was hypothesized that trimlines correspond instead to the transition between warm- and cold-based ice (Cohen et al., 2018; Coutterand, 2010; Seguinot et al., 2018). However, no geomorphological evidence from the Alps supporting this idea has been presented so far.

These modelling studies were performed with two kinds of ice flow models. Cohen et al. (2018) used a sophisticated model based on the Stokes equations, called Elmer/Ice (Gagliardini et al., 2013), which is capable of adequately reproducing the dynamics of ice within steep terrain, however, at high computational costs. Thus, this model cannot be used to simulate long time scales such as a full glacial cycle. By contrast, Becker et al. (2016), Becker et al. (2017), Jouvet et al. (2017), and Seguinot et al. (2018) used a model based on simplified mechanics deduced from the Stokes equations that is capable of simulating the ice dynamics of the entire Alps over the last 120,000 years (Seguinot et al., 2018). More precisely, they used the Parallel Ice Sheet Model (PISM, Bueler and Brown, 2009; PISM authors, 2019), a so-called hybrid ice sheet/ice stream model that relies on the shallow ice approximation (SIA, Hutter, 1983) and the shallow shelf approximation (SSA, Weis et al., 1999) to describe horizontal shearing and basal sliding respectively (Bueler and Brown, 2009). While the SIA is suitable for describing the horizontal shear deformation of vast continental ice sheets with negligible sliding, the SSA is suitable for describing plug-like flow as found in ice shelves or ice streams where sliding dominates horizontal shearing. The SIA has proved its worth for modelling the ice dynamics within ice sheets, when used with coarse horizontal resolution ($>$10 km) (e.g. Greve, 1997). Using such resolutions, the underlying assumptions for the SIA and the SSA are typically fulfilled i.e., shallowness of the ice and small ice surface and bedrock slopes. However, higher model resolution ($<$10 km) is necessary for resolving steep and complex terrain where the higher order stress gradient terms neglected in the SIA and the SSA become more important. SIA models have been assessed several times using Stokes models (e.g. Adhikari and Marshall, 2013; Brædstrup et al., 2016; Hindmarsh, 2004; Le Meur et al., 2004; Leysinger Vieli and Gudmundsson, 2004; Pattyn et al., 2008; Seddik et al., 2017). However, to our knowledge the applicability of the hybrid scheme at ice fields has not yet been assessed in a similar way. Despite this, the PISM hybrid model was used repeatedly to simulate the ice dynamics of ice fields, not only within the European Alps but also within other mountain ranges (e.g. Golledge et al., 2012; Yan et al., 2018; Ziemen et al., 2016). Another issue with high-resolution simulations employing the SIA within steep and complex terrain such as fjords or valleys is that high surface gradients can occur between adjacent grid cells resulting in high SIA shearing velocities. These require extremely small time steps to maintain numerical stability, which leads to an increase in

computational time (PISM authors, 2019). These high velocities increase the chance that more than the entire ice of a grid cell is drained within one time step, leading to mass conservation issues (Jarosch et al., 2013; Schäfer and Le Meur, 2007). To improve computational efficiency, PISM uses a scheme introduced by Schoof (2003) that limits the SIA ice flux in steep and complex terrain. However, it is currently not understood how this method of limiting SIA ice fluxes in mountainous topography affects the ice dynamics.

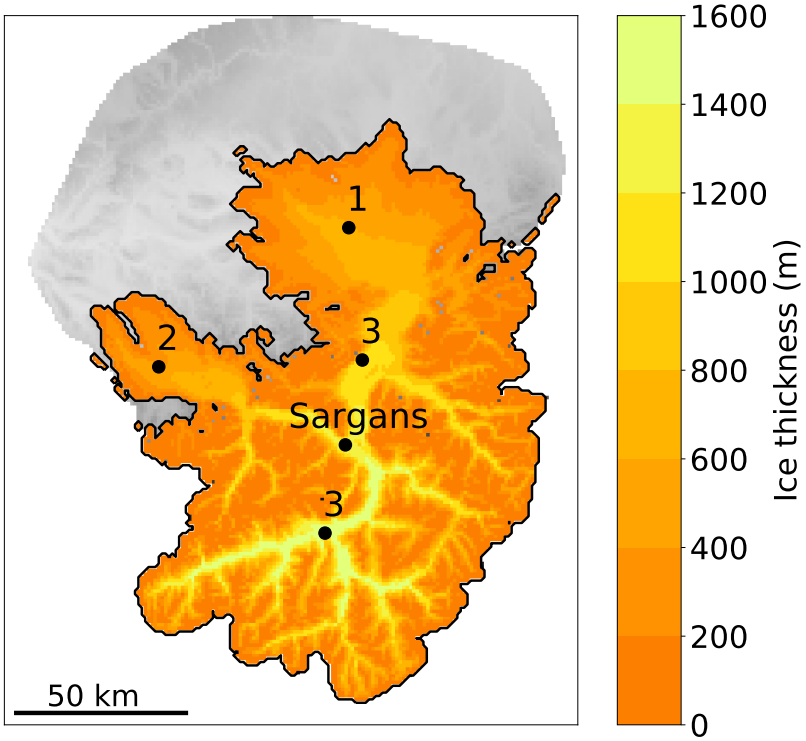


**Figure 2.1:** Modelled ice thickness of Rhine Glacier by Cohen et al. (2018). The numbers indicate the Rhine Glacier Piedmont Lobe (1), the Linth/Limmat Piedmont Lobe (2) and the main Rhine Valley in the ice field sector (3). The Rhine Glacier diffluence at Sargans is also indicated.

Cohen et al. (2018) recently applied a Stokes model to Rhine Glacier, a large north-central part of the AlpIF, during the LGM (Fig. 2.1). This study aims to remedy this situation[2] by assessing model results obtained with hybrid mechanics (PISM 0.7.3) against Stokes mechanics (Elmer/Ice 7.0) when applied to ice fields. Their work offers a unique opportunity for a comparison study with the PISM hybrid model, using the Elmer/Ice simulation as Stokes reference. We run PISM using a setup as similar as possible to the one described in Cohen et al. (2018), and compare the simulations of the two ice flow models in terms of horizontal shearing speeds, sliding speeds, ice thickness and basal temperatures. Further, we test the influence of the SIA ice-flux limiter scheme implemented in PISM on the ice flow at two different horizontal resolutions.

2 The fact that hybrid ice dynamics are poorly assessed at ice fields.

The paper is outlined as follows. In Section 2.2 the two ice flow models are described with an emphasis on similarities and differences as well as on the experimental setups. Section 2.3 presents the numerical experiments and the model results. Section 2.4 discusses how PISM performs compared to Elmer/Ice, the limits of the hybrid formulation for modelling ice fields as well as implications for previous studies employing PISM in the European Alps.

## 2.2 METHODS AND DATA

For comparison purposes, we apply PISM to Rhine Glacier during the LGM by closely following the Elmer/Ice model setup of Cohen et al. (2018). PISM and Elmer/Ice are both three-dimensional models that simulate ice flow, ice temperature and surface mass balance. Analogously to Cohen et al. (2018), we also use the present-day bedrock topography. The model is initialised based on the geomorphologically reconstructed ice thickness of Rhine Glacier from Benz-Meier (2003) and run for 3262 years[3]. While Cohen et al. (2018) interpolated the input dataset onto an unstructured grid with a mean horizontal resolution of $\sim$ 0.5 km, we interpolate the same data to a regular grid with a horizontal resolution of 1 km and 2 km[4]. For PISM, we also use the elevation-dependent surface mass balance parametrization of the "S1" setup of Cohen et al. (2018) where the equilibrium line altitude (ELA) lies at 1200 m above sea level. The ablation gradient is 1 m $a^{-1}$ $km^{-1}$ whereas the accumulation gradient is 0.25 m $a^{-1}$ $km^{-1}$. The accumulation rate is capped at 0.26 m $a^{-1}$. To model the ice temperature, PISM uses an enthalpy model (Aschwanden et al., 2012) with a constant vertical resolution of 50 m. By contrast, Elmer/Ice solves the heat equation with the constraints that the ice temperature is less or equal to the pressure melting point (Gagliardini et al., 2013) using 16 vertical layers with a finer resolution near the glacier bed. Further, in both models the thermal boundary conditions of the "S1" setup of Cohen et al. (2018) are applied, namely the geothermal heat flux of Medici and Rybach (1995) at the glacier bed and an elevation-dependent mean annual near surface air temperature at the glacier surface. The annual mean temperature at the ELA is taken as –12 °C with an elevation gradient of –6 °C $km^{-1}$. In both models, the initial vertical ice temperature profiles are estimated from the near surface air temperature, the geothermal heat flux and the accumulation rate. Following Cohen et al. (2018), frictional heating at the base of the glacier is neglected everywhere. In the PISM simulations, we set the ice thickness at the boundary of the Rhine Glacier catchment equal to zero, whereas in Elmer/Ice the ice flux across this boundary is set to zero. Using different boundary conditions in the two models has very little influence on our results since only a very small part of the Rhine Glacier ice drains across the boundary in the PISM simulations.

3 Cohen et al. (2018) aborted their simulation after 3262 years because the Rhine Glacier net mass balance was close to zero.

4 In this study, the data of Benz-Meier (2003) is interpolated to two grids one having a resolution of 1 km and the other one having a resolution of 2 km.

The way in which PISM and Elmer/Ice calculate ice velocity fields and displacement of mass is the key difference between the two models. In PISM, the evolution of the ice surface elevation $H$ is described by:

$$\frac{dH}{dt} = a - \vec{\nabla} \cdot \vec{Q}, \tag{2.1}$$

where $a$ is the mass balance and $\vec{Q}$ the two-dimensional ice flux in $x$ and $y$ directions. $\vec{Q}$ in PISM is equal to the sum of the SIA-induced flux $\vec{Q}_{SIA}$ and the SSA-induced flux $\vec{Q}_{SSA} = h \cdot \vec{v}_s$, where $\vec{v}_s$ is the sliding velocity computed by the SSA and $h$ the ice thickness. By contrast, Elmer/Ice calculates a three-dimensional velocity field from the Stokes equations and thus also considers the vertical component of the ice flow (Cohen et al., 2018; Gagliardini et al., 2013). Furthermore, Elmer/Ice employs the finite element method rather than the finite difference method used by PISM. We use the same sliding law for the SSA of PISM as Cohen et al. (2018) in Elmer/Ice, namely:

$$\vec{\tau}_b = \left( C_1 + (C_0 - C_1) \, \exp\left( -\frac{T_{pmp} - T}{\gamma} \right) \right) \vec{v}_s, \tag{2.2}$$

where $\vec{\tau}_b$ is a vector of the basal shear stress components, $C_0 = 1000$ Pa a m$^{-1}$ is the sliding parameter for temperate-based ice and $C_1 = 100,000$ Pa a m$^{-1}$ is the sliding parameter for cold-based ice. $C_1$ is used to suppress sliding where basal temperatures $T$ are below the the pressure melting point $T_{pmp}$. The exponential in Eq. (2.2) serves to smooth the transition between cold-based and temperate-based ice with a sub-melting sliding parameter $\gamma = 2$ K. This kind of sliding law is not included in PISM 0.7.3 and, therefore, we implemented it ourselves. The SIA ice flux of PISM, $\vec{Q}_{SIA}$, is described by:

$$\vec{Q}_{SIA} = -D \cdot \vec{\nabla} H, \tag{2.3}$$

where $D$ is the ice diffusivity resulting from the SIA,

$$D = \theta \cdot \frac{2EA(T)(\rho_i g)^n \, h^{n+2} \, |\vec{\nabla} H|^{n-1}}{(n+2)}. \tag{2.4}$$

$E = 1$ is the flow enhancement factor, $\rho_i = 917$ kg m$^{-3}$ the density of ice, $g = 9.81$ m s$^{-2}$ the gravitational acceleration, and $n = 3$ the Glen's flow law exponent, all having identical values in both models. The temperature-dependent rate factor $A(T)$ follows in all cases the Arrhenius relation described in Cohen et al. (2018). The parameter $\theta$ is a scaling factor for the SIA proposed by Schoof (2003) that takes values between zero and one. Using a multiple-scale expansion technique, Schoof (2003) showed that the effect of higher order stresses that arise when ice flows over

a bumpy bedrock can be parametrized by multiplying a factor $\theta$ with the classical SIA ice flux. However, the primary motivation for using the method of Schoof (2003), hereafter called Schoof scheme, in PISM is to reduce and smooth spikes in the diffusivity term (Eq. 2.4) induced by locally steep terrain. This allows to use longer time steps and therefore enhances the computational speed and reduces mass conservation errors (PISM authors, 2019). The Schoof scheme assumes that the typical length scale on which the topography changes is much greater than the ice thickness but much less than the lateral extent of the ice body – an assumption that is not always fulfilled in the case of the LGM Rhine Glacier or other alpine glaciers and ice fields. A further critical assumption is that the bedrock topography must nowhere protrude above the ice surface, i.e., the Schoof scheme is not valid near nunataks or near the glacier margin (Schoof, 2003). The Schoof scheme computes a smoothed version $b_s$ of the original bedrock $b_0$ over a length scale $\lambda$ as follows:

$$b_s(x,y) \;=\; \frac{1}{4\cdot\lambda^2}\int_{-\lambda}^{\lambda}\int_{-\lambda}^{\lambda} d\zeta_1 d\zeta_2 \; b_0(x+\zeta_1, y+\zeta_2). \tag{2.5}$$

Following Schoof (2003), $\theta$ is calculated with:

$$\begin{aligned}\theta(x,y) \;=\; &\left[\frac{1}{4\cdot\lambda^2}\int_{-\lambda}^{\lambda}\int_{-\lambda}^{\lambda} d\zeta_1 d\zeta_2 \right.\\ &\left.\left(1-\frac{b_r(x,y,\zeta_1,\zeta_2)}{\widetilde{h}(x,y)}\right)^{-\frac{n+2}{n}}\right]^{-n},\end{aligned} \tag{2.6}$$

where $n$ is the Glen's flow law exponent and $\widetilde{h}$ is the difference between the ice surface elevation $H$ and the smoothed bedrock, i.e. the ice thickness relative to $b_s$:

$$\widetilde{h} \;=\; H - b_s. \tag{2.7}$$

The residual bedrock topography, $b_r$, is given by:

$$b_r(x,y,\zeta_1,\zeta_2) \;=\; b_0(x,y) - b_s(x,y,\zeta_1,\zeta_2). \tag{2.8}$$

If $\theta$ is evaluated in areas where the ratio $\frac{b_r}{\widetilde{h}}$ is close or equal to one (large residual bedrock topography compared to ice thickness), Eq. (2.6) yields a $\theta$ close or even equal to zero. This is the case for example near nunataks or at the glacial margin in valleys. As a consequence, the ice flux due to horizontal shear deformation is drastically reduced or even shut down completely in such situations. By contrast, if $\theta$ is evaluated in areas where the ratio $\frac{b_r}{\widetilde{h}}$ is close to zero (small residual bedrock topography compared to ice thickness), Eq. (2.6) yields a $\theta$ close to one and Eq. (2.4) simplifies to the unweighted ice diffusivity. In practice, PISM calculates $\theta(x,y)$ with a fourth-order Taylor approximation of Eq. (2.6) to enhance computational

efficiency. The smoothing range is commonly taken as $\lambda = 5$ km which is the value recommended by Schoof (2003) for ice sheets and used by default in PISM. At a resolution of 1 km (2 km), this corresponds to a window of $11 \times 11$ ($6 \times 6$) grid cells. Using a smaller $\lambda$ results in less smoothing in Eq. (2.5) and consequently a residual bedrock topography $b_r$ closer to zero (Eq. 2.8). This way, the ratio between residual bedrock topography and ice thickness gets closer to zero. In turn, this leads to greater values for $\theta$ and therefore a diminished SIA flux reduction. Note that the Schoof scheme vanishes if $\lambda$ is set to zero. In that case, the smoothed bedrock $b_s$ is identical to the original bedrock $b_0$, which results in Eq. (2.6) yielding $\theta = 1$ everywhere as the residual bedrock topography $b_r$ is always zero.

## 2.3 RESULTS

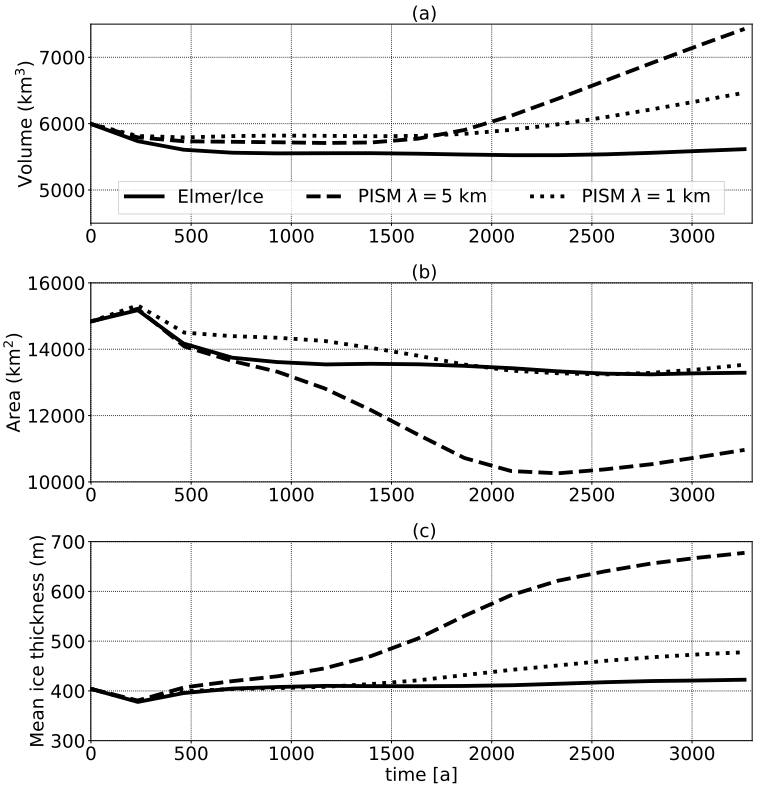


**Figure 2.2:** Temporal evolution of ice volume (a), ice covered area (b), and mean ice thickness (c) using a horizontal resolution of 1 km. The solid line represents the Elmer/Ice simulation, the dashed line PISM using $\lambda = 5$ km, and the dotted line PISM using $\lambda = 1$ km.

In this section, we present the results obtained with PISM and Elmer/Ice, the latter being taken directly from Cohen et al. (2018) and used as reference simulation. For this purpose, we initialize PISM with the geomorphologically reconstructed Rhine Glacier and run the model for 3262 years with an energy and surface mass balance forcing constant in time at a horizontal resolution of 1 km and 2 km. To compare

the PISM hybrid results with the Elmer/Ice Stokes results, we linearly interpolate the latter output to the regular grid used by PISM. We perform two simulations with PISM for each model resolution: one with the recommended value $\lambda = 5$ km for the Schoof scheme, and one with $\lambda = 1$ km ($\lambda = 2$ km for the simulation using a horizontal resolution of 2 km), which results in the smallest possible smoothing window of $3 \times 3$ grid cells and thus the smallest possible SIA flux reduction. For the detailed analysis, we use the 1 km simulations, whereas the 2 km simulations are only used in Sections 2.3.5 and 2.4.5 to investigate how the Schoof scheme interacts with model resolution. Running PISM without the Schoof scheme is not considered here because such a setup does not conserve mass reliably. The detailed comparison of the model results is carried out at the model year 3262, corresponding to the final state of the Elmer/Ice simulation of Cohen et al. (2018).

| Model | A ($km^2$) | V ($km^3$) | H (m) |
|---|---|---|---|
| Elmer/Ice | 13,291 | 5615 | 422 |
| PISM, $\lambda = 5$ km | 10,955 (–18%) | 7428 (+32%) | 677 (+60%) |
| PISM, $\lambda = 1$ km | 13,519 ( +2%) | 6466 (+15%) | 478 (+13%) |

**Table 2.1:** Glacierized area (A), ice volume (V), and mean ice thickness (H) obtained with Elmer/Ice and PISM 3262 years after initialization for the simulations using a horizontal resolution of 1 km. The percentage numbers give the deviation from Elmer/Ice.

Among the two PISM simulations using a horizontal resolution of 1 km and Elmer/Ice, the ice volume remains almost constant during the first 2000 years but starts to grow afterwards in both PISM simulations, especially in the PISM simulation with $\lambda = 5$ km (Fig. 2.2a). In all three simulations, the Rhine Glacier Piedmont Lobe retreats at the beginning and starts to slowly re-advance shortly after the year 2500 (Fig. 2.2b). The retreat is notably larger in PISM with $\lambda = 5$ km than in PISM with $\lambda = 1$ km and Elmer/Ice. The quick rise in ice covered area at the beginning of each simulations is due to nunataks that are ice-free in the initialized state but become ice covered in all three model runs. The mean ice thickness of Elmer/Ice remains almost constant over the entire 3262 years whereas PISM with $\lambda = 1$ km thickens slightly (Fig. 2.2c). In contrast, PISM with $\lambda = 5$ km thickens significantly over the modelled period. Elmer/Ice appears to be very close to an equilibrium state in the year 3262, whereas PISM with $\lambda = 1$ km and especially PISM with $\lambda = 5$ km show positive mass trends (Fig. 2.2). After 3262 years, Elmer/Ice depicts a Rhine Glacier with a glacierized area of 13,291 $km^2$, a volume of 5615 $km^3$, and thus an mean ice thickness of 422 m (Tab. 2.1). The PISM Rhine Glacier with $\lambda = 5$ km has a glacierized area 18% smaller than that of Elmer/Ice. This is mostly due to the fact that the Linth/Limmat and the Rhine Glacier Piedmont Lobes are significantly smaller (e.g. Fig. 2.3b). Simultaneously, PISM with $\lambda = 5$ km yields an ice volume 32% greater than the Elmer/Ice one. As a consequence, the mean ice thickness is overestimated by 255 m or 60%. Using PISM with $\lambda = 1$ km yields a glacierized area that agrees well with Elmer/Ice, overestimating it by only 2%.

This small area overestimation can be traced, for the most part, to the Rhine Glacier Piedmont Lobe that extends somewhat further to the east (e.g. Fig. 2.3c). The Rhine Glacier ice volume modelled by PISM with $\lambda = 1$ km is 15% greater than that of Elmer/Ice. Similarly, the mean ice thickness obtained with PISM with $\lambda = 1$ km is only 56 m or 13% greater than in Elmer/Ice.

### 2.3.1 *Shearing speeds*

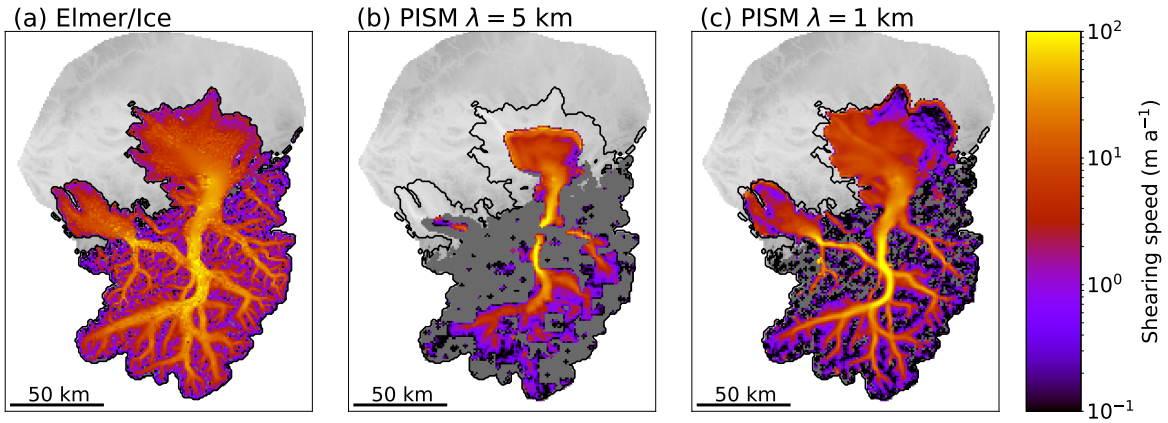


**Figure 2.3:** Shearing speeds of the 1 km simulations 3262 years after initialization modelled with Elmer/Ice (a), PISM with $\lambda = 5$ km (b), and PISM with $\lambda = 1$ km (c). Gray indicates areas where shearing speeds are exactly zero. The black line represents the ice extent produced by Elmer/Ice.

The shearing speeds (surface speed minus sliding speed) modelled by Elmer/Ice are mostly between 0.1 and 60 m $a^{-1}$ (Fig. 2.3a), whereas shearing speeds modelled by PISM range between 0 and 120 m $a^{-1}$ (Fig. 2.3b and c). In Elmer/Ice, the high shearing speeds are concentrated in the main Rhine Valley and the smaller tributary valleys. Outside the valleys the shearing speeds are small with values between 0.1 and 1 m $a^{-1}$. At the Rhine Glacier Piedmont Lobe, the Elmer/Ice shearing speeds continuously decrease towards the glacial margin in all directions. By contrast, the modelled shearing speeds in PISM with $\lambda = 5$ km are zero in most of the ice field sector of Rhine Glacier (Fig. 2.3b). Significant shearing speeds occur only at the lower main Rhine Valley and at the Rhine Glacier Piedmont Lobe. Using PISM with $\lambda = 1$ km the shearing speed pattern follows the large and most smaller valleys, similar to Elmer/Ice (Fig. 2.3c). At the ridges next to the alpine valleys the shearing speeds are smaller than 0.1 m $a^{-1}$ or zero which is significantly less than in Elmer/Ice. By contrast, the shearing speeds in the centre of the main Rhine Valley are about twice as large in PISM with $\lambda = 1$ km than in Elmer/Ice. Thus PISM with $\lambda = 1$ km captures the shearing speed pattern in the ice field sector but overestimates the high speeds and underestimates the low speeds there. At the western end of the Rhine Glacier Piedmont Lobe, shearing speeds obtained with PISM using $\lambda = 1$ km and with Elmer/Ice are very similar in magnitude and

decrease continuously towards the lobe margin. However, to the east and north the shearing speeds in PISM using $\lambda = 1$ km suddenly drop to 0.1 – 1 m $a^{-1}$, which is not the case for Elmer/Ice.

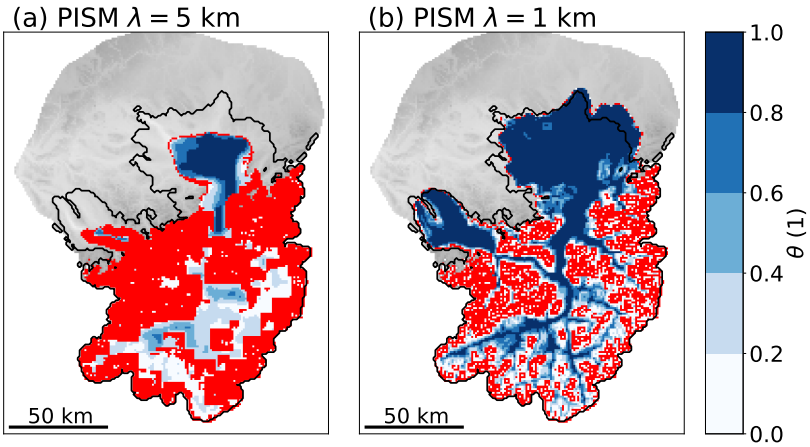


**Figure 2.4:** Spatial distribution of $\theta$ obtained with PISM using a horizontal resolution of 1 km and $\lambda = 5$ km (a) and $\lambda = 1$ km (b) 3262 years after initialization. Red indicates areas where $\theta$ is exactly zero. The black line represents the ice extent produced by Elmer/Ice.

For the two PISM simulations, the spatial distributions of the SIA ice flux limiter $\theta$ are shown in Fig. 2.4. Using PISM with $\lambda = 5$ km, $\theta$ is often zero in the alpine region of Rhine Glacier. Non-zero values for $\theta$ occur but are barely greater than 0.4. A pattern following the small or large valleys is hardly visible. $\theta$ is close to one at the centre of the Rhine Glacier Piedmont Lobe but takes smaller values towards the lobe edge. In PISM with $\lambda = 1$ km, $\theta$ values are close to one, not only at the Rhine Glacier Piedmont Lobe but also in some major alpine valleys (Fig. 2.4b). At the ridges next to the alpine valleys, $\theta$ is smaller than 0.2 and often also equal to zero as found in the PISM run using $\lambda = 5$ km.

### 2.3.2 *Sliding speeds*

The modelled sliding speeds of Elmer/Ice and PISM are mostly between 0.1 and 100 m $a^{-1}$ (Fig. 2.5). The highest speeds occur in the main Rhine Valley and the piedmont lobes. In the ice field sector of Rhine Glacier, both PISM and Elmer/Ice simulations yield similar results in terms of sliding speeds and pattern (Fig. 2.5). One exception is the diffluence of Rhine Glacier at Sargans that is produced by Elmer/Ice and PISM with $\lambda = 1$ km, but only very weak in the PISM simulation with $\lambda = 5$ km. Further, sliding speeds in the upper main Rhine Valley are larger in the PISM simulation with $\lambda = 5$ km than in Elmer/Ice (Fig. 2.5). The most notable feature is the 50 km long fast-flowing strip orientated in a north-eastward direction. Figures (2.6a) and (2.6b) compare the sliding speeds of Elmer/Ice with PISM using $\lambda = 5$ km and PISM using $\lambda = 1$ km respectively at every grid cell with ice coverage. The majority of points clusters up near the diagonal, indicating that the modelled sliding speeds of both PISM runs correlate well with the Elmer/Ice ones over the

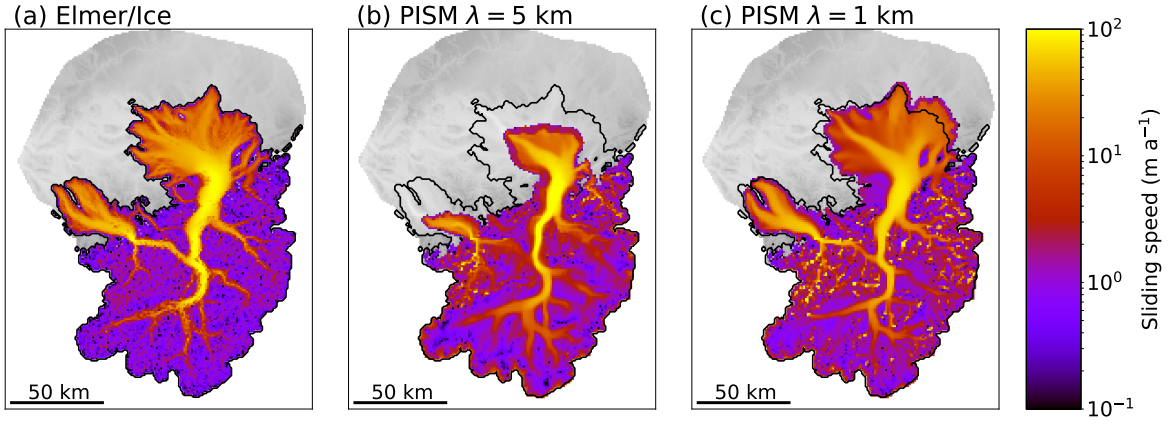


**Figure 2.5:** Sliding speeds of the 1 km simulations 3262 years after initialization modelled with Elmer/Ice (a), PISM with $\lambda = 5$ km (b), and PISM with $\lambda = 1$ km (c). The black line represents the ice extent produced by Elmer/Ice.

entire range of modelled speeds ($r = 0.79$ for PISM with $\lambda = 5$ km and $r = 0.61$ for PISM with $\lambda = 1$ km). This is particularly the case for sliding speeds greater than 10 m $a^{-1}$ (Fig. 2.6). Cold-based sliding speeds are between 0.1 and 10 m $a^{-1}$, while temperate sliding speeds are larger than 10 m $a^{-1}$.

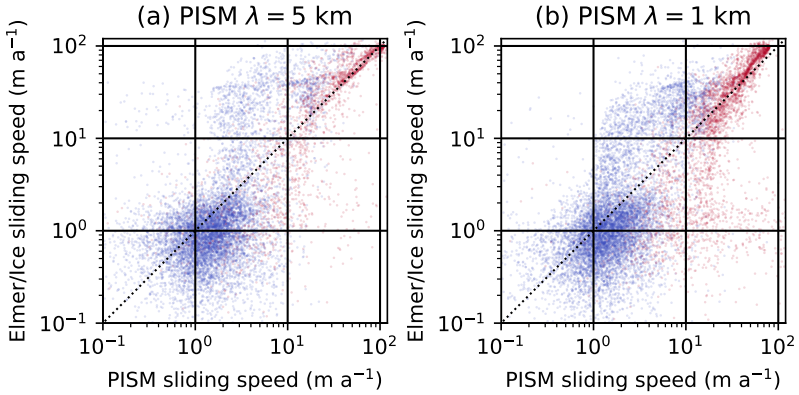


**Figure 2.6:** Sliding speeds of PISM using a resolution of 1 km vs. Elmer/Ice sliding speeds for the two different setups of PISM: $\lambda = 5$ km (a) and $\lambda = 1$ km (b). Red indicates a temperate base and blue a cold base. Dark colours indicate a clustering of dots. The ideal agreement follows the dotted diagonal. The correlation is $r = 0.79$ for $\lambda = 5$ km and $r = 0.61$ for $\lambda = 1$ km.

### 2.3.3 *Ice thickness deviation*

Differences in ice thickness between Elmer/Ice and PISM are shown in Fig. 2.7. PISM with $\lambda = 5$ km produces an ice thickness 300–500 m larger than that of Elmer/Ice in the ice field sector of Rhine Glacier, whereas the Limmat/Linth Lobe and the Rhine Glacier Piedmont Lobe are thinner and smaller than in Elmer/Ice (Fig. 2.7a). By contrast, the ice thickness of PISM with $\lambda = 1$ km agrees well with Elmer/Ice within

±100 m in the ice field sector of Rhine Glacier (Fig. 2.7b), while the Rhine Glacier Piedmont Lobe is 100–200 m thicker than in Elmer/Ice in most parts. The mean ice thicknesses of the three simulations and the deviation relative to Elmer/Ice are given in Tab. 2.1.

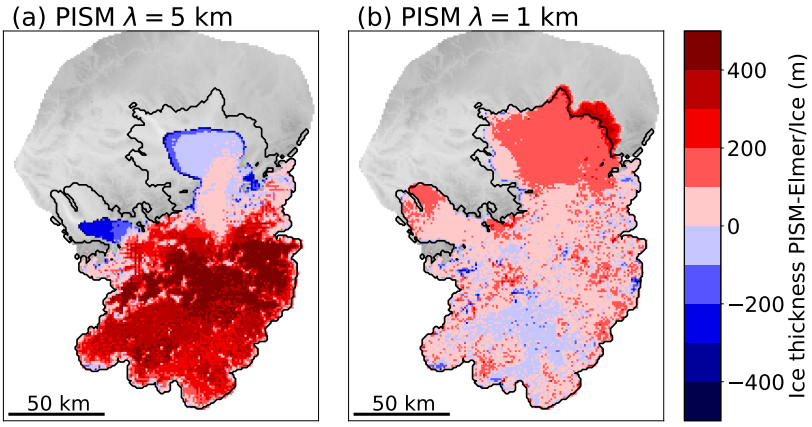


**Figure 2.7:** Modelled ice thickness deviations of the 1 km simulations between PISM with $\lambda = 5$ km and Elmer/Ice (a) and between PISM with $\lambda = 1$ km and Elmer/Ice (b) 3262 years after initialization. The black line represents the ice extent produced by Elmer/Ice.

### 2.3.4 *Basal thermal regime*

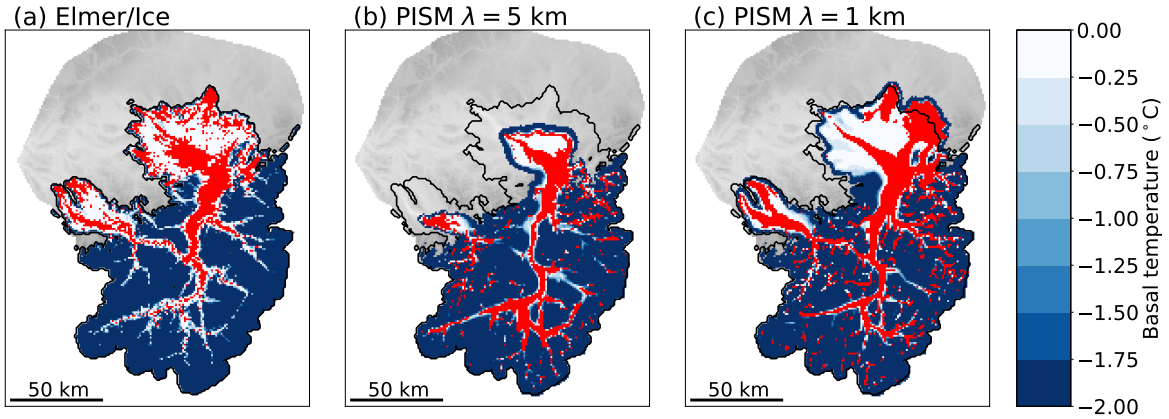


**Figure 2.8:** Basal temperatures of the 1 km simulations 3262 years after initialization modelled by Elmer/Ice (a), PISM with $\lambda = 5$ km (b), and PISM with $\lambda = 1$ km (c). Red indicates locations that are at the pressure melting point, i.e. temperate. The black line represents the ice extent produced by Elmer/Ice.

All three model runs depict Rhine Glacier as a polythermal glacier (Fig. 2.8). The mountainous area is mostly cold-based whereas the main valleys are temperate. The extent of temperate ice in the upper main Rhine Valley is greater in the results obtained with PISM than with Elmer/Ice. Especially PISM with $\lambda = 5$ km shows a much more extensive temperate area in the upper Rhine Valley part than Elmer/Ice

(Fig. 2.8b). In all three model runs, the Rhine Glacier Piedmont Lobe is temperate in a central narrow strip that is orientated to the north-west and slightly below the pressure melting point towards the lobe margin (Fig. 2.8). The Elmer/Ice run additionally shows several small patches of temperate ice outside the narrow strip, which is not the case in the two PISM simulations. In PISM with $\lambda = 1$ km, a spot in the north of the Piedmont Lobe and the area towards the north-east are entirely temperate which is clearly not the case in Elmer/Ice.

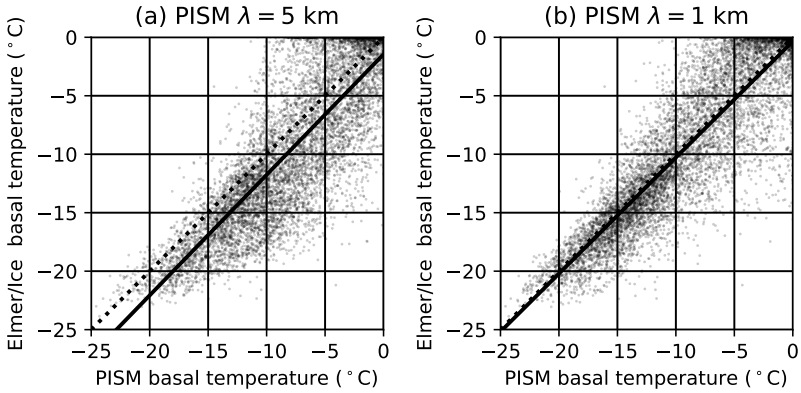


**Figure 2.9:** Basal temperatures modelled with PISM at a horizontal resolution of 1 km with $\lambda = 5$ km (a) and $\lambda = 1$ km (b) plotted against those modelled by Elmer/Ice. The solid black lines indicate corresponding linear regressions. The ideal agreement follows the dotted diagonal. The correlation is $r = 0.83$ for $\lambda = 5$ km and $r = 0.90$ for $\lambda = 1$ km.

The basal temperatures of both PISM simulations are plotted against the Elmer/Ice ones in Fig. 2.9. PISM with $\lambda = 5$ km yields basal temperatures that are on average 1.5 °C above the Elmer/Ice ones (Fig. 2.9a), whereas Elmer/Ice and PISM with $\lambda = 1$ km basal temperatures did not differ significantly, on average, at Rhine Glacier (Fig. 2.9b). The correlation of basal temperatures of Elmer/Ice and PISM with $\lambda = 5$ km is $r = 0.83$ and for Elmer/Ice and PISM with $\lambda = 1$ km $r = 0.90$.

### 2.3.5 *Using a coarser horizontal resolution*

| Model | A ($km^2$) | V ($km^3$) | H (m) |
|---|---|---|---|
| Elmer/Ice | 13,328 | 5639 | 423 |
| PISM, $\lambda = 5$ km | 10,568 (–21%) | 7358 (+30%) | 696 (+65%) |
| PISM, $\lambda = 2$ km | 12,628 (–5%) | 6447 (+14%) | 511 (+21%) |

**Table 2.2:** Glacierized area (A), ice volume (V), and mean ice thickness (H) obtained with Elmer/Ice and PISM 3262 years after initialization for the simulations using a horizontal resolution of 2 km. The percentage numbers give the deviation from Elmer/Ice.

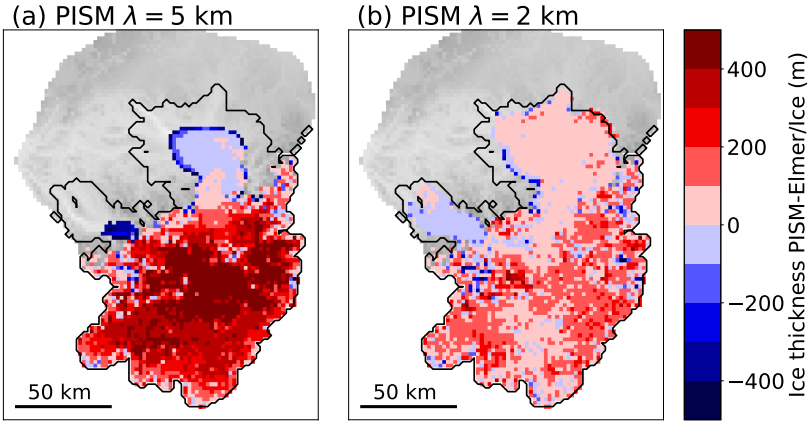


**Figure 2.10:** Modelled ice thickness deviations of the 2 km simulations between PISM with $\lambda = 5$ km and Elmer/Ice (a) and between PISM with $\lambda = 2$ km and Elmer/Ice (b) 3262 years after initialization. The black line represents the ice extent modelled with Elmer/Ice.

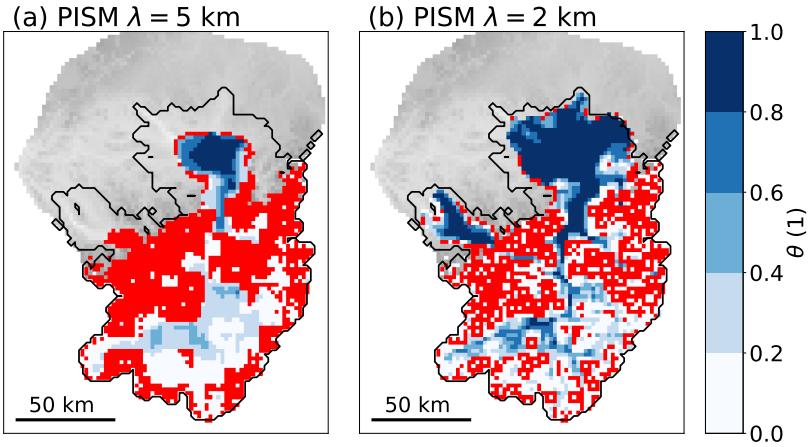


**Figure 2.11:** Spatial distribution of $\theta$ obtained with PISM using a horizontal resolution of 2 km and $\lambda = 5$ km (a) and $\lambda = 2$ km (b) 3262 years after initialization. Red indicates areas where $\theta$ is exactly zero. The black line represents the ice extent modelled with Elmer/Ice.

Running PISM with $\lambda = 5$ km at a resolution of 2 km results in an ice volume 30% greater and a mean ice thickness 65% greater than in Elmer/Ice (Tab. 2.2). Further, the glacierized area is 21% smaller than in Elmer/Ice. This is due to the reduced extent of the Linth/Limmat and Rhine Glacier Piedmont Lobes (Fig. 2.10a). In the ice field sector of Rhine Glacier, PISM with $\lambda = 5$ km produces an ice thickness 300–500 m greater than Elmer/Ice (Fig. 2.10a). $\theta$ is zero in a significant portion of the ice field and hardly reaches values larger than 0.4 (Fig. 2.11a). $\theta$ reaches values close to one only at the Rhine Glacier Piedmont Lobe. Using PISM with $\lambda = 2$ km at a resolution of 2 km results in a glacierized area only 5% smaller than in Elmer/Ice and an ice volume 14% larger than in Elmer/Ice (Tab. 2.2). The mean ice thickness is overestimated by 21% compared to Elmer/Ice. Figure 2.10b indicates that the ice thickness is overestimated by 100–200 m in the major part of the ice field sector. $\theta$ is close to one at the Piedmont Lobes (Fig. 2.11b) but hardly reaches values larger

than 0.8 in the alpine valleys. At the same time, $\theta$ is smaller than 0.2 and often zero at the mountains next to the main valleys.

## 2.4 DISCUSSION

### 2.4.1 *Using the default ice flux limiter*

Comparing results obtained with PISM using the default $\lambda = 5$ km with the reference Elmer/Ice simulation reveals comparable sliding speeds (correlation of $r = 0.79$, Fig. 2.5 and 2.6), but a significant underestimation of shearing speeds and a major ice thickness overestimation in the results obtained with PISM (Fig. 2.3 and 2.7). We attribute the few discrepancies in sliding speeds between Elmer/Ice and PISM with $\lambda = 5$ km to differences in basal temperatures. The absent diffluence at Sargans in PISM with $\lambda = 5$ km is caused by the cold-based conditions at the left branch in the PISM with $\lambda = 5$ km simulation whereas this area is temperate in Elmer/Ice (Fig. 2.8a and 2.8b). The sliding speeds in the main valley are higher than in Elmer/Ice because of the larger extent of temperate-based ice in the PISM with $\lambda = 5$ km simulation (Fig. 2.8a and b). Conversely, the poor representation of shearing speeds in PISM with $\lambda = 5$ km is caused by the scaling factor $\theta$ from the Schoof scheme that is applied to the SIA diffusivity in Eq. (2.4), with the consequence of decreasing the shearing speed to zero in most of the ice field sector of Rhine Glacier (Fig. 2.3b and Fig. 2.4a). The reduced ice flux then affects the modelled ice thickness and to a lesser extent also the basal temperatures. Because the modelled sliding speeds of PISM differ from Elmer/Ice only in a small part of the main Rhine Valley, the reduced ice flux due to shearing is compensated for by an increase in the ice thickness of 300–500 m in the ice field sector of Rhine Glacier (Fig. 2.7a). As a result of overestimated ice thickness in PISM with $\lambda = 5$ km, the total ice volume of Rhine Glacier is also overestimated by 32% (Tab. 2.1) despite the fact that the glaciated area is underestimated by 18% at the same time. Furthermore, the overestimated ice thickness in PISM using $\lambda = 5$ km better insulates the glacier bed from the cold surface temperatures, leading to 1.5 °C higher basal temperatures on average than in Elmer/Ice (Fig. 2.9a). Figure 2.2 suggests that the Elmer/Ice simulation is very close to an equilibrium state, whereas PISM using $\lambda = 5$ km shows a significant trend in ice volume, ice area, and mean ice thickness growth. Thus the deviations between PISM using $\lambda = 5$ km and Elmer/Ice would be even more substantial if the comparison was done after the year 3262.

### 2.4.2 *Improved agreement by reducing the ice flux limiter*

Using PISM with the smallest possible value of $\lambda = 1$ km instead of $\lambda = 5$ km results in a significantly improved agreement with the reference Elmer/Ice simulation in terms of shearing speeds and ice thickness. A smaller value for $\lambda$ reduces the influence of the Schoof scheme on the shearing speeds. $\theta$ is mostly one (i.e., the Schoof scheme does not affect the ice flow) at the Rhine Glacier Piedmont Lobe and a

notable portion of the ice field (Fig. 2.4b), resulting in shearing speeds more similar to those obtained with Elmer/Ice. However, notable deviations from Elmer/Ice shearing speeds remain at some parts of the Rhine Glacier Piedmont Lobe and the main Rhine Valley. PISM shearing speeds become significantly smaller compared with in Elmer/Ice towards the northern and eastern lobe margins while they are similar in the western margin. This pattern correlates with the distribution of cold-based and temperate areas (Fig. 2.8c). In PISM with $\lambda = 1$ km, there are no cold-based areas in the parts of the lobe with small shearing speeds. By contrast, the western part of the lobe is mostly cold-based (Fig. 2.8c) and shearing speeds are greater, comparable to the Elmer/Ice results. The reason for this correlation between temperate areas and low shearing speeds might be that the continuously temperate bed lowers the basal resistance and as a consequence reduces the surface slope which in turn reduces horizontal shearing. The parameter $\theta$ close to one brings about larger shearing speeds in the ice field sector than in PISM with $\lambda = 5$ km. These larger shearing speeds are more similar to Elmer/Ice in terms of pattern and amplitude (Fig. 2.3). Yet, in the middle of the main Rhine Valley, shearing speeds in PISM with $\lambda = 1$ km are up to two times larger than in Elmer/Ice. This is in line with findings by Le Meur et al. (2004) and Adhikari and Marshall (2013), who have also observed that the shearing speeds in the centre of a valley can be two to three times larger in SIA models than in Stokes models. Although their comparison studies were performed with a setup quite different from Rhine Glacier during the LGM (temperate valley glaciers with a length of 3–4 km and neglected sliding), the overestimated shearing speeds in valley glaciers occurs for the same reason: lateral and longitudinal stresses that add resistance to the ice flow are neglected in the SIA. Despite the improvements with respect to $\lambda = 5$ km, $\theta$ remains close to or at zero almost everywhere beyond the valley glaciers causing shearing speeds to be much smaller than in Elmer/Ice (Fig. 2.3c). The improvements in the shearing speeds also affect the modelled ice thickness. Using $\lambda = 1$ km, the modelled ice thickness of PISM deviates by less than $\pm$100 m from Elmer/Ice over most parts of Rhine Glacier (Fig. 2.7b). This is significantly better than the 300–500 m of ice thickness overestimation when using $\lambda = 5$ km and comparable to the uncertainties in trimeline-based ice surface elevation reconstructions in the Alps (Florineth, 1998; Florineth and Schlüchter, 1998). As a consequence, the overestimation in total ice volume relative to Elmer/Ice is reduced from +32% with $\lambda = 5$ km to only +15% with $\lambda = 1$ km and at the same time matching the ice extent calculated by Elmer/Ice (Tab. 2.1). The overestimated ice volume in PISM with $\lambda = 1$ km is mostly due to the lobe being 100–200 m thicker than given by Elmer/Ice. In contrast to Elmer/Ice, PISM using $\lambda = 1$ km shows a small growing trend in ice volume, ice area, and mean ice thickness growth (Fig. 2.2). Thus the deviations between PISM using $\lambda = 1$ km and Elmer/Ice would likely become larger if a comparison was done after the year 3262.

### 2.4.3 *Suitability of hybrid dynamics to model ice fields*

Our model results highlight the fact that the sliding speeds obtained by applying the PISM hybrid model agree reasonably with Elmer/Ice Stokes model. This supports the use of the SSA to compute sliding speeds as implemented in PISM. By contrast, calculating shearing speeds with the SIA is not always appropriate for an ice field like Rhine Glacier. In the mountainous terrain above the alpine valleys, the Schoof scheme scales the shearing speeds to zero and thus it is not clear from our comparison study how the SIA alone would perform in these areas. Nonetheless, Le Meur et al. (2004) found a strong correlation between steep bedrock gradients and increasingly overestimated SIA shearing speeds, which suggests that the hybrid model would likely fail as well to represent the ice dynamics in the steep part of Rhine Glacier like the mountains flanking the valley glaciers. By contrast, the SIA model performs reasonably well in the open plain where the Piedmont Lobe is situated (Fig. 2.3c). Despite the shortcomings of the SIA, the hybrid model with a flux limiter is capable of reproducing the Stokes ice thickness in the alpine valleys within $\pm 100$ m and matches the modelled extent of the Stokes model. The mean ice thickness is only 13% greater than in Elmer/Ice. Thus it is feasible to envisage employing a hybrid model at an ice field like Rhine Glacier during the LGM, but a detailed interpretation of shearing speeds in the valleys should be undertaken with care.

### 2.4.4 *Influence of the ice flux limiter on the ice thickness*

Our comparison study reveals that the capability of PISM to model Rhine Glacier in agreement with the Elmer/Ice Stokes model depends very much on the choice of the parameter $\lambda$ in the Schoof scheme. Using the default value of $\lambda = 5$ km, which is the recommended value for ice sheets, drastically reduces the ability of PISM to model shearing speeds and ice thickness in a reasonable way within complex and steep topographies such as the ice field sector of Rhine Glacier. More fundamentally, shearing speeds exactly equal to zero are clearly not expected in steep valleys and thus indicate that $\lambda = 5$ km is not a meaningful choice for modelling an ice field like Rhine Glacier. By reducing the effect of the Schoof scheme (i.e. $\lambda = 1$ km), shearing speeds can be recovered to some extent, and we obtain an ice thickness comparable to the Elmer/Ice results. The difference between using PISM with $\lambda = 5$ km and $\lambda = 1$ km seems to be more significant than between Elmer/Ice and PISM using $\lambda = 1$ km. This indicates that the choice for $\lambda$ is a key decision for applications like Rhine Glacier. However, the degree of ice thickness overestimation caused by the Schoof scheme might also depend on the parametrization of sliding. Indeed, the ice flux arises solely from the SSA (i.e., is governed exclusively by sliding) in areas where the Schoof scheme reduces shearing speeds to zero. Thus a different parametrization of sliding than in this study might well affect the ice thickness overestimation in a different way.

### 2.4.5 *Interaction between the Schoof scheme and model resolution*

When PISM is used with the default value $\lambda = 5$ km, the choice between a horizontal resolution of 1 km or 2 km does not seem to have a notable influence on the agreement with Elmer/Ice (Fig. 2.7a, 2.10a). In both cases, the ice thickness is similarly overestimated, which is caused by the Schoof scheme that reduces shearing speeds to zero at a major part of Rhine Glacier (Fig. 2.11a). If PISM is used at horizontal resolutions of 1 km and 2 km with the smallest non-zero value for $\lambda$ (i.e. $\lambda = 1$ km and $\lambda = 2$ km), the ice extent is in both cases consistent with Elmer/Ice but small differences in ice thickness overestimation emerge (Fig. 2.7b and 2.10b). In more detail, the PISM simulation using a resolution of 2 km and $\lambda = 2$ km overestimates the mean ice thickness by 88 m (+21%) whereas the mean overestimation for the simulation using a resolution of 1 km and $\lambda = 1$ km is only 56 m (+13%). In more detail, Fig. 2.7b and 2.10b suggest that the ice excess in the 2 km simulation is located predominantly in the ice field sector instead of at the Rhine Glacier Piedmont Lobe as it was the case in the 1 km simulation. We attribute this to the $\theta$ values in the main Rhine Valley which are smaller in the 2 km simulation than in the 1 km simulation (Fig. 2.4b and 2.11b). Thus, reducing $\lambda$ to its minimum value results in a significantly improved agreement with Elmer/Ice at horizontal resolutions of both 1 km and 2 km. Yet, the PISM results using a resolution of 2 km differ a bit more from the ones of Elmer/Ice. This is likely not only due to the Schoof scheme which yields slightly smaller $\theta$ values but also because a horizontal resolution of 2 km does not resolve the topography as well at a resolution of 1 km.

### 2.4.6 *Computational speed of PISM*

It must be stressed that achieving the improvements in shearing speeds and ice thickness of PISM by reducing $\lambda$ from 5 km to 1 km causes the computational time to roughly double. PISM integrates the ice dynamics explicitly with the forward-time central-space scheme using adaptive time stepping (Bueler and Brown, 2009). PISM takes the largest possible time step that maintains numerical stability in the SIA, the SSA and the enthalpy model. In our model setup it is almost always the SIA that requires the shortest time step. The largest possible time step for the SIA is proportional to the inverse of the highest SIA diffusivity (Eq. 2.4) on the model domain (Hindmarsh, 2001), which is controlled by the Schoof scheme in our case. Indeed, smaller $\lambda$ values (e.g. 1 km) allow for higher diffusivities, but then require shorter time steps, and therefore increase the computational time. Thus, there is a trade-off between improved computational efficiency and misrepresented shearing speeds and ice thicknesses when using the Schoof scheme to reduce computational time. The higher computational costs are a drawback for applying the $\lambda = 1$ km setup of PISM on longer periods like the last glacial cycle (120,000 years), or over the entire Alps (15 times larger area than Rhine Glacier) (Seguinot et al., 2018).

### 2.4.7 *Implications for previous PISM applications in the European Alps*

The significantly increased ice thickness resulting from the default setting in the Schoof scheme in PISM ($\lambda = 5$ km) raises the question whether it can explain the systematic overestimation found in previous PISM-based paleo modelling of the AlpIF (Becker et al., 2016; Becker et al., 2017; Seguinot et al., 2018). Among these studies, it is only Seguinot et al. (2018) who state the value of $\lambda$ they used. In their study, PISM was run with $\lambda = 5$ km. Unfortunately, they do not give ice thickness deviations for Rhine Glacier but for a larger neighbouring glacier, the Rhone Glacier. For this glacier, they found ice thickness overestimations averaging to 861 m (Seguinot et al., 2018) in the valley part, which is 1.5–3 times greater than what we have found for the valley part of Rhine Glacier. Nevertheless, a direct extrapolation of the ice thickness overestimation from Rhine Glacier to Rhone Glacier is difficult because the latter is considerably larger and includes significantly higher mountain peaks upon which the Schoof scheme might react differently. Apart from this, the earlier ice thickness overestimations are referenced to the geomorphologically reconstructed ice thicknesses and not a Stokes reference simulation like in this study. Further, Seguinot et al. (2018) used different sliding and mass balance parametrizations than this study. Thus a closer investigation is necessary to pin down in detail to what percentage the former ice thickness overestimations were caused by the Schoof scheme. But since Seguinot et al. (2018) used $\lambda = 5$ km, it seems likely that at least a part of their ice thickness overestimation was caused by their choice of $\lambda$.

## 2.5 CONCLUSIONS

We performed four simulations of Rhine Glacier during the LGM using the hybrid model PISM. Two simulations used a horizontal resolution of 1 km and two used 2 km. For each PISM resolution pair, we tested two degrees of flux limitation for the SIA: the default $\lambda = 5$ km and the smallest possible value for $\lambda$ which is equal to the model resolution. The model setup was very similar to the one employed earlier by Cohen et al. (2018) who used the Stokes model Elmer/Ice instead. We compared the PISM simulations to the reference Elmer/Ice simulation in terms of modelled ice speeds, ice thickness and basal temperatures in order to assess the ability of hybrid models to simulate ice fields and piedmont lobes. Based on this comparison we draw the following conclusions:

1. Using the default degree of ice flux limitation for PISM causes a strong underestimation of shearing speeds. As a consequence, the ice thickness in the ice field sector is overestimated by 300–500 m compared to Elmer/Ice. This mechanism has the potential to explain a sizeable part of the ice thickness overestimations found by earlier studies employing PISM in the European Alps. Nonetheless, a specialized study is necessary to illuminate this in detail because this study differs from earlier studies in the sliding and mass balance parametrizations as well as the reference ice thickness.

2. Using the weaker flux limiter, the hybrid SIA/SSA ice flow dynamics capture the large-scale dynamics at our ice field in good agreement with the Stokes ice dynamics. Sliding speeds and basal temperatures show a good agreement between the two models. Altough SIA shearing speeds remain overestimated in the main valleys, the hybrid scheme reproduces the Stokes ice thickness and extent well. However, the improved setup comes with increased computational costs.

There are some limitations of our study that are important to keep in mind. Our assessment of the hybrid scheme is specific to our choice for ice flow parameters as well as the parametrization of sliding. Further, the Schoof scheme might affect the modelled ice thickness and shearing speeds more strongly at smaller stages of Rhine Glacier or for glaciers located in more complex and steeper terrain. Using a different parametrizations of sliding might impact how the Schoof scheme affects modelled shearing speeds and ice thickness. For future studies involving applications similar to the one presented here, we strongly recommend evaluating the influence of the Schoof scheme on the PISM results and choose an appropriate $\lambda$. In our case, the best model results were achieved using $\lambda$ equal to the model resolution.

## ACKNOWLEDGEMENTS

MI is supported by the Swiss National Science Foundation (SNSF), project 200021-162444. JS was supported by SNSF project 200020-169558 and 200021-153179/1 to MF. MI is grateful to Kolumban Hutter for the interesting discussions, to Everarda van Dongen for the feedback on visualisations, and to Simon Förster for the support in Python and C++. Development of PISM is supported by NASA grant NNX17AG65G and NSF grants PLR-1603799 and PLR-1644277. We thank Tong Zhang and the anonymous referee for their comments which contributed to improve the manuscript.

# 3

# MODELLING THE ALPINE ICE FIELD OF THE LAST GLACIAL MAXIMUM WITH REGIONAL CLIMATE MODEL DATA

*"Der Gewalt fehlt es an Stärke wenn der Verstand die Überhand gewinnt."*

— Vier Fäuste für ein Halleluja (1971)

## 3.1 INTRODUCTION

The last glacial cycle began about 115 kiloannum Before the Present (ka BP) and has lasted until today. During a major part of the cycle, the European Alps hosted a large ice field, the Alpine Ice Field (AlpIF). The glaciers advanced and retreated during this period and reached their maximum stand during the Last Glacial Maximum (LGM) between 26 and 24 ka BP after which they retreated with smaller readvances (Hughes et al., 2013; Ivy-Ochs, 2015; Monegato et al., 2017; Preusser et al., 2011; Wirsig et al., 2016). In the European Alps, the glaciers imprinted erosion marks and left behind moraines and erratic boulders on their path. Such geomorphological evidence is fairly abundant and well dated for the LGM (e.g. Kelly et al., 2004; Wirsig et al., 2016). Therefore, the maximum ice extent during the LGM is well known today (Fig. 3.1, Bini et al., 2009; Ehlers et al., 2011; Geologische Bundesanstalt, 2013). There was also an older major glaciation during the last glacial cycle: the Marine Isotope Stage 4 (MIS4) at about 65 ka BP. Most evidence in the Alps from this period was erased by the glaciation during the LGM and therefore the MIS4 is much less understood than the LGM (Ivy-Ochs et al., 2008). There is evidence that the AlpIF extended beyond the LGM margin in the west of the Alps (Guiter et al., 2005) but remained within the later LGM advance elsewhere in the east (Reitner, 2005). So far, not enough evidence from the MIS4 has been discovered that would allow to reconstruct a maximum ice extent.

Several authors applied ice flow models to the AlpIF during the last glacial cycle. These studies shed light into past ice dynamics of the AlpIF and the climate driving it (e.g. Becker et al., 2016; Jouvet et al., 2017; Seguinot et al., 2018). Due to the lack of comprehensive LGM climate data, they all relied on present-day climate datasets and applied manipulations to them to approximate LGM conditions. Accordingly, Becker et al. (2016) inferred that the precipitation rates in the north might have been dryer than in the south as opposed to today's precipitation rates in order to match the geomorphologically reconstructed maximum ice extent of Ehlers et al. (2011). Likewise, Jouvet et al. (2017) demonstrated that the present-day precipitation pattern is not consistent with trajectories of boulders with known origin at Rhone Glacier. Seguinot et al. (2018) extended the modelling to the entire last glacial cycle of the AlpIF. They obtained model results depicting a too restricted glaciation in the south-west of the AlpIF. Therefore, they also suggested that different-from-today

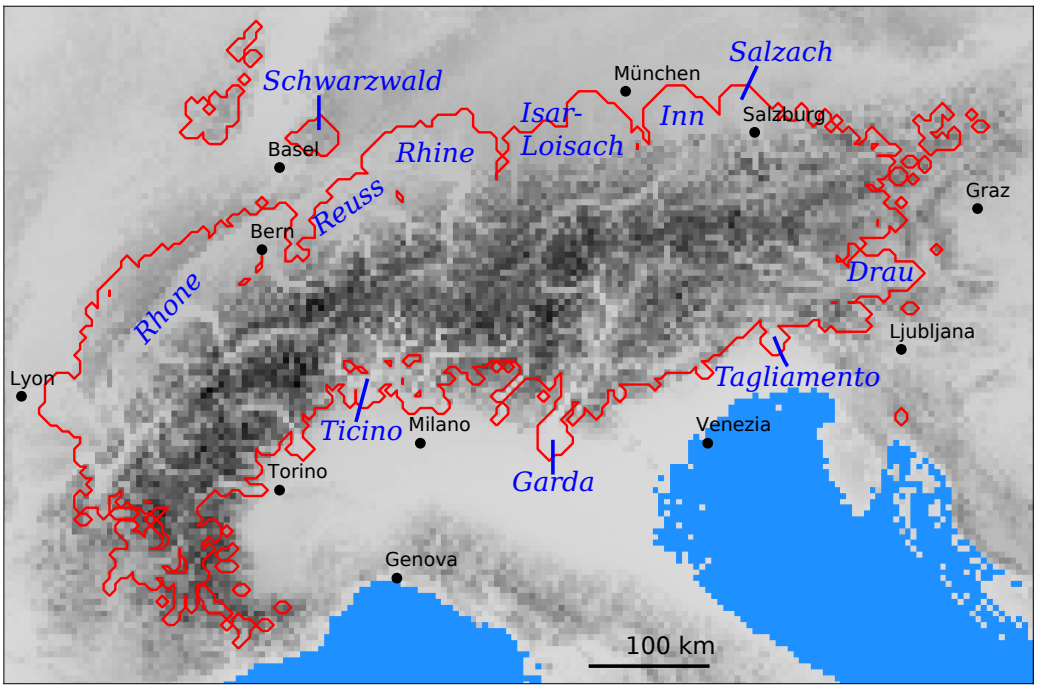


**Figure 3.1:** Map of the European Alps. The red outlines indicate the geomorphologically reconstructed maximum ice extent of the Alpine Ice Field during the Last Glacial Maximum of Ehlers et al. (2011). Names of glaciers are in blue italics.

temperature or precipitation patterns prevailed around the LGM. Thus, these studies emphasize that the lack of more representative climate data for the LGM climate in the Alps has so far represented a key limiting factor for modelling the AlpIF in agreement with geomorphological evidence. Višnjević et al. (2020) inferred possible climatic conditions prevailing during the LGM with an inverse model. They deduced equilibrium line altitudes from the geomorphologically reconstructed maximum ice extent using a simple ice flow model with an elevation dependent mass balance. Their main finding was an increase in the equilibrium line altitude from west to east and from north to south in the Alps. They concluded that this finding suggests that a zonal-circulation dominated conditions during the LGM meaning moisture arrived mainly from the west.

Today, a discrepancy remains between ice surface elevations obtained with ice flow modelling and inferred from geomorphological erosion marks (trimlines). Ice flow models repeatedly yield ice surface elevations 500–861 m greater than the erosion marks (Becker et al., 2016; Seguinot et al., 2018). This could partly be attributed to a flux limiting scheme that artificially creates up to 500 m of excess ice (Section 2 or Imhof et al. (2019)).

Global Climate Models (GCMs) simulating the climate during the LGM depicted a profoundly different-from-today climate (Hofer et al., 2012b; Hofer et al., 2012a; Löfverström et al., 2014; Merz et al., 2015). An important feature that the GCMs showed is a more zonal, southward shifted, and intensified North Atlantic storm track, which resulted in increased winter precipitation in the North Atlantic area

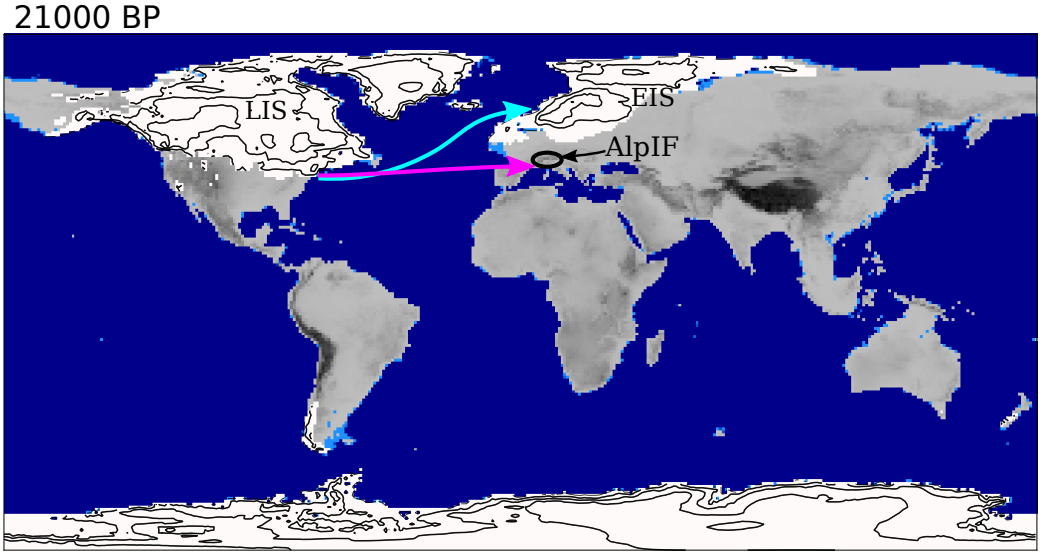


**Figure 3.2:** Continental ice sheets (white) at 21 ka BP from the ICE-7G dataset (Roy and Peltier, 2018). Labels identify the Eurasian Ice Sheet (EIS), the Laurentide Ice Sheet (LIS), and the Alpine Ice Field (AlpIF). Generalized present-day (turquoise) and Last Glacial Maximum (magenta) North Atlantic storm tracks after Woollings (2016) and Löfverström (2020). Black contour lines have an elevation spacing of 1000 m.

and south-western Europe during the LGM (Fig. 3.2). This southward shift and zonalisation was caused by the Laurentide Ice Sheet (Fig. 3.2) in North America as it expanded southwards and displaces the jet stream further south (Löfverström et al., 2016). The North Atlantic storm track then channeled humidity towards the European Alps. Therefore, GCMs suggested a rather zonal moisture transport arriving from west to the Alps during the LGM (Löfverström, 2020). This somewhat contradicted meteoric $\delta^{18}O$ records in speleothemes from north of the Alps that suggested a dominant moisture source south of the Alps (Luetscher et al., 2015). In any case, it is poorly understood today how variations in the Laurentide Ice Sheet geometry and the related changes in the position and direction of the North Atlantic storm track affected the glaciation in the Alps.

The GCMs are restricted to horizontal resolutions of hundreds of kilometres due to computational limitations. Therefore, they are unable to resolve the climate at smaller scales such as valleys in the European Alps and unable to capture crucial orographic effects that govern precipitation in mountainous terrain. Beside the GCMs there are also Regional Climate Models (RCMs), climate models that use a GCM as boundary condition and then dynamically downscale the climate step by step to a more refined resolution using several nested subdomains over the target area. The advantage of RCMs is that they can drastically increase the horizontal model resolution over this specific area at affordable computational costs. Recently, Velasquez et al. (2020), Velasquez and Raible (in prep), and Velasquez (in prep) dynamically downscaled the GCM datasets of Hofer et al. (2012b) and Merz et al. (2015) representative for the climates of today and two cold periods with

major glacier advances in the Alps during the last glacial cycle. They downscaled the GCM climate from a horizontal resolution of $1^\circ \times 1^\circ$ (corresponds roughly to 78 km $\times$ 111 km at a latitude of $45^\circ$) to a resolution of $2 \times 2$ km over the European Alps which allowed to resolve orographic precipitation. To our knowledge, this is the first time climate data representative for cold periods with major glaciations during the last glacial cycle resolves the climate at such a high resolution in the Alps. Therefore, these new climate datasets open new opportunities for paleo ice flow modelling in the Alps. Similar combinations of RCMs and ice flow models have appeared recently and proved to be promising for present-day and near future simulations at ice fields and ice caps (e.g. Schmidt et al., 2020; Ziemen et al., 2016). The two cold periods that Velasquez et al. (2020) and Velasquez and Raible (in prep) downscaled were the LGM at 21 ka BP (commonly known as 'global LGM', Hughes and Gibbard, 2015) and the MIS4 at 65 ka BP.

The main objectives of this study are:

- to investigate how variations in the climate triggered by changes in the ice surface elevation of the northern hemisphere ice sheets affect the modelled ice extent in the Alps,
- to explore whether the discrepancy between modelled and reconstructed surface elevation of the AlpIF affects orographic precipitation enough to have a feedback on the AlpIF itself,
- to evaluate the general benefit and potential of using RCM-based data to drive an ice flow model during the LGM.

In this study, we model the extent and the evolution of the AlpIF using the RCM-based paleo climate datasets of Velasquez et al. (2020) and Velasquez and Raible (in prep). They assembled several versions of downscaled climate datasets which are based on variations in surface elevation of the Laurentide Ice Sheet, the Eurasian Ice Sheet, and the AlpIF (Fig. 3.2). From these climate datasets, transient climate forcings are constructed using a temperature reconstruction from Antarctica. In order to model ice flow, thermodynamics, and mass balance of the AlpIF, we employ the Parallel Ice Sheet Model (PISM authors, 2019).

Section 3.2 describes the ice flow model along with the climate data and the transient climate forcings. The model results are presented in Section 3.3 and the discussion of the results is given in Section 3.4. A conclusion is drawn in Section 3.5.

## 3.2 METHODS AND DATA

We employ the Parallel Ice Sheet Model version 1.1 (PISM, PISM authors, 2019; Winkelmann et al., 2011) to perform transient ice flow simulations of the last glaciation in the European Alps using modelled high-resolution climate data. Here, we describe the ice flow model PISM, the climate data, and how the climate forcing is constructed.

### 3.2.1 *Ice flow model*

PISM is a three-dimensional ice sheet model that simulates the ice flow, the surface mass balance, and the ice and bedrock temperature. It employs a superposition of shallow ice approximation (SIA, Hutter, 1983) and shallow shelf approximation (SSA, Weis et al., 1999) to calculate the ice transport due to horizontal shearing and basal sliding respectively. We employ the Patterson-Budd law (PISM authors, 2019) for the temperature-dependent rate factor $A(T)$ of the SIA and the SSA. PISM uses the SIA in combination with a scheme that reduces the ice-flux (Schoof, 2003). This scheme uses a smoothed bedrock topography and parametrizes higher order stresses that arise when an ice sheet flows over bumpy bedrock at a length scale $\lambda$. We follow Imhof et al. (2019) who recommends using a value for $\lambda$ equal to the horizontal model resolution to prevent overestimation of the ice thickness. To calculate sliding velocities, we employ a linear sliding law for the SSA, similar to Chapter 2 (for more details see Appendix A).

To model englacial and bedrock temperature, PISM uses an enthalpy model (Aschwanden et al., 2012) with a constant vertical resolution of 50 m in the ice and 100 m in the bedrock. The thermal boundary conditions are the annual mean air temperature at the surface and the geothermal heat flux of Goutorbe et al. (2011) at the bottom of a 3 km thick bedrock.

To model the surface mass balance, a positive degree day (PDD) model is employed (Hock, 2003; PISM authors, 2019; Seguinot, 2013). Ablation is proportional to the integral of positive Celsius temperature over time, the so-called positive degree days. Accumulation is equal to the precipitation for temperatures below the freezing point and decreases linearly to zero between 0 °C and 2 °C. The mass balance model used here takes monthly average temperature and precipitation, as well as temperature standard deviation as inputs (Section 3.2.3). Therefore, it takes into account sub-monthly temperature variations by assuming normally distributed temperature variations around the mean monthly value. To calculate the ablation, the positive degree days are multiplied with a degree day factor $DDF$ that is different for snow ($DDF_s$) and ice ($DDF_i$). 60% of the melt is assumed to refreeze while the rest is removed from the model (Braithwaite et al., 1994; Reeh, 1991). For the degree day factors, $DDF_s = 0.006$ m d$^{-1}$ °C$^{-1}$ and $DDF_i = 0.016$ m d$^{-1}$ °C$^{-1}$ has been used for snow and ice respectively. This choice for the $DDF$s resulted in a reasonable glacier extent using a steady state present-day climate. These are rather high values for $DDF$s but still in the range of measured values (Hock, 2003).

The model bedrock elevation is taken from Jarvis et al. (2008) interpolated to a regular grid with a horizontal resolution of 5 km. Today's glaciers have not been removed from the bedrock as they are small compared to the glaciers of the last glacial cycle and in any case cannot be resolved properly using the 5 km resolution. We apply PISM to a rectangular subdomain (900 km × 600 km) of this bedrock elevation dataset which covers the entire European Alps (Fig. 3.1). At the domain boundary, a Dirichlet boundary condition is applied by setting the ice thickness to zero.

### 3.2.2 *Climate data*

The climate data used to drive the ice flow model PISM is taken from Velasquez et al. (2020) and Velasquez and Raible (in prep). They used a Regional Climate Model (RCM), the Weather Research and Forecast model (WRF, Skamarock et al., 2008), to dynamically downscale five Global Climate Model (GCM) simulations of Hofer et al. (2012b) and Merz et al. (2015) from a horizontal resolution of $1° \times 1°$ to a horizontal resolution of $2 \times 2$ km. This RCM takes the GCM as boundary condition and gradually increases the resolution over four nested subdomains within a specified region on the globe. The outermost subdomain covers entire Europe and the innermost with the most refined resolution covers solely the European Alps (Fig. 3.3).

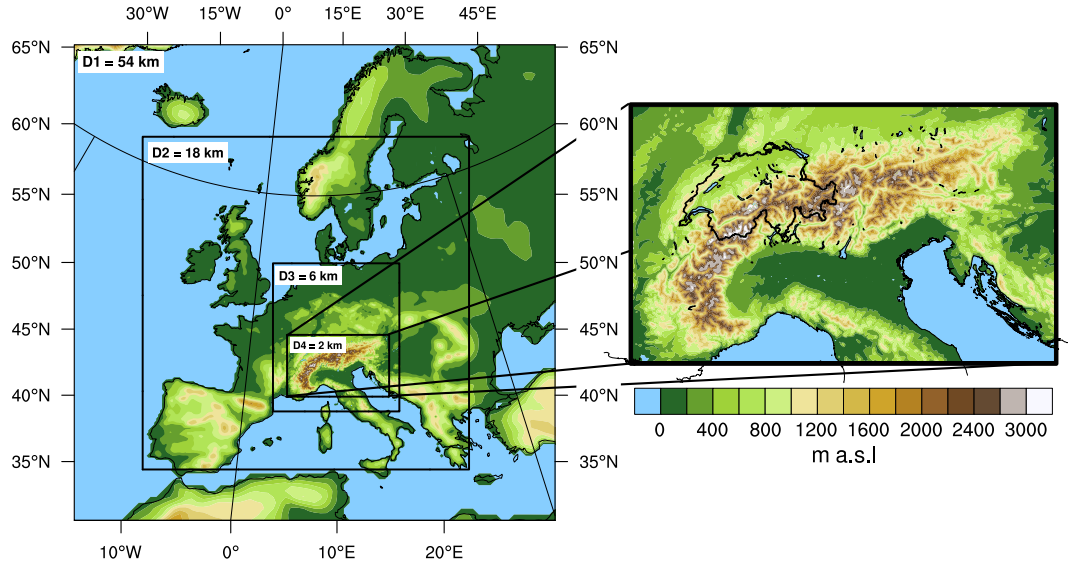


**Figure 3.3:** The four nested subdomains used by the regional climate model Weather Research and Forecast model shown along with the present-day topography. The number in the upper left corner of each subdomain indicates its lateral resolution. Modified from Velasquez et al. (2020).

The GCM datasets of Hofer et al. (2012b) and Merz et al. (2015) are for Present-Day (PD), Last Glacial Maximum (LGM), and Marine Isotope Stage 4 (MIS4) conditions, here designated with the superscript $G$ for 'global' (Tab. 3.2). The PD$^G$ and the LGM$^G$ run used an orbital and atmospheric forcing for the year 1990 and the year 21 ka BP respectively (Tab. 3.1). Additionally, the LGM$^G$ run used adjusted vegetation and soil types, the ICE-5G ice sheet reconstruction of Peltier (2004) (21 ka BP) for the Eurasian Ice Sheet (EIS) and the Laurentide Ice Sheet (LIS), and a sea level lowered by 120 m. The MIS4$^G$ runs used an orbital and atmospheric forcing for the year 65 ka BP and three different surface elevations for the LIS and the EIS (Tab. 3.1). Like the LGM$^G$ run, the MIS4$^G_{NH100}$ run employed the ice surface elevation from the LGM 21 ka ago, whereas in MIS4$^G_{NH67}$ and MIS4$^G_{NH125}$ these ice thicknesses were scaled to 67% and 125% respectively for the LIS and the EIS. The subscript $NH$ in the MIS4 simulations indicates the scaling for the Northern Hemisphere Ice Sheets

| | PD | LGM | MIS4 |
|---|---|---|---|
| Total solar irradiation (W $m^{-2}$) | 1361.77 | 1360.89 | 1360.89 |
| Eccentricity | 0.016708 | 0.018994 | 0.020713 |
| Obliquity (°) | 23.441 | 22.949 | 22.564 |
| Angular precession (°) | 102.72 | 114.43 | 15.22 |
| $Co_2$ (ppm) | 353.9 | 185 | 205 |
| $CH_4$ (ppb) | 1693.6 | 350 | 460 |
| $N_2O$ (ppb) | 310.1 | 200 | 210 |
| Sea level offset rel. today (m) | 0 | –120 | –80 |

**Table 3.1:** This table shows the atmospheric and orbital forcing used in the present-day (PD), the Last Glacial Maximum (LGM), and the Marine Isotope Stage 4 (MIS4) global climate model simulation of Hofer et al. (2012b) and Merz et al. (2015) along with the sea level offset relative to the present.

(LIS+EIS) in the GCM. In all $MIS4^G$ simulations, the sea level is lowered by 80 m with respect to today. Hofer et al. (2012b) used an LGM bathymetry and topography for the MIS4 simulations which do not represent MIS4 conditions correctly in the GCM simulations. Further, there is no maximum ice extent reconstruction for the Alpine Ice Field (AlpIF) of the MIS4. Therefore, the three MIS4 simulations serve solely to evaluate how the size of the continental ice sheets influence the glaciation in the Alps (Hofer et al., 2012b). A modelled reconstruction of the AlpIF during the MIS4 is not anticipated here.

| GCM run | RCM run | length | $T_{lowland}$ | $TSA_{lowland}$ | $P_{lowland}$ | $P_{alps}$ |
|---|---|---|---|---|---|---|
| $LGM^G$ | $LGM_{E100}$ | 30 a | -3.6 °C | 22.96 °C | 0.87 m $a^{-1}$ | 1.13 m $a^{-1}$ |
| $LGM^G$ | $LGM_{E50}$ | 12 a | -4.19 °C | 22.38 °C | 0.92 m $a^{-1}$ | 1.2 m $a^{-1}$ |
| $LGM^G$ | $LGM_{E150}$ | 12 a | -3.82 °C | 22.45 °C | 0.91 m $a^{-1}$ | 1.2 m $a^{-1}$ |
| $LGM^G$ | $LGM_{alpsless}$ | 21 a | -3.85 °C | 23.19 °C | 0.88 m $a^{-1}$ | 1.09 m $a^{-1}$ |
| $PD^G$ | PD | 30 a | 9.65 °C | 17.95 °C | 1.0 m $a^{-1}$ | 1.42 m $a^{-1}$ |
| $MIS4^G_{NH67}$ | $MIS4_{NH67}$ | 21 a | -1.2 °C | 20.67 °C | 0.85 m $a^{-1}$ | 1.13 m $a^{-1}$ |
| $MIS4^G_{NH100}$ | $MIS4_{NH100}$ | 21 a | -2.05 °C | 21.44 °C | 0.97 m $a^{-1}$ | 1.26 m $a^{-1}$ |
| $MIS4^G_{NH125}$ | $MIS4_{NH125}$ | 21 a | -2.12 °C | 21.13 °C | 0.98 m $a^{-1}$ | 1.25 m $a^{-1}$ |

**Table 3.2:** Overview of Global Climate Model (GCM) runs, the corresponding downscaled Regional Climate Model (RCM) runs along with the length of the RCM datasets. The table also lists annual mean temperature 100 m above the surface (T) and precipitation (P) as well as the temperature seasonal amplitude 100 m above the surface (TSA) on the lowlands and within the Alps (outside/within the geomorphologically reconstructed maximum ice extent of Ehlers et al. (2011), Fig. 3.1).

| RCM dataset | Description |
|---|---|
| $LGM_{E100}$ | Climate data representative for the LGM at 21 ka BP. It is treated as reference LGM climate here. The LIS and the EIS have an ice surface elevation for 21 ka BP according to Peltier (2004) in the GCM and in the RCM. The AlpIF has a surface elevation following Seguinot et al. (2018) for 21 ka BP. |
| $LGM_{E50}$ | Analogous to $LGM_{E100}$, however, the ice thickness of the EIS is scaled to 50% in the RCM. |
| $LGM_{E150}$ | Analogous to $LGM_{E100}$, however, the ice thickness of the EIS is scaled to 150% in the RCM. |
| $LGM_{alpsless}$ | Analogous to $LGM_{E100}$, however, the ice thickness of the AlpIF is reduced in the RCM. The reduction is 600 m at ice surface elevations above 2000 m. Between ice surface elevations of 2000 m and 500 m, the ice thickness reduction is scaled from 600 m to zero. |
| PD | Climate data representative for the year 1990 using today's glacier and ice sheet topography in the GCM and the RCM. |
| $MIS4_{NH100}$ | Climate data for the MIS4 at 65 ka BP. The LIS and the EIS have an ice surface elevation for 21 ka BP according to Peltier (2004) in the GCM and in the RCM. The AlpIF has a surface elevation following Seguinot et al. (2018) for 21 ka BP. |
| $MIS4_{NH67}$ | Analogous to $MIS4_{NH100}$, however, the ice thickness of the LIS and the EIS are scaled to 67% in the GCM and the RCM. |
| $MIS4_{NH125}$ | Analogous to $MIS4_{NH100}$, however, the ice thickness of the LIS and the EIS are scaled to 125% in the GCM and the RCM.. |

**Table 3.3:** Overview for the glacial boundary conditions for the Laurentide and the Eurasian Ice Sheet (LIS,EIS) and the Alpine Ice Field (AlpIF) of the eight Regional Climate Model (RCM) datasets of Velasquez et al. (2020) and Velasquez and Raible (in prep).

Each of the global runs was downscaled once using the RCM, except for the $LGM^G$ run, for which four versions were produced (Tab. 3.2). These used different surface elevation for the EIS and the AlpIF in the RCM surface elevation. The $LGM_{E100}$ run used ice surface elevations of 21 ka BP for the EIS from Peltier (2004) and the AlpIF from Seguinot et al. (2018) and is treated as a reference LGM climate here. The $E$ in the subscript of the LGM simulations indicates the scaling that is applied to the EIS in the RCM subdomains. The $LGM_{E50}$ and the $LGM_{E150}$ run employed ice thicknesses for the EIS that were scaled to 50% and 150% of the original ice thickness respectively. By contrast, the RCM used a reduced ice thickness for the AlpIF in the $LGM_{alpsless}$ simulation to account for the current ice surface elevation disagreement between the geomorphologically reconstructed and the modelled ice surface elevation (Becker et al., 2016; Cohen et al., 2018; Seguinot et al., 2018). The

ice thickness was reduced by 600 m at surface elevations above 2000 m. Between ice surface elevations of 2000 m and 500 m, the ice thickness reduction was scaled from 600 m to zero. An overview for the different boundary conditions used in the eight climate datasets is summarized in Tab. 3.3. In the following, we refer to the LGM and the MIS4 datasets as 'glacial' datasets.

The downscaled datasets consist of daily mean air temperature and daily total precipitation and have a length of between 12 and 30 years (Tab. 3.2). Usually the 2 m near surface temperature would be used for the energy and mass balance calculation. Here, however, we use the air temperature about 100 m above the surface instead. The 2 m near surface temperature contains a strong artefact in summer temperatures that arises from the ice albedo mask used in the RCM, which is not the case for the temperature about 100 m above the surface. The artefact in the 2 m near surface temperature leads to square-shaped artefact in the modelled ice extent, in particular when the glaciers are near the reconstructed maximum extent. The 100 m temperature is adjusted using a temperature lapse rate for any deviation to the ice surface elevation before used for the energy and mass balance calculation (see Sec. 3.2.3).

RCMs tend to overestimate precipitation in mountainous terrain (Gómez-Navarro et al., 2018). In order to account for this bias, Velasquez et al. (2020) and Velasquez and Raible (in prep) applied a bias correction to all precipitation data following Velasquez et al. (2020). Precipitation was corrected separately within elevation intervals of 400 m and individually for each month of the year. The correction was calibrated with RhiresD observational dataset of MeteoSchweiz (2013) and the RCM PD precipitation by empirical quantile mapping (e.g. Lafon et al., 2013). Then, the quantile mapping was applied to the precipitation of all RCM datasets listed in Tab. 3.2. For more details, the reader is referred to Velasquez et al. (2020) and Velasquez (in prep). Although this bias correction method might not perfectly recover all elevation dependent biases during all seasons in the RCM datasets, the datasets are treated as 'truth' here.

From each of the eight downscaled datasets, we calculate a one-year dataset consisting of long-term monthly means for temperature and precipitation as well as long-term monthly temperature standard deviation. Compressing datasets with daily resolution to monthly resolution and including temperature variations in terms of a standard deviation is common for PD and near future simulations of the Greenland Ice Sheet involving PDD models (e.g. Rogozhina and Rau, 2014; Wilton et al., 2017). Further, this reduces the amount of data that has to be read and handled by the ice flow model and thus makes it possilbe to run PISM faster. The role of averaging over 12 or 30 years has been tested. The comparison between the averaged full 30 years and only the first 12 years of the $\mathrm{LGM}_{E100}$ dataset show hardly any difference (not shown here). Therefore, for each dataset the averages are calculated from the entire respective dataset.

For the PD, the RCM yields annual mean temperatures of 9.65 °C in the lowlands i.e. outside the area glaciated during the LGM (Tab. 3.2). The annual mean temperatures of the four LGM datasets $\mathrm{LGM}_{E50}$, $\mathrm{LGM}_{E100}$, $\mathrm{LGM}_{E150}$, and $\mathrm{LGM}_{alpsless}$

vary hardly from each other and are 12–13 °C cooler than the PD dataset. The temperature seasonal amplitude in the lowlands (TSA, June July August mean temperature minus December, January, February mean temperatures) is about 18 °C in the PD dataset and enhanced by roughly 2.5–5 °C in the glacial datasets. The temperature lapse rates of the PD dataset is $\gamma = -6$ K km$^{-1}$ but amounts only to $\gamma = -4.5$ K km$^{-1}$ in the LGM and MIS4 datasets.

Annual precipitation rates of the PD dataset are on average 1 m a$^{-1}$ in the low lands but more than 40 % greater in the Alps (Tab. 3.2). The LGM and MIS4 datasets show somewhat similar total annual precipitation rates in the low lands as the PD dataset, being only 2-15 % dryer. In the Alps, the drying is more pronounced with 10-22 % less precipitation than in the PD dataset. The annual mean precipitation for the four LGM climate forcings is given in Fig. B.9 together with the precipitation deviation relative to the LGM$_{E100}$ dataset. An analogous visualization for the MIS4 forcings and the PD climate forcing is given in Fig. B.12 in Appendix B. Spatial differences in precipitation between the PD and the LGM$_{E100}$ dataset are rather heterogeneous (Fig. B.9e). Therefore, the model domain is divided in three subdomains:

1. a western subdomain encompassing mostly Rhone Glacier,
2. a north-eastern subdomain encompassing the Reuss, Rhine, Isar-Loiscach, Inn, and Salzach Glaciers,
3. a southern subdomain encompassing the Ticino, Garda, Tagliamento and Drau Glaciers.

While the annual precipitation hardly changes in the western subdomain, precipitation is reduced by 43 % in the north-eastern and by 17 % in the southern subdomain with respect to the PD climate dataset. Variations between the LGM and the MIS4 climates are much smaller (Fig. B.9f-h and B.12e-h).

Figure B.1 shows the winter mean air velocity at the pressure level of 700 hPa (≈3000 m above sea level), when most precipitation falls in the Alps during the glacial climates. Over the Iberian Peninsula, enhanced wind from the west indicate the presence of the North Atlantic storm track during the LGM and MIS4. Similar to today, air is advected predominantly from west, however, slightly more from south. Figures for temperature, temperature standard deviation, precipitation, and wind velocity for different seasons are presented in Appenix B.

### 3.2.3 *Transient climate forcing*

The study of Seguinot et al. (2018) highlights the importance of using a transient climate forcing. Therefore, such a strategy is also pursued in our study. Seven transient climate forcings are constructed from the steady-state snapshot climates, a time dependent signal that is applied to the glacial temperature field and precipitation rates that are linearly interpolated between the PD rates and the glacial rates.

Formerly, transient climate forcings were created by applying a reconstructed temperature time series to PD temperatures. To use the same approach for the new glacial datasets, a uniform temperature increase is applied to the temperature data. Therefore, the temperatures of the glacial datasets $T_{GL}(x, y)$ are manipulated as follows to obtain a transient temperature field $T(t, x, y)$:

$$\begin{aligned} T(t,x,y) &= T_{GL}(x,y) + a + \phi(t) \cdot \Delta T + \\ &\quad \gamma \cdot (S_{mod}(t,x,y) - S_{clim}(x,y)), \end{aligned} \tag{3.1}$$

where $a$ is an uniform temperature increase, $\phi(t)$ is a climate signal scaled with parameter $\Delta T$, $\gamma$ is the atmospheric temperature lapse rate, $S_{mod}(x, y, t)$ is the modelled ice surface elevation, and $S_{clim}(x, y)$ is the climate reference surface elevation. The glacial temperatures are increased by $a = 9$ °C to obtain a similar accumulation area with the PDD model as using the real PD dataset (not shown here). $a$ takes a smaller value than the actual temperature difference between the PD and the glacial datasets because of the increased temperature standard deviation in the glacial datasets that increase melt rates (Fig. B.8). The transiency in temperature is constructed by modulating a climate signal $\phi(t)$ corresponding to the last 50 ka to the temperature field $T_{GL}(x, y)$. For our signal, we chose the reconstructed temperature time series from the European Project for Ice Coring in Antarctica (EPICA, Jouzel and Masson-Delmotte, 2007), similar to Seguinot et al. (2018). The signal is interpolated to a temporal resolution of 10 years and smoothed with a floating-average with a window size of 100 years to achieve a homogeneous resolution during the last 50 ka. Then, an offset is applied to the EPICA temperature signal such that the present-day value corresponds to zero. After this, the signal is scaled such that the period between 27 ka BP and 22 ka BP has an average offset of $\Delta T$ °C. The offset $\Delta T$ serves as a tuning parameter that is chosen such that the maximum modelled ice extent agrees best with the geomorphologically reconstructed maximum extent of the LGM for each simulation individually. The corresponding signal for $\Delta T = 8.3$ °C is shown in Fig. 3.4a. To take into account temperature changes due to the evolving ice surface elevation, a lapse rate of $\gamma = -4.5$ K km$^{-1}$ is multiplied with the difference between the modelled ice surface elevation $S_{mod}(x, y, t)$ and the climate reference surface elevation $S_{clim}(x, y)$ (Eq. 3.1). By contrast, temperature standard deviation is assumed to be constant in time at the values of the glacial dataset.

The interpolation between PD precipitation rates ($P_{PD}$) and glacial precipitation rates ($P_{GL}$) follows a time dependent Precipitation Index $PI(t)$ that is deduced from the temperature signals (Fig. 3.4b):

$$P(t,x,y) = P_{PD}(x,y) \cdot PI(t) + P_{GL}(x,y) \cdot (1 - PI(t)), \tag{3.2}$$

where the $PI(t)$ consists of piecewise averages over 1000 years and is scaled such that $0 \leq PI(t) \leq 1$.

To compare our simulations driven with the RCM LGM climates with earlier studies, we perform one additional simulation by constructing an artificial reference LGM climate solely relying on the RCM PD climate dataset by following Seguinot

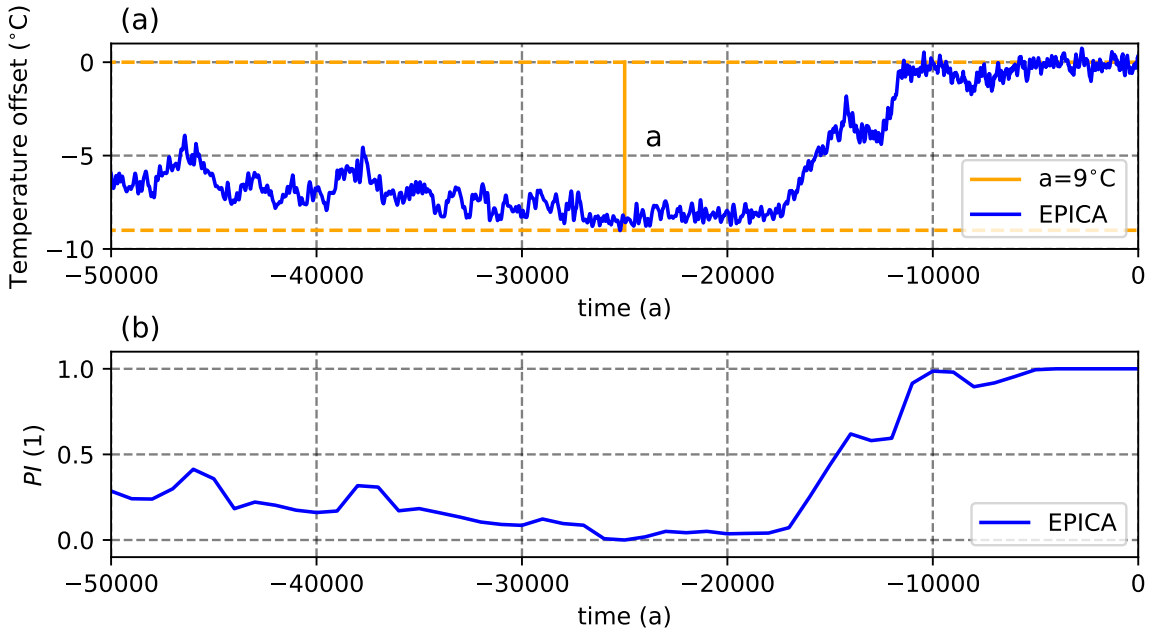


**Figure 3.4:** (a) Temperature signal from the European Project for Ice Coring in Antarctica (EPICA, blue) that is applied to the regional climate model temperature data and the uniform temperature increase $a = 9$ °C (orange) that is used in all glacial datasets. (b) the EPICA signal at a sampling rate of 1000 years and scaled to values between zero and one, used as Precipitation Index ($PI$) to linearly interpolate between present-day and glacial precipitation rates.

et al. (2018). Such an approach has been used so far due to the lack of more representative data for the LGM. Analogously to the other simulations, the EPICA temperature signal is applied to the PD temperatures, however, this time with $a = 0$ °C and the PD lapserate of $\gamma = -6$ K km$^{-1}$ (Eq. 3.1). We impose a precipitation change of 7.3 % K$^{-1}$ of temperature change due to the EPICA temperature signal:

$$P(t,x,y) \quad = \quad P_{PD}(t,x,y) \cdot 1.073^{\phi(t)\cdot\Delta T}. \tag{3.3}$$

Hereafter, we refer to this sort of climate forcing as 'PD-based'.

In addition to the eight forcings from above, two simulations with mixed climate forcings are performed. The first simulation uses temperature and standard deviation from the PD-based forcing in combination with precipitation interpolated between PD and LGM$_{E100}$ rates identical to Eq. (4.2) (labelled as T$_{PD}$P$_{LGM}$). The second simulation employs temperature and standard deviation of the LGM$_{E100}$ simulation in combination with the PD precipitation that is reduced depending on the temperature offset prescribed by the EPICA signal as in Eq. (4.3) (labelled as T$_{LGM}$P$_{PD}$). The aim of these simulations is to determine whether the changes in modelled ice extent that result from using the LGM dataset instead of the PD dataset are primarily driven by the LGM precipitation or the LGM temperature.

## 3.3 RESULTS

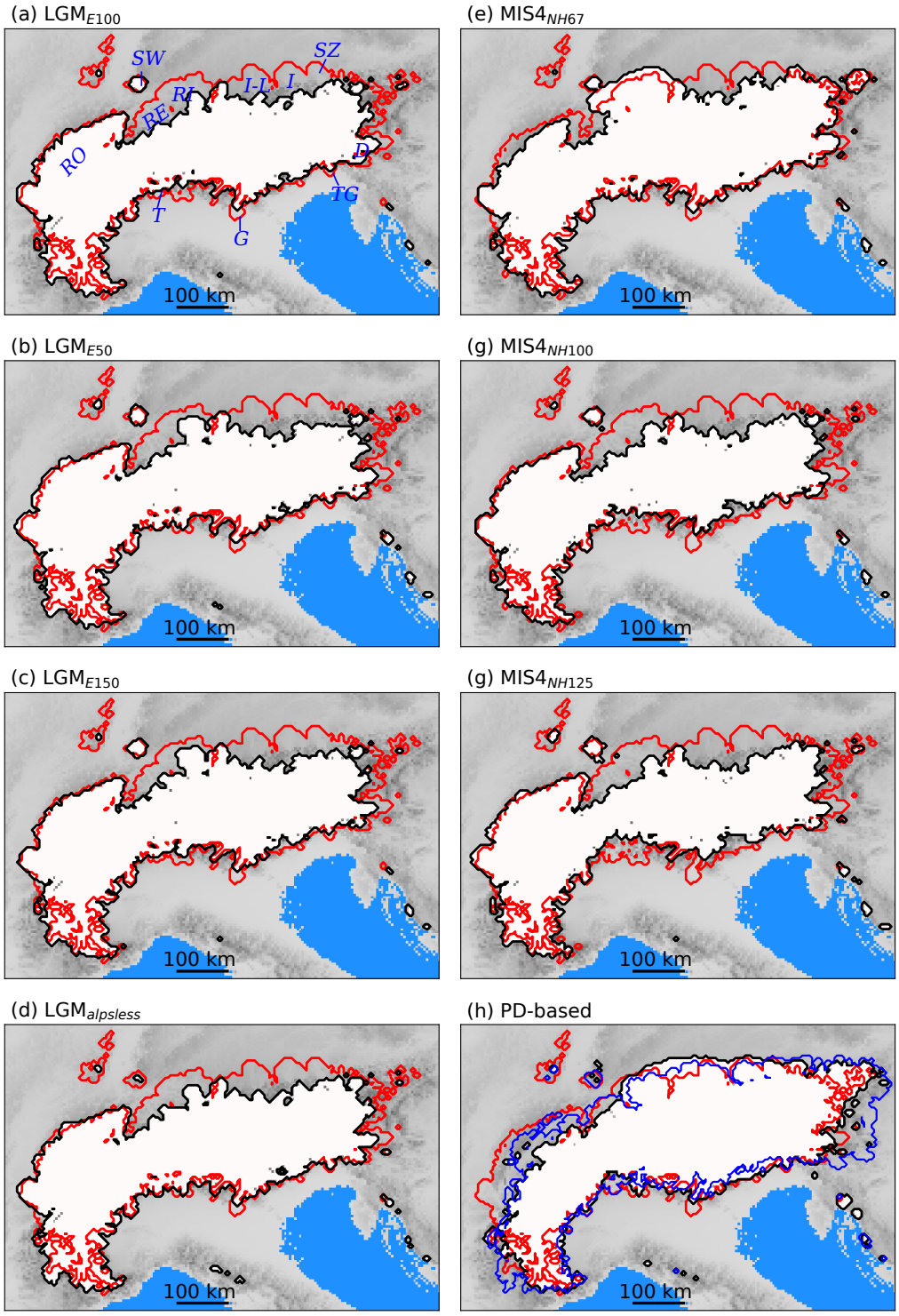


**Figure 3.5:** Modelled maximum ice extent (white with black outline) of the eight simulations driven with LGM, MIS4, and PD-based forcings. The red outlines indicate the geomorphologically reconstructed maximum ice extent of the LGM by Ehlers et al. (2011). The blue outline in (h) indicates the modelled extent of Seguinot et al. (2018). In (a), names of glaciers are indicated in blue italics.

| Climate forcing | $\Delta T$ |
|---|---|
| $LGM_{E100}$ | –8.3 °C |
| $LGM_{E50}$ | –8.0 °C |
| $LGM_{E150}$ | –8.0 °C |
| $LGM_{alpsless}$ | –8.4 °C |
| $MIS4_{NH67}$ | –9.8 °C |
| $MIS4_{NH100}$ | –8.5 °C |
| $MIS4_{NH125}$ | –8.5 °C |
| PD-based | –11.4 °C |
| $T_{PD}P_{LGM}$ | –10.3 °C |
| $T_{LGM}P_{PD}$ | –10.0 °C |

**Table 3.4:** Overview of climate forcings used in the ice flow simulations including the tuned temperature offset $\Delta T$ for Eq. (3.1) and (4.3).

Table 3.4 lists the ten simulations performed using the transient climate forcings described in Section 3.2.2. The simulations can be divided into four groups:

1. The first group consists of the simulations forced with the $LGM_{E100}$, the $LGM_{E50}$, the $LGM_{E150}$, and the $LGM_{alpsless}$ climate which are all variants for the Last Glacial Maximum (LGM).

2. The second group is forced with the $MIS4_{NH67}$, the $MIS4_{NH100}$, and the $MIS4_{NH125}$ climates which are climate variants for the older intermediate glacial maximum stand of the Marine Isotope Stage 4 (MIS4).

3. The third group represents one control simulation that is performed using solely data of the Present-Day (PD) climate dataset (PD-based).

4. And fourth, two simulations that combine PD temperature with $LGM_{E100}$ precipitation data and vice versa ($T_{PD}P_{LGM}$ and $T_{LGM}P_{PD}$).

The first group of simulations investigates how the height of the Eurasian Ice Sheet and the Alpine Ice Field in the regional climate model affects the glaciation in the Alps during the LGM. Further, we aim to assess the general benefits of using regional climate model data to overcome the lack of paleo climate data for ice flow modelling. The second group investigates the influence of the northern hemisphere ice sheets in the global climate model on the modelled ice distribution in the Alpine Ice Field, whereas the PD-based simulation serves as a reference simulation for the climate forcings employed in earlier studies. The two simulations of the fourth group are only used to evaluate whether it is temperature or precipitation that is the leading cause for the differences between modelled ice extent of simulations driven with the PD and the $LGM_{E100}$ climate forcing.

For each of the simulations the temperature signal is tuned individually with $\Delta T$ such that the modelled maximum ice extent lies close to but does not reach beyond

the geomorphological reconstruction for the LGM (Tab. 3.4, Fig. 3.5). Since there is no complete ice extent reconstruction for the MIS4, the simulations driven with the MIS4 climates are nonetheless tuned to the geomorphologically reconstructed LGM ice extent.

### 3.3.1 *Results obtained with Last Glacial Maximum climate forcings*

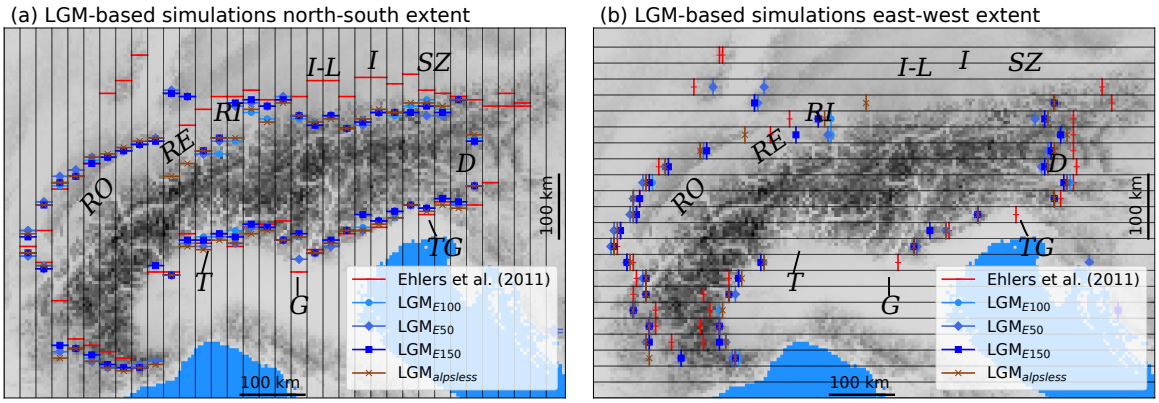


**Figure 3.6:** The median northernmost and southernmost maximum ice extent of the reconstructed and modelled Alpine Ice Field in vertical strips with a horizontal spacing of 25 km (a). The geomorphological reconstruction of Ehlers et al. (2011) (red) along with the simulations LGM$_{E100}$ (light blue dots), LGM$_{E50}$ (blue diamonds), LGM$_{E150}$ (dark blue cubes), and LGM$_{alpsless}$ (purple crosses). Names of glaciers are indicated in black italics. (b) shows the analogous figure for the easternmost and westernmost maximum ice extent.

The simulations forced with the LGM$_{E100}$, the LGM$_{alpsless}$, the LGM$_{E50}$, and the LGM$_{E150}$ climate are in good agreement with the reconstructed maximum extent in the west and in decent agreement in the south of the Alps (Fig. 3.5a-d). The modelled Rhone Glacier is in equally close agreement with the reconstructed LGM extent in all four simulations. While the extent in the south of the Alps is matched fairly well, the lobes outside the Alps are poorly developed in particular the one of Garda Glacier. However, in all the simulations the ice extent in the north and east is clearly underestimated. Every glacier between Reuss Glacier and Salzach Glacier clearly do not reach near the reconstructed extent. Also Drau Glacier in the eastern Alps never reaches the reconstruction.

Figure 3.6a compares the median northernmost and southernmost ice extent of the four LGM simulations and the geomorphological reconstruction. The three simulations based on either a thinner or thicker Eurasian Ice Sheet in the regional climate model (LGM$_{E50}$ and LGM$_{E150}$) or a lower Alpine Ice Field surface elevation (LGM$_{alpsless}$) produce an almost identical maximum extent as the simulation that used the reference LGM$_{E100}$ climate. The same holds for the median westernmost and easternmost ice extent (Fig. 3.6b).

### 3.3.2 *Results obtained with Marine Isotope Stage 4 climate forcings*

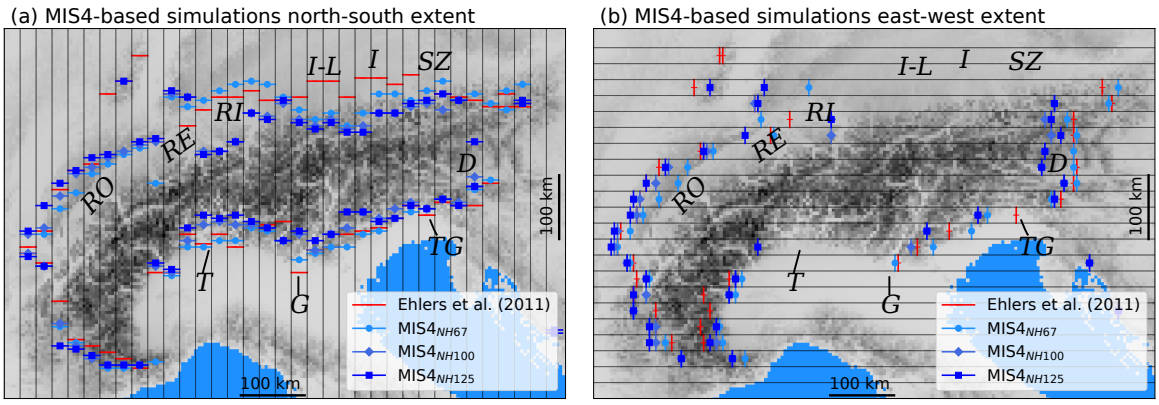


**Figure 3.7:** The median northernmost and southernmost maximum ice extent of the reconstructed and modelled Alpine Ice Field in vertical strips with a horizontal spacing of 25 km (a). The geomorphological reconstruction of Ehlers et al. (2011) (red) along with the simulations $MIS4_{NH67}$ (light blue dots), $MIS4_{NH100}$ (blue diamonds), and $MIS4_{NH125}$ (dark blue cubes). Names of glaciers are indicated in black italics. (b) shows the analogous figure for the easternmost and westernmost maximum ice extent.

The model results obtained with the MIS4 climates are tuned to the reconstructed LGM extent as no such data exists for the MIS4. The maximum ice extent reached by the $MIS4_{NH100}$ and $MIS4_{NH125}$ driven simulations show a similar pattern as in the model results obtained with the LGM-based climate forcings (Fig. 3.5e-g). While in the west Rhone Glacier is in close agreement with the geomorphological reconstruction, all glaciers in the north between Reuss Glacier and Salzach Glacier clearly do not come near the reconstructions. Also the glaciers on the southern side of the Alps between Ticino and Drau Glacier remain within the reconstructed extent. The simulation driven with the $MIS4_{NH67}$ forcing, which is based on a thinned Laurentide Ice Sheet and Eurasian Ice Sheet in the global climate model, stands out from all MIS4- and LGM-driven simulations. The north-eastern branch of Rhone Glacier is underdeveloped compared to the south-western branch (Fig. 3.5e). Further, the simulation driven with the $MIS4_{NH67}$ climate is the only simulation driven with a glacial dataset that allowed ice to reach the reconstructed ice extent at Rhine Glacier in the central northern part of the Alpine Ice Field and at the very eastern end of the Alpine Ice Field. There is even a small side lobe in the north-west of Rhine Glacier that touches the Schwarzwald Ice Cap, which lies however beyond the reconstructed LGM ice extent. But again, all glaciers in the north east of Rhine Glacier do not reach near the reconstruction. Yet, the $MIS4_{NH67}$ median north-south ice extent east of Rhine Glacier and Ticino Glacier is more extensive and closer to the reconstructed extent than in the simulations driven with the $MIS4_{NH100}$ and $MIS4_{NH125}$ forcings (Fig. 3.7a). On top of that, the modelled ice extent also reaches further east (Fig. 3.7b).

### 3.3.3 *Results obtained with the Present-Day-based climate forcing*

The maximum ice extent reached by the simulation relying solely on the PD dataset of the regional climate model is given in Fig. 3.5h. This figure also shows the corresponding maximum ice extent obtained by Seguinot et al. (2018) in blue who used the WorldClim present-day observational dataset (Hijmans et al., 2005). Our simulation depicts an Alpine Ice Field with an extensive glaciation in the north-east reaching the reconstructed maximum ice extent of the LGM between Rhine Glacier and Salzach Glacier, similar to Seguinot et al. (2018). In the very east of the Alps, our simulation is also in fairly good agreement with the reconstructed extent, whereas Seguinot et al. (2018) obtained a much more extensive glaciation in that area. But at the same time, Rhone Glacier is essentially absent in our PD-based simulation and also remains well within the reconstructed extent in the simulation of Seguinot et al. (2018). Therefore, the PD-based simulation results in a similar disagreement with reconstructions as the earlier study of Seguinot et al. (2018), also depicting an extensive glaciation in the north-east and a too small glaciation in the west at Rhone Glacier.

### 3.3.4 *Results obtained with forcings mixing precipitation and temperature of the present-day and the Last Glacial Maximum datasets*

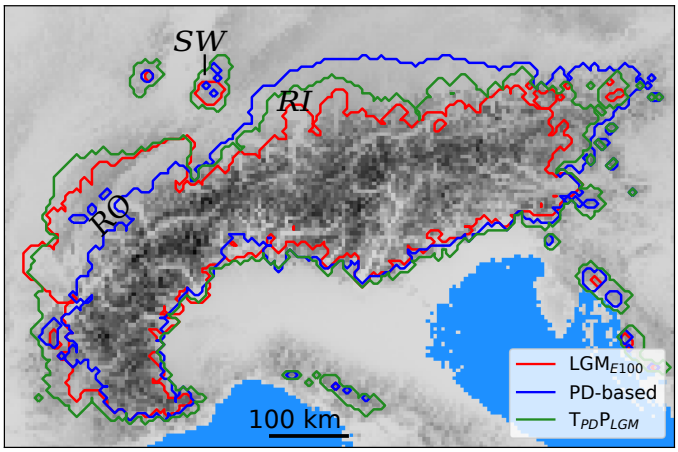


**Figure 3.8:** Maximum ice extent reached by the simulations forced with the PD-based (blue), the LGM$_{E100}$ (red), and the T$_{PD}$P$_{LGM}$ (green) climate forcings. Names of glaciers are indicated with black italics.

Figure 3.8 shows modelled maximum ice extent reached by the simulations forced with the PD-based, the LGM, and the T$_{PD}$P$_{LGM}$ climates. Along the southern boundary of the Alps, all simulations show a similar extent. The PD-based simulation (blue) shows little glaciation in the western Alps, in particular near Rhone Glacier, whereas the glaciers in the north-east extend far out into the lowlands. Exchanging the PD precipitation with the LGM$_{E100}$ precipitation rates results in a much larger

Rhone Glacier and reduced the ice extent in the north-east ($T_{PD}P_{LGM}$, green). Using also the LGM temperature ($LGM_{E100}$, red), does not change Rhone Glacier and reduces the ice extent in the north-east a little further. This suggests that changes in precipitation are of first order importance and changes in temperature rather of secondary importance.

The simulation driven with the $T_{LGM}P_{PD}$ climate shows a Rhine Glacier engulfing the Schwarzwald Ice Cap and expanding all the way to the northern model boundary while all other glaciers remain well within the Alps. Therefore, this simulation is not considered and not shown here.

## 3.4 DISCUSSION

### 3.4.1 *The impact of the northern hemisphere ice sheet surface elevation on the ice extent in the Alpine Ice Field*

Global climate models suggest a strong link between the size of the Laurentide Ice Sheet (LIS) and the position/direction of the North Atlantic storm track and thus precipitation in south-west Europe during the last glacial cycle. In addition to this, our ice flow simulations with the Marine Isotope Stage 4 (MIS4) climates, which employed various ice thicknesses for the LIS and the Eurasian Ice Sheet (EIS) in the global climate model, support a link to the extent of the Alpine Ice Field (AlpIF). The simulation driven with the $MIS4_{NH67}$ climate, which employs a thinned LIS and EIS, leads to a notably larger ice extent in the north-east and the east of the AlpIF than the other two simulations that employed the unchanged or thickened LIS and EIS ($MIS4_{NH100}$ and $MIS4_{NH125}$, Fig. 3.7a,b). The reason for the improved ice extent in the north and east is that the precipitation of the $MIS4_{NH67}$ climate is reduced by 17 % in the western Alps relative to the $MIS4_{NH100}$ and $MIS4_{NH125}$ climates (Fig. B.12e,g), while elsewhere precipitation rates remain unchanged. The reduced precipitation rates in the west necessitate a $\Delta T$ roughly 1.3 °C cooler than the other two MIS4 simulations to reach the reconstructed Last Glacial Maximum (LGM) maximum ice extent (Tab. 3.4). This suggests that the size of the large continental ice sheets in the northern hemisphere is a control for the east-west distribution of precipitation and ice in the Alps. The reason for this connection is likely related to a northward shift and/or a weakening of the North Atlantic storm track induced by the lowered ice surface elevation of the LIS as pointed out by Hofer et al. (2012b). This connection perhaps also exists in the LGM forcings and could play a role for the east-west imbalance of ice in the Alps obtained with these forcings (see discussion in Section 3.4.2). It should be kept in mind that the ice thickness of the LIS and the EIS in the global climate model was scaled in the vertical only and not in the horizontal (Hofer et al., 2012b). This is clearly not realistic since both the extent and surface topography are subject to changes in a retreating or advancing ice sheet. It is difficult to say to what extent this simplification affects the overall modelled climate and if it could explain the remaining imbalance of ice and precipitation between the west and the north-east of the Alps.

The simulations where only the ice surface elevation of the EIS is increased or reduced in the regional climate model ($LGM_{E50}$, $LGM_{E100}$, and $LGM_{E150}$ climates) show hardly any influence on the precipitation (Fig. B.9e,f). As a consequence, the ice flow model results show no notable differences in ice extent of the AlpIF (Fig. 3.6a,b). Thus, the size of the EIS alone appears to have little to no influence on the glaciation in the European Alps during the LGM.

The AlpIF topography used for the regional climate model simulations was taken from Seguinot et al. (2018) and depicts a surface elevation up to 861 m higher than geomorphological reconstructions based on trimlines. This raises the question whether this disagreement could affect orographic precipitation. Nonetheless, lowering the AlpIF ice surface elevation by up to 600 m in the regional climate model ($LGM_{alpsless}$) has only a limited influence on the precipitation distribution with a minor drying in the southern and the western Alps (Fig. B.9h) and neither a large impact on the modelled ice extent (Fig. 3.6a,b). This implies that the deviations of 500–861 m currently prevailing between geomorphological ice thickness reconstructions of the AlpIF and modelled ice thicknesses (Becker et al., 2016; Imhof et al., 2019; Seguinot et al., 2018) are unlikely to play an important role for the modelled climate, at least for ice flow modelling purposes at the scale of the entire Alps as presented here. However, the $LGM_{alpsless}$ climate deviates on the small scale from the $LGM_{E100}$ implying that uncertainties in the ice surface elevation might affect the ice distribution locally (Fig. B.9h).

Unlike in any other simulation, Rhine Glacier is modelled in fairly good agreement with the reconstructed LGM extent using the $MIS4_{NH67}$ climate (Fig. 3.5e). However, this should be interpreted with caution. The reason is a so-called cold pool, cold air that is trapped in a topographical depression (Li et al., 2015). All glacial climate datasets show a cold pool in the summer temperatures in the area of the Rhine Glacier Lobe terminus with warmer temperatures southwards closer to the Alps (Fig. B.5a–g). Thus, glacier ice flowing from the Alps to this area is susceptible to undergo runaway growth and filling the cold pool. This can be seen from a westward extension of the Rhine Glacier Lobe, just south of the Schwarzwald Ice Cap. This cold pool occurs in all the MIS4 and LGM climate datasets and likely limits the capability of modelling Rhine Glacier in agreement with the reconstructed extent as the glacier terminus should be in the ablation zone and not the accumulation zone. Cold pools are a natural phenomenon whose representation depends on model resolution and rain microphysical parametrizations (Li et al., 2015; Squitieri and Gallus, 2020). It is not clear to what extent the cold pool in our datasets is modelled realistically or if it is rather an artefact.

### 3.4.2 *Atmospheric circulation and precipitation distribution driving the Alpine Ice Field during the Last Glacial Maximum*

Most climate models indicate that a zonal pattern dominated across the North Atlantic and southern Europe and that thus moisture flow towards the Alps was mostly from the west (e.g. Ludwig et al., 2016; Löfverström, 2020; Löfverström et al.,

2016). Our Present-Day-based (PD-based) simulation and the earlier simulation of Seguinot et al. (2018) suggest a precipitation shift from the eastern to the western Alps during the LGM compared to today. Indeed, all LGM climate datasets show a major shift of precipitation to the west. However, this shift is too strong such that the modelled glaciation between Reuss Glacier and Salzach Glacier remains far too small compared to the Rhone Glacier in the west. Therefore, our study supports an enhanced moisture transport to the western Alps during the LGM as indicated by the inverse glacier modelling study of Višnjević et al. (2020) and most global climate model studies. The winter wind velocities of Velasquez et al. (2020) and Velasquez and Raible (in prep) also hint at winds predominantly from the west or slight south-west which perhaps correlates with the moisture transport (Fig. B.1). A detailed analysis of the preferential directions in which moisture arrives at the Alps is currently not available. Therefore, it is not possible to provide a well-founded explanation why this strong precipitation gradient forms between the east and the west and how variations in the height of the northern hemisphere ice sheets change the moisture transport to the AlpIF during the LGM. A necessity of an increase in moisture advection from south, as proposed by Florineth and Schlüchter (2000), Luetscher et al. (2015), and Becker et al. (2016), is not evident based on our modelling results but cannot be ruled out either. The reason for the east-west discrepancy in modelled ice extent obtained with the LGM climates needs to be investigated more closely as well as the direction of moisture advection to the Alps. Here, we only provide hypotheses for the east-west discrepancy in modelled ice extent discovered in this study:

A) **The direction of moisture advection was more west orientated than in the regional climate model datasets.**

   Assuming that the dominant part of humidity was advected from west to south-west in the LGM forcings, a more western flow regime might provide more precipitation to the glaciers east of Reuss Glacier and thus result in larger glaciers there. Indeed, a comparison between various global climate models has yielded small differences in the direction the North Atlantic storm track arrives in western Europe (Löfverström, 2020). These model-to-model variations in direction might affect the precipitation distribution in the Alps and might lead to a precipitation distribution more favourable for the glaciers in the north-east of the AlpIF.

B) **The discrepancy is caused by a time lag between the global LGM and the LGM in the Alps.**

   The LGM climate forcings are based on the reconstructed maximum size of the LIS and the EIS as well as orbital parameters and greenhouse gas concentrations corresponding to the global LGM at 21 ka BP. Indeed, the maximum ice extent of the AlpIF was reached between 26 ka BP and 24 ka BP (Ivy-Ochs, 2015; Monegato et al., 2017) and thus likely earlier than 21 ka BP. A timing difference between the maximum extent of the AlpIF and the global

LGM could therefore amount to several millennia. The MIS4 experiments employing various ice surface elevations for the LIS and the EIS indicate that lowering their ice surface elevation results in a more favourable east-west balance of ice in the AlpIF by reducing precipitation in the west. Therefore, the underestimated modelled ice extent in the north-east could indicate that the climate consistent with the mapped AlpIF LGM extent prevailed before the LIS and the EIS reached their maximum extent.

C) **There were at least two different climatic conditions that lead to asynchronous maximum extents of glaciers in the east and the west during the LGM.**

In this case, our results would imply a time lag between the maximum extent of Rhone Glacier in the west and the glaciers east of Reuss Glacier. Currently there is no evidence for or against an asynchronous behaviour of glaciers in the east and the west. If different climatic conditions are responsible for the maxima in the east and the west, they can only be separated by few millennia as the dates form the AlpIF have measurement uncertainty of only $\pm 500 - 2000$ years (Monegato et al., 2017; Wirsig et al., 2016). For now, the waning and waxing of the AlpIF during the LGM appears to be synchronous at least between Rhine Glacier in the north and Garda and Tagliamento Glacier in the south of the Alps (Monegato et al., 2017). Nonetheless, for several glaciers such as Garda (Monegato et al., 2017), Tagliamento (Monegato et al., 2007), Rivoli Glacier (Ivy-Ochs et al., 2018), Reuss (Reber et al., 2014), and Rhine Glacier (Preusser et al., 2011) two distinct glacier expansions close to the maximum are known during the LGM, indicating two climatic extrema that contributed to the maximum ice extent.

### 3.4.3 *Regional climate model data for paleo ice flow modelling applications*

None of the LGM or MIS4 climate forcings built from regional climate model datasets leads to a modelled AlpIF that fully agrees with the geomorphologically reconstructed LGM extent all around the AlpIF, in particular in the north between Reuss and Salzach Glacier, where significant discrepancies prevail. By contrast, the simulation relying only on the PD climate dataset results in an extensive glaciation in the north-east, close to the LGM extent reconstruction between Rhine Glacier and Salzach Glacier, but by far not reaching the mapped LGM extent in the west at Rhone Glacier. This is similar to the results obtained by Seguinot et al. (2018) (Fig. 3.5h). As a consequence, the LGM climate does not yield a modelled AlpIF that agrees better with the reconstructed maximum extent than using the PD-based LGM forcing. However, the LGM forcing requires little changes to produce an AlpIF ice extent that is in acceptable agreement with reconstructions. In the time interval with the lowest temperatures, the maximum temperature offset applied to $\mathrm{LGM}_{E100}$ is about $\Delta T \cdot \phi(t) = -8.5\ ^\circ C$, which almost equalized the initial $a = 9\ ^\circ C$ offset. This indicates that there is a general consistency between the LGM climate dataset, the ice

flow model, and the geomorphologically reconstructed LGM ice extent. Therefore, using a climate dataset obtained with a regional climate model is a promising approach to overcome the lack of paleo climate datasets in the European Alps.

## 3.5 CONCLUSIONS

In this chapter, the Alpine Ice Field was modelled using climate datasets obtained with a regional climate model by Velasquez et al. (2020) and Velasquez and Raible (in prep). One dataset was for present-day conditions and seven datasets were for glacial conditions using various glacial topographies. The climate datasets were arranged in seven climate forcings that linearly interpolate between the present-day precipitation and a glacial climate and one forcing that solely relies on the present-day dataset. The interpolation between the present-day and the glacial precipitation followed the reconstructed temperature time series of the EPICA ice core from Antarctica. The EPICA temperature time series was also modulated to the temperature fields. For this purpose, the EPICA signal was scaled such that the modelled maximum ice extent reached to the geomorphologically reconstructed maximum ice extent. Based on these model results, the following conclusions are drawn:

1. The size of Laurentide and the Eurasian Ice Sheets in the global model had a notable impact on the east-west distribution of precipitation and ice in the Alps during glacial conditions, however, not so much on the north-south distribution. Climate data using a Laurentide Ice Sheet and Eurasian Ice Sheet with a lowered ice surface elevation show dryer conditions in the western Alps that resulted in a modelled maximum ice extent in better agreement with the reconstruction. Although the climate used in this experiment is more representative for the Marine Isotope Stage 4, this relationship might also exist during the Last Glacial Maximum (LGM).

2. The discrepancy of 500–861 m between modelled and geomorphologically reconstructed ice surface elevation of the Alpine Ice Field has a small impact on the modelled precipitation and almost no influence on the modelled maximum ice extent at the scale of the entire Alps. However, the discrepancy might be relevant locally for smaller glaciers.

3. This ice flow modelling study supports enhanced moisture advection from west during the LGM, similar to earlier ice flow and climate modelling studies. Nonetheless, the shift in precipitation towards the western Alps is too strong in the glacial regional climate model datasets. Reasons for this could be model-to-model variations in the global climate model data for the direction of the North Atlantic storm track during the LGM, a time lag between the LGM in the Alps and the global LGM, or at least two different climatic extrema close to each other during the LGM that lead to the geomorphologically reconstructed ice extent.

4. We found that forcing an ice flow model with regional climate model data for the LGM is an overall useful and promising approach to overcome that lack of paleo climate data. Ice flow model results obtained with this forcing data are roughly consistent with the geomorphological evidence, despite the clear east-west ice extent discrepancy. Rhone Glacier in the western Alps was particularly well reproduced using the LGM climate. Thus, this forcing dataset could be suitable for a more detailed modelling study for the evolution of Rhone Glacier.

## DATA AVAILABILITY

Ice thickness and bedrock elevation data of the simulations driven with the $\mathrm{LGM}_{E100}$, $\mathrm{MIS4}_{NH66}$, $\mathrm{MIS4}_{NH100}$, and PD-based climate forcings is published as Imhof (2021b).

# 4

# A NUMERICAL RECONSTRUCTION OF THE LGM RHONE GLACIER AND ITS ICE DYNAMICS

*"Sieht aus wie Bohnen, riecht wie Bohnen, sind Bohnen."*
— Der Supercop (1980)

## 4.1 INTRODUCTION

During the last glacial cycle, a vast ice field covered the European Alps. This Alpine Ice Field reached a maximum extent during the Last Glacial Maximum (LGM) roughly between 26 and 24 kiloannum before present (ka BP) (Monegato et al., 2017). The north-west of the Alpine Ice Field was drained by Rhone Glacier, one of the largest glacier drainage systems of the Alpine Ice Field (Fig. 4.1b). It connected glaciers from the Bernese Alps, the Valais, the Jura, and the French Alps. In the lowlands, the glaciers formed one massive ice body that extended from Lyon to Wangen an der Aare (Coutterand, 2010; Ehlers et al., 2011). Thanks to the abundance of geomorphological evidence in this area, Rhone Glacier is today fairly well studied (e.g. Coutterand, 2010; Graf et al., 2015; Ivy-Ochs et al., 2006; Kelly et al., 2004). Geomorphological reconstructions of Rhone Glacier typically show Valais Glacier as the main source of ice which is then divided into two branches by the Jura mountains, one turning to north-east and terminating in Wangen an der Aare (Solothurn Lobe) and one branch flowing to the south-west terminating just outside Lyon (Southern-Branch and Lyon Lobe, Fig. 4.1a, b) (Bini et al., 2009; Buoncristiani and Campy, 2004; Coutterand, 2010). The Solothurn Lobe is joined by Aare Glacier and the Southern-Branch by Arve Glacier. The ice body formed by Solothurn Lobe, Southern-Branch, and Lyon Lobe is here called Rhone Glacier Lobe.

Glacial deposits at the first Jura ridge (near Mont Tendre) suggested that it hosted its own ice cap, the Jura Ice Cap (Fig. 4.1b), and that the Jura was not overtopped by ice from the Alps during the LGM (Buoncristiani and Campy, 2011; Campy, 1992). At most, some alpine ice might have flowed over the first Jura ridge and reached Val de Travers (Graf et al., 2015). In Fig. 4.1a and b, this furthest extent of alpine ice in the Jura is indicated by the black dashed line going through Val de Travers.

For the highest parts of the Rhone Valley, the former maximum ice surface elevation was reconstructed based on so-called trimlines. Trimlines are the transition between glacially eroded rock and frost weathered rock situated on top. The transition is interpreted as the maximum ice surface elevation reached by the glaciers in the Alps (Florineth and Schlüchter, 1998; Kelly et al., 2004). In the lowlands, little is known about the former ice surface elevation. According to Graf et al. (2015), boulders deposited onto the Jura at the orographic left side of the Solothurn Lobe indicate a maximum ice surface elevation of ≈1200 m north-east of Mont Tendre and ≈1000 m north of Neuchâtel (black crosses in Fig. 4.1c).

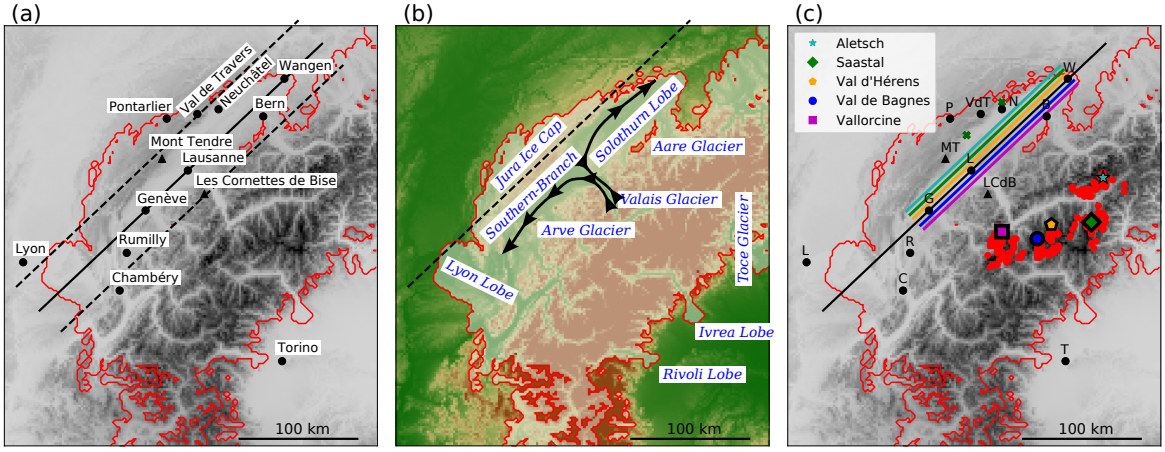


**Figure 4.1:** (a) Overview map of model domain with names of towns (black dots) and mountains (black triangles). The red outline indicates the geomorphologically reconstructed ice extent at the LGM (Ehlers et al., 2011). The black line roughly follows the centre ice flow direction of the Solothurn Lobe and the Southern-Branch. The northern black dashed line indicates the first Jura ridge which separates the Jura mountains from the lowlands. The southern dashed line separates the lowlands from the Alps. (b) The formerly glaciated area is shaded in white. The names of the individual parts of Rhone Glacier and some neighbouring glaciers are labelled in blue italics. This dashed line delineates roughly the Jura Ice Cap from Rhone Glacier. The black arrowed lines indicate the assumed ice flow directions of ice coming from Valais Glacier (Buoncristiani and Campy, 2011). (c) The red dots indicate the areas for which Kelly et al. (2004) mapped the trimline elevation and the dark green crosses indicate the locations in the Jura where the LGM ice surface elevation is known from deposited boulders (Graf et al., 2015). The five lithological origin areas of erratic boulders considered in this study are indicated: Vallorcine (magenta square), Val de Bagnes (blue dot), Val d'Hérens (orange pentagon), Saastal (green diamond), and the Aletsch area (turquoise star). The coloured lines parallel to the black line indicate roughly where along the Solothurn Lobe and the Southern-Branch the five types of boulders have been deposited (lines not representative for deposition in cross direction).

In recent decades, ice flow models have provided a complementary picture to the one inferred from geological evidence for the glaciation in the Alps during the last glacial cycle (e.g. Haeberli and Schlüchter, 1987; Seguinot et al., 2018). Ice flow models simulate the flow of ice due to deformation and sliding over the glacier bed, ice temperature, and the glacier mass balance. In particular, they have provided new insight into the interactions with the climate (e.g. Becker et al., 2016; Jouvet et al., 2017; Seguinot et al., 2018).

Former ice flow modelling studies all relied on either present-day climate datasets which they have modified (e.g. Seguinot et al., 2018) or an heuristic elevation dependent mass balance (e.g. Cohen et al., 2018). The lack of representative climate data for the LGM in the Alps was a central limitation of such studies. This lack of data was recently remedied by Velasquez et al. (2020), Velasquez and Raible (in prep) and Velasquez (in prep) who downscaled present-day and LGM global

climate model output of Hofer et al. (2012b), and Merz et al. (2015) to a horizontal resolution of 2 km over the European Alps using a regional climate model. In Chapter 3, we showed that this LGM regional climate model dataset required little adjustment to produce an ice extent matching the reconstructed ice extent of the Alpine Ice Field. In particular, the LGM dataset allowed for a good match with the geomorphologically reconstructed ice extent at Rhone Glacier (Fig. 4.1). Besides the reconstructed maximum ice extent, other evidence was not used to assess the capabilities of the new LGM regional climate model dataset of Velasquez et al. (2020) and Velasquez and Raible (in prep).

Often, ice flow models were unable to reproduce the trimline as former maximum ice surface elevation (e.g. Becker et al., 2016; Cohen et al., 2018; Seguinot et al., 2018). For instance, Seguinot et al. (2018) modelled an ice surface elevation on average 861 m greater than interpreted from trimlines at Rhone Glacier. Their model relies on simplified ice dynamics, namely the Shallow Ice Approximation (SIA, Hutter, 1983) and the Shallow Shelf Approximation (SSA, Weis et al., 1999). To improve computational speed and to prevent mass conservation issues on steep and mountainous topography, the numerical scheme of Schoof (2003) is used to limit the ice flux induced by the SIA. Imhof et al. (2019) showed that this scheme can lead to an artificial ice thickness overestimation of $300 - 500$ m, in particular in mountainous areas. This problem with the flux limiting scheme was shown for the smaller neighbouring Rhine Glacier, which occupies an area with smaller mountains (Chapter 2 or Imhof et al., 2019). It is currently not understood to what extent this ice thickness overestimation caused by the ice flux limiting scheme of Schoof (2003) also affects Rhone Glacier. Further, the impact of the ice flux limiting scheme on the discrepancy between modelled ice surface elevation and mapped trimline elevations is unknown.

As of today, sliding of glacier ice over ground remains incompletely understood (Hock et al., 2017; Ritz et al., 2015). As a result, the parametrization of sliding in ice flow models is subject to large uncertainties. The parameters in most sliding laws need to be tuned for each application individually. So far, only Jouvet et al. (2017) tested different sliding parameters at the Alpine Ice Field. Yet, they analysed only the impact on the boulder transport at Rhone Glacier and omitted any investigation on the modelled ice thickness. Thus, it remains largely unknown how the choice of sliding parameters affects the modelled ice thickness of the Alpine Ice Field.

The Rhone Glacier transported countless erratic boulders from the Rhone Valley to the lowlands. Lithological origin areas could be identified for numerous boulders mostly from the southern tributaries near the village of Vallorcine (Vallorcine conglomerate and Mont Blanc Granite), Val de Bagnes and Val d'Hérens (gneiss, Arolla gneiss), Saastal (Allalin Gabbro), and the Aletsch area (Aare granites) (Burkhard and Spring, 2004; Jouvet et al., 2017; Spring, 2004). These five locations of origin are indicated in Fig. 4.1c. Boulders from these areas are common along the Jura between Genève and Wangen (Burkhard and Spring, 2004; Graf et al., 2015). Although the Aare granites from the upper Rhone Valley are only rarely found on the Solothurn Lobe (Jouvet et al., 2017). Further, the boulders of the five locations are common on

the orographic left and the right side of the Solothurn Lobe (Jouvet et al., 2017). In contrast to the area north-east of Genève, erratic boulders from the Valais hardly exist in the area of the Lyon Lobe (Coutterand et al., 2009). This is surprising given that many reconstructions picture Rhone Glacier to flow towards Solothurn and Lyon at the same time. One would expect the boulders originating in the southern tributaries to stay on the orographic left side of Rhone Glacier and thus not to reach the Solothurn Lobe. This seemingly contradictory phenomenon that boulders from the southern Valais travelled to the Solothurn Lobe is hereafter referred to as the 'boulder diversion'.

Kelly et al. (2004) proposed that this boulder diversion was caused by the ice flow from the southern tributaries of Valais Glacier. The southern tributaries might have dominated Valais Glacier due to increased precipitation in the south and thus pushed boulders from southern tributary glaciers to the orographic right hand side of Valais Glacier and therefore to the Solothurn Lobe. This hypothesis was tested by Jouvet et al. (2017) using an ice flow modelling approach. They employed various spatial precipitation variations on a present-day climate dataset. They found that the present-day precipitation distribution across Rhone Glacier is inconsistent with boulders being diverted to the Solothurn Lobe. Therefore, Jouvet et al. (2017) inferred precipitation changes relative to today that are necessary to transport erratic boulders from southern tributaries of Valais Glacier towards the Solothurn Lobe. Indeed, they found that a local increase in precipitation rates over the southern tributaries of Valais Glacier slightly favours a diversion boulders to the Solothurn Lobe, similar to the explanation proposed by Kelly et al. (2004). However, Jouvet et al. (2017) showed that the boulder diversion is in fact more sensitive to a precipitation gradient between the Mont Blanc area and the Valais compared to a north-south precipitation gradient within the Valais.

Jouvet et al. (2017) only considered steady-state climates and only the advance phase until the reconstructed ice extent is reached. Therefore, they did not account for the transient nature of climate and its potential influences on boulder diversion and deposition. This is an important shortcoming because boulders were not only deposited during the time of maximum ice extension but also during periods of retreat. Using a transient climate forcing, Seguinot et al. (2018) showed that the Alpine Ice Field was very dynamic and that glaciers of different sizes reacted differently to climatic perturbations. This variability might have contributed to the boulder diversion at Rhone Glacier. However, it remains unknown how the ice dynamics and flow pattern of Rhone Glacier evolved during the LGM and to what extent the transport of boulders was affected by the transient evolution of Rhone Glacier.

This chapter focuses on the following research questions:

- What improvements for ice flow modelling can an LGM climate dataset from a regional climate model provide over a present-day dataset? How does transiency in the climate forcing affect the boulder diversion and deposition of Rhone Glacier?

- How thick was Rhone Glacier? How much were previous model results affected by the flux limiting scheme? Is an improved match with reconstructed ice surface elevations achievable with increased sliding speeds?
- How did the ice dynamics and the flow pattern of Rhone Glacier evolve over the LGM? How was the boulder transport from the Valais to the lowlands affected by evolving ice dynamics?

In this study, we use an ice flow model and climate data obtained with a regional climate model for LGM and present-day conditions to simulate the ice dynamics and ice flow pattern of Rhone Glacier transiently for the last 50,000 years. Further, the transport and the deposition of boulders originating in the Valais are computed using the modelled ice velocity field. To model ice dynamics, ice temperature and surface energy and mass balance, we employ the Parallel Ice Sheet Model (PISM, PISM authors, 2019). Analogous to Chapter 3, the climate forcing is constructed by interpolating between a present-day and an LGM climate dataset obtained by Velasquez et al. (2020) and Velasquez and Raible (in prep) following a temperature reconstruction from Antarctica. This setup has proved to yield good agreement between modelled and geomorphologically reconstructed maximum ice extent at Rhone Glacier and is therefore used here too. A simulation relying only on the present-day dataset is also performed to assess the benefits of the LGM climate dataset more deeply. In addition to using the temperature reconstruction from Antarctica, we also use a temperature reconstruction from Greenland which is characterized by stronger and more frequent variations. Further, we test how the ice flux limiter in PISM and a parameter of the sliding law affect the modelled ice thickness at Rhone Glacier.

In Section 4.2, the model data and the model setup are described. Section 4.3 presents the model results and Section 4.4 discusses the model results in context of existent literature. We conclude in Section 4.5.

## 4.2 METHODS AND DATA

We employ the Parallel Ice Sheet Model version 1.1 (PISM, PISM authors, 2019; Winkelmann et al., 2011) to perform a total of five ice flow simulations of Rhone Glacier at a resolution of 2 km. The simulations cover the last 50,000 years using transient climate forcings based on LGM and present-day climate of regional climate model datasets by Velasquez et al. (2020) and Velasquez and Raible (in prep). Here, the ice flow model, the climate forcing, and the computation of boulder trajectories are described.

### 4.2.1 *Ice flow model*

We use PISM on a model domain covering an area of 504 km $\times$ 442 km which covers the entire Rhone Glacier catchment including the Jura (Fig. 4.1). The bedrock

topography is taken from Jarvis et al. (2008) and interpolated to a grid with a 2 km resolution. PISM simulates the ice dynamics, the mass balance, and the temperature of the ice and the underlying bedrock. This section describes each of these 'sub-models'.

PISM is a so-called hybrid model, meaning it uses the Shallow Ice Approximation (SIA, Hutter, 1983) to calculate the ice transport due to horizontal shearing and the Shallow Shelf Approximation (SSA, Weis et al., 1999) to calculate the ice transport due basal sliding. In PISM, the ice flux calculated with the SIA is modified with the ice flux limiting scheme of Schoof (2003). This scheme parametrizes higher-order stresses exerted by bedrock undulations on the ice at a length scale $\lambda$. In PISM, however, the main motivation of using the scheme is to improve computational speed and reduce mass conservation errors. The flux limiting scheme reduces the horizontal shearing velocities calculated with the SIA in steep mountainous areas. The larger the bedrock undulations, the stronger the reduction of the ice flow. The length scale $\lambda$ determines the half-width of the area where the underlying bedrock is smoothed and is an integer n-fold of the model resolution. The smaller $\lambda$ the less smoothing is applied to the bedrock and the less the SIA-induced ice flux is reduced. For more details about the ice flux limiting scheme of PISM, the reader is referred to Section 2.2 and Schoof (2003) or the PISM manual (PISM authors, 2019). Following Chapter 2 and Imhof et al. (2019), we take the smallest possible value for $\lambda$, which is the model's spatial resolution ($\lambda = 2$ km). This minimizes ice thickness overestimations in steep areas. Additionally, one experiment is made with $\lambda = 5$ km which was used in earlier studies such as Seguinot et al. (2018) and leads to substantial overestimation of the ice thickness.

In this study, we employ the same linear sliding law as in Chapter 3. This involves two sliding parameters: one for warm-based ice ($C_1$) and one for cold-based ice ($C_0$) (Eq. A.1, Appendix A). Between basal temperatures of 0 °C and –0.5 °C, the sliding parameter is interpolated between $C_1$ and $C_0$. Analogous to Chapter 3, we take $C_1 = 1000$ Pa a m$^{-1}$ and $C_0 = 1,000,000$ Pa a m$^{-1}$. Additionally, also $C_1 = 300$ Pa a m$^{-1}$ is tested, which leads to less resistance exerted from the bed to the glacier and thus higher sliding speeds. Using $C_1 = 300$ Pa a m$^{-1}$, the highest ice surface speed is ≈1.3 km a$^{-1}$ and occurs in the narrow part of the lower Valais Glacier. The present-day Seward-Malaspina Glacier system in Alaska resembles the Rhone Glacier system in the sense that ice from a heavily glaciated alpine valley is forced through a narrow valley and flows onto a plain where a vast piedmont glacier lobe is formed (Fig. 1.2). With long-term surface speeds of ≈1-2 km a$^{-1}$ in the narrow part, this is one of the fastest non-tidewater glaciers existing today (Burgess et al., 2012; Cotton et al., 2014; Healey et al., 2012). Thus, the ice surface speeds at Rhone Glacier modelled with $C_1 = 300$ Pa a m$^{-1}$ are not larger than those observed at the Seward-Malaspina Glacer system. This implies that such a high speed can indeed be reached by a glacier. Nonetheless, it should be kept in mind that size and most likely basal conditions of the two glaciers are not the same. Yet, this is the only available point of reference regarding ice surface speed.

The surface mass balance is modelled identically to Chapter 3 by using a Positive Degree Day (PDD, Hock, 2003) model where melt is proportional to the integral of positive Celsius temperature over time. Accumulation is equal to the precipitation for temperatures below 0 °C and decreases linearly to zero between 0 °C and 2 °C. The PDD model takes monthly mean temperature, precipitation, and temperature standard deviation as input. The reader is referred to Section 3.2.1 for further details concerning the PDD model and the parameter choice.

PISM simulates the englacial and bedrock temperatures at a vertical resolution of 50 m and 100 m respectively. The annual mean air temperature is used as the thermal boundary at the ice surface while the geothermal heat flux of Goutorbe et al. (2011) is applied the bottom of a 3 km thick bedrock.

### 4.2.2 *Climate forcing*

Our ice flow model is forced with a transient climate forcing constructed from climate data of Velasquez et al. (2020) and Velasquez and Raible (in prep) and reconstructed temperature time series inferred from ice cores from Antarctica and Greenland. The temperature time series are used as climate signals to construct transient climate forcings. We adopt the method used in Chapter 3.

Velasquez et al. (2020) and Velasquez and Raible (in prep) used a regional climate model to downscale global climate model data of Hofer et al. (2012b) and Merz et al. (2015) to a resolution of 2 km over the European Alps for Present-Day (PD) and Last Glacial Maximum (LGM) climate conditions. Here, we use the PD dataset which is representative for the year 1990 (PD dataset in Section 3.2.2) and the LGM dataset which is representative for 21 ka BP ($\text{LGM}_{E100}$ in Section 3.2.2). Each of the datasets is 30 years long and consists of daily means for air temperature and precipitation. From these steady-state climate datasets, we calculate one-year datasets consisting of long-term monthly means for temperature and precipitation as well as long-term monthly temperature standard deviation. This averaging is done to reduce the size of data PISM has to read which results in an overall faster computation. Illustrations of the PD and the LGM climate data and how they differ from each other are given in Appendix B. For more details about the climate data, the reader is referred to Section 3.2.2, Velasquez et al. (2020), Velasquez and Raible (in prep), and Velasquez (in prep).

We build transient climate forcings for the PDD mass balance model by modulating climate signals to the temperature data and by interpolating between the PD and the LGM precipitation data following the same signals, analogous to Section 3.2.3. The covered time period lasts from 50 ka BP to today. To obtain a transient temperature field $T(t,x,y)$, the temperatures of the LGM dataset $T_{LGM}(x,y)$ are processed as follows:

$$\begin{aligned} T(t,x,y) &= T_{LGM}(x,y) + a + \phi(t)\cdot\Delta T + \\ &\quad \gamma\cdot(S_{mod}(t,x,y) - S_{clim}(x,y)), \end{aligned} \tag{4.1}$$

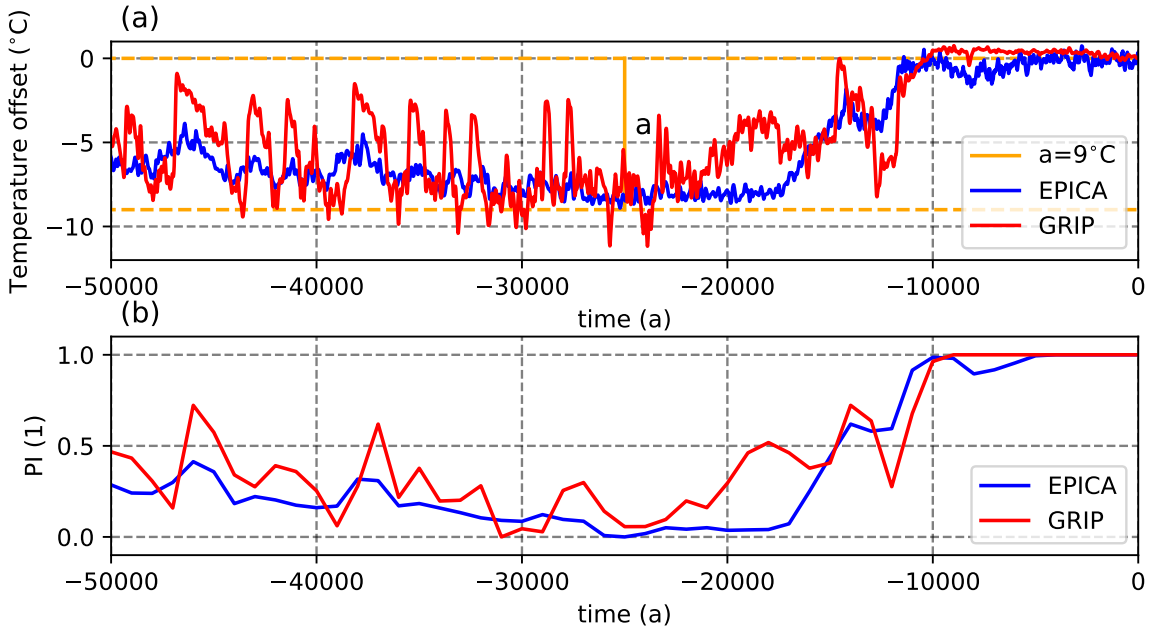


**Figure 4.2:** (a) Reconstructed temperature signals from EPICA (blue) and GRIP (red) that are applied to the temperature data and the uniform temperature increase of $a = 9$ °C (orange). The signals have been drawn with $\Delta T = 8.2$ °C for EPICA and $\Delta T = 7.6$ °C for GRIP. (b) the EPICA (blue) and GRIP (red) signal for the Precipitation Index ($PI$) at a sampling rate of 1000 years and scaled to values between zero and one which is used to linearly interpolate between present-day and Last Glacial Maximum precipitation rates.

where $a = 9$ °C is an uniform temperature increase, $\phi(t)$ is a climate signal, $\Delta T$ is a scaling factor for the climate signal, $\gamma = -4.5$ K km$^{-1}$ is the atmospheric temperature lapse rate, $S_{mod}(x, y, t)$ is the modelled ice surface elevation, and $S_{clim}(x, y)$ is the climate reference surface elevation. Analogous to Chapter 3, ΔT is used to tune the modelled maximum ice extent to the geomorphologically reconstructed LGM ice extent of Ehlers et al. (2011). The atmospheric temperature lapse rate is used to take into the elevation feedback that arises from changing ice surface elevations.

Climate signals $\phi(t)$ for temperature and precipitation rates are derived again from the European Project for Ice Coring in Antarctica (EPICA, Jouzel and Masson-Delmotte, 2007). In this study, we additionally test the climate signal from the Greenland Ice Core Project (GRIP, Seierstad et al., 2014), which is a temperature reconstruction with stronger and more frequent variations (Fig. 4.2a). The GRIP signal is available as a $\delta^{18}$O history sampled in 50 year bins. As Seguinot et al. (2018), we translate this signal to a temperature signal using the quadratic equation of Johnsen et al., 1995. The signals are interpolated to a temporal resolution of 10 years and smoothed with a floating-average with a window size of 100 years to achieve a homogeneous resolution during the last 50 ka. Then, an offset is applied to the signals such that the present-day value corresponds to zero. After this, the signal is scaled such that the period between 27 ka BP and 22 ka BP has an average offset of $\Delta T$ °C. Figure 4.2a shows the two signals used in this chapter.

The interpolation between PD precipitation rates ($P_{PD}$) and glacial precipitation rates ($P_{LGM}$) follows a time dependent Precipitation Index $PI(t)$ that is deduced from the climate signals (Fig. 4.2b):

$$P(t,x,y) \quad = \quad P_{PD}(x,y) \cdot PI(t) + P_{LGM}(x,y) \cdot (1 - PI(t)), \tag{4.2}$$

where the $PI(t)$ consists of piecewise averages over 1000 years and is scaled such that $0 \leq PI(t) \leq 1$ (Fig. 4.2b). In the remainder of this chapter, we call the forcing consisting of this type of precipitation interpolation and the temperature field of Eq. (4.1) as 'LGM+PD'.

We perform one simulation by constructing an artificial PD-based climate only relying on the PD climate dataset of the regional climate model of Velasquez et al. (2020), analogous to former studies such as Seguinot et al. (2018). To do so, we use temperature data of the PD climate dataset ($T_{PD}(x,y)$), set $a = 0$ °C, and use the PD lapse rate of $\gamma = -6$ K km$^{-1}$ in Eq. (4.1), analogous to the Chapter 3. A precipitation change of 7.3 % K$^{-1}$ is imposed per degree of temperature change from the climate signal $\phi(t)$:

$$P(t,x,y) \quad = \quad P_{PD}(t,x,y) \cdot 1.073^{\phi(t) \cdot \Delta T}. \tag{4.3}$$

If the EPICA temperature signal is used for $\phi(t)$, it is not possible to find a $\Delta T$ such that the reconstructed extent is matched (blue outline in Fig. 4.4e). Therefore, we set $\phi(t)$ to the GRIP temperature signal for which it is possible to find a suitable $\Delta T$ and apply it to the PD temperatures. Hereafter, we refer to this sort of climate forcing as 'PD-based'.

### 4.2.3 *Calculation of boulder transport and deposition*

To simulate the transport of erratic boulders, we deploy tracers on the ice surface and integrate their trajectory with the ice surface velocity field. For this, we choose five locations with specific lithologies commonly found in the lowlands, namely Vallorcine, Val de Bagnes, Val d'Hérens, Saastal, and the Aletsch area (Fig. 4.1c). Every 50 years, boulders are deployed on the ice surface at the five designated locations. The ice extent and the 2D surface ice velocity field are also updated every 50 years. However, the integration time step for the boulder transport is half a year. We integrate the transport of boulders using a fourth-order Runge-Kutta method with a post-processing script, similar to Jouvet et al. (2017). Deposited boulders that have been overridden by re-advancing ice are assumed to be destroyed i.e. reworking of deposited boulders is not considered.

## 4.3 RESULTS

All five simulations (Tab. 4.1) start at 50 ka BP, are initialized with ice free conditions, and use the temperature reconstructions following EPICA or GRIP to impose transiency in the climate with different degrees of variability. If not indicated

| signal | $\lambda$ | $C_1$ | $\Delta$T | climate forcing | comment |
|---|---|---|---|---|---|
| EPICA | 2 km | 1000 Pa a $m^{-1}$ | –8.2 °C | LGM+PD | reference simulation |
| **GRIP** | 2 km | 1000 Pa a $m^{-1}$ | –7.6 °C | LGM+PD | |
| EPICA | **5 km** | 1000 Pa a $m^{-1}$ | –8.0 °C | LGM+PD | |
| EPICA | 2 km | **300 Pa a $m^{-1}$** | –8.3 °C | LGM+PD | |
| **GRIP** | 2 km | 1000 Pa a $m^{-1}$ | –13.0 °C | **PD-based** | |

**Table 4.1:** Overview of the model settings used in the five simulations. The changes relative to the reference simulation are bold.

differently, the climate forcing consists of an interpolation between the LGM and the present-day (PD) climate data of Velasquez et al. (2020) and Velasquez and Raible (in prep) (LGM+PD, Tab. 4.1). For each simulation, the temperature offset $\Delta T$ is chosen such that the reconstructed maximum extent of Rhone Glacier is matched (see Tab. 4.1). The first simulation is treated as a reference simulation, which uses the EPICA signal, $\lambda = 2$ km, and $C_1 = 1000$ Pa a $m^{-1}$ (Tab. 4.1). The second simulation uses the GRIP signal to evaluate how a more rapidly changing climate affects Rhone Glacier, in particular the boulder transport. The third simulation uses a stronger ice flux limitation for the shallow ice approximation ($\lambda = 5$ km) to investigate its role for the discrepancy between trimline elevation and modelled ice thickness found in former ice flow modelling studies (Seguinot et al., 2018). The impact of higher sliding speeds on boulder transport and modelled ice thickness is tested in the fourth simulation. Finally, the fifth simulation uses the PD-based climate forcing which employs only the pattern of the PD climate data. This simulation is intended to show how representative LGM climate data of a regional climate model can improve the match between the modelled and the reconstructed Rhone Glacier.

### 4.3.1 *Time evolution of glacier area and volume*

| | max. area | max. volume | $t_{max}$ |
|---|---|---|---|
| Reference (E) | 49,404 $km^2$ | 35,944 $km^3$ | 24.5 ka BP |
| GRIP (G) | 50,300 $km^2$ | 37,903 $km^3$ (+5 %) | 29.4 ka BP |
| $\lambda = 5$ km (E) | 51,528 $km^2$ | 41,241 $km^3$ (+15 %) | 24.5 ka BP |
| 300 Pa a $m^{-1}$ (E) | 43,720 $km^2$ | 26,073 $km^3$ (–27 %) | 23.7 ka BP |
| PD-based (G) | 61,816 $km^2$ | 40,981 $km^3$ (+14 %) | 29.4 ka BP |

**Table 4.2:** Overview for the maximum ice covered area and volume as well as the timing of the maximum area $t_{max}$. Percentages for the maximum volume are relative to the reference simulation. 'G' marks simulations using the GRIP climate signal and 'E' marks the simulations using the EPICA climate signal.

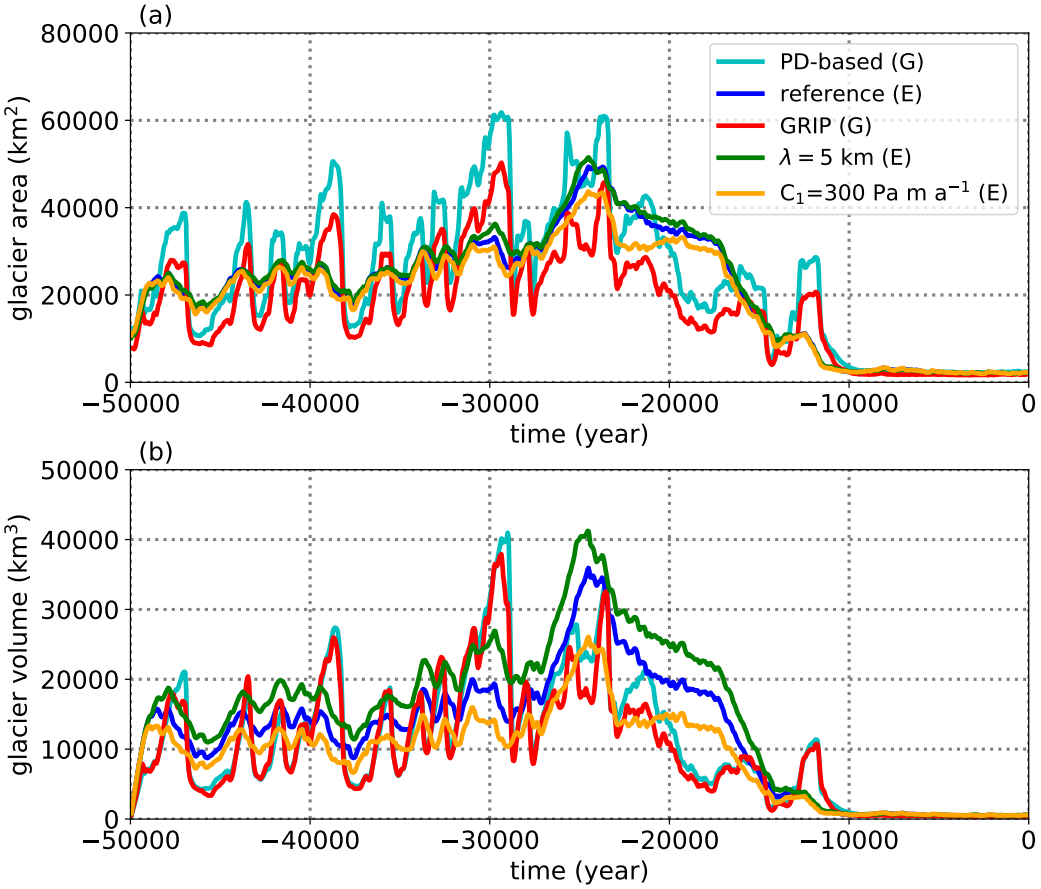


**Figure 4.3:** Evolution of the glaciated area (a) and volume (b) of the reference simulation (blue), the simulation driven with GRIP (red), the simulation with $\lambda = 5$ km (green), the simulation with $C_1 = 300$ Pa a m$^{-1}$ (orange), and the simulation using the PD-based data (turquoise). 'G' marks simulations using the GRIP climate signal and 'E' marks the simulations using the EPICA climate signal.

Figure 4.3a shows how the ice surface area evolves over time for all simulations. The size of Rhone Glacier modelled with the smooth EPICA climate signal is subject to slower changes over time compared to the GRIP simulations. In the simulations that use the GRIP climate signal, Rhone Glacier is most of the time out of balance and either advances or retreats rather quickly. The three simulations driven with the EPICA signal show relatively little variations in glaciated area prior to the LGM and one single maximum ice extent at 24.5 ka BP in the reference and the $\lambda = 5$ km simulation and a maximum ice extent at 23.7 ka BP in the $C_1 = 300$ Pa a m$^{-1}$ simulation. In these simulations, the LGM is followed by a gradual retreat (Fig. 4.3a). In contrast to the simulations driven with the EPICA climate signal, the two simulations using the GRIP climate signal show many rapid advances and retreats with hardly any stagnant phases. A notable feature of the GRIP simulations is the distinct double maximum for the ice extent. The first and largest maximum is reached at 29.4 ka BP, the second and smaller maximum at 23.7 ka BP (Fig. 4.3a). Only the PD-based simulation surpasses a maximum glacier

area of 60,000 km$^2$, while all other simulations driven with the LGM climate forcing are around 50,000 km$^2$ or less.

The evolution of the glacier volume is similar to the evolution of the glacier surface area (Fig. 4.3b). However, the maximum ice volumes produced by the five simulations differ from each other. The reference and the GRIP simulation produce a similar maximum ice volume of 35,944 km$^3$ and 37,903 km$^3$ respectively. The ice volume of the $\lambda = 5$ km simulation and the PD-based simulation are the largest with 41,241 km$^3$ and 40,981 km$^3$ respectively, while the $C_1 = 300$ Pa a m$^{-1}$ simulation produces the smallest ice volume with 26,073 km$^3$ (Tab. 4.2). The maximum volumes and the maximum ice extents are reached synchronously.

### 4.3.2 *Maximum ice extent*

Figure 4.4 shows the modelled maximum ice extent of the reference simulation (Fig. 4.4a), the GRIP simulation (Fig. 4.4b), the $\lambda = 5$ km simulation (Fig. 4.4c), the $C_1 = 300$ Pa a m$^{-1}$ simulation (Fig. 4.4d), and the PD-based simulation (Fig. 4.4e). In general, all five simulations lead to a maximum ice extent more or less in agreement with the geomorphological reconstruction of Ehlers et al. (2011) at the Rhone Glacier catchment and surrounding glaciers with a few smaller local deviations.

The reference simulation and the simulation using $\lambda = 5$ km result in a highly similar ice extent (Fig. 4.4a,c). The Lyon Lobe is matched very well while the Solothurn Lobe is slightly too extensive. The Jura Ice Cap is mostly in agreement with the geomorphological reconstruction, however, the north-western edge is not reached. The Ivrea and Rivoli Lobes are also well captured by these two simulations.

The simulation which is using the more variable climate signal, GRIP, matches the Solothurn and Lyon Lobes remarkably well (Fig. 4.4b). The Jura Ice Cap is mostly matched but again the north-western most edge is not reached. The Rivoli and in particular the Ivrea Lobe in the south are too extensive. Further, there is an ice patch in the lowlands outside the reconstructed ice extent at the upper right corner (Fig. 4.4b).

The simulation using increased sliding speeds, $C_1 = 300$ Pa a m$^{-1}$, shows a Lyon Lobe that lies within the geomorphologically reconstructed extent while the modelled terminus at the Solothurn Lobe lies beyond the reconstructions (Fig. 4.4d). The Jura Ice Cap is extremely small and only covers the surroundings of Mont Tendre. The Ivrea and Rivoli Lobes are in good agreement with the reconstructed extent.

The PD-based simulation, which uses only the PD dataset, shows a Solothurn Lobe modelled slightly too large (Fig. 4.4e). The Lyon Lobe on the other end does not reach the reconstructed maximum extent. The Jura Ice Cap reaches far beyond the reconstructed maximum ice extent. Unlike in all other simulations, the area north of Aare Glacier and east of the Solothurn Lobe is extensively glaciated. The Rivoli and the Ivrea Lobes south of the Alps are both well reproduced.

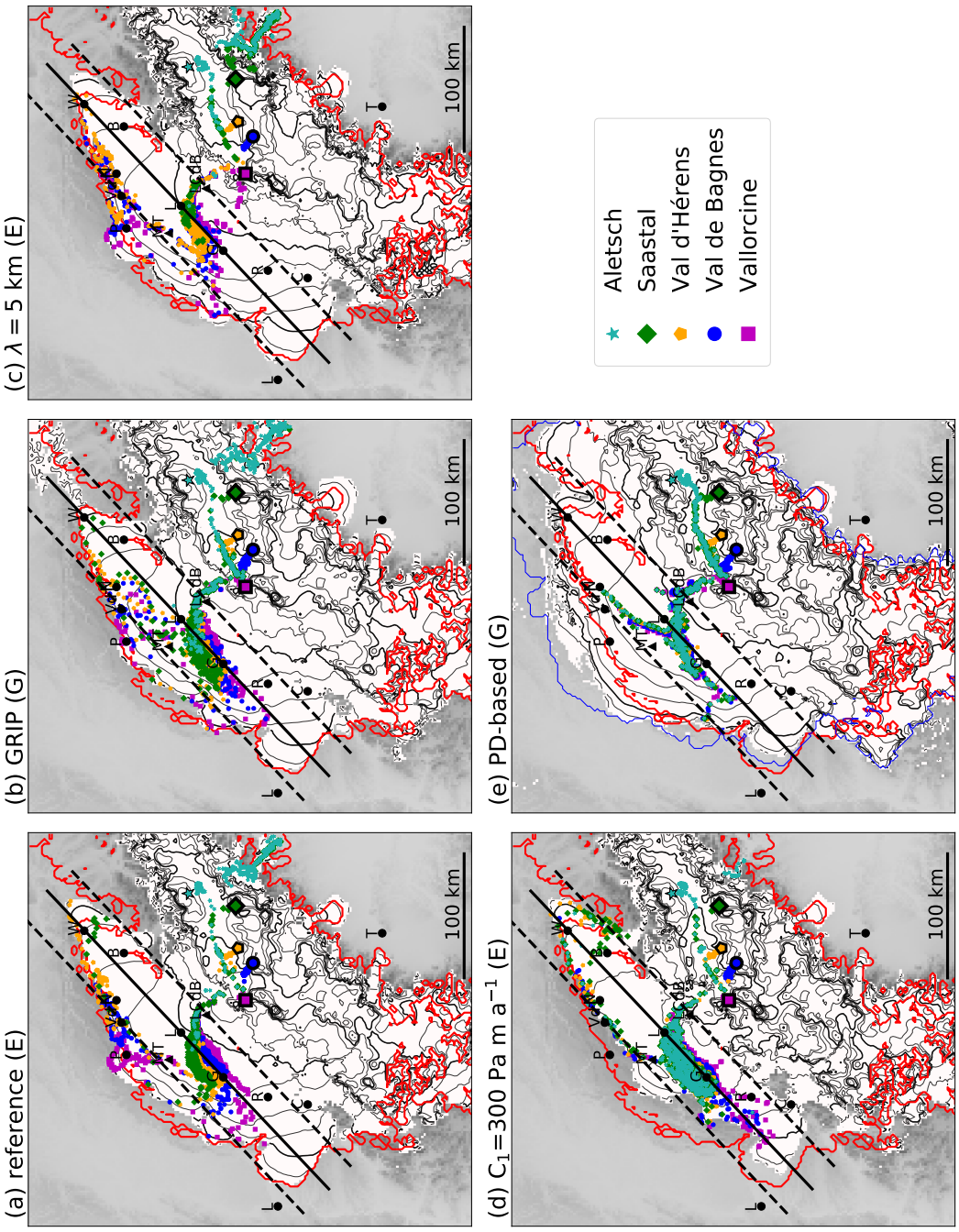


**Figure 4.4:** Modelled maximum ice extent reached by the reference simulation with EPICA (a), the simulation driven with GRIP (b), the simulation with $\lambda = 5$ km (c), the simulation with $C_1 = 300$ Pa a m$^{-1}$ (d), and the simulation using the PD-based climate forcing (e). The blue outline in (e) indicates the maximum extent if the PD-based climate forcing is used with the EPICA climate signal. 'G' marks simulations using the GRIP climate signal and 'E' marks the simulations using the EPICA climate signal. The red outlines indicate the geomorphologically reconstructed maximum ice extent (Ehlers et al., 2011). The coloured symbols indicate the locations where the simulations deposit erratic boulders from the Valais. The different origins of boulders are indicated by the symbols with a black frame. The black line roughly follows the centre ice flow direction of the Solothurn Lobe and the Southern-Branch and is used to measure the boulder diversion in Fig. 4.6. The thick (thin) black contour lines have an elevation spacing of 1000 m (250 m).

### 4.3.3 *Maximum ice thickness*

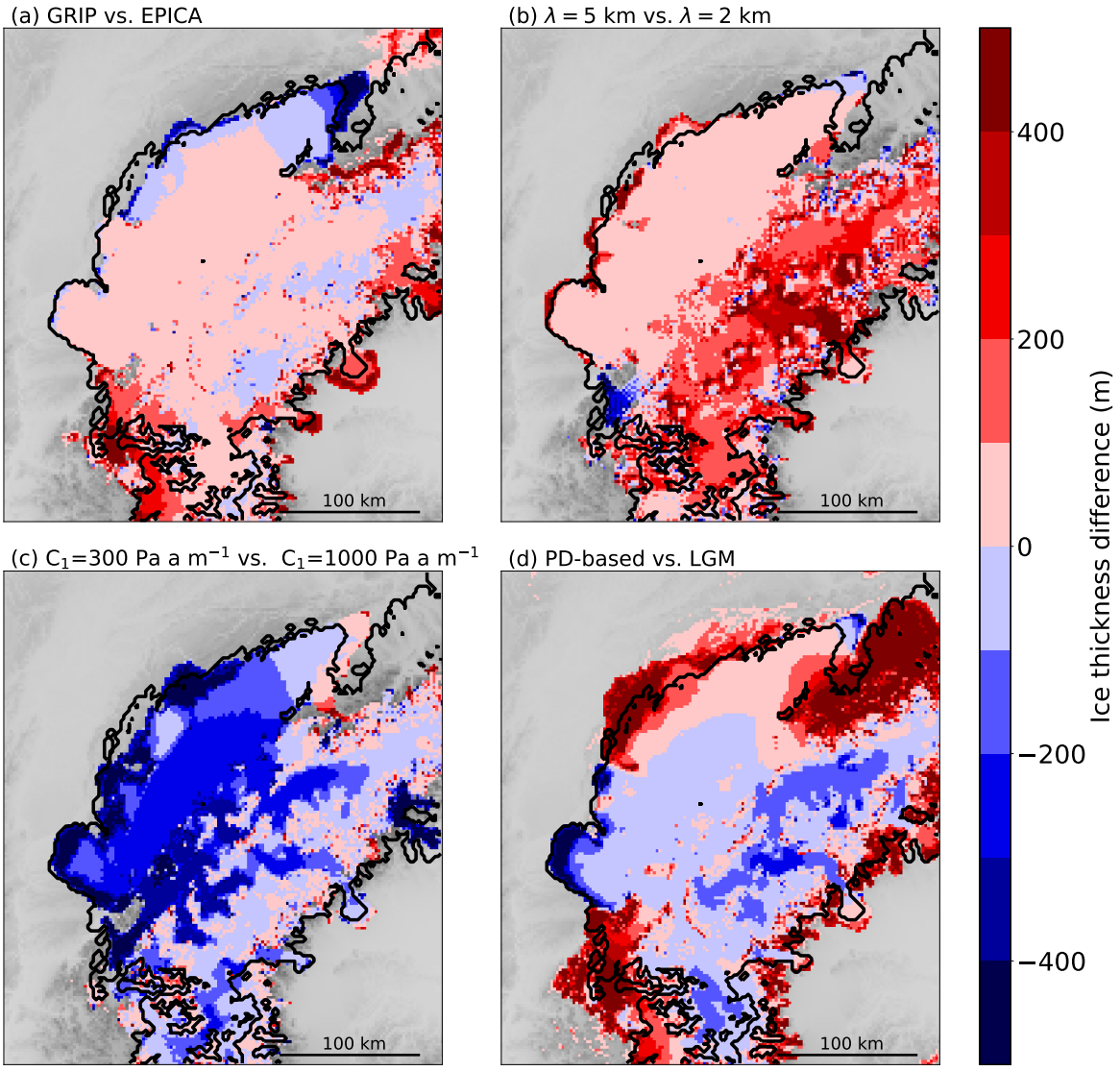


**Figure 4.5:** Deviation in maximum ice thickness relative to the reference simulation for the GRIP simulation (a), the $\lambda = 5$ km simulation (b), the $C_1 = 300$ Pa a m$^{-1}$ simulation (c), and the PD-based simulation (d). The black outlines indicate the geomorphologically reconstructed maximum ice extent (Ehlers et al., 2011).

Thickness differences are minor between the reference EPICA and the GRIP simulation (Fig. 4.5a). They are mostly restricted to the termini of the Ivrea and the Rivoli Lobes which are both thicker using the GRIP signal and the terminus of the Solothurn Lobe which is thinner using the GRIP signal. The Southern-Branch and the Lyon Lobe have the same thickness in the two simulations.

The simulation using $\lambda = 5$ km yields ice thicknesses between 100 m and 500 m thicker in the Alps than the reference simulation that is using $\lambda = 2$ km (Fig. 4.5b). This concerns especially Valais Glacier and the glacier feeding the Ivrea Lobe. Also,

the ice volume is about 15 % larger than in the reference simulation (Tab. 4.2). The Solothurn Lobe, the Southern-Branch, and the Lyon Lobe have about the same thickness and are at most 0–100 m thicker in the $\lambda = 5$ km simulation.

The simulation with increased sliding speeds ($C_1 = 300$ Pa a m$^{-1}$) produces a Rhone Glacier that is generally thinner, 100–300 m on the Southern-Branch and the Solothurn Lobe and in the main valley of Valais Glacier (Fig. 4.5c). This is also reflected in the ice volume that is about 27 % smaller that in the reference simulation (Tab. 4.2).

The PD-based simulation produces maximum ice thicknesses similar to the reference simulation at most parts of the Lyon Lobe, the Southern-Branch, and the Solothurn Lobe, deviating at most by ±100 m (Fig. 4.5d). However, the ice thickness in the PD-based simulation is more than 500 m greater north of Aare Glacier and at the northern edge of the Jura Ice Cap. Further, most of Valais Glacier is 100–200 m thinner in the PD-based simulation compared to the reference simulation.

All five simulations produce an ice surface elevation which is on average significantly above the trimline elevation reconstructed by Kelly et al. (2004) (Tab. 4.3). The reference and the GRIP simulation both yield an ice surface elevation that lies ≈607–622 m above the trimlines. In the case of the simulation with $C_1 = 300$ Pa a m$^{-1}$ and the PD-based simulation this mismatch is 552–570 m and thus somewhat smaller. At 874 m, the simulation with the stronger flux limitation, $\lambda = 5$ km, yields by far the greatest mean difference between modelled ice surface elevation and trimlines.

All five simulations yield an ice surface elevation significantly higher than interpreted from boulder deposition elevation along the Jura by Graf et al. (2015). The ice surface elevation obtained with the reference, the GRIP, the $\lambda = 5$ km, and the PD-based simulation are all between 626 and 680 m greater than inferred by Graf et al. (2015) (Tab. 4.3). The $C_1 = 300$ Pa a m$^{-1}$ simulation yields a smaller deviation of 515 to 530 m.

| | Trimlines | Mont Tendre | Neuchâtel |
|---|---|---|---|
| reference (E) | +607 m ± 184 m | +626 m | +636 m |
| GRIP (G) | +622 m ± 175 m | +641 m | +632 m |
| $\lambda = 5$ km (E) | +874 m ± 222 m | +641 m | +670 m |
| $C_1 = 300$ Pa a m$^{-1}$ (E) | +570 m ± 220 m | +465 m | +522 m |
| PD-based (G) | +552 m ± 205 m | +660 m | +680 m |

**Table 4.3:** Mean deviation between the mapped trimline elevations of Kelly et al. (2004) (red dots, Fig. 4.1c) and modelled maximum ice surface elevation for all five simulations. Overestimation of modelled ice surface elevation relative to the estimated ice surface elevation by Graf et al. (2015) near Mont Tendre and Neuchâtel (green crosses in Fig. 4.1c). 'G' marks simulations using the GRIP climate signal and 'E' marks the simulations using the EPICA climate signal.

### 4.3.4 *Final deposition location of modelled boulders*

In all five simulations, the deposition locations of erratic boulders originating from the Valais show a similar pattern (Fig. 4.4). Differences concern mostly individual lithologies or a specific area of Rhone Glacier.

In the reference simulation, boulders from Val d'Hérens and Val de Bagnes are deposited primarily along and within the Jura next to the Solothurn Lobe. However, they never reach the centre or the orographic right side of the Solothurn Lobe (Fig. 4.4a). The boulders from Vallorcine cross the Jura east of Mont Tendre and are not deposited on the Solothurn Lobe. Only few boulders from Saastal reach the Solothurn Lobe and boulders from the Aletsch area are entirely absent. The majority of boulders originating from Vallorcine, Val d'Hérens, Val de Bagnes, and Saastal are deposited in the area of the Southern-Branch. Yet, boulders from Saastal reach the Solothurn Lobe only rarely. Several boulders from Saastal travel to the Toce Glacier catchment south of the Alps. Boulders from the Aletsch area never or only barley reach Lausanne and are transported commonly to the catchment of Toce Glacier. No boulders from the Valais are deposited at or near the Lyon Lobe.

The simulation driven with the GRIP climate signal shares a high degree of similarity with the reference simulation that used the EPICA climate signal. The only notable difference from the reference simulation is the fact that some boulders from Vallorcine, Val de Bagnes, Val d'Hérens, and Saastal are deposited closer to the centre line of the Solothurn Lobe north of Lausanne (Fig. 4.4b).

The boulder depositional locations in the $\lambda = 5$ km simulation also share many similarities with the reference simulation (Fig. 4.4c). In contrast to the reference simulation, boulders from Saastal are almost absent from the Solothurn Lobe and the Southern-Branch in the $\lambda = 5$ km simulation but are more common in the Toce Glacier catchment.

Analogous to the reference simulations, results obtained with increased sliding speeds ($C_1 = 300$ Pa a m$^{-1}$) lead to a boulder deposition along the Jura mountains, in particular for those from Saastal but also for many originating from Val d'Hérens, Val de Bagnes, and Aletsch area (Fig. 4.4d). Only boulders from Vallorcine are not deposited on the Solothurn Lobe but rather on the Southern-Branch. Unlike the other three simulations, the $C_1 = 300$ Pa a m$^{-1}$ simulation allows boulders from Val d'Hérens and Saastal to be transported to the orographic right side of the Solothurn Lobe. Moreover, several boulders from the Aletsch area are deposited at Toce Glacier in this simulation.

In the simulation using the PD-based climate, boulders originating from all five lithological origins are deposited along the Jura at the Southern-Branch and the Solothurn Lobe (Fig. 4.4e). Boulders are deposited closely together regardless of their origin. On the Solothurn Lobe, the boulders are deposited on a narrow line between Lausanne and Neuchâtel. Boulders from the Aletsch area are common on Solothurn Lobe and Southern-Branch but never flow into the Toce Glacier catchment.

### 4.3.5 *Evolution of boulder deposition along the Solothurn Lobe*

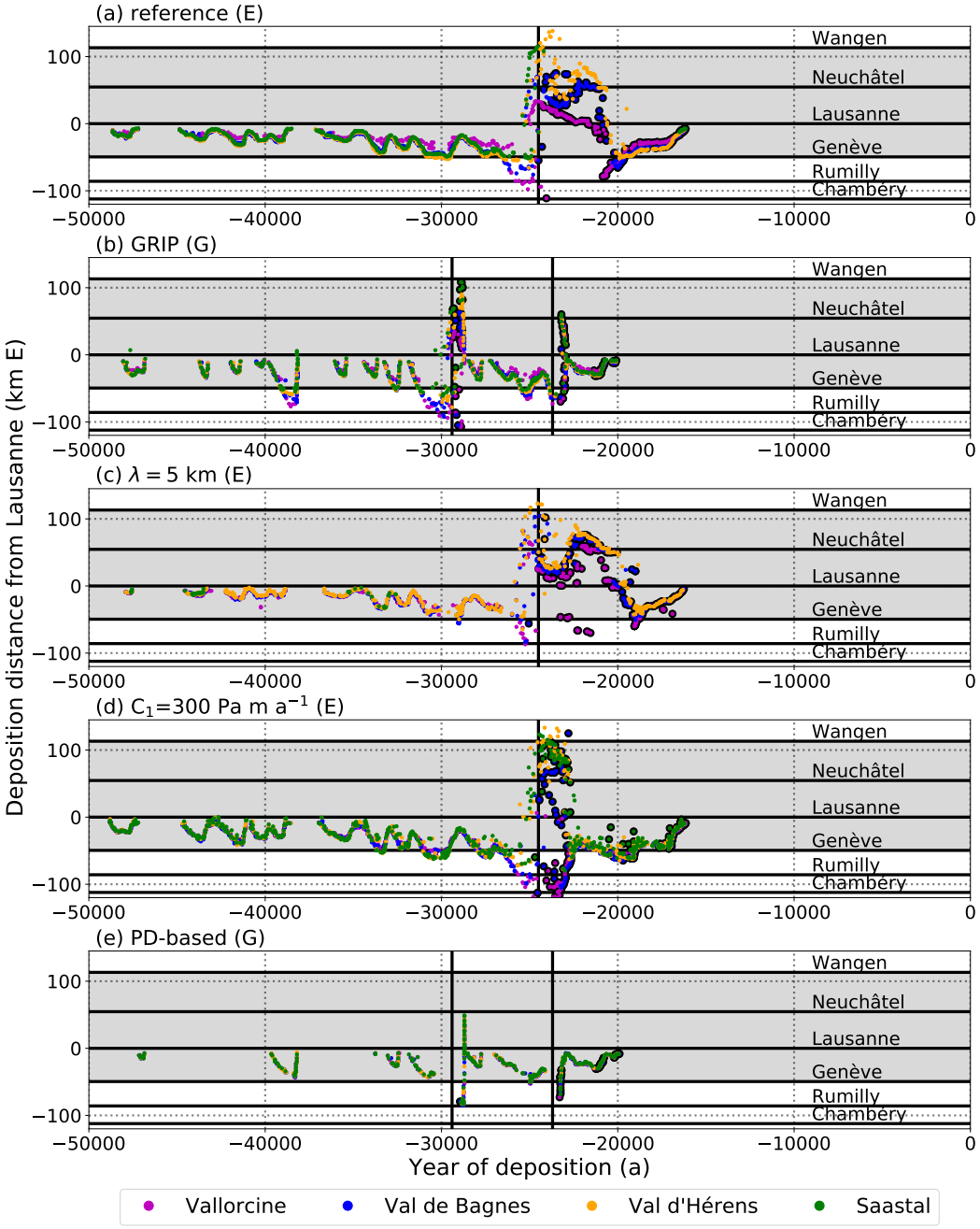


**Figure 4.6:** Modelled depositional locations of modelled boulders along the centre line of the Solothurn Lobe and the Southern-Branch (black line in Fig. 4.4). The x-axis represents the time the boulders were deposited by Rhone Glacier. Vertical black lines indicate the timing of the maximum ice extents. Deposited boulders which are never overridden and destroyed by advancing ice have a black frame. Boulders deposited within the Valais are not shown. The grey background indicates the area where boulders from the Valais are found today. The figure shows results obtained with the reference simulation (a), the GRIP simulation (b), the simulation using $\lambda = 5$ km (c), the simulation using $C_1 = 300$ Pa a m$^{-1}$ (d), and the simulation using the PD-based climate (e). 'G' marks simulations using the GRIP climate signal and 'E' marks the simulations using the EPICA climate signal.

To illustrate the modelled boulder diversion towards the Solothurn Lobe, we plot the deposition distance of boulders from the Valais (Vallorcine, Val de Bagnes, Val d'Hérens, Saastal) to Lausanne, projected to the black line in Fig. 4.4 or 4.6. The time coordinate indicates the time when the glacier deposits the boulder. The grey background between Genève and Wangen (Fig. 4.6) indicates the range where boulders from the Valais are commonly found today. A boulder is diverted towards the Solothurn Lobe if it is deposited east of Lausanne i.e. if it lies above Lausanne on the $y$-axis. Four simulations allowed boulders from the Valais to be transported to the entire range of depositional locations observed today without being overriden and destroyed until the present (black framed dots, Fig. 4.6). Almost all surviving boulders are deposited after the maximum ice extent is reached (black vertical lines in Fig. 4.6) and during retreat phases. For most of the time before the maximum ice extent is reached, boulders from the Valais only reach the area between Lausanne and Genève and are overridden and destroyed until the present. Then, the depositional location shifts to Wangen within a few millennia before Rhone Glacier reaches its maximum extent (Fig. 4.6). In particular, boulders from Val d'Hérens reach the Solothurn Lobe terminus while boulders from Vallorcine and Val de Bagnes have little chance to be transported as far as Neuchâtel. The boulders that are transported to the area between Neuchâtel and Wangen have travel times between 500 and 1500 years.

The reference simulation shows a temporary reduction in diversion just after the maximum glacier extent is reached (Fig. 4.6a). During the diversion, only a few boulders from Saastal are deposited on the Solothurn Lobe and Southern-Branch. At around 20 ka BP the diversion stops and boulders are again deposited between Lausanne and Genève.

The simulation driven with the GRIP climate signal shows two major events with boulders being diverted towards Wangen (Fig. 4.6b). These two events of diversion occur shortly after the maximum extents are reached and end both immediately afterwards. Boulders deposited by the first advance are not overridden mostly between Neuchâtel and Wangen. Most boulders deposited during the second smaller advance between Lausanne and Neuchâtel are never overridden until the end of the simulation.

The $\lambda = 5$ km simulation is similar to the reference simulation. However, the boulders from Saastal never reach the Solothurn Lobe. There is also a temporary reduction in boulder diversion just after the maximum glacier extent is reached (Fig. 4.6c). The diversion also ends at around 20 ka BP.

In the simulation with increased sliding speeds ($C_1 = 300$ Pa a $m^{-1}$), many boulders from Val de Bagnes are deposited well beyond Neuchâtel and are never overridden and destroyed (Fig. 4.6d). This is not the case in the other four simulations where boulders from Val de Bagnes only barely reach Neuchâtel. However, all boulders from Vallorcine and some from Val de Bagnes are deposited near Rumilly and Chambéry during the LGM. After the maximum extent is reached, the boulder diversion becomes continuously weaker and ceases entirely at about 22 ka BP.

In the PD-based simulation, boulders are diverted towards the Solothurn Lobe only once for a short time after the maximum ice extent is reached at 29.4 ka BP (Fig. 4.6e). The diversion behaviour hardly differs between the boulders from the five considered origins. No boulder reaches the area between Neuchâtel and the terminus of the Solothurn Lobe. Furthermore, all the diverted boulders on the Solothurn Lobe are overridden and destroyed by the end of the simulation.

### 4.3.6 *Modelled alpine boulders invading the Jura mountains*

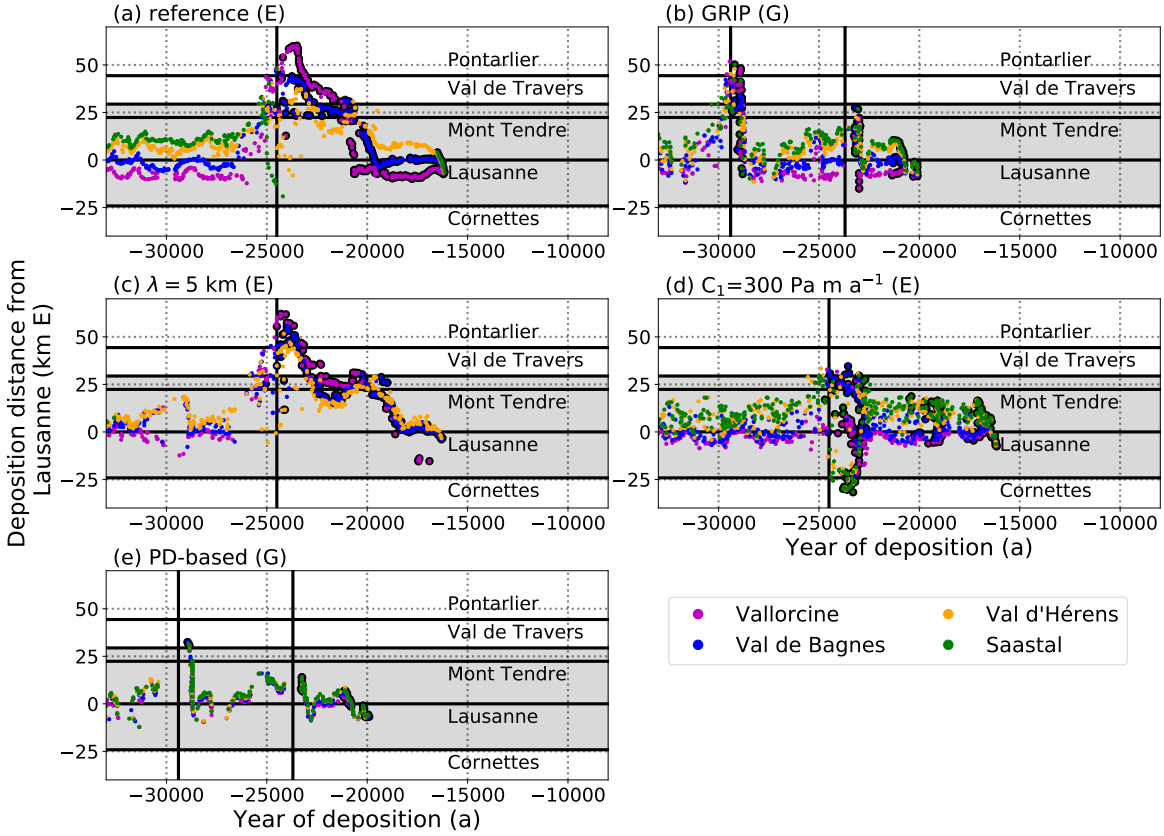


**Figure 4.7:** Modelled depositional distance from the black centre line orientated along the Genève-Lausanne axis (see Fig. 4.4). The x-axis represents the time when the boulders were deposited by Rhone Glacier. The vertical black line indicates the timing of maximum ice extents. Deposited boulders that were not crushed by advancing ice have a black frame. Boulders deposited within the Valais are not shown. The gray background indicates approximately the width of the Solothurn Lobe and the Southern-Branch which was reached by ice from the Valais. The figure shows the reference simulation (a), the GRIP simulation (b), the simulation using $\lambda = 5$ km (c), the simulation using $C_1 = 300$ Pa a m$^{-1}$ (d), and the PD-based simulation (e). 'G' marks simulations using the GRIP climate signal and 'E' marks the simulations using the EPICA climate signal.

In order to visualize the degree of Jura mountain invasion by our modelled alpine boulders, Fig. 4.7 shows the distance between the deposition location of boulders

from the Valais and the black line along the Southern-Branch and Solothurn Lobe shown in Figs. 4.1a and 4.4. Fig. 4.7 thus visualizes to what extent boulders invaded the Jura in each of the four simulations. In the reference and $\lambda = 5$ km simulation, boulders from Vallorcine, Val de Bagnes, and Val d'Hérens are deposited well beyond Val de Travers and even Pontarlier after the maximum extent is reached (Fig. 4.7a,c). Boulders from Val de Bagnes and Val d'Hérens are rarely transported that far. The first and largest maximum extent in GRIP simulation transports boulders from Vallorcine, Val de Bagnes, and Val d'Hérens across the Jura to the area between Val de Travers and Pontarlier for a short time (Fig. 4.7b). In the simulation with increased sliding speeds ($C_1 = 300$ Pa a m$^{-1}$), no boulders are transported beyond Val the Travers and thus no invasion of the Jura occurs (Fig. 4.7d). In the PD-based simulation, alpine boulders hardly invade the Jura and are not transported beyond Val de Travers (Fig. 4.7e). The deposition cross distance from the centre line hardly depends on the boulders' location of origin.

### 4.3.7 *Ice flow dynamics of Rhone Glacier throughout the Last Glacial Maximum*

In all simulations, Rhone Glacier changed the ice flow direction in the area where the Valais Glacier meets the Solothurn Lobe and the Southern-Branch before the maximum ice extent is reached. The evolution of this flow direction change is similar in all simulations. Therefore, the evolution of the direction changes and its impact on the boulder transport is described and illustrated only for the reference simulation (Fig. 4.8). However, the boulder deposition pattern of the $C_1 = 300$ Pa a m$^{-1}$ and PD-based simulations stands out from the other simulations (Fig. 4.4). Therefore, we also briefly describe their ice dynamics and boulder transport, but only during the maximum extension.

- At 26 ka BP, the Rhone Glacier piedmont lobe splits in two arms, one flowing in north-east direction forming the Solothurn Lobe and one flowing in south-west direction forming the Southern-Branch (Fig. 4.8a). All boulders from Vallorcine, Val de Bagnes, Val d'Hérens, and Saastal are transported southwards to the Southern-Branch while boulders from the Aletsch area travel south towards Toce Glacier.

- At 25.5 ka BP, new boulders coming from Val de Bagnes, Val d'Hérens, and Saastal no longer travel southwards but instead changed flow direction towards the Solothurn Lobe (Fig. 4.8b). However, many boulders previously deployed on the ice in these three valleys and in Vallorcine are still on the Southern-Branch and keep travelling further southwards.

- At 25 ka BP, all boulders now leaving the Valais are diverted towards the Solothurn Lobe (Fig. 4.8c). The ice divide separating the Solothurn Lobe from the Southern-Branch has moved from between Mont Tendre and east of Lausanne to between Mont Tendre and Les Cornettes de Bise within 1000 years. Thus, the Southern-Branch is now disconnected from Valais Glacier. Yet,

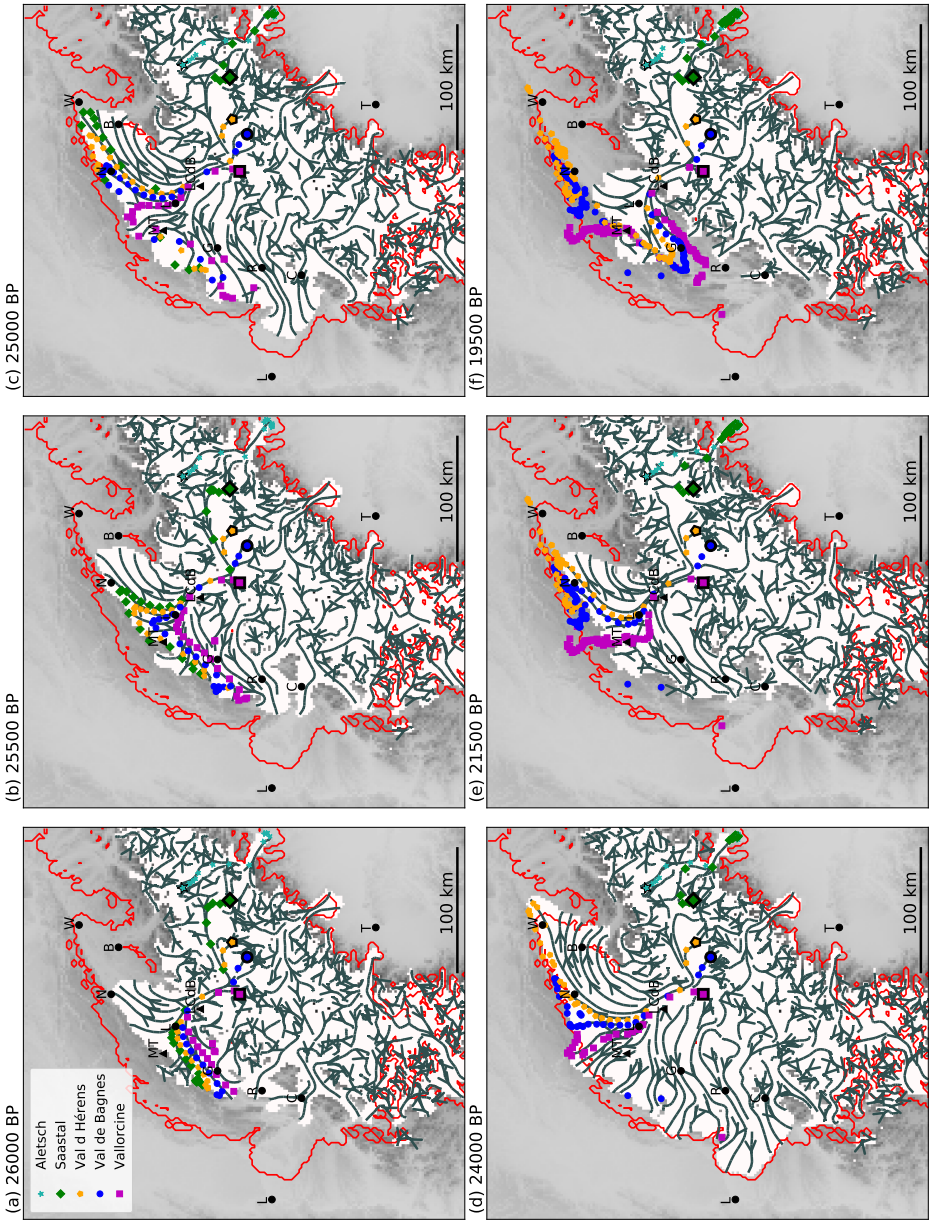


**Figure 4.8:** Modelled ice extent and ice flow lines of the reference simulation at 26 ka BP (a), 25.5 ka BP (b), 25 ka BP (c), 24 ka BP (d), 21.5 ka BP (e), and 19.5 ka BP (f). The red outlines indicate the geomorphologically reconstructed maximum ice extent (Ehlers et al., 2011). The coloured symbols indicate the locations of erratic boulders from the Valais at the respective time. The origins of boulders are indicated by the symbols with a black frame. The grey streamlines indicate ice flow directions at the respective times. Black dots indicate towns and black triangles indicate mountains labelled in Fig. 4.1a.

numerous boulders from the Valais remain on the ice surface of the Southern-Branch and continue their journey south-westwards. Boulders from Saastal have also changed direction and now flow to the Toce Glacier catchment and thus leave Rhone Glacier in the upper Valais. In the meantime, a transfluence

over the Jura appears north-west of Mont Tendre and boulders from Vallorcine are transported into the Jura.

- At 24 ka BP, several transfluences over the Jura appear also south-west of Mont Tendre when the glaciers are close to their maximum (Fig. 4.8d). Now also boulders from Val de Bagnes are transported onto the Jura mountains. Solely boulders from Val d'Hérens are transported to the terminus of the Solothurn Lobe.

- At 21.5 ka BP, Rhone Glacier is retreating. Boulders from Vallorcine start to change their trajectory back towards the Southern-Branch. However, boulders coming from Val d'Hérens and Val de Bagnes are still transported towards the Solothurn Lobe (Fig. 4.8e).

- At 19.5 ka BP, the diversion has ended and boulders from Vallorcine, Val de Bagnes, and Val d'Hérens are transported to the Southern-Branch (Fig. 4.8f). Yet, boulders from Saastal and the Aletsch area are still transported towards the Toce Glacier catchment.

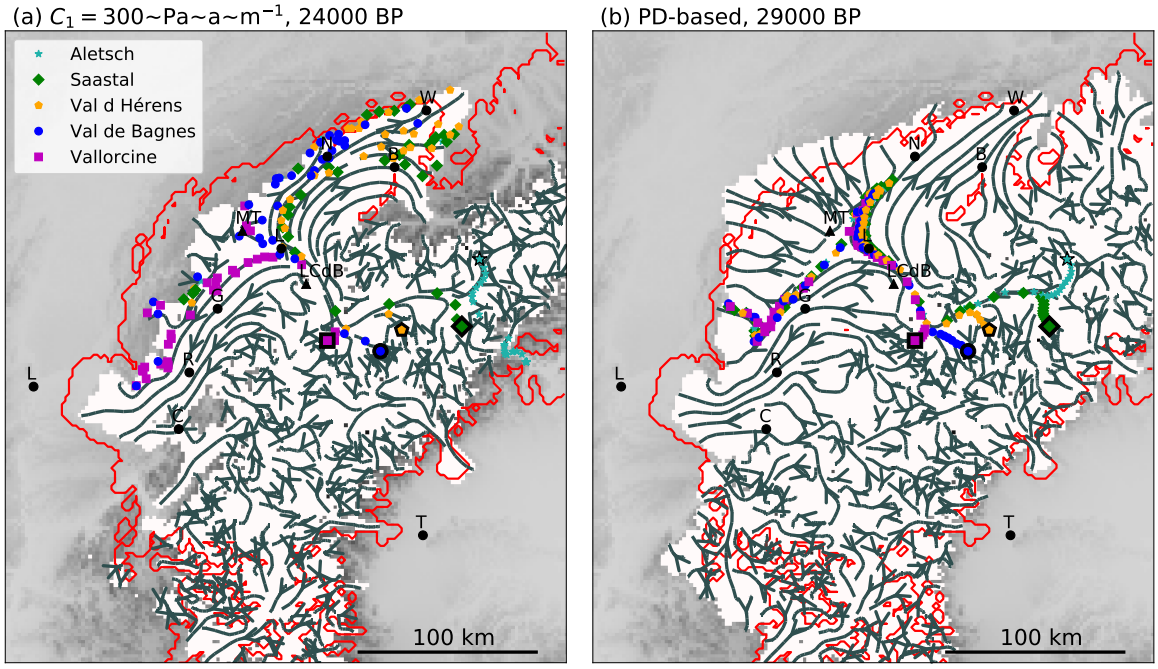


**Figure 4.9:** Modelled ice extent and ice flow lines of the $C_1 = 300$ Pa a m$^{-1}$ simulation at 24 ka BP (a) and the PD-based simulation at 29 ka BP (b). The red outlines indicate the geomorphologically reconstructed maximum ice extent (Ehlers et al., 2011). The coloured symbols indicate locations of erratic boulders from the Valais at the respectives times. The origins of boulders is indicated by the symbols with a black frame. The grey streamlines indicate ice flow direction at the respective times.

The $C_1 = 300$ Pa a m$^{-1}$ simulation, which uses increased sliding speeds, resembles the reference simulation until the boulder diversion starts to develop but differs

from it, in particular when the ice reaches its maximum extent. The invasion of the Jura is minor and hardly affects boulder trajectories (Fig. 4.9a). Boulders from Saastal remain in the Rhone Glacier system and are diverted to the orographic right side of the Solothurn Lobe together with boulders from Val d'Hérens and Val de Bagnes. However, boulders from Vallorcine mostly continue to travel towards the Southern-Branch. Boulders from the Aletsch area are transported towards the Toce Glacier system.

In the simulation driven with the PD-based climate forcing, the trajectories of all five boulder lithologies lie close together (Fig. 4.9b). The large Jura Ice Cap inhibits the boulders from Valais to invade the Jura. The boulders from all five locations are diverted almost simultaneously towards the Solothurn Lobe. Similar to the reference simulation, several boulders remain on the Southern-Branch and continue their journey south-westwards.

## 4.4 DISCUSSION

The discussion contains two main topics. First, the role of climatic inputs are discussed in Sections 4.4.1 and 4.4.2. Second, Sections 4.4.3 and 4.4.4 discuss the comparison with ice thicknesses of geomorphological reconstructions and former ice flow modelling studies as well as aspects of the ice dynamics of the Rhone Glacier.

### 4.4.1 *Little influence by the choice of transient signal for modelling Rhone Glacier*

It is largely unknown how the dynamics of Rhone Glacier are affected by the tranciency in the climate. To provide insight in this open question, we tested how two different climate signals impact the modelled Rhone Glacier: The EPICA signal which is smooth and the GRIP signal which has stronger and more frequent variations. First, we discuss the impact of the climate signal choice on the ice extent and then the impact on the boulder transport.

#### *Ice extent*

The modelled ice extent and ice thickness of Rhone Glacier obtained with the GRIP climate signal is similar to the result of the reference EPICA simulation. Lobes smaller than the Lyon Lobe are larger with the GRIP signal, such as the Aare and the Toce Glacier and the Ivrea and the Rivoli Lobe (Fig. 4.4a,b, Fig. 4.5a). The Solothurn Lobe, which is the only lobe within the model domain that is larger than the Lyon Lobe, is smaller using the GRIP signal. The reason might be that the smaller glaciers are steeper than the large ones and thus react quicker to rapid climate changes (Zekollari et al., 2020). The quick oscillations characterizing the GRIP climate signal allow the smaller steep glaciers in the south of the Alps to grow rapidly and reach a near equilibrium position while these oscillations do not last long enough to allow large and flat glaciers such as the Solothurn Lobe to reach an equilibrium with the climate.

In the GRIP simulation, an ice patch forms in the north-east of the model domain (Fig. 4.4b). The formation of this ice patch is caused by a so-called cold pool the LGM temperature data, cold air that is trapped in a topographical depression (Li et al., 2015). In Chapter 3, this cold pool is also responsible for ice accumulation in the lowlands. It is not known if the cold pool in the LGM dataset is an artefact or if it is modelled realistically.

*Boulder diversion*

The climate signal does not greatly affect the boulder diversion. The boulder diversion starts shortly before the maximum ice extent is reached (EPICA: 24.5 ka BP, GRIP: 29.4 ka BP), regardless of the climate signal used (Fig. 4.6a,b). However, the diversion only lasts for a short time in the GRIP simulation, whereas the diversion continuously weakens until 20 ka BP in the EPICA reference simulation. Thus, the climate signal determines for how long the diversion prevails and therefore drives the numbers of boulders that are diverted and deposited. The invasion of the Jura by alpine boulders is weaker in the GRIP simulation (Fig. 4.7a,b). In the EPICA simulation an invasion of the Jura occurs shortly after the maximum extent is reached (Fig. 4.7a). Therefore, the short time Rhone Glacier spends near the maximum extent in the GRIP simulation might be the reason why no significant invasion develops. The boulder diversion is discussed in more detail in Section 4.4.4.

In general, both the reference EPICA simulation and the GRIP simulation succeed at transporting boulders from the Valais to the area where they are observed today, namely between about Genève and Wangen at the Solothurn Lobe terminus (Fig. 4.6a,b). However, boulders are deposited closer to the centre line of the Solothurn Lobe with the GRIP signal (Fig. 4.4a,b). This is caused by the more rapid glacier retreats following the periods of diversion. In addition to this, there are the two major glacier advances with a boulder diversion in the GRIP simulation (Fig. 4.6). Unfortunately, the boulder distribution on the Solothurn Lobe and the Southern-Branch is not studied in such detail to assess further the modelled boulder depositional locations.

### 4.4.2 *Importance of representative climate data for modelling Rhone Glacier*

Former ice flow studies modelled the Alpine Ice Field during the LGM based on the present-day (PD) spatial distribution of climate data (Becker et al., 2016; Jouvet et al., 2017; Seguinot et al., 2018). They pointed out the importance of spatial changes in the climate between today and the LGM for ice flow modelling. In this work, we use a regional climate model dataset to force an ice flow model at Rhone Glacier during the LGM and evaluate more deeply the added value of the new data by comparing results to the former approach. We first discuss the effect of the climate data on the ice extent and second on the boulder transport.

*Ice extent*

The PD-based simulation can be tuned fairly close to geomorphologicaly reconstructed ice extent, similar to the reference LGM+PD simulation (Fig. 4.4a,e). However, it is not possible to match the reconstructed extent with the PD climate when using the smooth EPICA signal (blue outline in Fig. 4.4e) but only with the GRIP signal which has stronger and more frequent variations. Apparently, no equilibrium state corresponding to the reconstructed extend can be found with the PD-based climate forcing. This might be caused by the elevation feedback that is stronger in the PD-based climate forcing ($\gamma = -6$ K km$^{-1}$) than in the LGM+PD climate forcing ($\gamma = -4.5$ K km$^{-1}$). Due to the steeper lapse rate in the PD-based climate forcing, the elevation feedback becomes very strong once the Solothurn Lobe and the Southern-Branch are blocked by the Jura. The extent can be matched with the GRIP climate signal, but probably only because of the frequent rapid warmings that stop the elevation feedback.

The modelled extent of the PD-based simulation is significantly larger than with the LGM climate used in the reference simulation (Tab. 4.2, Fig. 4.3). The main reasons are the extensive glaciation north of Aare Glacier and the large Jura Ice Cap. The extensive glaciation north of Aare Glacier is likely caused by the larger precipitation rates in the PD dataset in this region (Fig. B.9e). The large Jura Ice Cap might be related to the stronger temperature lapse rate in the PD dataset increasing the elevation feedback, which is an important mechanism for the build-up and demise of ice caps (Schmidt et al., 2020). The stronger elevation feedback in the PD-based simulation might also contribute to the overestimated size of the Jura Ice Cap compared to the geomorphologically reconstructed ice extent. Due to the larger ice extent in the Jura and north of Aare Glacier, the maximum ice volume of the PD-based simulation is also larger than in the reference simulation. Overall, the LGM+PD simulation and the PD-based simulation perform extent-wise similarly well at Rhone Glacier. However, the PD-based climate data results in an overestimated Jura Ice Cap and relies on a rapidly changing climate signal to match the reconstructed extent, which indicates that the LGM+PD climate forcing is better suited for modelling the glaciation in the western Alps.

*Boulder diversion*

The PD-based simulation and the reference LGM+PD simulation both produce a boulder diversion at Rhone Glacier. In the PD-based simulation, the boulder trajectories and deposition locations do not depend on the origin locations (Fig. 4.4e, 4.9b). This is perhaps related to the low PD precipitation rates within the Valais compared to the surroundings, which might result in boulder trajectories lying close together (Fig. B.12d). While boulders from the Valais only reach the area between Lausanne and Neuchâtel on the Solothurn Lobe in the PD-based simulation, several boulders reach the terminus at Wangen in the reference simulation (Fig. 4.6a,e). However, boulders dated to the LGM were found near the terminus of the Solothurn Lobe (Ivy-Ochs et al., 2006) which indicates that the diversion in the PD-based

setup is too weak. By contrast, the reference LGM+PD simulation reproduces the observed depositional extent on the Solothurn Lobe better. The Solothurn Lobe in the PD-based simulation, in which the GRIP climate signal was used, stays only for a short time near the maximum ice extent. This likely hampers boulders to reach the Solothurn Lobe terminus (Fig. 4.3). Further, most of the boulders that are transported towards the Solothurn Lobe are destroyed by later glacier advances. However, the GRIP simulation, which uses the LGM+PD climate forcing, has no problem transporting boulders to the terminus which also remain there (Fig. 4.6b). Overall, this indicates that using the LGM climate data of the regional climate model in addition to the PD climate dataset is more consistent with the boulder diversion and thus better suited to model Rhone Glacier.

The large Jura Ice Cap in the PD-based simulation and the poor boulder diversion represent a strong contrast to the reference LGM+PD simulation. By contrast, there are only small differences in ice extent and boulder deposition between the reference and the GRIP simulation (little climate variability vs. strong climate variability, see discussion in Section 4.4.1). This suggests that using the climate snapshot with the LGM climate pattern has a larger impact on the model results than the transient climate signal.

In contrast to this study, Jouvet et al. (2017) were not able to produce a boulder diversion using the PD climate pattern. There are two causes that might contribute to this disagreement. First, we use the PD regional climate model datasets of Velasquez et al. (2020) in this study and not the WorldClim PD observational dataset of Hijmans et al. (2005) as Jouvet et al. (2017) did. Using different PD datasets for constructing a PD-based climate forcing for the LGM is known to notably affect the modelled ice extent (Seguinot et al., 2014) and might therefore also affect calculated boulder trajectories. And second, Jouvet et al. (2017) did not include the area west of and south of Chambéry in their model domain meaning they did not model the Lyon Lobe and the glaciers in the very south of the Alps. This might have reduced the ice flux feeding the Southern-Branch and thus affected the boulder diversion in their study. The fact that Jouvet et al. (2017) used a stationary climate likely plays a secondary role as the occurrence of the boulder diversion does not seem to be affected by how the LGM is approached (see discussion in Section 4.4.1).

### 4.4.3 *The impact of ice dynamics on the maximum ice thickness of Rhone Glacier*

So far, there is a discrepancy between modelled and geomorphologically reconstructed ice surface elevations at Rhone Glacier (Becker et al., 2017; Seguinot et al., 2018). We tested the influence of two ice dynamical parametrizations on the ice thickness, namely the SIA flux limiting scheme of Schoof (2003) used by PISM and a poorly constrained sliding parameter. Our experiments show that the SIA flux limiting scheme of PISM plays an important role for the modelled ice thickness near the trimlines of Rhone Glacier in the Alps but not so much for the piedmont lobes outside the Alps (Fig. 4.5b). Further, increasing sliding speeds results in thinner glacier lobes on the lowland which also has an impact on the boulder transport

(Figs. 4.6a,d 4.7a,d, 4.9a). Using a climate signal with stronger and more frequent variations than the EPICA signal hardly affects the modelled ice thickness (Fig. 4.5a). Also the PD-based simulation, which uses only the PD climate dataset, results in virtually the same ice thickness as the reference LGM+PD simulation (Fig. 4.5d). Differences are mostly due to changes in ice extent. We next discuss the modelled ice thickness inside the Alps in the context of the parameter $\lambda$ from the flux limiting scheme of Schoof (2003). In a second step, we focus on the ice thickness at the piedmont lobes of Rhone Glacier and how increased sliding affects them.

*Thickness inside the Alps*

The parameter $\lambda$ determines how strong the ice flux due to horizontal shearing, i.e. the SIA, is suppressed. Low values result in a weak ice flux reduction and large values in a strong flux reduction. The reduction in shear velocities is necessary to prevent massconservation issues. The simulation that uses a strong flux limitation ($\lambda = 5$ km), as it was used in previous PISM-based studies at Rhone Glacier (Seguinot et al., 2018), yields ice thicknesses significantly larger than in the reference simulation which uses $\lambda = 2$ km. Within the Alps, the ice thickness of the $\lambda = 5$ km simulation is between 100 m and 500 m thicker than the reference simulation. Imhof et al. (2019) modelled Rhine Glacier with PISM with a horizontal resolution of 2 km and $\lambda = 5$ and 2 km for the ice flux limiting scheme of Schoof (2003) and compared the PISM results to the ones obtained with a reference Stokes model. They noted a surface elevation overestimation of 300–500 m with the simulation using $\lambda = 5$ km as opposed to results from the Stokes model run that are similar to results with PISM and $\lambda = 2$ km. Therefore, the ice thickness discrepancy of 100–500 m introduced by using $\lambda = 5$ km in our study for Rhone Glacier is in the same range as the discrepancy of ≈300–500 m found by Imhof et al. (2019) (or Chapter 2) for Rhine Glacier. This implies that the higher mountains and the overall greater size of Rhone Glacier do not alter much the ice thickness bias due to the flux limiting scheme of Schoof (2003). Hence, it is likely that the ice flux limiting scheme of Schoof (2003), which PISM relies on, causes thickness overestimations in the range 100–500 m also elsewhere within the Alps if $\lambda = 5$ km is chosen. This further discourages the use of $\lambda = 5$ km in PISM and suggests a $\lambda$ equal to the model resolution.

The $\lambda = 5$ km simulation yields an ice surface elevation lying on average 874 m above the trimlines mapped by Kelly et al. (2004) (Fig. 4.1c, Tab. 4.3). This is comparable to the 861 m discrepancy discovered by Seguinot et al. (2018) who also used $\lambda = 5$ km in their simulation. For our reference simulation, which uses $\lambda = 2$ km, the surface elevation lies on average 607 m above the trimline elevation. This suggests that up to 267 m (or 30%) of the discrepancy between modelled ice surface elevation and trimline elevation at Rhone Glacier identified by Seguinot et al. (2018) is related to their choice for $\lambda$ and therefore a bad numerical setting.

The discrepancy of 607 m between modelled ice surface elevation and trimline elevation obtained with $\lambda = 2$ km remains significant and is not in line with interpreting trimlines as former maximum ice surface elevation at Rhone Glacier.

Interestingly, Cohen et al. (2018) made a similar finding by using a Stokes ice flow model at Rhine Glacier that does not rely on any flux limiting scheme. Their model results suggest an ice surface elevation lying 500 to 700 m above the trimline-based ice surface reconstruction, which is similar to our simulations using $\lambda = 2$ km. This implies that discrepancies between trimline elevation and modelled maximum ice surface elevation are likely not only inherent to PISMs reliance on the ice flux limiting scheme of Schoof (2003) or its simplified ice dynamics and occur also with other more sophisticated ice flow models that do not need any flux limiting scheme.

Former ice flow modelling studies propose to reinterpret the trimlines as transition between cold-based and warm-based ice to explain their overestimated ice thicknesses (Cohen et al., 2018; Seguinot et al., 2018). So far no geological evidence from the Alps has been presented that supports or challenges this reinterpretation. However, such evidence was presented for the Fennoscandinavian Ice Sheet (Fabel et al., 2002), the British-Irish Ice Sheet (Ballantyne and Stone, 2015), and the Laurentide Ice Sheet (Briner et al., 2003).

*Ice thickness in the lowlands*

The overestimated ice thickness in the reference simulation and the fact that basal sliding is poorly understood motivates testing higher sliding speeds. Therefore, we tested reducing the sliding parameter from from $C_1 = 1000$ Pa a m$^{-1}$ to $C_1 = 300$ Pa a m$^{-1}$ to increase sliding speeds. This reduction causes the Solothurn Lobe, Southern-Branch, and Lyon Lobe to thin by 100–300 m (Fig. 4.5c), which is enough to impact the boulder transport. By contrast, the scheme of Schoof (2003) has little to no influence on the ice dynamics over a flat bedrock and therefore hardly affects the ice thickness at the parts of Rhone Glacier situated on flat ground such as the Solothurn Lobe, Southern-Branch, and Lyon Lobe (Fig. 4.5b).

The reduced ice thickness in the $C_1 = 300$ Pa a m$^{-1}$ simulation no longer allows for an invasion of the Jura mountains by alpine ice and boulders from the Valais (Fig. 4.7d). According to Campy (1992) and Buoncristiani and Campy (2011) no alpine boulders and no alpine sediments from the LGM could be attributed to the LGM in the Jura. Thus, the results with $C_1 = 300$ Pa a m$^{-1}$ are better in line with geological evidence than the ones of the reference simulation which employs $C_1 = 1000$ Pa a m$^{-1}$ and shows a significant ice invasion of the Jura (Fig. 4.7a). Still, the $C_1 = 300$ Pa a m$^{-1}$ simulation yields a Solothurn Lobe that is 465-522 m thicker than inferred from two boulder fields at the Jura. This is an improvement relative to the 626-636 m overestimation in the reference simulation. The reason for the discrepancy between modelled ice surface elevation and maximum boulder deposition elevation at the Jura is not known. Likely the overestimated length of the Solothurn Lobe is responsible for parts of the discrepancy. In addition, the thickness overestimation at the lobe could be a result of inappropriate ice dynamics either due to unrealistic sliding speeds or creep flow. Ice from the LGM is known to be less viscous than ice from the present (Gilbert et al., 2016). Further, PISM overestimates the ice thickness of the Rhine Glacier Piedmont Lobe by 100–200 m compared to a

Stokes model (Chapter 2, Fig. 2.7). This might indicate that the hybrid ice dynamics of PISM tend to overestimate the thickness of piedmont lobes, perhaps because of shortcomings of the hybrid ice dynamics .

It is worth noting that the $C_1 = 300$ Pa a $m^{-1}$ simulation becomes susceptible for invading the Jura if the air temperaturs is decreased by another 0.1 °C. An invasion of the Jura took in fact place in an earlier and more extensive glaciation (Buoncristiani and Campy, 2011; Campy, 1992).

The fact that a thinner Rhone Glacier results in a boulder diversion also reaching the orographic right side of the Solothurn Lobe and no invasion of the Jura occurs might suggest that the sliding parameter used in Chapters 2 and 3 and Cohen et al. (2018) is too large for the glaciers of the Alpine Ice Field. The original $C_1 = 1000$ Pa a $m^{-1}$ used by Cohen et al. (2018) was taken from a model setup tuned for the present-day Greenland Ice Sheet (personal communication Denis Cohen). Since sliding is still an incompletely understood process, parameters of any sliding law have to be tuned for each application individually (Hock et al., 2017). It is therefore not clear if a value for the Greenland Ice Sheet is also suitable for alpine glaciers of the LGM.

In general, it seems that the $C_1 = 300$ Pa a $m^{-1}$ simulation produces the best agreement with geomorphological evidence. In particular, the wide distribution of Valais boulders at the Solothurn Lobe terminus and the inhibited invasion of the Jura by alpine boulders set this simulation apart from all others. By contrast, Jouvet et al. (2017) noticed no significant influence of increased sliding rates on the modelled boulder trajectories. The reason for this might be related to the different sliding law they used. Furthermore, they only halved their sliding parameter, which might have resulted in too little changes in the ice dynamics and ice thickness to affect the boulder transport.

### 4.4.4 *Rhone Glacier ice dynamics and boulder transport*

The evolution of the ice flow dynamics and the boulder transport at Rhone Glacier during the last glacial cycle are still poorly understood. Our model results of Rhone Glacier provide new insight regarding changing ice flow direction, transfluences to Toce Glacier, and boulder deposition at the Lyon and Solothurn Lobe.

#### *Change in ice flow direction*

The model results obtained with PISM suggest that significant dynamic changes occurred on the Rhone Glacier Lobe around the LGM and had a great impact on the transport of erratic boulders originating from the Valais. The reference simulation indicates that Rhone Glacier changed its ice flow direction in the area of Lausanne about 1500 years before the maximum extent was reached from mostly flowing towards Genève to flowing entirely towards Wangen (Fig. 4.8). This change in direction towards Wangen correlates in all five simulations with the maximum ice extent (Fig. 4.6). This indicates that the diversion of boulders towards the Solothurn

Lobe is mostly driven by the glacier extent and that the variability in the climate forcing, or variations in the ice dynamics are of secondary importance for the occurrence of the boulder diversion at Rhone Glacier. Thus, the mechanism guiding boulders from the Valais to the Solothurn Lobe is related to the dynamics of the vast piedmont lobe and not so much to the ice dynamics inside the Valais as proposed by Kelly et al. (2004). Similar to our study, Jouvet et al. (2017) concluded that the diversion is mainly driven by the precipitation gradient between the Arve Glacier catchment (Mont Blanc area) and the Valais Glacier catchment which would mostly affect the dynamics of the Southern-Branch which lies in between these two glacier catchments.

*Transfluences from the Valais to Toce Glacier*

Similar to Becker et al. (2017), our modelling suggests that ice from the uppermost region of Valais Glacier flowed out of the Rhone Glacier catchment and into the Toce Glacier catchment. Erosion marks at the Simplon pass indeed support such transfluences from Rhone Glacier to Toce Glacier (Kelly et al., 2004). However, none of the boulders deposited in the Toce Glacier catchment could so far be identified to stem from Valais (Braakhekke et al., 2020). In this light, boulders in our simulations that are transported from the Aletsch area and Saastal to Toce Glacier should be interpreted with care. In particular, boulders from Saastal are today common on the Solothurn Lobe, thus it would be surprising if the tributary coming from Saastal was diverted towards Toce Glacier during the LGM. This calls into question the model results obtained in the reference, GRIP, and $\lambda = 5$ km simulations. Most likely the transfluence was not as strong as suggested by any of our simulations and did not drain a large part of the ice in the Rhone Valley. Perhaps the modelled ice surface elevation is still too high within the Alps.

*Ice from Valais never reached Lyon Lobe*

Ice and boulders from the Valais never reached the Lyon Lobe in any of the five simulations presented in this study. This does not line up with old geological maps of Rhone Glacier that suggest that the ice from the Valais flowed both to the Solothurn and the Lyon Lobe at the same time during the LGM (e.g. Buoncristiani and Campy, 2002). However, all our model results agree rather well with Coutterand et al. (2009) who did not find boulder lithologies from the Valais within the Lyon Lobe. Coutterand et al. (2009) describes the Lyon Lobe being fed only by glacier ice from the French Alps, which agrees with all five simulation (Fig. 4.8d and Fig. 4.9a,b).

*Boulders at the Solothurn Lobe*

In all five simulations, boulders are predominantly deposited at the orographic left side of the Solothurn Lobe at the foot of the Jura mountains (Fig. 4.4). The clustering of boulders at the orographic left side of the Solothurn Lobe arises from the fact that

the ice from the southern valleys of the Valais travels mostly along the Jura (Fig. 4.8). Burkhard and Spring (2004) found that the boulder block fields along the foot of the Jura are composed of Valais boulders from various different valleys. Indeed, our ice flow simulations show various lithologies from the Valais being deposited close to each other along the Jura.

All simulations except for the $C_1 = 300$ Pa a $m^{-1}$ simulation fail to transport boulders to the orographic right side of the Solothurn Lobe (Fig. 4.4d). The $C_1 = 300$ Pa a $m^{-1}$ simulation transports boulders from Saastal and Val d'Hérens to the orographic right side of the Solothurn Lobe terminus between Bern and Wangen. This is a result of the reduced ice thickness at the Solothurn Lobe, which inhibited the invasion of the Jura by alpine ice. The orographic right side of the Solothurn Lobe terminus is today indeed fairly rich in boulders from Val de Bagnes (Ivy-Ochs et al., 2004) but also from Val d'Hérens (Jouvet et al., 2017) and Vallorcine (Itten, 1953). Thus the $C_1 = 300$ Pa a $m^{-1}$ simulation is the only simulation that reproduces these boulder fields on the orographic right side, albeit without boulders from Val de Bagnes or Vallorcine. In general, the boulders from Vallorcine are the ones that have the least chance of being diverted towards the Solothurn Lobe. During the flow direction change, they are the last ones to change direction from Southern-Branch bound to Solothurn Lobe bound (Fig. 4.8b). This is related to their eastern source within the Valais.

*Boulder gap between Bern and Lausanne*

In no simulation erratic boulders from the Valais reach the area between Bern and Lausanne at the orographic right side of the Solothurn Lobe. In general, erratic boulders exist in this area today, however, information about their lithological origin or deposition age is hardly available. Few communities provide some details on the erratic boulders existing on their ground, but they do not provide scientific references. In the community of Ried bei Kerzers, west of Bern, there are boulders from near Saastal (Amphibolit) and Vallorcine (Vallorcine Conglomerate and Mont Blanc Granite) (Ried bei Kerzers, 2020). Also further south, near Fribourg at Pierrafortscha, an erratic boulder made of Mont Blanc Granite exists (Region Fribourg, 2020) and thus likely originates from close to Vallorcine. A deposition date is not available for any of these boulder, but since both these sites lie well within the reconstructed extent of the Solothurn Lobe, it is likely that they were deposited some time after the LGM.

There is no obvious explanation for the fact that all of our simulations fail to transport boulders to the area between Bern and Lausanne at the orographic right side of the Solothurn Lobe. However, it seems unlikely that the reason for this mismatch is related to the ice dynamics of Valais Glacier because all boulders leaving the Valais travel rather closely together along the southern Jura (Fig. 4.8, 4.9), indicating that disturbances in the Valais have a limited effect on the boulder trajectories on the Solothurn Lobe or the Southern-Branch. Similarly, Jouvet et al. (2017) suggest that surging of southern tributaries probably had a limited effect

on the boulder diversion. The main reason for the boulder gap between Bern and Lausanne is likely related to a misrepresentation of the lobe dynamics in all our simulations. Perhaps, periodic surging of the Southern-Branch and the Solothurn Lobe might have allowed boulders from the Valais to reach the area between Bern and Lausanne. The Malaspina piedmont glacier (Alaska) of today surges alternately to the south-south-west and the south-east (Muskett et al., 2008) resulting in distorted middle moraines forming a zigzag pattern that reaches a large proportion of the piedmont lobe terminus (Fig. 1.2). Nonetheless, the idea that such a surge behaviour also occurred at Rhone Glacier is highly speculative and has already been hypothesized by Burkhard and Spring (2004). No evidence for a periodic surging behaviour has been identified for any glacier of the Alpine Ice Field so far.

*Boulders as indicator for ice flow lines*

Our modelling results show that the Southern-Branch separates from Valais Glacier within less than 1000 years and is absorbed by Arve Glacier and other glaciers originating in the French Alps. This also concerns the Valais boulders situated on the Southern-Branch at this moment. Therefore, these Valais boulders are not deposited in the context of a continuous flow line that originated in the Valais and ended near the LGM extent of the Southern-Branch. Erratic boulders are used to reconstruct former ice flow directions by assuming that origin and deposition location are connected by a permanent flow line (e.g. Braakhekke et al., 2020; Coutterand, 2010). This might need to be done with care with Valais boulders in the area between Mont Tendre and Rumilly.

## 4.5 CONCLUSIONS

In this chapter, the Rhone Glacier was modelled transiently using the Parallel Ice Sheet Model over the last 50,000 years. The climate data was taken from a regional climate model that was specifically adapted for Last Glacial Maximum conditions in the European Alps (Velasquez and Raible, in prep; Velasquez et al., 2020). The transient climate was constructed by modulating a climate signal deduced from an Antarctic ice core to the climate dataset. Besides one reference simulation, three simulations were performed for testing three different model parameters for their influence on the ice thickness, the ice dynamics, and the boulder transport from the Valais. First, a climate signal from Greenland was used which had more frequent and stronger climate variations than the reference climate signal from Antarctica. Second, the Parallel Ice Sheet Model relies on an ice flux limiting scheme for which we used more rigorous flux limitation identical to older studies. And third, a lower value for an uncertain parameter in the sliding law was used which leads to increased sliding speeds. A fifth simulation was performed using only modified present-day climate data from the regional climate model dataset, analogous to earlier studies. We draw

the following conclusions based on the results obtained from the five performed ice flow simulations:

1. **Climate data**

   The LGM climate data taken from a regional climate model is more favourable for modelling Rhone Glacier than modified present-day climate data as used formerly. The reconstructed maximum ice extent of Rhone Glacier could be matched by both approaches with regional discrepancies, except for the Jura Ice Cap which was too large using only the present-day climate pattern. The simulations using the LGM climate enabled a boulder transport that reliably reached the Solothurn Lobe terminus, which was not the case for the simulation employing a modified present-day climate. Therefore, using LGM climate data of a regional climate model represents a promising perspective to overcome the lack of data for paleo ice flow modelling. In our study, boulder trajectories were a useful information to validate and judge model results.

   The variability of the climate signal had little impact on the boulder diversion and deposition at Rhone Glacier. The occurrence of the boulder diversion towards the Solothurn Lobe appeared to depend on the glacier extent rather than on the climate signal. The transient forcing was, however, decisive for the duration the boulder diversion prevails and thus the number of boulders being diverted.

2. **Rhone Glacier ice thickness**

   The ice flux limiting scheme of the Parallel Ice Sheet Model was responsible for about 267 m of excess ice in the trimline area and up to 500 m in alpine valleys in previous studies. A discrepancy of 607 m still prevailed between modelled ice surface elevation and reconstructed trimline elevation at Rhone Glacier. Thus ice flow modelling still contradicts the interpretation of trimlines as former maximum ice surface elevation, even if the effects of the ice flux limiting scheme are minimized. A possible reinterpretation of trimlines in the Alps as cold-warm based ice boundary remains open.

   Higher sliding speeds lead to a thinning of the Solothurn Lobe, Southern-Branch, and Lyon Lobe by 100 to 300 m. However, the modelled Solothurn Lobe was still about 500 m thicker than suggested by boulders deposited on the Jura southern flank. The reason for this discrepancy is likely related to the overestimated length of the Solothurn Lobe in this simulation. Other factors might also contribute to this overestimation such as lack of tuning of sliding and ice rheological parameters in the ice flow model or shortcomings of the shallow ice dynamics employed by the Parallel Ice Sheet Model.

3. **Ice dynamics**

   In all our simulations, the Rhone Glacier ice dynamics experienced substantial changes depending on the size of the glacier. At smaller sizes of Rhone Glacier, the boulders from the Valais were transported towards Genève. Our model

results showed that the ice divide that separates the Southern-Branch from the Solothurn Lobe undergoes a westward shift once the ice extent is close to the reconstructed LGM ice extent. This resulted in a redirection of ice and boulders transported by Valais Glacier towards the Solothurn Lobe and thus establishes the boulder diversion. As a result of the direction change, boulder deposition locations do not necessarily correspond to an ice flow line that persisted for a continuous period, in particular at the Southern-Branch.

4. **Boulder deposition**

   Our simulations using the LGM climate data were all able to reproduce the Valais boulder deposition locations extending from the Southern-Branch to the terminus of the Solothurn Lobe. The absence of Valais boulders from the Lyon Lobe was reproduced as well. Thus, these simulations captured the large scale field observations. The simulation that used a parametrization that allows for higher sliding speeds stood out from all simulations. Its reduced ice thickness resolved the strong tendency of alpine boulders invading the Jura mountains instead of being transported to the Solothurn Lobe. This also resulted in a more efficient transport of Valais boulders to the orographic right hand side of the Solothurn Lobe terminus. In general the simulation with increased sliding resulted in the best overall agreement with geomorphological evidence.

   No simulation transported a single boulder to the area between Lausanne and Bern at the orographic right had side of the Solothurn Lobe. Yet, boulders from the Valais exist today in this area. The cause for this disagreement between field observation and model results could not be resolved. A speculative explanation involves unstable ice dynamics (periodic surging) of the Solothurn Lobe and the Southern-Branch.

## DATA AVAILABILITY

Ice thickness, bedrock elevation, pressure adjusted basal temperature, and surface and basal ice velocity data of the reference simulation and the simulation using increased sliding speeds ($C_1 = 300$ Pa a m$^{-1}$) is published as Imhof (2021a).

## SUPPLEMENTARY MATERIAL

An animation of the simulation using $C_1 = 300$ Pa a m$^{-1}$ is available at:
`https://youtu.be/4va0ZuLNqjI` (English)
`https://youtu.be/r296jFYYOMY` (German)
`https://youtu.be/5HowvtqcuRM` (French)

# 5

# CONCLUSION

*"Aber so ist das nun mal im Leben, die reichsten sind immer die ärmsten Schweine." - "Reichtum muss ja auch was Negatives haben."*

— Vier Fäuste gegen Rio (1984)

## 5.1 SUMMARY

In this thesis, I studied the glaciation in the European Alps during the Last Glacial Maximum (LGM) using ice flow models and climate model data. The focus lay on a model comparison of ice flow models of different complexities, utilizing modelled LGM climate data to force the ice flow model, and reconstructing thickness and ice dynamics of Rhone Glacier during the LGM. Here, I summarize the contributions of this work by going back to the initial research questions posed in Section 1.6:

1. **RQ1: Is a hybrid ice flow model like PISM an adequate model choice to simulate ice fields such as the Alpine Ice Field?**

   To answer this question, I assessed model results of the simplified ice flow model PISM against the Stokes ice flow model Elmer/Ice for Rhine Glacier during the LGM (Chapter 2). The comparison of the two ice flow model results shows that the default parametrization of a flux limiting scheme used by PISM for the SIA causes a strong underestimation of shearing speeds compared to Elmer/Ice. In turn, this causes a 300–500 m overestimation in modelled ice thickness in PISM. Reducing the influence of the flux limiting scheme in PISM to its minimum permits to obtain shearing velocities and ice thicknesses in better agreement with Elmer/Ice. In general, the hybrid ice flow mechanics of PISM produce sliding speeds, ice extent and basal temperatures in good agreement with the Stokes model results. Thus, employing a hybrid ice flow model at ice fields is advisable provided a suitable parametrization of the flux limiting scheme is used for the SIA, especially in view of interpreting the ice thickness.

2. **RQ2: What is the added value of using regional climate model data instead of cooled present-day climate data for modelling the Alpine Ice Field during the LGM?**

   I approached this question by modelling the entire Alpine Ice Field transiently over the last 50'000 years using regional climate model data for present-day and LGM conditions as well as reconstructed temperature time series (Chapter 3). The ice extent modelled with the climate data for the LGM is roughly consistent with the geomorphologically reconstructed extent. Albeit, the modelled ice

extent in the east is too small while the extent in the west could be matched well. Using only the present-day climate results in the opposite situation and a qualitatively similar match with the reconstructed extent. However, the maximum ice extent obtained with the LGM climate dataset is better in agreement with geological evidence if modelled boulder deposition locations are also taken into account. Modelling solely Rhone Glacier in Chapter 4, I showed that modelled deposition locations of boulders from the Valais agree better with field evidence when using the LGM climate dataset instead of cooled present-day climate data. Thus, using regional climate model data instead of cooled present-day data as climate forcing allows to model the Alpine Ice Field with greater confidence than in previous studies.

Using regional climate model data also allows identifying a potential connection between the thickness of the northern hemisphere ice sheets and the distribution of ice between the eastern and western Alps. Climate data based on thinned ice sheets in North America and northern Europe improves the match with the reconstructed maximum ice extent in the east of the Alpine Ice Field. This connection might be related to changes in the moisture transport towards the Alps initiated by the lower ice sheets.

3. **RQ3: How thick was Rhone Glacier during the LGM? And how did the ice flow of Rhone Glacier evolve over the LGM?**

   These research questions were tackled with detailed simulations of Rhone Glacier (Chapter 4). I tested how the amplitude of climatic variations, sliding speeds, and strength of the ice flux limiting scheme affect the Rhone Glacier ice thickness and ice dynamics.

   The simulations of Rhone Glacier provide new insight into the discrepancy between reconstructed and modelled ice thicknesses. I could attribute 267 m ice thickness overestimation found in earlier studies to an unsuitable parameter choice in a flux limiting scheme used by PISM. Yet, a 607 m discrepancy remains between modelled ice surface elevation and mapped trimline elevation. Similarly, the modelled ice thickness at the Rhone Glacier Lobe exceeds the maximum ice thickness inferred from deposited boulders at the Jura by 465–636 m in all setups. The thickness discrepancy at the lobe might be related to the overestimated length of the Solothurn Lobe in the simulations or the lack of tuning of sliding and ice rheological parameters in the ice flow model. Further, these simulations suggest that the ice thickness of the Rhone Glacier Lobe is decisive for the boulder distribution between the Jura Mountains and the Solothurn Lobe. If Rhone Glacier is thick enough to invade the Jura mountains, boulders from the Valais tend to be deposited in the Jura instead of the lowlands in contradiction to present-day observations of deposited LGM erratic boulders.

   The results emphasize the transient character of the ice flow direction of Rhone Glacier during the LGM. All results suggest that the ice from Valais Glacier

first flowed southwards to Genève, and then changed its direction towards the Solothurn Lobe shortly before the maximum ice extent was reached (see Fig. 4.1 for location names). This change in flow direction seems to be dependent on the size of Rhone Glacier and results in a deposition of erratic boulders coming from the Valais spanning from Rumilly to Wangen, similar to field evidence.

## 5.2 OUTLOOK

Several issues and limitations of current knowledge or data availability were highlighted in the course of this thesis. Based on the outcome of my work, I recommend to devote further research to the following topics:

1. **How did the evolution of the Laurentide and Eurasian Ice Sheets affect the precipitation distribution and ice extent in the Alps around the LGM?**

   Modelling the LGM Alpine Ice Field with an LGM forcing based on regional climate model data of Velasquez et al. (2020), Velasquez and Raible (in prep), and Velasquez (in prep) results in a strong east-west imbalance between modelled and reconstructed maximum ice extents. We know from the climate data of Velasquez and Raible (in prep) that the size of the Laurentide and Eurasian Ice Sheets affects the east-west distribution of precipitation in the Alps. Therefore, I suggest to investigate how the Alpine Ice Field evolved in dependence of the precipitation changes induced by the size evolution of the Laurentide and Eurasian Ice Sheets around the LGM. This could be done by creating several climate snapshots with a global climate model from the build up phase before the global LGM to the deglaciation of the Laurentide and Eurasian Ice Sheets and then downscale these datasets over the Alps to a higher resolution. Such experiments could hint whether the maximum ice extent of the Alpine Ice Field during the LGM was caused by more than one climatic pattern or shed light into the timing difference between the global LGM and the LGM in the Alps.

2. **Compiled datasets of geological evidence**

   Geomorphological data that is digitally available as homogeneous dataset is highly useful for validating data generated with ice flow models. This is for example the case for the trimline elevation in the Rhone Valley which were made available by Kelly et al. (2004). Information concerning boulder depositional location, place of origin, and depositional time is available only for few boulders and scattered across the literature, which is not easy to use in the context of ice flow modelling. In Chapter 4, this lack of data restricted the interpretation of our results. Thus, assembling a homogeneous boulder dataset listing their deposition and origin location would be a great benefit for future studies. This is true not only for Rhone Glacier but also any glacier of the Alpine Ice Field. Information about where which boulder lithologies were deposited by Rhone Glacier would be valuable for further assessing

the modelled boulder deposition and understanding the dynamics of Rhone Glacier. Drumlin orientations, which indicate the last ice flow direction, are another piece of geological information that has not been exploited to date, but could be beneficial for assessing ice flow modelling in future research.

3. **Trimlines in the Alps: what do they correspond to?**

   Ice flow models have repeatedly yielded results contradicting the common idea of interpreting trimlines in the Alps as a former maximum ice surface elevation, including the work presented in this thesis. This gap between geomorphological interpretation and model results calls for a detailed investigation. Since it could be proven that the trimlines in other mountain ranges correspond to the former boundary between cold and warm-based ice, I suggest to prioritize testing this hypothesis using an ice flow modelling approach. For this purpose, one needs to model the basal temperatures at sub-kilometre model resolution in order to resolve the trimline. Further, high confidence in the representation of ice dynamics is required because the trimlines in the Alps are situated in steep and rigid terrain. This requirement is best fulfilled by a three-dimensional Stokes ice flow model.

4. **A mass conserving scheme for shallow ice approximation models**

   PISM relies on the SIA ice flux limiting scheme of Schoof (2003) to enhance computational speed and avoid mass conservation violations on rugged terrain. This scheme was designed for neither of these purposes and I could show that it causes a strong reduction of shear velocities, which results in an artificial overestimation of modelled ice thicknesses near mountains. This can be problematic for modelling the ice thickness realistically, in particular on rough terrains like the Alps. Simply turning off the scheme of Schoof (2003) in PISM results in non-practically high computational costs and mass conservation issues on the topography used in this thesis. There is currently no proper solution for mass conservation issues in PISM, which should be remedied. In Appendix C, I describe the nature of the mass conservation issue most SIA models have in common and propose a computationally fast scheme to recover the problem without causing artificially overestimated ice thicknesses. The scheme caps surface gradients in dependence of the ice thickness and is easy to implement in existing models. My new scheme could be a promising alternative to the scheme of Schoof (2003) currently used by PISM. Yet, further assessment of the new method is needed.

5. **Modelling a present-day analogue of the vast glaciers of the Alpine Ice Field**

   A common issue in paleo glacier modelling is the lack of observations to tune the model, generating large uncertainties. This is typically the case for sliding, which can only be estimated very roughly from indirect evidence. Identifying a present-day analogue glacier, which is as comparable as possible

in terms of size, basal conditions, and catchment could be a way to bypass this restriction. Modelling such a present-day analogue could help finding suitable parametrizations for sliding which could be transferred to the Alpine Ice Field. The Malaspina-Seward Glacier system in Alaska, USA and Yukon, Canada represents a promising candidate for such a present-day analogue (Fig. 1.2). Malaspina Glacier is the largest piedmont glacier in the world and resembles the piedmont lobes of the Alpine Ice Field. It has a comparable size to Reuss Glacier. The topographic setting resembles many of the former alpine glaciers in terms of a large Alpine valley that evacuates ice through a comparably narrow gorge and then fans out as piedmont lobe in a plain. Further, glaciers of the Alpine Ice Field were mostly warm-based, which is also the case for the Malaspina-Seward Glacier system.

# A

## APPENDIX: SLIDING LAW

To calculate sliding velocities, we employ a linear sliding law for the SSA:

$$\vec{\tau}_b \;=\; \min\left(C_0, C_1 - (T - T_{melt}) \cdot \frac{(C_0 - C_1)}{0.5\ ^\circ C}\right) \cdot \vec{v}_s, \tag{A.1}$$

where $\vec{\tau}_b$ is the basal shear stress, $C_0 = 1,000,000$ Pa a m$^{-1}$ is the sliding parameter for cold-based ice, $C_1 = 1000$ Pa a m$^{-1}$ is the sliding paramete for warm-based ice, $T_{melt} = 273.15$ K is the melting temperature of ice, $T$ is the basal temperature, and $\vec{v}_s$ is the sliding velocity. This sliding law is very similar to the one used in Chapter 2 or Cohen et al. (2018). The sliding parameter for cold-based ice ($C_0$) is, however, increased by a factor of 10 to suppress sliding in cold based areas more rigurously. To keep things simple, the transition between warm and cold-based ice is taken linear instead of exponential. This type of sliding law is not included in PISM 1.1 and therefore we implemented it ourselves.

# B

# APPENDIX: WEATHER RESEARCH AND FORECAST MODEL CLIMATE DATA

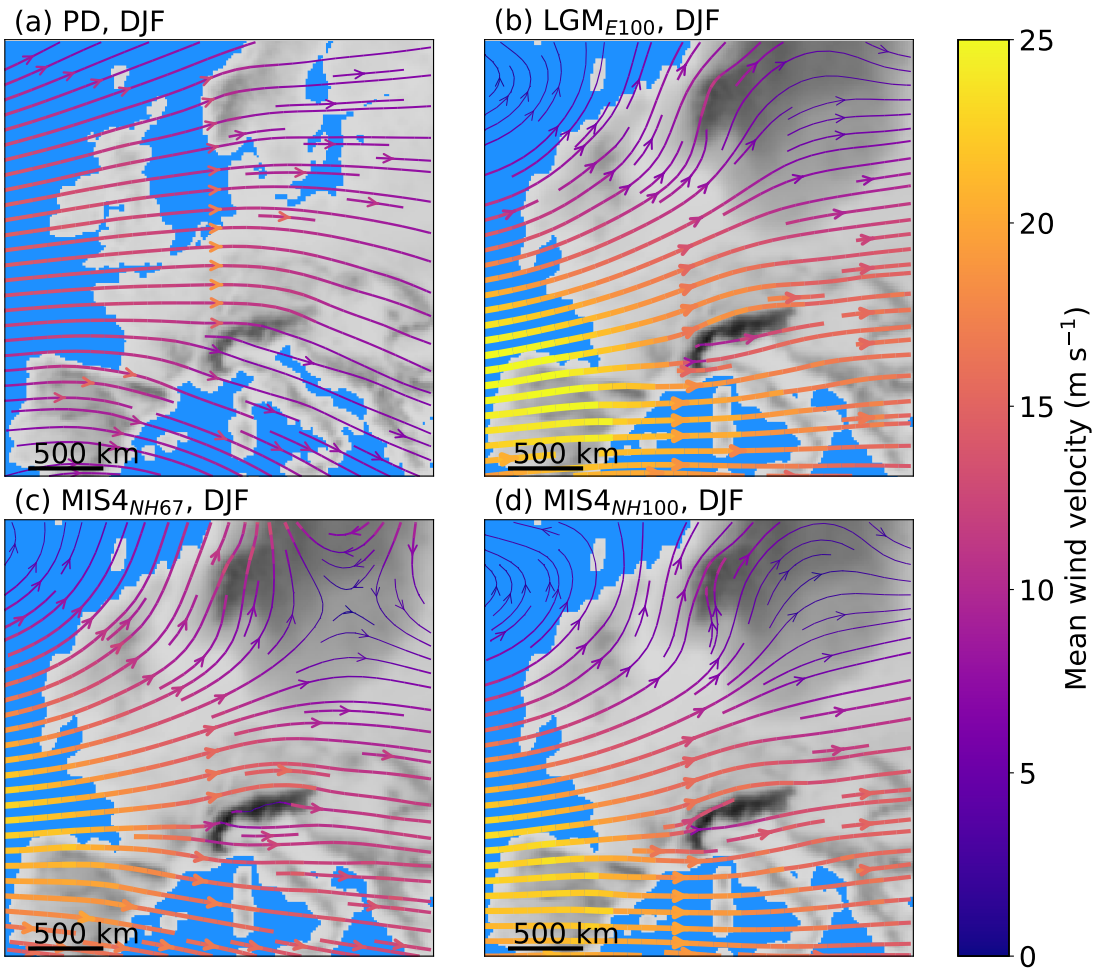


**Figure B.1:** Winter (December, January, February) mean wind velocity of Velasquez et al. (2020) and Velasquez and Raible (in prep) at the pressure level of 700 hPa (≈3000 m above sea level) over Europe for the PD (a), LGM$_{E100}$ (b), MIS4$_{NH67}$ (c) and MIS4$_{NH100}$ (d) climates on the D02 WRF subdomain (Fig. 3.3).

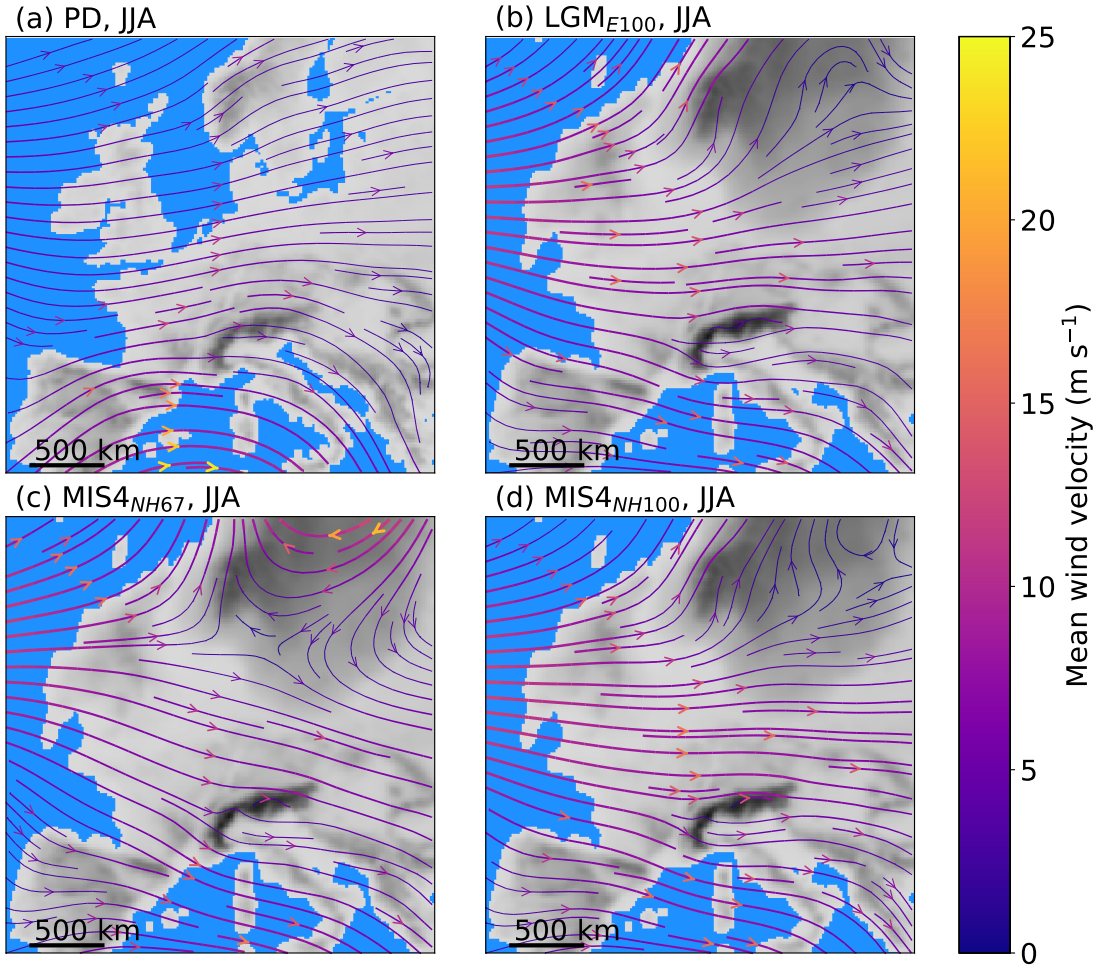


**Figure B.2:** Summer (June, July, August) mean wind velocity of Velasquez et al. (2020) and Velasquez and Raible (in prep) at the pressure level of 700 hPa (≈3000 m above sea level) over Europe for the PD (a), LGM$_{E100}$ (b), MIS4$_{NH67}$ (c) and MIS4$_{NH100}$ (d) climates on the D02 WRF subdomain.

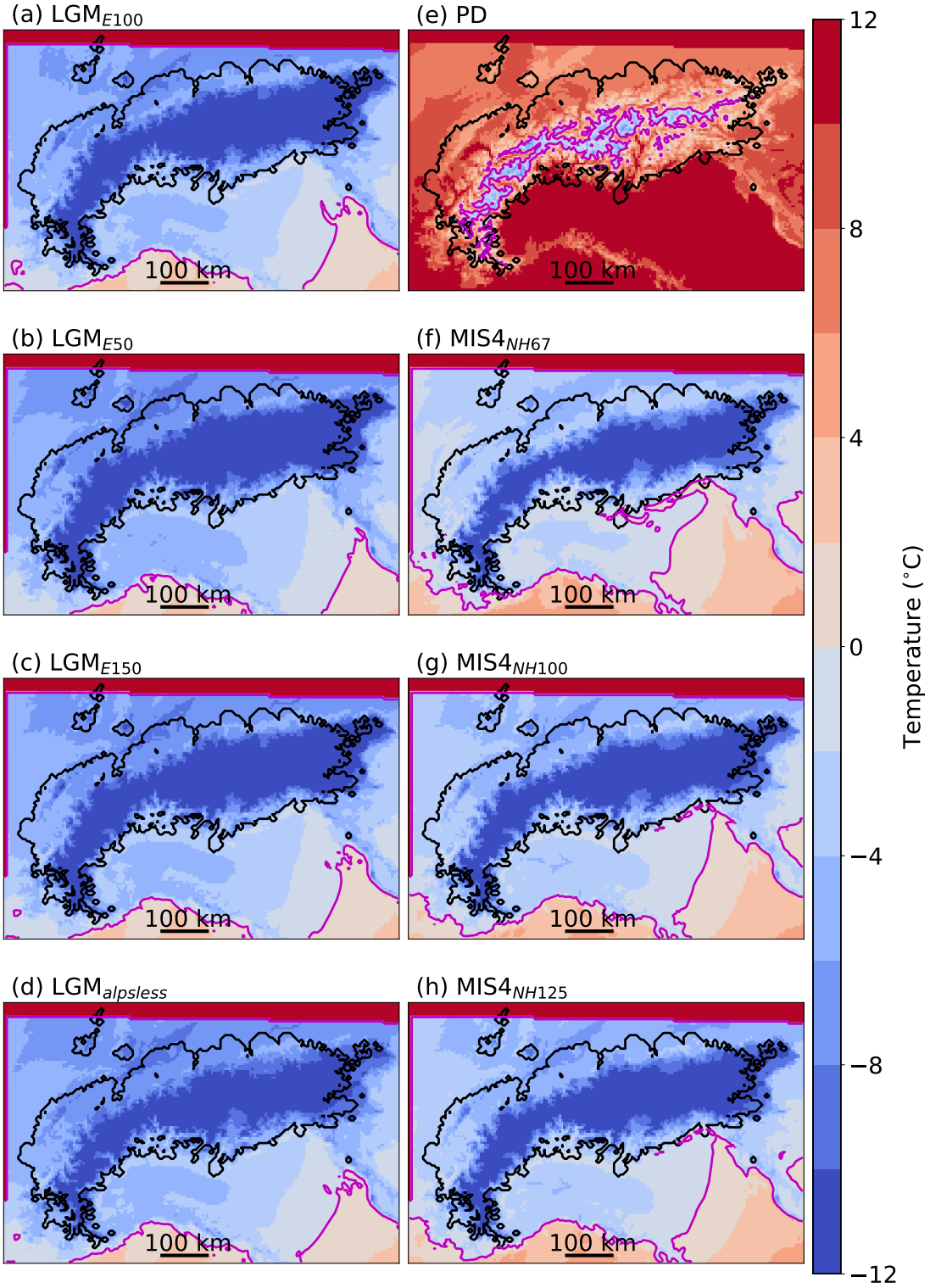


**Figure B.3:** Annual mean temperatures of all eight WRF simulations of Velasquez et al. (2020) and Velasquez and Raible (in prep): LGM$_{E100}$ (a), LGM$_{E50}$ (b), LGM$_{E150}$ (c), LGM$_{alpsless}$ (d), MIS4$_{NH67}$ (e), MIS4$_{NH100}$ (f), MIS4$_{NH125}$ (g), PD (h). The black outline indicates the geomorphologically reconstructed maximum ice extent of the LGM of Ehlers et al. (2011). The magenta line indicates the 0 °C line.

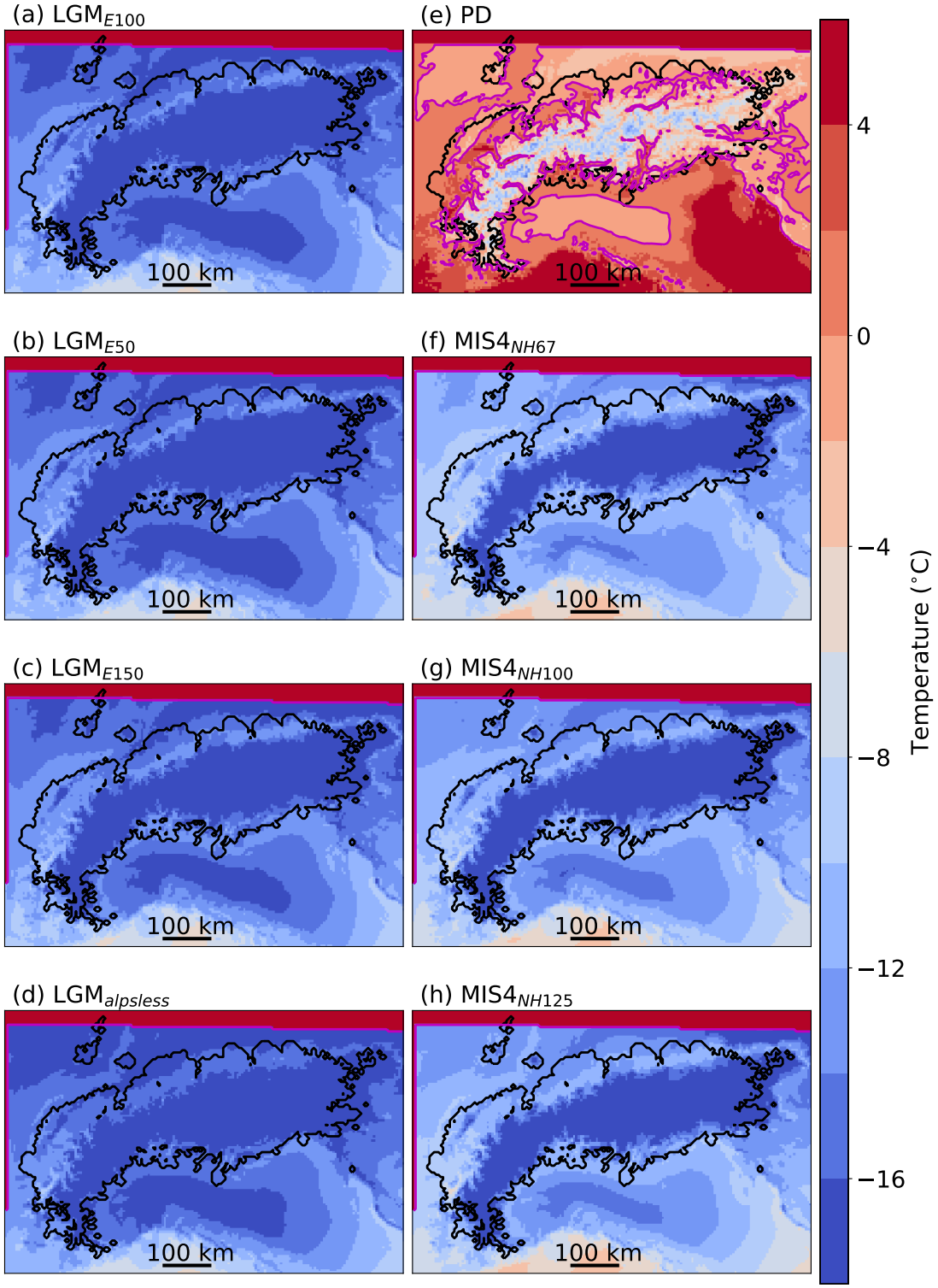


**Figure B.4:** Analogous to Fig. B.3, but for winter (December, January, February) mean temperature.

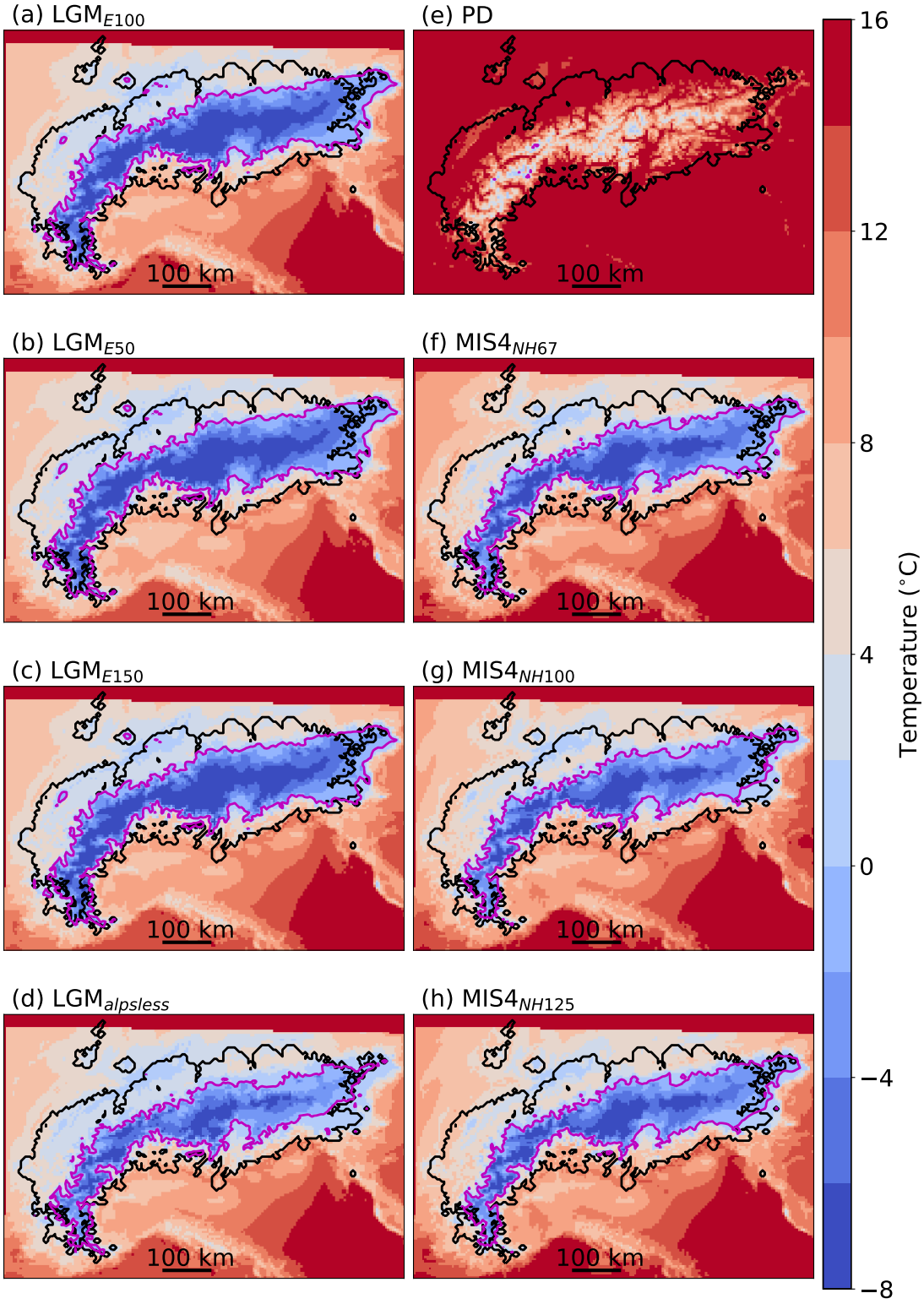


**Figure B.5:** Analogous to Fig. B.3, but for summer (June, July, August) mean temperature.

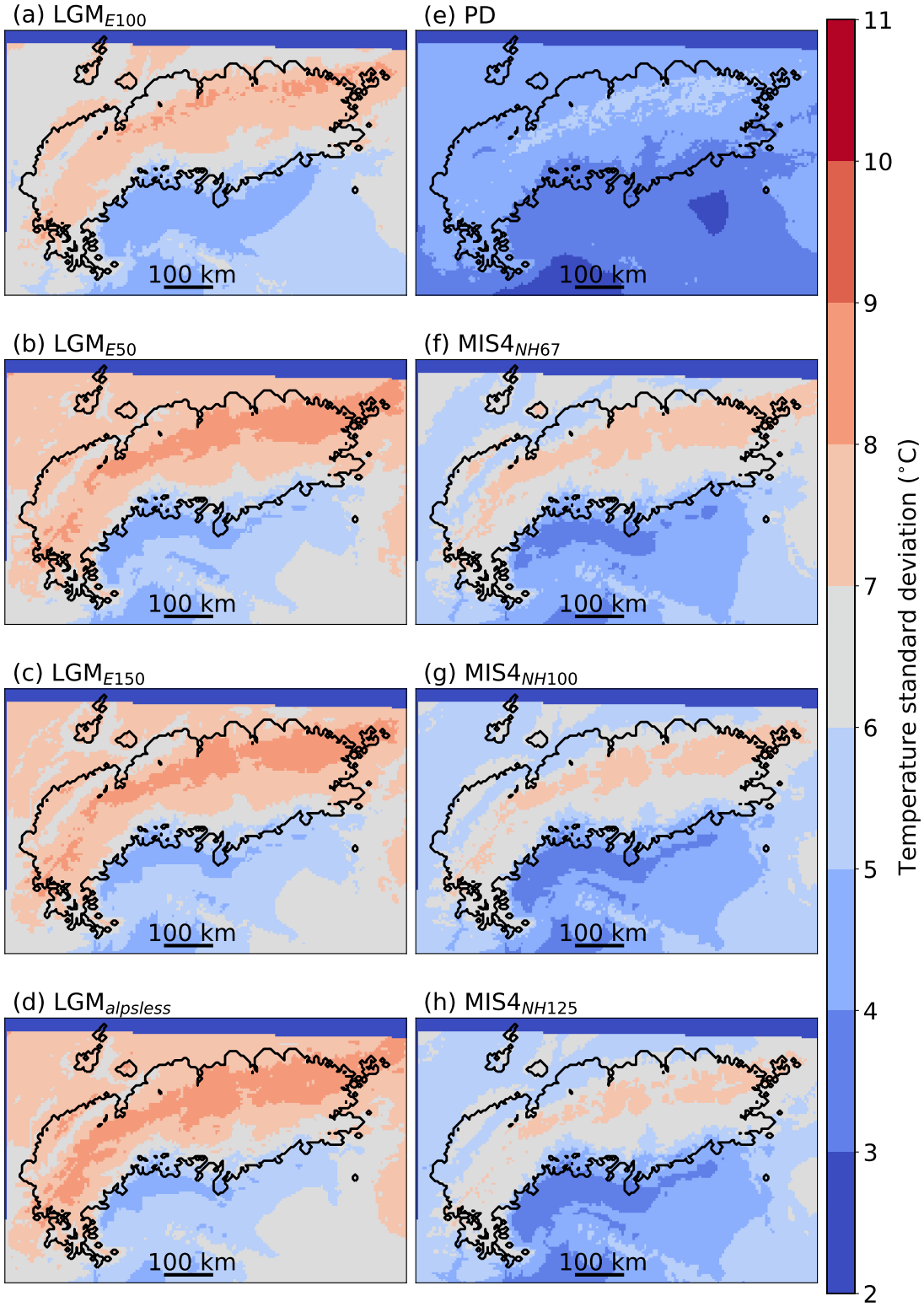


**Figure B.6:** Annual mean temperature standard deviations of all eight WRF simulations of Velasquez et al. (2020) and Velasquez and Raible (in prep): LGM$_{E100}$ (a), LGM$_{E50}$ (b), LGM$_{E150}$ (c), LGM$_{alpsless}$ (d), MIS4$_{NH67}$ (e), MIS4$_{NH100}$ (f), MIS4$_{NH125}$ (g), PD (h). The black outline indicates the geomorphologically reconstructed maximum ice extent of the LGM of Ehlers et al. (2011).

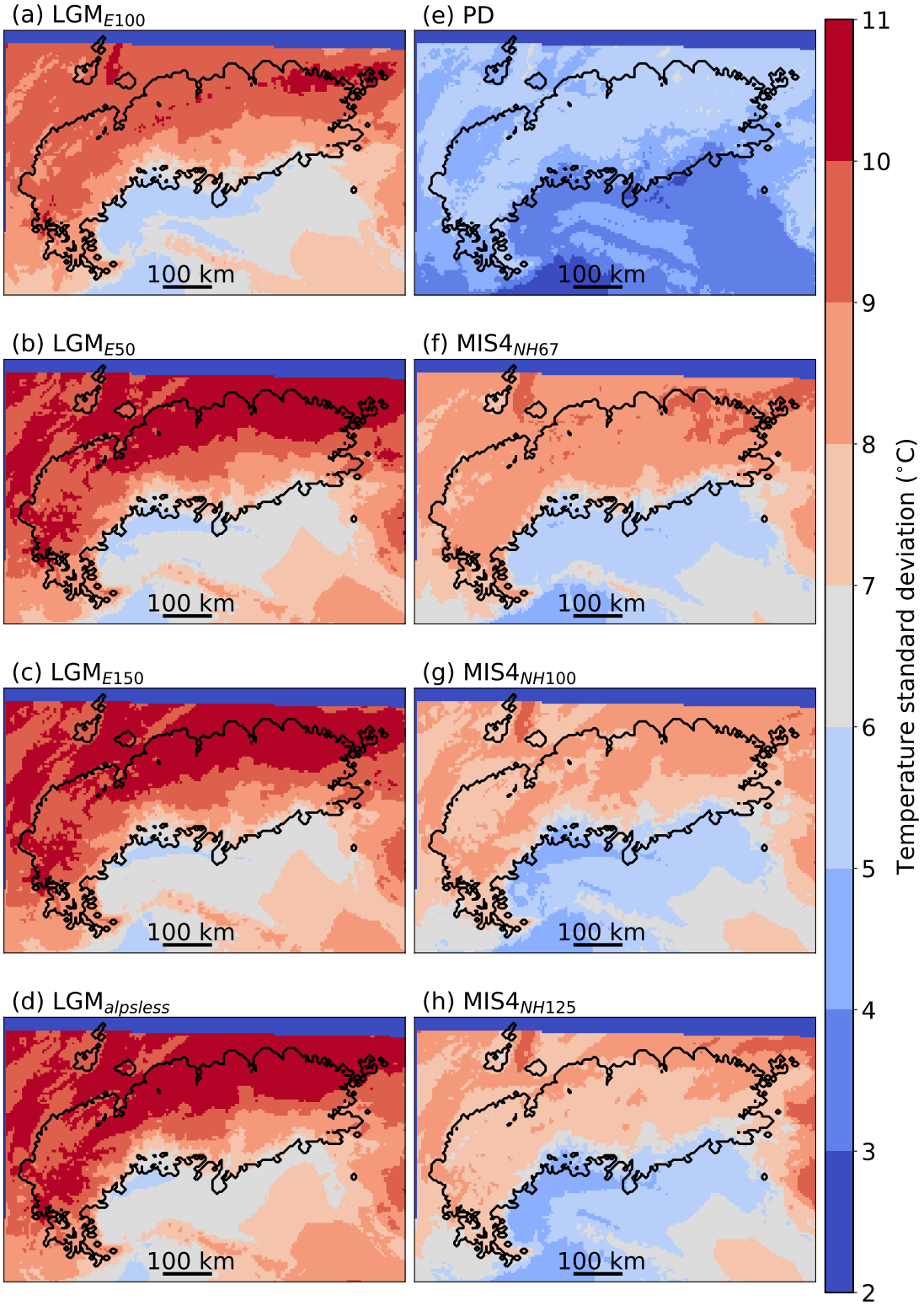


**Figure B.7:** Analogous to Fig. B.6, but for winter (December, January, February) mean temperature standard deviations.

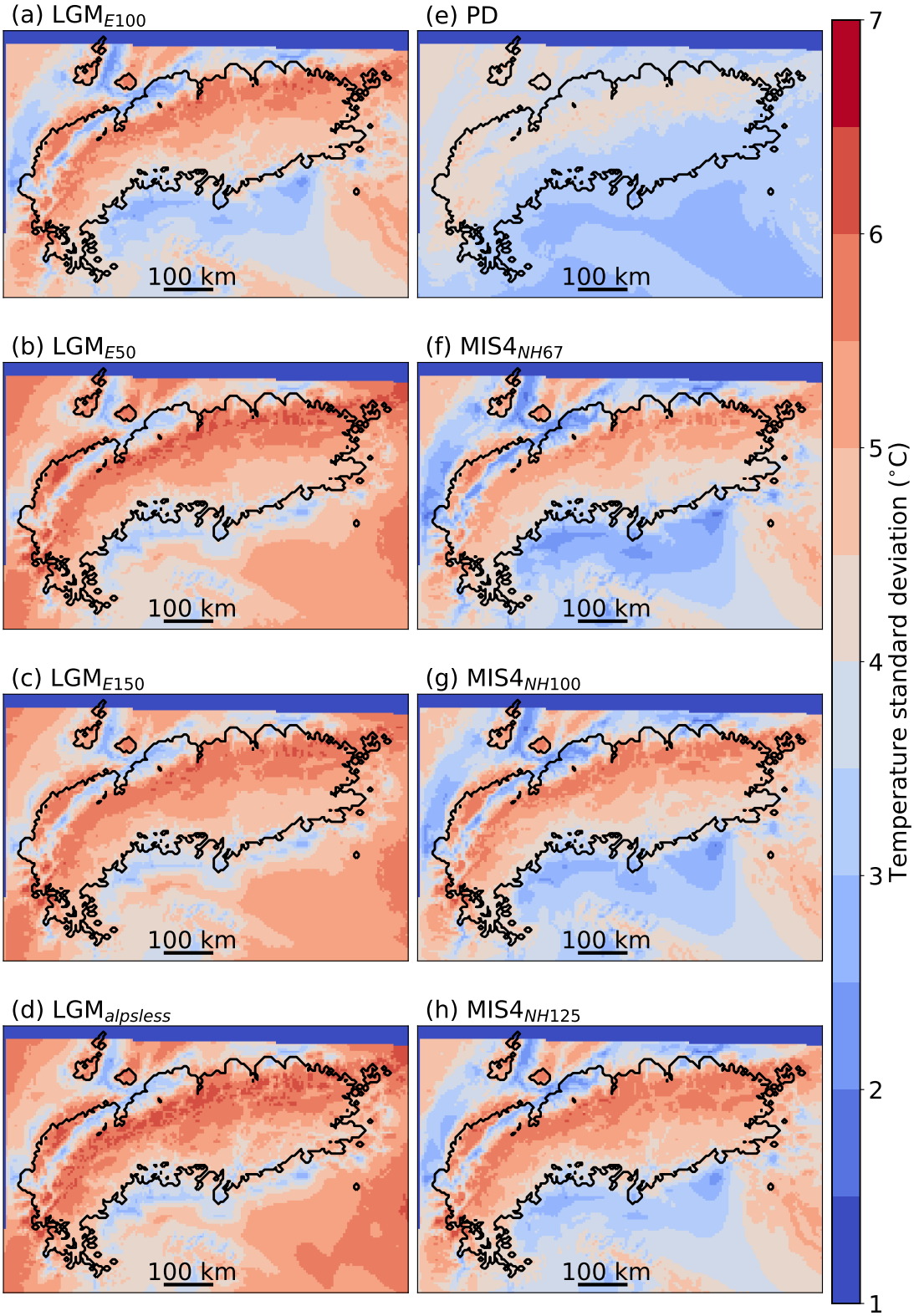


**Figure B.8:** Analogous to Fig. B.6, but for summer (June, July, August) mean temperature standard deviations.

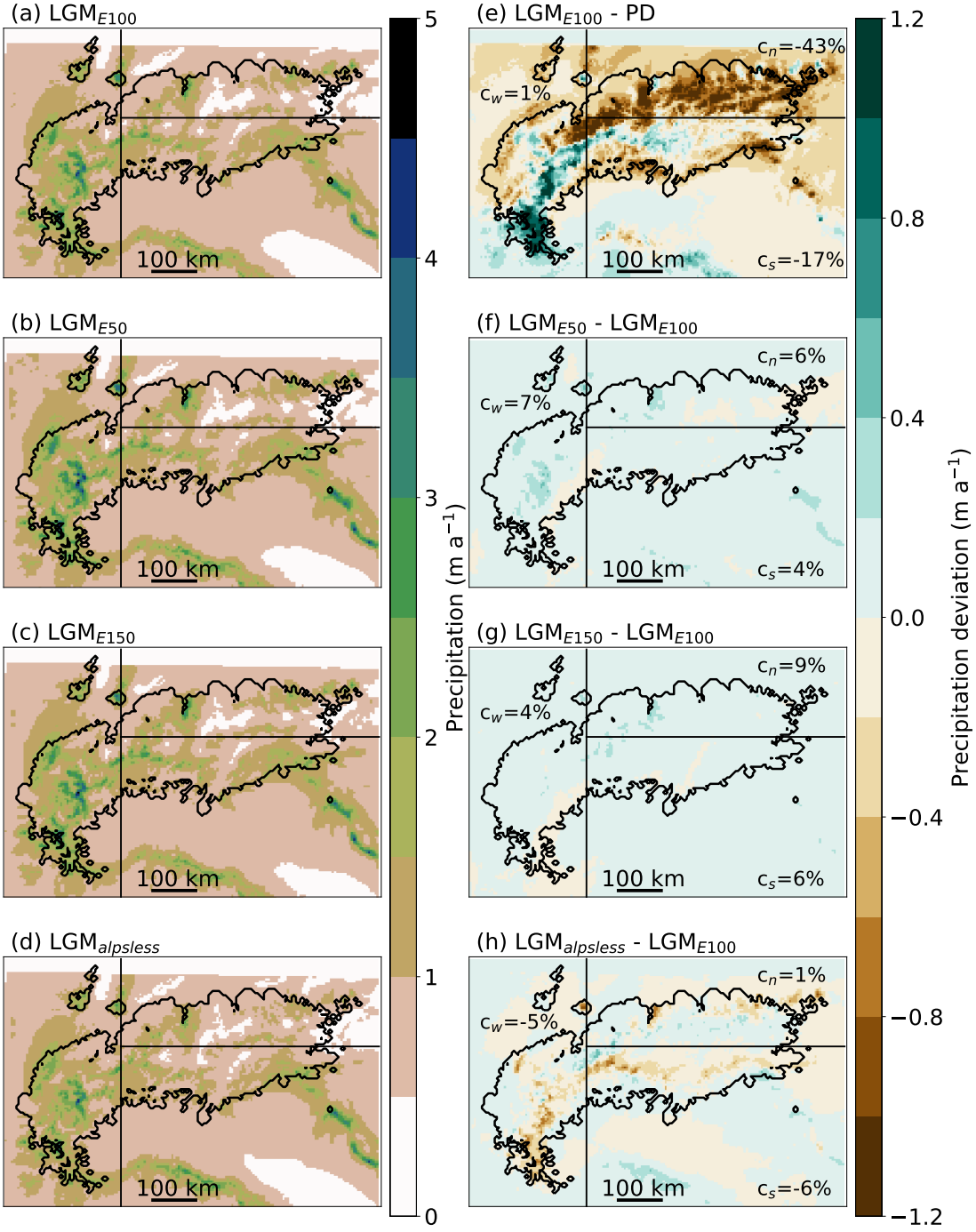


**Figure B.9:** Annual mean precipitation of the LGM$_{E100}$ (a), LGM$_{E50}$ (b), LGM$_{E150}$ (c), and LGM$_{alpsless}$ (d) WRF climate datasets of Velasquez et al. (2020) and Velasquez and Raible (in prep). Precipitation deviation relative to the PD or the LGM$_{E100}$ data are given in (e)–(h). The black outline indicates the geomorphologically reconstructed maximum ice extent of the LGM of Ehlers et al. (2011). The domain is divided into three sectors: a western, a north-eastern and a southern sector (black lines). $c_w$, $c_n$, and $c_s$ indicate the relative change in precipitation inside the formerly glaciated area for the corresponding sectors.

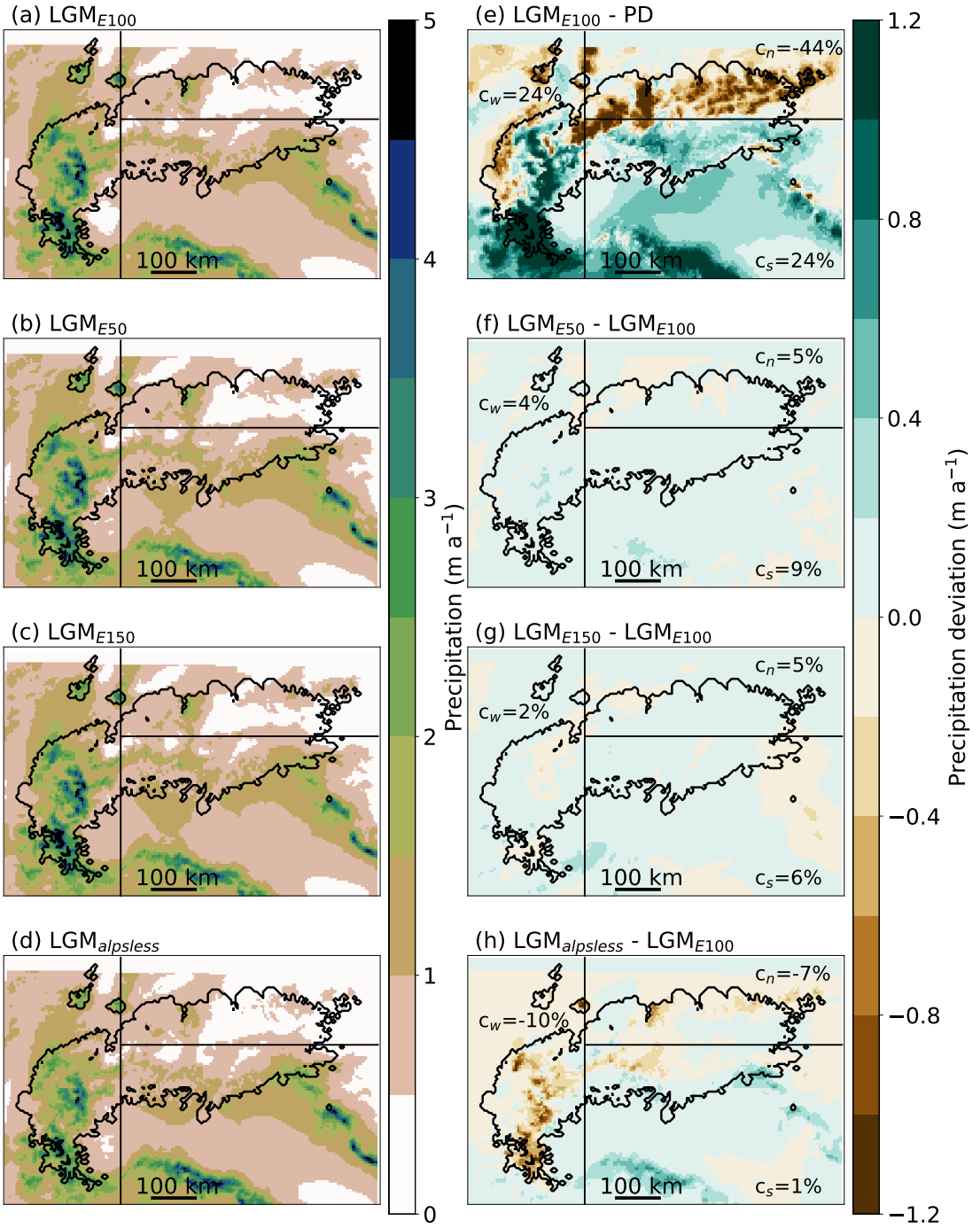


**Figure B.10:** Analogous to Fig. B.9, but for winter (December, January, February) mean precipitation rate.

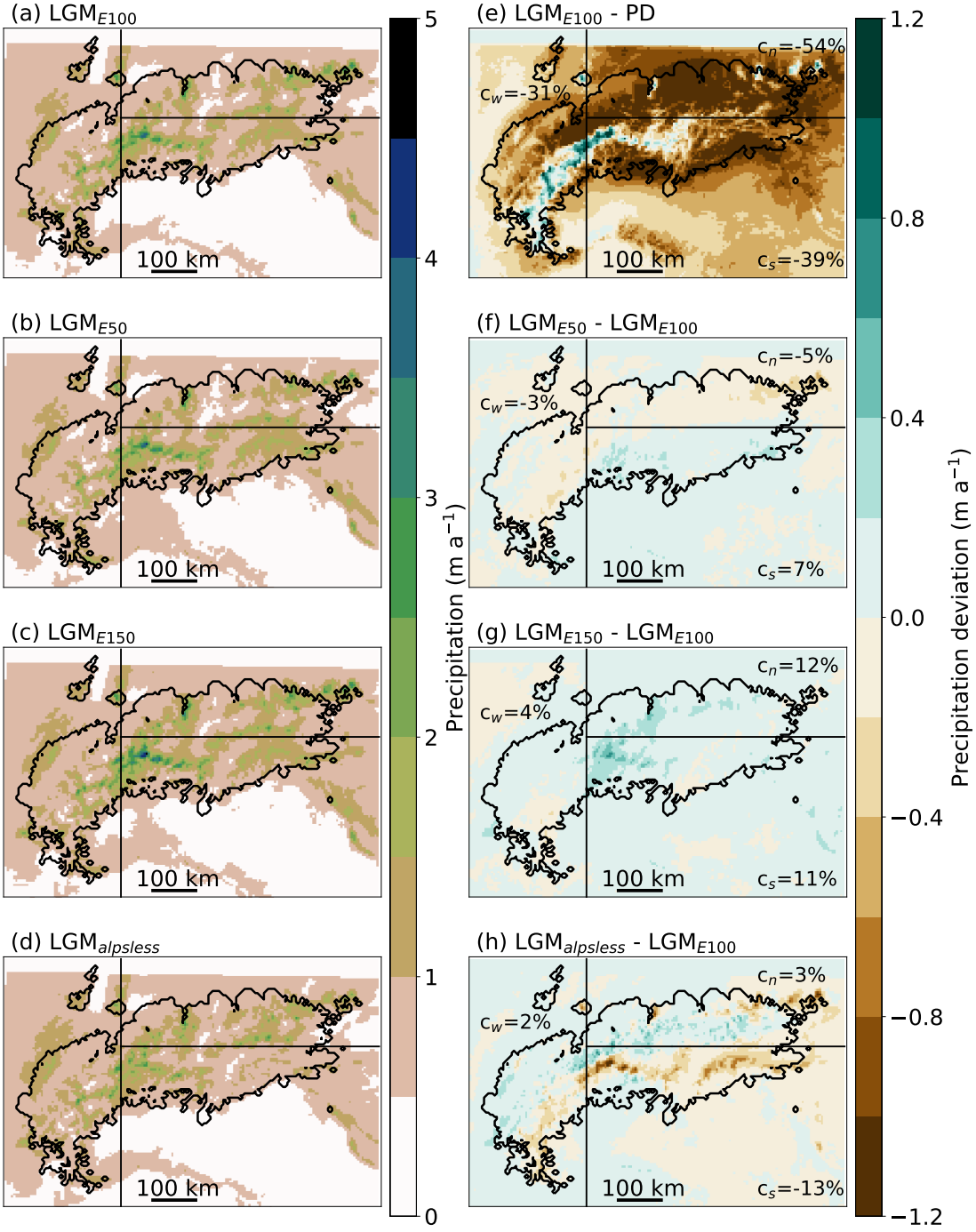


**Figure B.11:** Analogous to Fig. B.9, but for summer (June, July, August) mean precipitation rate.

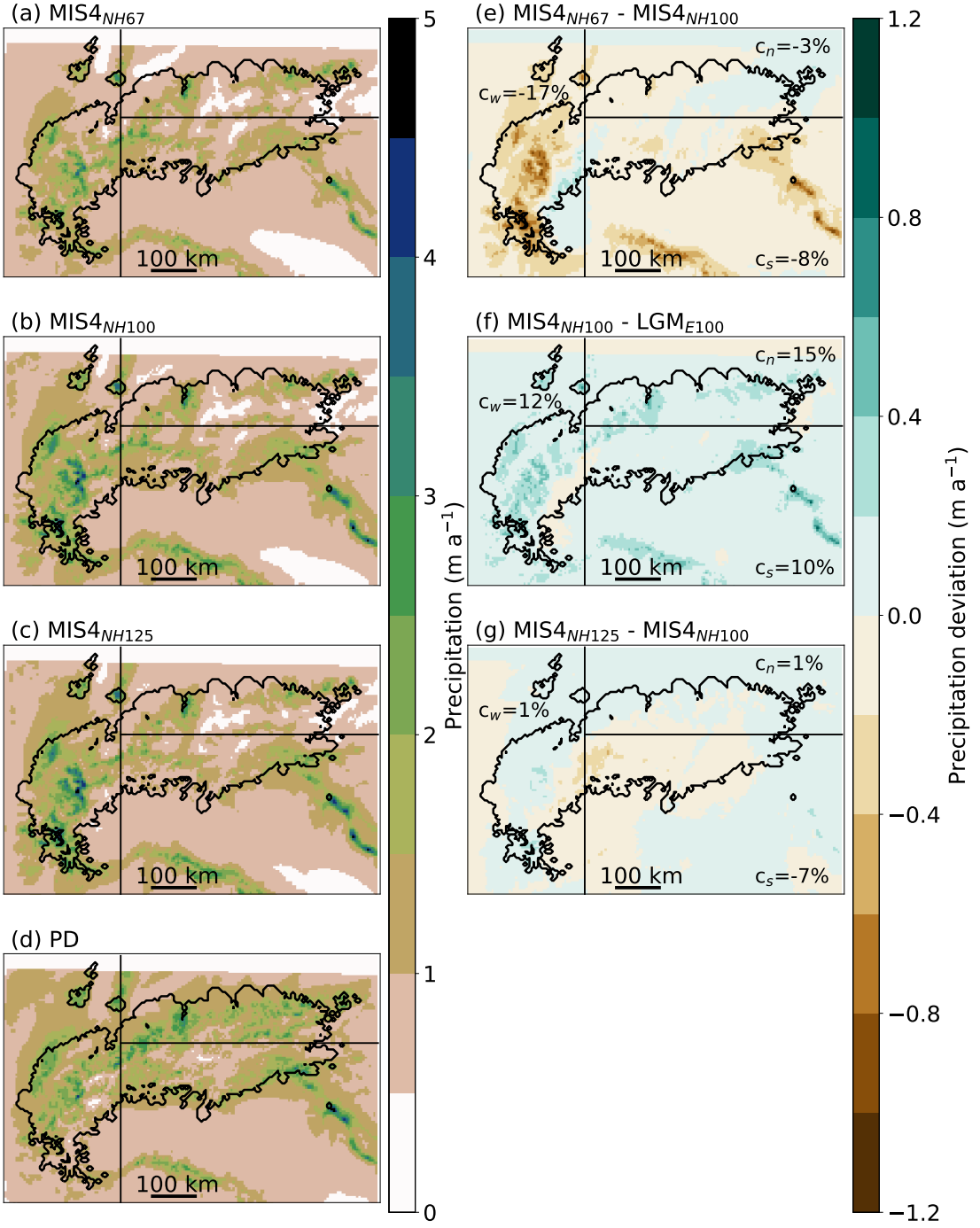


**Figure B.12:** Annual mean precipitation of the MIS4$_{NH67}$ (a), MIS4$_{NH100}$ (b), MIS4$_{NH125}$ (c), and PD (d) WRF climate datasets of Velasquez et al. (2020) and Velasquez and Raible (in prep). Precipitation deviation relative to the LGM$_{E100}$ or MIS4$_{NH100}$ are given in (e)–(g). The black outline indicates the geomorphologically reconstructed maximum ice extent of the LGM of Ehlers et al. (2011). The domain is divided into three sectors: a western, a north-eastern and a southern sector (black lines). $c_w$, $c_n$, and $c_s$ indicate the relative change in precipitation inside the formerly glaciated area for the corresponding sectors.

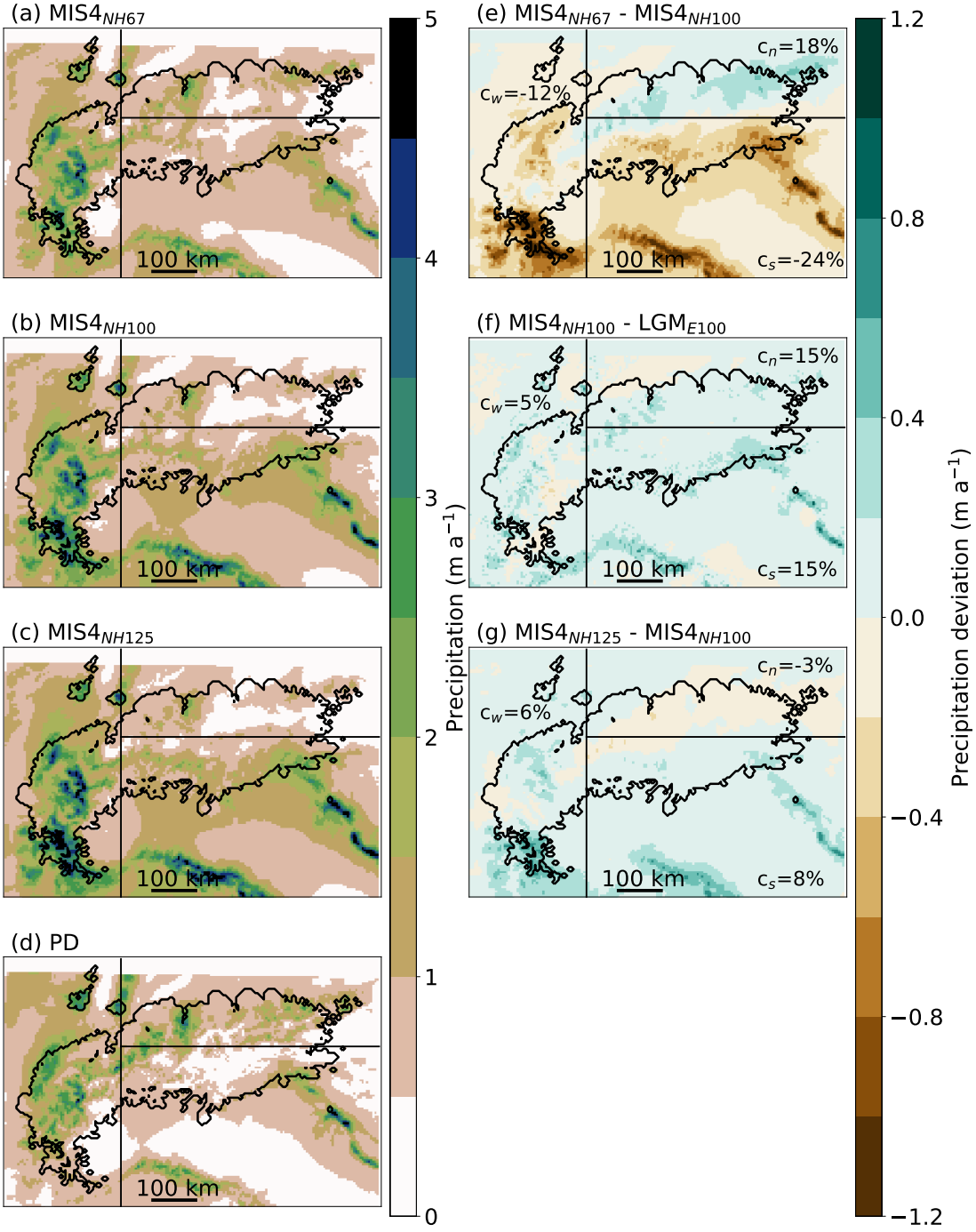


**Figure B.13:** Analogous to Fig. B.12, but for winter (December, January, February) mean precipitation rate.

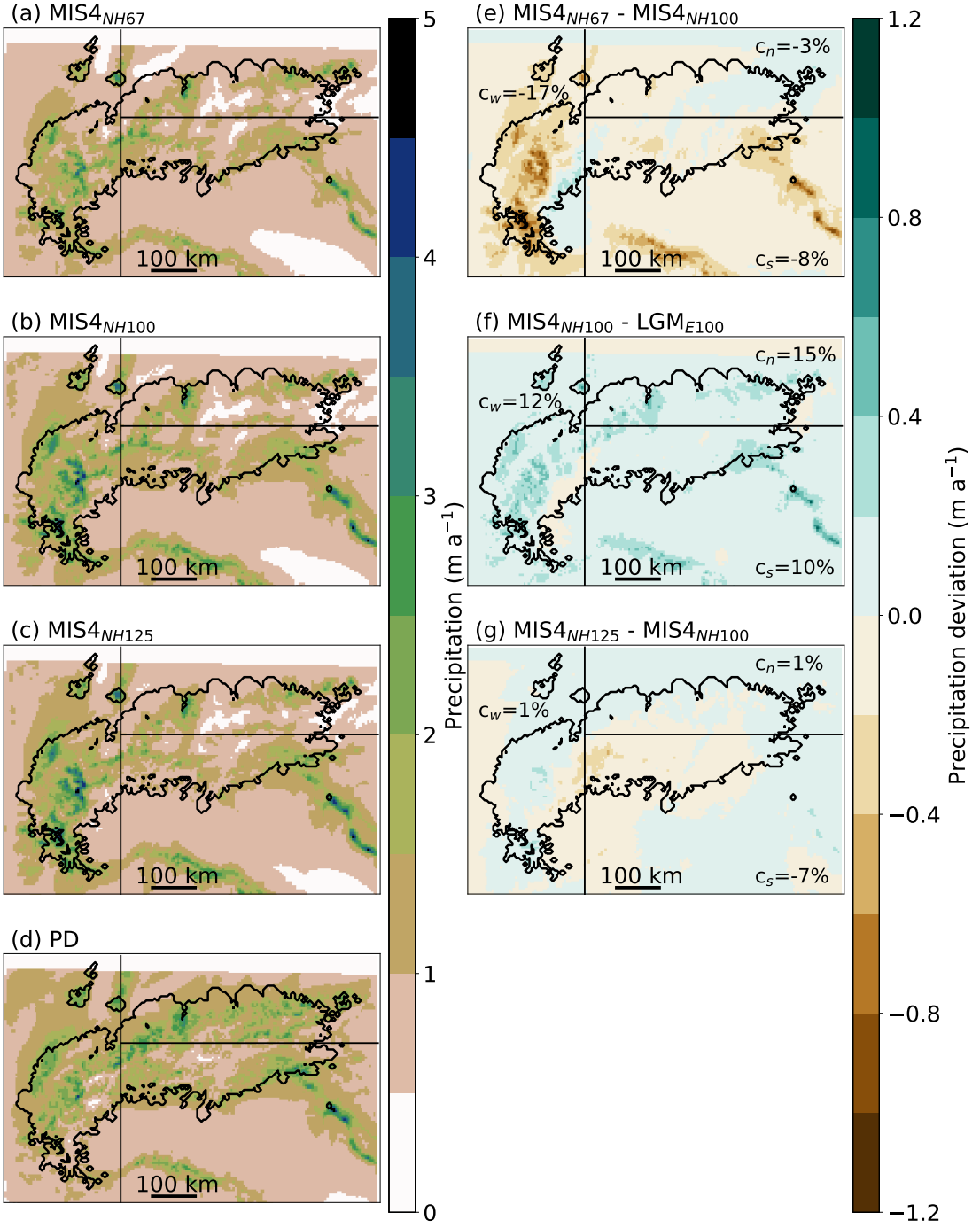


**Figure B.14:** Analogous to Fig. B.12, but for summer (June, July, August) mean precipitation rate.

# C

# APPENDIX: A SIMPLE SURFACE GRADIENT SCHEME FOR SIA MODELS TO STRICTLY INHIBIT NEGATIVE ICE THICKNESSES

*"Du hältst durch und ich halte durch und nächstes Jahr gehen wir einen saufen."*
— Zwei Himmelshunde auf dem Weg zur Hölle (1972)

## C.1 INTRODUCTION

Ice flow models based on the Shallow Ice Approximation (SIA, Hutter, 1983) have low computational costs allowing for both large-scale and long-term simulations that are hardly feasible with more sophisticated and computationally expensive ice flow models. Therefore, SIA ice flow models are broadly used for paleoglacier reconstructions (e.g. Seguinot et al., 2018), long-term evolutions of ice sheets (e.g. Sutter et al., 2019), and also in global glacier modelling (e.g. Maussion et al., 2019; Zekollari et al., 2019). Unfortunately, SIA-based ice flow models suffer mass conservation issues that emerge on steep terrain (Jarosch et al., 2013). At some grid cells more ice may be removed than there is present, leading to negative ice thicknesses which is physically not meaningful. Further, negative ice thicknesses can cause numerical instabilities. To avoid these issues, the affected grid cells are typically filled with extra ice at the price of violating mass conservation.

Here, a new numerical scheme for SIA models is presented that recovers negative ice thicknesses and thus mass conservation violations. The scheme is specifically adapted for one of the most common implementations of SIA models, namely those integrated explicitly forward-in-time centred-in-space on a regular grid. The proposed scheme caps surface differences with the uppstream ice thickness in the computation of surface gradients. This new scheme is simple, strictly mass conserving, and computationally cheap.

The appendix is organized as follows. Section C.2 introduces the mathematical model. Then, Section C.3 describes the issue with negative ice thicknesses and proposes a new surface gradient capping scheme that resolves this issue. The strict positivity of the ice thickness is proved in Section C.4. The capability of the new scheme is demonstrated by performing a test against an analytical solution following Jarosch et al. (2013) in Section C.5. Last, an application on a rugged real world topography highlights practical advantages compared to other schemes in Section C.6.

## C.2 THE SIA ICE FLOW MODEL

Here, an ice flow model is considered where the vertically integrated SIA velocity was inserted into the mass continuity equation. For simplicity, a flow-line (1D) model is considered[1]:

$$\frac{\mathrm{d}h}{\mathrm{d}t} = -\partial_x q + \dot{m}, \tag{C.1}$$

$$q = -\Gamma h^{n+2} |\partial_x S|^{n-1} \partial_x S, \tag{C.2}$$

$$\Gamma = \frac{2A(\rho g)^n}{n+2}, \tag{C.3}$$

where $S(x,t) = h(x,t) + b(x)$ is the ice surface elevation, $h$ is the ice thickness, $b$ is the bedrock elevation, $\partial_x$ is the partial derivative in $x$ directions, $q$ is the horizontal ice flux, $A$ is the rate factor in Glen's flow law (Glen, 1953), $n$ is the power law exponent, $\rho$ is the density of ice, $g$ is the gravitational acceleration, and $\dot{m}(x,t)$ is the mass balance. To solve Eq. (C.1–C.3) numerically, it is often interpreted as a diffusion equation (Hindmarsh and Payne, 1996; Huybrechts and Payne, 1996; Mahaffy, 1976):

$$\frac{\mathrm{d}h}{\mathrm{d}t} = \partial_x (D \partial_x S) + \dot{m}, \tag{C.4}$$

where the ice diffusivity $D$ is:

$$D = \Gamma h^{n+2} |\partial_x S|^{n-1}. \tag{C.5}$$

In this chapter, Eq. (C.4) is integrated with an Euler forward-in-time centred-in-space scheme on a regular staggered Arakawa C-grid (Arakawa and Lamb, 1977) where diffusivities and surface gradients are calculated at the grid cell interfaces (Fig. C.1a). This discretization and integration is commonly used in ice flow modelling (e.g. Bueler and Brown, 2009; Neff et al., 2016). Let $h_i^k$ be an approximation of $h$ at time step $k$ and grid position $i \cdot \Delta x$ where $\Delta x$ denotes the horizontal grid spacing. The time step length separating $h_i^k$ and $h_i^{k+1}$ is denoted with $\Delta t$. The discretization of Eq. (C.4) and (C.5) then becomes:

$$\frac{h_i^{k+1} - h_i^k}{\Delta t} = \frac{1}{\Delta x} \left( D_{i+\frac{1}{2}}^k \frac{S_{i+1}^k - S_i^k}{\Delta x} - D_{i-\frac{1}{2}}^k \frac{S_i^k - S_{i-1}^k}{\Delta x} \right) + \dot{m}_i^k. \tag{C.6}$$

There are several ways to calculate the staggered diffusivity $D_{i+\frac{1}{2}}^k$. Here, the so-called M2 discretization is considered (Hindmarsh and Payne, 1996; Jarosch et al., 2013) where the staggered diffusivity $D_{i+\frac{1}{2}}^k$ is given by:

$$D_{i+\frac{1}{2}}^k = \Gamma \left( \frac{h_{i+1}^k + h_i^k}{2} \right)^{n+2} \left| \frac{S_{i+1}^k - S_i^k}{\Delta x} \right|^{n-1}, \tag{C.7}$$

1 Equations for a corresponding ice flow model in two dimensions are given in Appendix D.

$D^k_{i-\frac{1}{2}}$ is calculated analogously. Any explicit forward-in-time numerical integration scheme becomes unstable if too long time steps are chosen. Based on a stability analysis of Hindmarsh (2001), choosing a time step smaller than $\Delta t_{max}$ ensures numerical stability on a one dimensional ice flow model employing the M2 discretization:

$$\Delta t_{max} = \frac{1}{2n}\frac{(\Delta x)^2}{D^k_{max}}, \tag{C.8}$$

$$D^k_{max} = max(D^k_{i+\frac{1}{2}}, D^k_{i-\frac{1}{2}}), \tag{C.9}$$

where $D^k_{max}$ is the largest value of the diffusivity on the domain at the current time step.

## C.3 NEGATIVE ICE THICKNESSES IN SIA ICE FLOW MODELS

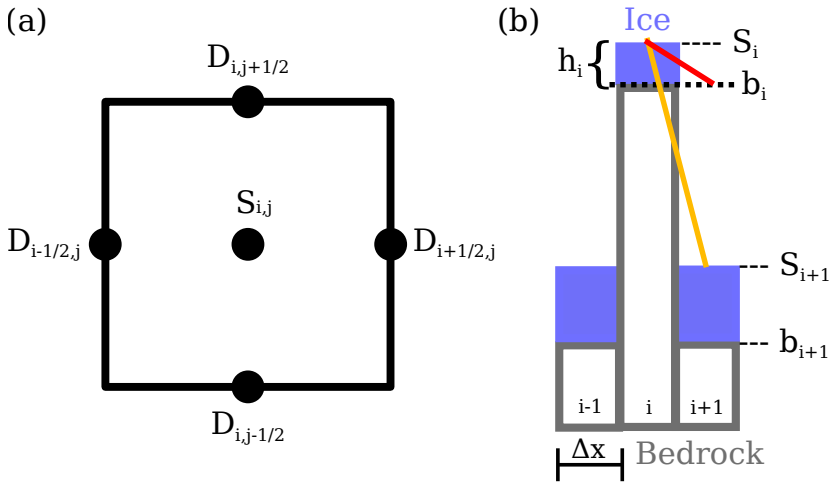


**Figure C.1:** (a) 2D Staggered Arakawa C-grid where the surface elevation lies at the centre of the grid cell and the diffusivities and surface gradients are evaluated at the grid cell boundary. (b) Illustration of the worst-case scenario for mass conservation in $x$ direction where $\Delta x$ represents the lateral resolution of the grid (for visualisation reasons the $y$ direction is not drawn, but looks analogous to the $x$ direction). The ice leaves the grid cell at $i$ to both directions. The orange line indicates the conventional surface gradient and the red line indicates the proposed surface gradient that ensures mass conservation.

A central issue of the M2 and other discretizations is that the ice flux at $i + \frac{1}{2}$ ($q^k_{i+\frac{1}{2}}$) does not necessarily go to zero if the upstream ice thickness, $h^k_i$ or $h^k_{i+1}$, goes to zero (Jarosch et al., 2013). Therefore, the ice thickness in the projected time step can become negative. In the following, the term 'upstream' refers to the one of two neighbouring grid cells that is drained by the other one. In SIA models, the ice flow direction only depends on the sign of the surface gradient and therefore upstream always refers to the grid cell with a higher surface elevation.

To illustrate the issue with negative ice thicknesses, we consider the case with $b_i > S^k_{i+1}$ and $h^k_{i+1} > 0$ (similar to Fig. C.1b). For simplicity, the mass balance term is ignored. Discretizising Eq. (C.2) with the M2 discretization scheme yields:

$$q^k_{i+\frac{1}{2}} = -\Gamma \left( \frac{h^k_i + h^k_{i+1}}{2} \right)^{n+2} \left| \frac{S^k_{i+1} - S^k_i}{\Delta x} \right|^{n-1} \left( \frac{S^k_{i+1} - S^k_i}{\Delta x} \right), \tag{C.10}$$

Remembering $S^k_i = h^k_i + b_i$ and letting $h^k_i \to 0$ yields:

$$\lim_{h^k_i \to 0} q^k_{i+\frac{1}{2}} = -\Gamma \left( \frac{h^k_{i+1}}{2} \right)^{n+2} \left| \frac{S^k_{i+1} - b_i}{\Delta x} \right|^{n-1} \left( \frac{S^k_{i+1} - b_i}{\Delta x} \right) > 0, \tag{C.11}$$

which does not converge to zero because no factor in Eq. (C.11) goes to zero as the upstream ice thickness $h^k_i$ goes to zero. This results in an ice flux larger than zero although no ice can be drained from $i$. In fact, the ice flux even becomes independent of the upstream ice thickness $h^k_i$ and only depends on the upstream bedrock elevation $b_i$ and the downstream ice surface elevation $S^k_{i+1}$ and ice thickness $h^k_{i+1}$. Thus, in an integration this would lead to a negative ice thickness at $i$. Negative ice thicknesses are not a physically valid solution. Usually, negative ice thicknesses are simply set to zero ($h^k_i = \max(h^k_i, 0)$) in most ice flow models, which introduces artificial ice into the model and breaks mass conservation. The problem with negative ice thicknesses can also be seen as an obstacle problem with inequality constrain $h(x,t) >= 0$ (Jouvet and Bueler, 2012).

## C.4 A SCHEME THAT MAINTAINS NON-NEGATIVE ICE THICKNESSES

The issue of negative ice thicknesses and non-zero ice fluxes out of ice-free grid cells has already been tackled by other authors. For example, Jarosch et al. (2013) applied a flux limiter function to Eq. (C.5), which is treated as a hyperbolic conservation law. (Bueler, 2016) reinterpreted Eqs. (C.1 – C.2) as a nonlinear diffusion-advection equation, which is solved with a finite volume element scheme and fulfils the constraint that ice thickness is non-negative. Here, a different and much simpler approach is taken to ensure that the ice flux depends on the upstream ice thickness and that strict positivity in ice thickness is guaranteed. The approximate surface gradient ($\partial_x S$) that is multiplied with the diffusivity is proposed to be capped in dependence on the upstream ice thicknesses:

$$\partial_x S((i + \frac{1}{2}) \cdot \Delta x, t) \sim \min \left( \max \left( \frac{-h^k_i}{\Delta x}, \frac{S^k_{i+1} - S^k_i}{\Delta x} \right), \frac{h^k_{i+1}}{\Delta x} \right). \tag{C.12}$$

Hereafter, this new gradient scheme will be referred to as UPstream SURface Gradient cappING (UPSURGING). A similar capping scheme was developed and successfully applied to a zero-inertia model, a simplification to the 2D shallow water equations, to ensure positivity of the water depth (Wang et al., 2011). Figure C.1b

illustrates how UPSURGING caps the surface gradients (red line) compared to the conventional surface gradient (orange line). UPSURGING is only activated where the upstream bedrock elevation ($b_i$, Fig. C.1b) is greater than the downstream surface elevation ($S^k_{i+1}$ or $S^k_{i-1}$) and therefore simplifies to the ordinary surface gradients in areas where the bedrock is at lower elevation than the neighbouring surface elevation.

The remainder of this section illustrates that UPSURGING **(1)** resolves the issue of non-zero ice fluxes out of ice-free grid cells and **(2)** indeed results in strict positivity of the ice thickness.

**(1)** Revisiting the non-zero ice flux out of ice-free grid cells (Eq. C.11), and applying UPSURGING to the surface gradients yields:

$$\begin{aligned}\lim_{h^k_i \to 0} q^k_{i+\frac{1}{2}} &= -\Gamma \left(\frac{h^k_{i+1}}{2}\right)^{n+2} \left|\frac{S^k_{i+1} - b_i}{\Delta x}\right|^{n-1} \cdot \\ &\quad \min\left(\max\left(\frac{0}{\Delta x}, \frac{S^k_{i+1} - b_i}{\Delta x}\right), \frac{h^k_{i+1}}{\Delta x}\right) = 0, \end{aligned} \tag{C.13}$$

and indeed the ice flux $q^k_{i+\frac{1}{2}} \to 0$ with $h^k_i \to 0$ despite $\frac{S^k_{i+1}-b_i}{\Delta x} < 0$, which resolves the issue of the original Eq. C.11.

**(2)** Considering a grid cell at $i$ that is drained to both sides (Fig. C.1b), it is possible to show that the following property regarding strict ice thickness positivity holds:

$$h^k_i \geq 0 \Rightarrow h^{k+1}_i \geq 0, \quad \text{for all} \quad \Delta t \leq \Delta t_{max} \quad \text{and} \quad n \geq 1, \tag{C.14}$$

if the UPSURGING scheme is used. UPSURGING cannot (and is not meant to) recover negative ice thicknesses caused by the mass balance term. Therefore, we set $\dot{m}^k_i = 0$. We assume $h^{k+1}_i$ to be defined as in Eq. (C.6) and use the UPSURGING scheme (Eq. C.12) in the gradient computation:

$$\begin{aligned} h^{k+1}_i &= h^k_i + \frac{\Delta t}{\Delta x}\left(D^k_{i+\frac{1}{2}} \min\left(\max\left(\frac{-h^k_i}{\Delta x}, \frac{S^k_{i+1} - S^k_i}{\Delta x}\right), \frac{h^k_{i+1}}{\Delta x}\right) - \right. \\ &\quad \left. D^k_{i-\frac{1}{2}} \min\left(\max\left(\frac{-h^k_{i-1}}{\Delta x}, \frac{S^k_i - S^k_{i-1}}{\Delta x}\right), \frac{h^k_i}{\Delta x}\right)\right). \end{aligned} \tag{C.15}$$

Remembering that the grid cell at $i$ is drained to both sides implies $S^k_{i+1} < S^k_i$ and $S^k_i > S^k_{i-1}$ and thus:

$$\begin{aligned} h^{k+1}_i &= h^k_i + \frac{\Delta t}{\Delta x}\left(D^k_{i+\frac{1}{2}} \max\left(\frac{-h^k_i}{\Delta x}, \frac{S^k_{i+1} - S^k_i}{\Delta x}\right) - \right. \\ &\quad \left. D^k_{i-\frac{1}{2}} \min\left(\frac{S^k_i - S^k_{i-1}}{\Delta x}, \frac{h^k_i}{\Delta x}\right)\right). \end{aligned} \tag{C.16}$$

Therefore, the ice thickness in the next time step is at least:

$$h_i^{k+1} \geq h_i^k + \frac{\Delta t}{\Delta x}\left(D^k_{i+\frac{1}{2}}\frac{-h_i^k}{\Delta x} - D^k_{i-\frac{1}{2}}\frac{h_i^k}{\Delta x}\right), \tag{C.17}$$

$$\geq h_i^k\left(1 - \frac{\Delta t}{(\Delta x)^2}(D^k_{i+\frac{1}{2}} + D^k_{i-\frac{1}{2}})\right). \tag{C.18}$$

Thus, $h_i^{k+1} \geq 0$ if:

$$\Delta t \leq \frac{(\Delta x)^2}{(D^k_{i+\frac{1}{2}} + D^k_{i-\frac{1}{2}})}. \tag{C.19}$$

This allows identifying the largest time step $\Delta t_p$ that ensures strict ice thickness positiveness in the future time step using the UPSURGING scheme:

$$\frac{(\Delta x)^2}{(D^k_{i+\frac{1}{2}} + D^k_{i-\frac{1}{2}})} \geq \frac{1}{2}\frac{(\Delta x)^2}{D^k_{max}} := \Delta t_p, \tag{C.20}$$

where $D^k_{max}$ is the largest diffusivity at timestep $k$ on the model domain. Comparing $\Delta t_p$ to the constraint on the time step regarding numerical stability Eq. (C.8) ($\Delta t_{max} = \frac{1}{2n}\frac{(\Delta x)^2}{D^k_{max}}$) implies that $\Delta t_p \geq \Delta t_{max}$ for all Glen's power law exponents $n \geq 1$. In that case, choosing a $\Delta t \leq \Delta t_{max}$ guarantees not only numerical stability but also $h_i^{k+1} \geq 0$ if UPSURGING is used. The restriction of $n \geq 1$ should not be of concern because the plausible range for $n$ is 2–4 with the best value being $n = 3$ (Cuffey and Paterson, 2010). Using an analogous procedure as above, it is possible to show that condition C.14 also holds in two dimensions if UPSURGING is used.

## C.5 MASS CONSERVATION BENCHMARK TEST

| Constant | Value | Units |
|---|---|---|
| n | 3 | [] |
| A | 1e–16 | $\mathrm{Pa}^{-3}\ \mathrm{a}^{-1}$ |
| $\rho$ | 910 | $\mathrm{kg\ m}^{-3}$ |
| g | 9.81 | $\mathrm{m\ s}^{-2}$ |

**Table C.1:** Values for the constants used in the model.

Here, the performance of the UPSURGING scheme is assessed in terms of mass conservation by computing the benchmark solution proposed by Jarosch et al. (2013) and comparing to their analytical solution (orange line in Fig. C.2). In this test, a glacier is built up from ice-free conditions for 50,000 years until it reaches a steady state shape. The test includes a 500 m high bedrock step that is expected to cause

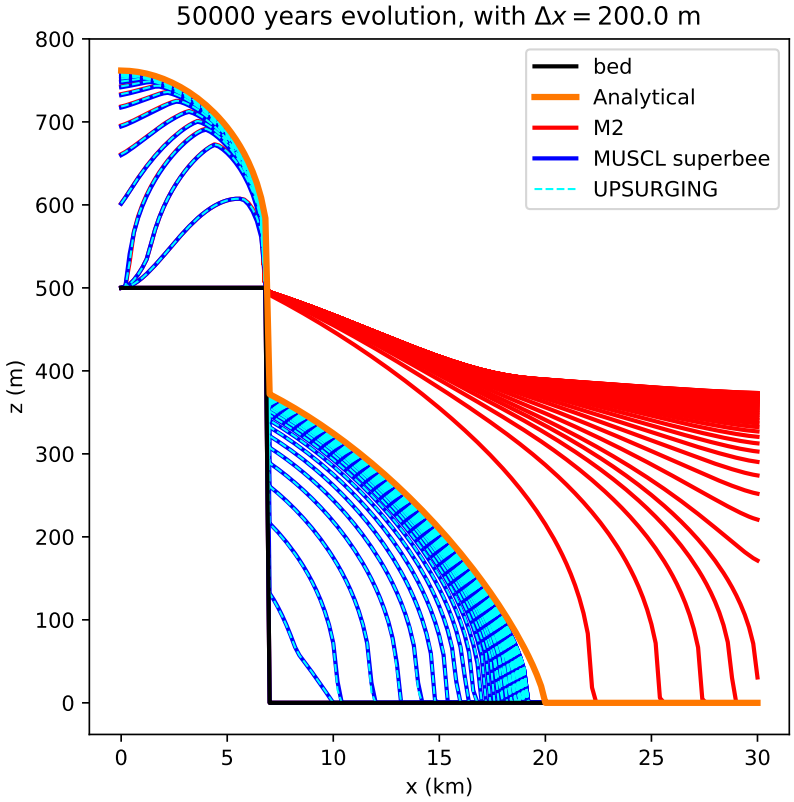


**Figure C.2:** Benchmark test for mass conservation of Jarosch et al. (2013) at a grid resolution of $\Delta x = 200$ m. The figure shows the bedrock (black), the analytical solution (orange), and the simulations using the ordinary M2 scheme (red), the MUSCL superbee flux limiter of Jarosch et al. (2013) (blue), and the UPSURGING scheme (cyan dashed). Snapshots are shown for every 1000 years during the total model period of 50,000 years. This-figure was created using `https://github.com/alexjarosch/sia-fluxlim/blob/master/sia_fluxlim`.

negative ice thicknesses at the last high-ground grid cell in most SIA-based model schemes (Fig. C.2). Table C.1 lists the values for the model constants used for this benchmark test. The grid spacing is taken $\Delta x = 100$, 200, 500, and 1000 m. The mass balance depends solely on the x coordinate. For more details, the reader is referred to Jarosch et al. (2013).

Three SIA implementations are tested on this setup and compared to the analytical solution at the model year 50,000: the ordinary M2 scheme (red), the MUSCL superbee flux limiter of Jarosch et al. (2013) (blue), and the M2 scheme modified with UPSURGING (cyan dashed) (Fig. C.2, only $\Delta x = 200$ m simulations shown). The ordinary M2 simulation produces negative ice thicknesses at the bedrock step and therefore artificially generates mass. As a result, the 2D volume is overestimated by 116.912 to 143.719 % compared to the analytical solution (Tab. C.2). Therefore, the M2 scheme performs poorly in this situation at the tested range of resolutions. In contrast to the M2 scheme, the MUSCL superbee and UPSURGING scheme never attain negative ice thicknesses. The MUSCL superbee and the UPSURGING solution

| $\Delta x$ | $\Delta V$ M2 | $\Delta V$ MUSCL | $\Delta V$ UPSURGING |
|---|---|---|---|
| 1000 m | 116.912 % | −7.588 % | −8.323 % |
| 500 m | 132.095 % | −5.075 % | −5.115 % |
| 200 m | 140.830 % | −3.092 % | −2.972 % |
| 100 m | 143.719 % | −2.412 % | −2.306 % |

**Table C.2:** Volume error (%) relative to the analytical solution of the benchmark test of the three SIA schemes at various horizontal resolutions.

produce very similar ice volumes that deviate only by –7.588 to –2.412 % and –8.323 to –2.306 % respectively from the analytical solution (Tab. C.2). Further, the deviation between the results obtained with MUSCL superbee and UPSURGING and the analytical solution decrease with refined resolution. Also, the two schemes show a similar degree of deviation from the analytical solution throughout the tested range of resolutions (Tab. C.2). At intermediate points in time of the 50,000 years model period, the MUSCL superbee and UPSURGING scheme again yield essentially the same results (Fig. C.2). Therefore, we conclude that the UPSURGING scheme passes this benchmark test with comparable success to the MUSCL superbee scheme and without notable short comings in accuracy.

| $\Delta x$ | M2 | MUSCL | UPSURGING |
|---|---|---|---|
| 1000 m | 3.1 s | 9.5 s | 2.7 s |
| 500 m | 7.6 s | 10.5 s | 28.4 s |
| 200 m | 54.8 s | 74.6 s | 1201.6 s |
| 100 m | 292.7 s | 341.4 s | 23′243.8 s |

**Table C.3:** Computational time of the three schemes to complete the benchmark test at various horizontal resolutions.

At resolutions smaller than 1000 m, the MUSCL superbee flux limiter performs the test in a shorter time than the UPSURGING scheme (Tab. C.3). The reason for the high computational costs of the UPSURGING scheme is the large diffusivity at the cliff that requires to take very short time steps. The MUSCL superbee flux limiter does not have this issue because it reduces the diffusivity at the cliff and therefore does not require the model to take small time steps. Whether this drawback comes into play on natural topographies is to be investigated. Sudden cliffs with a height of 500 m are not common in glacier beds.

## C.6 PERFORMANCE IN A 2D ICE FLOW MODEL AT A REAL-WORLD TOPOGRAPHY

This section presents a 2D application of the MUSCL superbee and the UPSURGING scheme on a real world topography to investigate the viability of each of the two

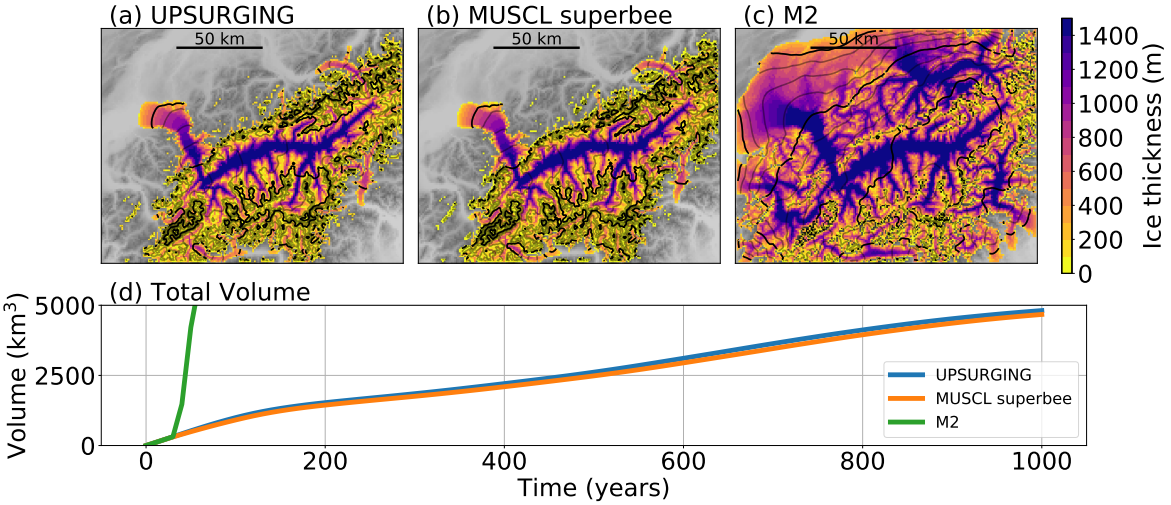


**Figure C.3:** Model results obtained with the three SIA model implementations UPSURGING (a), MUSCL superbee (b), and M2 (c) at the Valais, Switzerland at a horizontal resolution of 1 km after 1000 years. The thick (thin) black contour lines have an elevation spacing of 1000 m (250 m). Panel (d) shows the volume evolution of the three simulations.

schemes. The M2 scheme is only used to illustrate what happens if the issue with negative ice thicknesses is ignored. The model domain spans 180 km × 140 km rectangle covering the present-day Valais in Switzerland (Fig. C.3). The bedrock elevation is taken from Jarvis et al. (2008) and interpolated to a horizontal resolution of 1 km. For the surface mass balance, a constant-in-time equilibrium line altitude (ELA) mass balance model is applied:

$$\dot{m}_{i,j} \quad = \quad \min((S_{i,j} - ELA) \cdot m_{grad}, m_{max}), \tag{C.21}$$

where $ELA = 2100$ m is the equilibrium line altitude, $m_{grad} = 0.007$ a$^{-1}$ is the mass balance gradient, and $m_{max} = 2$ m a$^{-1}$ is the maximum accumulation. The model is initialized ice free and the above described surface mass balance is applied for 1000 years. The ice thickness is held at zero at the model boundary. The 2D SIA models use the same values for the model constants as in the benchmark test from Section C.5 (Tab. C.1). Details about the 2D discretization are given in Appendix D. This setup serves only as a practical example of the two schemes and does not aim at reconstructing any past glacier.

Similar to the benchmark test from Section C.5, the UPSURGING and MUSCL superbee simulations attain an almost identical ice extent (Fig. C.3a,b) with similar ice volumes of 4810.8 km$^3$ and 4672.7 km$^3$ respectively. In terms of ice thickness, the UPSURGING simulation deviates by less than ±50 m from the MSUCL superbee simulation in most areas (Fig. C.4). Only the largest glaciers are a few grid cells longer and therefore 100–200 m thicker using the UPSURGING scheme instead of the MUSCL superbee flux limiter. This is perhaps related to how each of the two schemes adjusts the ice flux or the surface gradients at the glacier terminus. By contrast, the M2 simulation reaches the domain boundary in many areas (Fig. C.3c) and attains by far the largest ice volume (Fig. C.3d, 16'638.4 km$^3$). The reason for

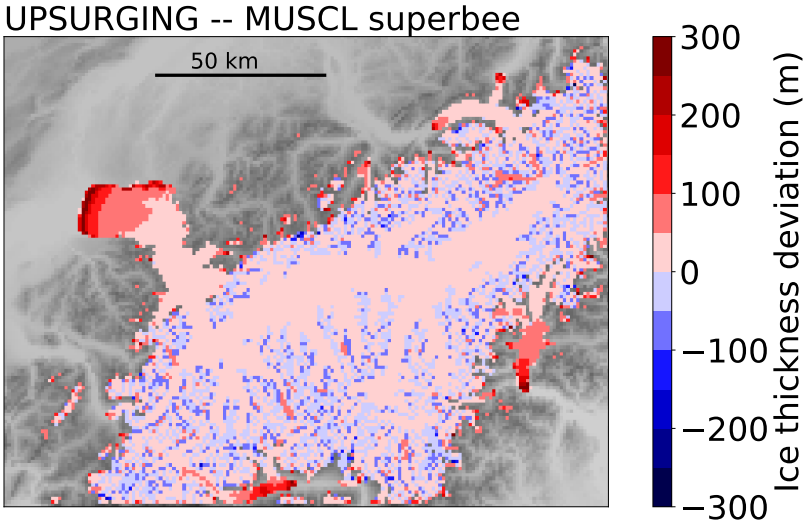


**Figure C.4:** Difference in ice thickness at the year 1000: UPSURGING – MUSCL superbee.

the tremendous ice volume in the M2 simulation is that 28'2986.4 km$^3$ of ice are generated by forcing negative ice thicknesses to zero during the 1000 year model period. By contrast, the UPSURGING simulation did not generate any artificial mass at all and the MUSCL superbee simulation only 0.1 km$^3$ during the entire 1000 year, which is too little to affect the model results. The majority of this leak occurs within the first 30 years of the simulation. However, this experiment demonstrates that the MUSCL flux limiter introduced by Jarosch et al. (2013) can allow a small mass leak.

| Scheme | UPSURGING | MUSCL | M2 |
|---|---|---|---|
| Computation time | 1.4 h | 23.6 h | 9.0 h |

**Table C.4:** Computational time to perform the experiment at the Rhone Valley

The most interesting difference between the three simulations, especially the UPSURGING and the MUSCL superbee simulation, is the computational time they require (Tab. C.4). The UPSURGING simulation takes about 17 times less time than the MUSCL superbee simulation to complete the 1000 year long experiment, which is a significant speed-up. The computational savings of the UPSURGING scheme have two reasons: The UPSURGING scheme requires only 1'472'966 time steps whereas the MUSCL scheme requires 2'264'618. Thus, the UPSURGING scheme is able to take time steps that are on average 1.5 times longer than in the MUSCL superbee scheme. The remaining speed-up of factor $\approx$ 11 is related to reduced calculation time of one iteration. A key feature of the MUSCL superbee scheme is that the diffusivity is calculated twice at every grid cell boundary. Which one of the two diffusivities is used in the ice flow calculation (Jarosch et al., 2013) depends on the surface elevation and ice thickness of the surrounding grid cells. By contrast, the UPSURGING scheme neither requires calculating each diffusivity twice nor sorting out calculations and is therefore more economic. The implementation of the MUSCL

superbee scheme used here is directly taken from Jarosch et al. (2013) and could be implemented in more efficient ways (personal communication Alexander Jarosch). Therefore, the 17 time computational benefit of UPSURGING might be an upper bound.

## C.7 CONCLUSIONS

In this Appendix, the UPstream SURface Gradient cappING (UPSURGING) scheme was introduced. UPSURGING is a method that strictly ensures positivity of the ice thickness in SIA ice flow models, which avoids mass conservation issues. It is strictly positivity-conserving given a time step is used that satisfies the numerical stability criterion of Hindmarsh (2001) and the power law exponent is chosen $n$ greater or equal to 1. The UPSURGING scheme was proven to work for SIA models that are reformulated as a diffusion equation and integrated explicitly with an Euler forward-in-time centred-in-space scheme on a regular Cartesian, staggered grid. It is important to note that the proof presented here does not guarantee the scheme to work in other kinds of SIA model implementations, for example for implicit models, SIA models based on the advection equation or models using a Runge-Kutta time integration. However, the UPSURGING scheme does not put requirements on how the diffusivity is calculated, except that it is calculated at the grid cell boundary. Thus, the proposed gradient capping scheme also works for discrectizations of the diffusivity other than M2.

UPSURGING compared well with the earlier introduced MUSCL superbee flux limiter at the benchmark test of Jarosch et al. (2013). On a real world topography the two schemes produced almost identical model results. The lower computational cost, about a factor of 17 in our test on the real world topography, was a promising benefit that UPSURGING could offer over the MUSCL superbee flux limiter. UPSURGING could be of benefit for studies that tackle many small alpine glaciers at the same time or studies tackling large ice sheets that flow through rugged mountain ranges. Yet, investigating the performance of UPSURGING and other positivity-conserving schemes with respect to accuracy and computational speed in other topographical settings is advised to confirm and expand the conclusions drawn based on the applications presented in this appendix.

The UPSURGING scheme could also be used in hybrid ice flow models such as the Parallel Ice Sheet Model (PISM). In the case of PISM, it might allow turning off the scheme of Schoof (2003) which can cause overestimated ice thicknesses in mountainous terrain (Chapter 4). Nonetheless, it should be kept in mind that UPSURGING cannot resolve any negative ice thickness issues arising from the shallow shelf approximation dynamics which are used to calculate the ice transport due to sliding.

## ACKNOWLEDGEMENTS

I am grateful to Guillaume Jouvet, Alexander Jarosch, Kolumban Hutter, Julien Seguinot, Eef van Dongen, and Ludovic Räss for their valuable comments on UPSURGING. I used the python model code of Alexander Jarosch's 2D MUSCL superbee implementation and his 1D step test from GitHub for the simulations presented here:
`https://github.com/alexjarosch/sia-fluxlim/blob/master/sia_fluxlim`

## CODE AVAILABILITY

The code implementation of UPSURGING, M2, and MUSCL superbee used in Section C.6 is available on GitHub:
`https://github.com/michael-imhof/sia-upsurging`

# D

## APPENDIX: EQUATIONS FOR A 2D SIA-MODEL

This appendix provides the corresponding 2D equations for the shallow ice approximation flow model from Section C:

$$\frac{\mathrm{d}h}{\mathrm{d}t} = -\vec{\nabla}\cdot\vec{q} + \dot{m}, \tag{D.1}$$

$$\vec{q} = -\Gamma h^{n+2}|\vec{\nabla}S|^{n-1}\vec{\nabla}S, \tag{D.2}$$

$$\Gamma = \frac{2A(\rho g)^n}{n+2}, \tag{D.3}$$

where $\vec{\nabla} = (\partial_x, \partial_y)$ is the gradient in $x$ and $y$ directions and $\vec{q}$ is the horizontal ice flux.

$$\frac{\mathrm{d}h}{\mathrm{d}t} = \vec{\nabla}\cdot(D\vec{\nabla}S) + \dot{m}, \tag{D.4}$$

where the ice diffusivity $D$ is:

$$D = \Gamma h^{n+2}|\vec{\nabla}S|^{n-1}. \tag{D.5}$$

The discretization of Eq. (D.4) and (D.5) then becomes:

$$\frac{h^{k+\Delta t}_{i,j} - h^k_{i,j}}{\Delta t} = \frac{1}{\Delta x}\left( D^k_{i+\frac{1}{2},j}\frac{S^k_{i+1,j} - S^k_{i,j}}{\Delta x} - D^k_{i-\frac{1}{2},j}\frac{S^k_{i,j} - S^k_{i-1,j}}{\Delta x} + D^k_{i,j+\frac{1}{2}}\frac{S^k_{i,j+1} - S^k_{i,j}}{\Delta x} - D^k_{i,j-\frac{1}{2}}\frac{S^k_{i,j} - S^k_{i,j-1}}{\Delta x}\right) + \dot{m}^k_{i,j}, \tag{D.6}$$

The M2 discretization of the staggered diffusivity $D^k_{i+\frac{1}{2},j}$ is given by:

$$D^k_{i+\frac{1}{2},j} = \Gamma\left(\frac{h^k_{i+1,j} + h^k_{i,j}}{2}\right)^{n+2}|\vec{\nabla}S^k_{i+\frac{1}{2},j}|^{n-1}, \tag{D.7}$$

$$|\vec{\nabla}S^k_{i+\frac{1}{2},j}| = \left[\left(\frac{S^k_{i+1,j} - S^k_{i,j}}{\Delta x}\right)^2 + \left(\frac{1}{4}\left(\frac{S^k_{i,j+1} - S^k_{i,j}}{\Delta x} + \frac{S^k_{i,j} - S^k_{i,j-1}}{\Delta x} + \frac{S^k_{i+1,j+1} - S^k_{i+1,j}}{\Delta x} + \frac{S^k_{i+1,j} - S^k_{i+1,j-1}}{\Delta x}\right)\right)^2\right]^{\frac{1}{2}}. \tag{D.8}$$

$D^k_{i-\frac{1}{2},j}$, $D^k_{i,j+\frac{1}{2}}$, and $D^k_{i,j-\frac{1}{2}}$ are calculated analogously. According to Hindmarsh (2001), a time step smaller than $\Delta t_{max}$:

$$\Delta t_{max} = \frac{1}{2n+2}\frac{(\Delta x)^2}{D^k_{max}}, \tag{D.9}$$

$$D^k_{max} = max(D^k_{i+\frac{1}{2},j}, D^k_{i-\frac{1}{2},j}, D^k_{i,j+\frac{1}{2}}, D^k_{i,j-\frac{1}{2}}), \tag{D.10}$$

ensures numerical stability for two dimensional ice flow models using the M2 discretization.

# BIBLIOGRAPHY


Adhikari, S. and S. J. Marshall (2013). "Influence of high-order mechanics on simulation of glacier response to climate change: insights from Haig Glacier, Canadian Rocky Mountains". In: *The Cryosphere* 7.5, 1527. DOI: 10.5194/tc-7-1527-2013.

Agassiz, Louis (1840). *Etudes sur les glaciers*. Soleure: Jent et Gassmann.

Arakawa, Akio and Vivian R. Lamb (1977). "Computational Design of the Basic Dynamical Processes of the UCLA General Circulation Model". In: *General Circulation Models of the Atmosphere*. Ed. by Julius Chang. Vol. 17. Methods in Computational Physics: Advances in Research and Applications. Elsevier, 173. DOI: https://doi.org/10.1016/B978-0-12-460817-7.50009-4.

Aschwanden, A., E. Bueler, C. Khroulev, and H. Blatter (2012). "An enthalpy formulation for glaciers and ice sheets". In: *Journal of Glaciology* 58.209, 441. DOI: doi:10.3189/2012JoG11J088.

Aschwanden, A., M. A. Fahnestock, and M. Truffer (2016). "Complex Greenland outlet glacier flow captured". In: *Nature Communications* 7.10524. DOI: 10.1038/ncomms10524.

Ballantyne, Colin K. and John O. Stone (2015). "Trimlines, blockfields and the vertical extent of the last ice sheet in southern Ireland". In: *Boreas* 44.2, 277. DOI: 10.1111/bor.12109.

Becker, P., J. Seguinot, G. Jouvet, and M. Funk (2016). "Last Glacial Maximum precipitation pattern in the Alps inferred from glacier modelling". In: *Geographica Helvetica* 71.3, 173. DOI: 10.5194/gh-71-173-2016.

Becker, P., M. Funk, Ch. Schlüchter, and K. Hutter (2017). "A study of the Würm glaciation focused on the Valais region (Alps)". In: *Geographica Helvetica* 72.4, 421. DOI: 10.5194/gh-72-421-2017.

Benz-Meier, C (2003). "Der würmeiszeitliche Rheingletscher-Maximalstand: Digitale Rekonstruktion, Modellierung und Analyse mit einem Geographischen Informationssystem." PhD thesis. Geographischen Institut der Universität Zürich.

Bini, A. et al. (2009). *Die Schweiz während des letzteiszeitlichen Maximums (LGM, 1 : 500 000) - GeoKarte500.* (Kompil.) Bundesamt für Landestopografie swisstopo. Wabern.

Braakhekke, Jochem, Susan Ivy-Ochs, Giovanni Monegato, Franco Gianotti, Silvana Martin, Stefano Casale, and Marcus Christl (2020). "Timing and flow pattern of the Orta Glacier (European Alps) during the Last Glacial Maximum". In: *Boreas* 49.2, 315. DOI: 10.1111/bor.12427.

Brædstrup, C. F., D. L. Egholm, S. V. Ugelvig, and V. K. Pedersen (2016). "Basal shear stress under alpine glaciers: insights from experiments using the iSOSIA and Elmer/Ice models". In: *Earth Surface Dynamics* 4.1, 159. DOI: 10.5194/esurf-4-159-2016.

Braithwaite, Roger J., Martin Laternser, and W. Tad Pfeffer (1994). "Variations of near-surface firn density in the lower accumulation area of the Greenland ice sheet, Pâkitsoq, West Greenland". In: *Journal of Glaciology* 40.136, 477. DOI: 10.3189/S002214300001234X.

Briner, J.P., G.H. Miller, P.T. Davis, P.R. Bierman, and M. Caffee (2003). "Last Glacial Maximum ice sheet dynamics in Arctic Canada inferred from young erratics perched on ancient tors". In: *Quaternary Science Reviews* 22.5, 437. DOI: https://doi.org/10.1016/S0277-3791(03)00003-9.

Bueler, E. and J. Brown (2009). "Shallow shelf approximation as a "sliding law" in a thermomechanically coupled ice sheet model". In: *J. Geophys. Res. – Earth Surface* 114.F3. DOI: 10.1029/2008JF001179.

Bueler, Ed (2016). "Stable finite volume element schemes for the shallow-ice approximation". In: *Journal of Glaciology* 62.232, 230–242. DOI: 10.1017/jog.2015.3.

Buoncristiani, J.F. and M. Campy (2002). *Carte du dernier maximulm glacier (LGM) extraite de la commission de l'INQUA*.

– (2004). "Expansion and retreat of the Jura ice sheet (France) during the last glacial maximum". In: *Sedimentary Geology* 165.3. Sedimentary Records of Quaternary ice-sheet retreats and ice-calving events, 253. DOI: https://doi.org/10.1016/j.sedgeo.2003.11.007.

– (2011). "Quaternary Glaciations in the French Alps and Jura". In: vol. 15. Dev. Quaternary Sci. Amsterdam: Elsevier, 117. DOI: 10.1016/b978-0-444-53447-7.00010-6.

Burgess, E., R. Forster, and Chr. Larsen (2012). "Flow velocities of Alaskan glaciers". In: *Nature Communications*. DOI: 10.1038/ncomms3146.

Burkhard, M. and J. Spring (2004). "Erratic boulders of the ancient Rhone glacier and the dispersal pattern of Mt.Blanc granites". In: *2nd Swiss Geoscience Meeting*. Lausanne, 102.

Campy, Michel (1992). "Palaeogeographical relationships between Alpine and Jura glaciers during the two last Pleistocene glaciations". In: *Palaeogeography, Palaeoclimatology, Palaeoecology* 93.1, 1. DOI: https://doi.org/10.1016/0031-0182(92)90180-D.

Charpentier, Jean de (1841). *Essai sur les glaciers et sur le terrain erratique du bassin du Rhône*. Lausanne: Ducloux. DOI: 10.3931/e-rara-8464.

Clark, Peter U., David Archer, David Pollard, Joel D. Blum, Jose A. Rial, Victor Brovkin, Alan C. Mix, Nicklas G. Pisias, and Martin Roy (2006). "The middle Pleistocene transition: characteristics, mechanisms, and implications for long-term changes in atmospheric pCO2". In: *Quaternary Science Reviews* 25.23. Critical Quaternary Stratigraphy, 3150. DOI: https://doi.org/10.1016/j.quascirev.2006.07.008.

Cohen, D., F. Gillet-Chaulet, W. Haeberli, H. Machguth, and U. H. Fischer (2018). "Numerical reconstructions of the flow and basal conditions of the Rhine glacier, European Central Alps, at the Last Glacial Maximum". In: *The Cryosphere* 12.8, 2515. DOI: 10.5194/tc-12-2515-2018.

Cotton, M. M., R. L. Bruhn, J. Sauber, E. Burgess, and R. R. Forster (2014). "Icesurface morphology and flow on Malaspina Glacier, Alaska: Implications for regional tectonics in the Saint Elias orogen". In: *Tectonics* 33, 581. DOI: doi:10.1002/2013TC003381.

Coutterand, S. (2010). "Étude géomorphologique des flux glaciaires dans les Alpes nord-occidentales au Pléistocène récent: du maximum de la dernière glaciation aux premières étapes de la déglaciation". PhD thesis. Université de Savoie.

Coutterand, Sylvain, Philippe Schoeneich, and Gérard Nicoud (2009). "Le lobe glaciaire lyonnais au maximum würmien: glacier du Rhône ou/et glaciers savoyard ?" In: *Neige et glace de montagne : Reconstitution, dynamique, pratiques*. Ed. by Ludovic Ravanel Philip Deline. Vol. 8. Cahiers de Géographie. EDYTEM, 11. DOI: doi:10.18172/cig.2750.

Cuffey, K.M. and W.S.B. Paterson (2010). *The Physics of Glaciers*. ISBN 978-0-12-369461-4. Elsevier, Burlington, MA, USA.

Dahl-Jensen, Dorthe et al. (2013). "Eemian interglacial reconstructed from a Greenland folded ice core". In: *Nature* 493.7433, 489. DOI: 10.1038/nature11789.

Ehlers, J., P. L. Gibbard, and P. D. Hughes (2011). *Quaternary Glaciations - Extent and Chronology - A Closer Look*. Vol. 15. Dev. Quaternary Sci. Amsterdam: Elsevier.

Fabel, Derek, Arjen P. Stroeven, Jon Harbor, Johan Kleman, David Elmore, and David Fink (2002). "Landscape preservation under Fennoscandian ice sheets determined from in situ produced $^{10}$Be and $^{26}$Al". In: *Earth and Planetary Science Letters* 201.2, 397. DOI: https://doi.org/10.1016/S0012-821X(02)00714-8.

Florineth, D. (1998). "Surface geometry of the Last Glacial Maximum (LGM) in the Southeastern Swiss Alps (Graubünden) and its paleoclimatological significance". In: *Eiszeitalter u. Gegenwart* 48.

Florineth, D. and C. Schlüchter (1998). "Reconstructing the Last Glacial Maximum (LGM) ice surface geometry and flowlines in the Central Swiss Alps". In: *Eclogae. Geol. Hel.* 91, 391.

– (2000). "Alpine Evidence for Atmospheric Circulation Patterns in Europe during the LGM". In: *Quaternary Research* 54.

Gagliardini, O. et al. (2013). "Capabilities and performance of Elmer/Ice, a new-generation ice sheet model". In: *Geoscientific Model Development* 6.4, 1299.

Geologische Bundesanstalt, (Hrsg.) (2013). *Der Alpenraum zum Höhepunkt der letzten Eiszeit - Posterkarte - Geol. B.-A., Wien*.

Gilbert, A., G. E. Flowers, G. H. Miller, B. T. Rabus, W. Van Wychen, A. S. Gardner, and L. Copland (2016). "Sensitivity of Barnes Ice Cap, Baffin Island, Canada, to climate state and internal dynamics". In: *Journal of Geophysical Research: Earth Surface* 121.8, 1516. DOI: 10.1002/2016JF003839.

Glen, J. W. (1952). "Experiments on the Deformation of Ice". In: *Journal of Glaciology* 2.12, 111–114. DOI: 10.3189/S0022143000034067.

Glen, J. W. (1953). "Rate of Flow of Polycrystalline Ice". In: *Nature* 172, 721.

Golledge, N. R., A. N. Mackintosh, B. M. Anderson, K. M. Buckley, A. M. Doughty, D. J.A. Barrell, G. H. Denton, M. J. Vandergoes, B. G. Andersen, and J. M. Schaefer (2012). "Last Glacial Maximum climate in New Zealand inferred from a mod-

elled Southern Alps icefield". In: *Quaternary Sci. Rev.* 46.0, 30. DOI: 10.1016/j.quascirev.2012.05.004.

Gómez-Navarro, J. J., C. C. Raible, D. Bozhinova, O. Martius, J. A. García Valero, and J. P. Montávez (2018). "A new region-aware bias-correction method for simulated precipitation in areas of complex orography". In: *Geoscientific Model Development* 11.6, 2231. DOI: 10.5194/gmd-11-2231-2018.

Goutorbe, B., J. Poort, F. Lucazeau, and S. Raillard (2011). "Global heat flow trends resolved from multiple geological and geophysical proxies". In: *Geophysical Journal International* 187, 1405. DOI: 10.1111/j.1365-246X.2011.05228.x.

Graf, Angela, Naki Akçar, Susan Ivy-Ochs, Stefan Strasky, PeterW. Kubik, Marcus Christl, Martin Burkhard, Rainer Wieler, and Christian Schlüchter (2015). "Multiple advances of Alpine glaciers into the Jura Mountains in the Northwestern Switzerland". In: *Swiss Journal of Geosciences*, 1. DOI: 10.1007/s00015-015-0195-y.

Greve, R. (1997). "Application of a polythermal three-dimensional ice sheet model to the Greenland Ice Sheet: response to a steady-state and transient climate scenarios". In: *Journal of Climate* 10.5, 901.

Guiter, Frédéric, Anne Triganon, Valérie Andrieu-Ponel, Philippe Ponel, Jean-Pierre Hébrard, Gérard Nicoud, Jacques-Louis De Beaulieu, Simon Brewer, and Frederic Guibal (2005). "First evidence of 'in situ' Eemian sediments on the high plateau of Evian (Northern Alps, France): implications for the chronology of the Last Glaciation". In: *Quaternary Science Reviews* 24.1, 35. DOI: 10.1016/j.quascirev.2004.06.011.

Haeberli, W. and C. Schlüchter (1987). "Geological evidence to constrain modelling of the Late Pleistocene Rhonegletscher (Switzerland)". In: *The Physical Basis of Ice Sheet Modelling, Proceedings of the Vancouver Symposium* IAHS Publ. no. 170, 333.

Healey, R., B. Hallet, G. Roe, E. D. Waddington, and E. Rignot (2012). "Spatial distribution of glacial erosion rates in the St. Elias range, Alaska, inferred from a realistic model of glacier dynamics". In: *Journal of Geophysical Research* 117. DOI: 10.1029/2011JF002291.

Heyman, Barbara M., Jakob Heyman, Thomas Fickert, and Jonathan M. Harbor (2013). "Paleo-climate of the Central European uplands during the Last Glacial Maximum based on glacier mass-balance modeling". In: *Quaternary Research* 79.1, 49. DOI: http://dx.doi.org/10.1016/j.yqres.2012.09.005.

Hijmans, R. J., S. E. Cameron, J. L. Parra, P. G. Jones, and A. Jarvis (2005). "Very high resolution interpolated climate surfaces for global land areas". In: *International Journal of Climatology* 25.15, 1965.

Hindmarsh, R. C. A. (2004). "A numerical comparison of approximations to the Stokes equations used in ice sheet and glacier modeling". In: *Journal of Geophysical Research* 109.F01012. DOI: 10.1029/2003JF000065.

Hindmarsh, Richard C. A. (2001). "Notes on Basic Glaciological Computational Methods and Algorithms". In: *Continuum Mechanics and Applications in Geophysics and the Environment*. Ed. by Brian Straughan, Ralf Greve, Harald Ehrentraut, and Yongqi Wang. Berlin, Heidelberg: Springer Berlin Heidelberg, 222. DOI: 10.1007/978-3-662-04439-1_13.

Hindmarsh, Richard C. A. and Antony J. Payne (1996). "Time-step limits for stable solutions of the ice-sheet equation". In: *Annals of Glaciology* 23, 74–85. DOI: 10.3189/S0260305500013288.

Hock, Regine (2003). "Temperature index melt modelling in mountain areas". In: *Journal of Hydrology* 282, 104.

Hock, Regine, Jennifer K. Hutchings, and Michael Lehning (2017). "Grand Challenges in Cryospheric Sciences: Toward Better Predictability of Glaciers, Snow and Sea Ice". In: *Frontiers in Earth Science* 5, 64. DOI: 10.3389/feart.2017.00064.

Hofer, D., C. C. Raible, A. Dehnert, and J. Kuhlemann (2012b). "The impact of different glacial boundary conditions on atmospheric dynamics and precipitation in the North Atlantic region". In: *Climate of the Past* 8.3, 935. DOI: 10.5194/cp-8-935-2012.

Hofer, D., C. C. Raible, N. Merz, A. Dehnert, and J. Kuhlemann (2012a). "Simulated winter circulation types in the North Atlantic and European region for preindustrial and glacial conditions". In: *Geophysical Research Letters* 39.15. DOI: 10.1029/2012GL052296.

Hughes, Anna L. C., Richard Gyllencreutz, Øystein S. Lohne, Jan Mangerud, and John Inge Svendsen (2016). "The last Eurasian ice sheets – a chronological database and time-slice reconstruction, DATED-1". In: *Boreas* 45.1, 1. DOI: https://doi.org/10.1111/bor.12142.

Hughes, Philip, Philip Gibbard, and Jürgen Ehlers (2013). "Timing of glaciation during the last glacial cycle: Evaluating the concept of a global 'Last Glacial Maximum' (LGM)". In: *Earth-Science Reviews* 125, 171. DOI: 10.1016/j.earscirev.2013.07.003.

Hughes, Philip D. and Philip L. Gibbard (2015). "A stratigraphical basis for the Last Glacial Maximum (LGM)". In: *Quaternary International* 383. The Quaternary System and its formal subdivision, 174. DOI: https://doi.org/10.1016/j.quaint.2014.06.006.

Hutter, K. (1983). *Theoretical glaciology*. D. Reidel Publishing Company/Tokyo, Terra Scientific Publishing Company.

Huybrechts, Philippe and Tony Payne (1996). "The EISMINT benchmarks for testing ice-sheet models". In: *Annals of Glaciology* 23, 1–12. DOI: 10.3189/S0260305500013197.

Imhof, Michael A., Denis Cohen, Julien Seguinot, Andy Aschwanden, Martin Funk, and Guillaume Jouvet (2019). "Modelling a paleo valley glacier network using a hybrid model: an assessment with a Stokes ice flow model". In: *Journal of Glaciology* 65.254, 1000–1010. DOI: 10.1017/jog.2019.77.

Imhof, Michael Andreas (2021a). *A numerical reconstruction of the LGM Rhone Glacier and its ice dynamics [dataset]*. Version 1. DOI: 10.5281/zenodo.4640819.

– (2021b). *Modelling the Alpine ice Field of the Last Glacial Maximum with regional climate model data [dataset]*. Version 1. DOI: 10.5281/zenodo.4640232.

Itten, H. (1953). "Schutz von Naturdenkmälern. Mitteilungen der Naturforschenden". In: *Gesellschaft in Bern* Neue Folge 10, 85.

Ivy-Ochs, S. (2015). "Glacier variations in the European Alps at the end of the last glaciation". In: *Cuadernos de Investigacion Geografica* 2.295.

Ivy-Ochs, S., J. Schäfer, P. W. Kubik, H.-A. Synal, and C. Schlüchter (2004). "Timing of deglaciation on the Northern Alpine foreland (Switzerland)". In: *Eclogae Geologicae Helvetiae* 97.1, 47.

Ivy-Ochs, Susan, Hanns Kerschner, Anne Reuther, Max Maisch, Rudolf Sailer, Joerg Schaefer, Peter W. Kubik, Hans-Arno Synal, and Christian Schlüchter (2006). "The timing of glacier advances in the northern European Alps based on surface exposure dating with cosmogenic 10Be, 26Al, 36Cl, and 21Ne". In: DOI: 10.1130/2006.2415(04).

Ivy-Ochs, Susan, Hanns Kerschner, Anne Reuther, Frank Preusser, Klaus Heine, Max Maisch, Peter W. Kubik, and Christian Schlüchter (2008). "Chronology of the last glacial cycle in the European Alps". In: *Journal of Quaternary Science* 23.6-7, 559. DOI: 10.1002/jqs.1202.

Ivy-Ochs, Susan et al. (2018). "New geomorphological and chronological constraints for glacial deposits in the Rivoli-Avigliana end-moraine system and the lower Susa Valley (Western Alps, NW Italy)". In: *Journal of Quaternary Science* 33.5, 550. DOI: 10.1002/jqs.3034.

Jarosch, A. H., C. G. Schoof, and F. S. Anslow (2013). "Restoring mass conservation to shallow ice flow models over complex terrain". In: *The Cryosphere* 7.1, 229. DOI: 10.5194/tc-7-229-2013.

Jarvis, A., H.I. Reuter, A. Nelson, and E. Guevara (2008). *Hole-filled SRTM for the globe Version 4*. available from the CGIAR-CSI SRTM 90m Database.

Johnsen, Sigfus J., Dorthe Dahl-Jensen, Willi Dansgaard, and Niels Gundestrup (1995). "Greenland palaeotemperatures derived from GRIP bore hole temperature and ice core isotope profiles". In: *Tellus B: Chemical and Physical Meteorology* 47.5, 624. DOI: 10.3402/tellusb.v47i5.16077.

Jouvet, G., J. Seguinot, S. Ivy-Ochs, and M. Funk (2017). "Modelling the diversion of erratic boulders by the Valais Glacier during the Last Glacial Maximum". In: *Journal of Glaciology* 63.239, 487. DOI: 10.1017/jog.2017.7.

Jouvet, Guillaume and Ed Bueler (2012). "Steady, Shallow Ice Sheets as Obstacle Problems: Well-Posedness and Finite Element Approximation". In: *SIAM Journal of Applied Mathematics*, 1292.

Jouzel, Jean and Valerie Masson-Delmotte (2007). *EPICA Dome C Ice Core 800KYr deuterium data and temperature estimates*. data set. Supplement to: Jouzel, Jean; Masson-Delmotte, Valerie; Cattani, Olivier; Dreyfus, Gabrielle; Falourd, Sonia; Hoffmann, G; Minster, B; Nouet, J; Barnola, Jean-Marc; Chappellaz, Jérôme A; Fischer, Hubertus; Gallet, J C; Johnsen, Sigfus J; Leuenberger, Markus; Loulergue, Laetitia; Luethi, D; Oerter, Hans; Parrenin, Frédéric; Raisbeck, Grant M; Raynaud, Dominique; Schilt, Adrian; Schwander, Jakob; Selmo, Enrico; Souchez, Roland; Spahni, Renato; Stauffer, Bernhard; Steffensen, Jørgen Peder; Stenni, Barbara; Stocker, Thomas F; Tison, Jean-Louis; Werner, Martin; Wolff, Eric W (2007): Orbital and millennial Antarctic climate variability over the past 800,000

years. Science, 317(5839), 793-797, https://doi.org/10.1126/science.1141038. DOI: 10.1594/PANGAEA.683655.

Kelly, J., J.F. Buoncristiani, and C. Schlüchter (2004). "A reconstruction of the Last Glacial Maximum (LGM) ice surface geometry in the western Swiss Alps and contiguous Alpine regions in Italy and France". In: *Eclogae geol. Hel.* 57.

Kleman, Johan, Krister Jansson, Hernán De Angelis, Arjen P. Stroeven, Clas Hättestrand, Göran Alm, and Neil Glasser (2010). "North American Ice Sheet build-up during the last glacial cycle, 115–21kyr". In: *Quaternary Science Reviews* 29.17, 2036. DOI: https://doi.org/10.1016/j.quascirev.2010.04.021.

Lafon, Thomas, Simon Dadson, Gwen Buys, and Christel Prudhomme (2013). "Bias correction of daily precipitation simulated by a regional climate model: a comparison of methods". In: *International Journal of Climatology* 33.6, 1367. DOI: 10.1002/joc.3518.

Le Meur, E., O. Gagliardini, Th. Zwinger, and J. Ruokolainen (2004). "Glacier flow modelling: a comparison of the Shallow Ice Approximation and the full-Stokes solution". In: *Comptes Rendus Physique* 5.7, 709. DOI: 10.1016/j.crhy.2004.10.001.

Leysinger Vieli, G. J.-M. C. and G. H. Gudmundsson (2004). "On estimating length fluctuations of glaciers caused by changes in climatic forcing". In: *Journal of Geophysical Research* 109. DOI: 10.1029/2003JF000027.

Li, Zhujun, Paquita Zuidema, Ping Zhu, and Hugh Morrison (2015). "The Sensitivity of Simulated Shallow Cumulus Convection and Cold Pools to Microphysics". In: *Journal of the Atmospheric Sciences* 72.9, 3340. DOI: 10.1175/JAS-D-14-0099.1.

Lisiecki, Lorraine E. and Maureen E. Raymo (2005). "A Pliocene-Pleistocene stack of 57 globally distributed benthic $\delta^{18}$O records". In: *Paleoceanography* 20.1. DOI: 10.1029/2004PA001071.

Löfverström, M., R. Caballero, J. Nilsson, and J. Kleman (2014). "Evolution of the large-scale atmospheric circulation in response to changing ice sheets over the last glacial cycle". In: *Climate of the Past* 10.4, 1453. DOI: 10.5194/cp-10-1453-2014.

Ludwig, Patrick, Erik J. Schaffernicht, Yaping Shao, and Joaquim G. Pinto (2016). "Regional atmospheric circulation over Europe during the Last Glacial Maximum and its links to precipitation". In: *Journal of Geophysical Research: Atmospheres* 121.5, 2130. DOI: 10.1002/2015JD024444.

Luetscher, Marc, R. Boch, H. Sodemann, C. Spötl, H. Cheng, R. L. Edwards, S. Frisia, F. Hof, and W. Müller (2015). "North Atlantic storm track changes during the Last Glacial Maximum recorded by Alpine speleothems". In: *Nature* 5. DOI: 10.1038/ncomms7344.

Löfverström, Marcus (2020). "A dynamic link between high-intensity precipitation events in southwestern North America and Europe at the Last Glacial Maximum". In: *Earth and Planetary Science Letters* 534, 116081. DOI: https://doi.org/10.1016/j.epsl.2020.116081.

Löfverström, Marcus and Juan M. Lora (2017). "Abrupt regime shifts in the North Atlantic atmospheric circulation over the last deglaciation". In: *Geophysical Research Letters* 44.15, 8047. DOI: 10.1002/2017GL074274.

Löfverström, Marcus, Rodrigo Caballero, Johan Nilsson, and Gabriele Messori (2016). "Stationary Wave Reflection as a Mechanism for Zonalizing the Atlantic Winter Jet at the LGM". In: *Journal of the Atmospheric Sciences* 73.8, 3329. DOI: 10.1175/JAS-D-15-0295.1.

Mahaffy, M. W. (1976). "A three-dimensional numerical model of ice sheets: Tests on the Barnes Ice Cap, Northwest Territories". In: *Journal of Geophysical Research (1896-1977)* 81.6, 1059. DOI: 10.1029/JC081i006p01059.

Maussion, F. et al. (2019). "The Open Global Glacier Model (OGGM) v1.1". In: *Geoscientific Model Development* 12.3, 909. DOI: 10.5194/gmd-12-909-2019.

Medici, F. and L. Rybach (1995). *Geothermal Map of Switzerland 1995 (Heat Flow Density)*. Tech. rep. 30. Swiss Geophysical Commission.

Merz, Niklaus, Christoph C. Raible, and Tim Woollings (2015). "North Atlantic Eddy-Driven Jet in Interglacial and Glacial Winter Climates". In: *Journal of Climate* 28.10, 3977. DOI: 10.1175/JCLI-D-14-00525.1.

MeteoSchweiz, Zürich (2013). *Documentation of MeteoSwiss gridded data product, daily precipitation: RhiresD*.

Monegato, Giovanni, Cesare Ravazzi, Marta Donegana, Roberta Pini, Gilberto Calderoni, and Lucia Wick (2007). "Evidence of a two-fold glacial advance during the last glacial maximum in the Tagliamento end moraine system (eastern Alps)". In: *Quaternary Research* 68.2, 284. DOI: 10.1016/j.yqres.2007.07.002.

Monegato, Giovanni, Giancarlo Scardia, Irka Hajdas, Francesca Rizzini, and Andrea Piccin (2017). "The Alpine LGM in the boreal ice-sheets game". In: *Scientific Reports* 7, 1. DOI: 10.1038/s41598-017-02148-7.

Muskett, Reginald R., Craig S. Lingle, Jeanne M. Sauber, Austin S. Post, Wendell V. Tangborn, and Bernard T. Rabus (2008). "Surging, accelerating surface lowering and volume reduction of the Malaspina Glacier system, Alaska, USA, and Yukon, Canada, from 1972 to 2006". In: *Journal of Glaciology* 54.188, 788–800. DOI: 10.3189/002214308787779915.

Neff, B., Andreas Born, and Thomas Stocker (2016). "An ice sheet model of reduced complexity for paleoclimate studies". In: *Earth System Dynamics* 7, 397. DOI: 10.5194/esd-7-397-2016.

Palacios, David, Antonio Gómez-Ortiz, Nuria Andrés, Lorenzo Vázquez-Selem, Ferran Salvador-Franch, and Marc Oliva (2015). "Maximum extent of Late Pleistocene glaciers and last deglaciation of La Cerdanya mountains, Southeastern Pyrenees". In: *Geomorphology* 231, 116. DOI: https://doi.org/10.1016/j.geomorph.2014.10.037.

Pattyn, F. et al. (2008). "Benchmark experiments for higher-order and full-Stokes ice sheet models (ISMIP-HOM)". In: *The Cryosphere* 2.2, 95. DOI: 10.5194/tc-2-95-2008.

Peltier, W.R. (2004). "Global glacial isostasy and the surface of the ice-age earth: The ICE-5G (VM2) Model and GRACE". In: *Annual Review of Earth and Planetary Sciences* 32.1, 111. DOI: 10.1146/annurev.earth.32.082503.144359.

PISM authors (2019). *PISM, a Parallel Ice Sheet Model*. http://www.pism-docs.org.

Preusser, Frank, Rudolf Hans Graf, Oskar Keller, Edgar Krayss, and Christian Schlüchter (2011). "Quaternary glaciation history of northern Switzerland". In: *E&G Quaternary Science Journal* 60.2-3, 282. DOI: 10.3285/eg.60.2-3.06.

Reber, Regina, Naki Akçar, Susan Ivy-Ochs, Dmitry Tikhomirov, Reto Burkhalter, Conradin Zahno, Aron Lüthold, Peter W. Kubik, Christof Vockenhuber, and Christian Schlüchter (2014). "Timing of retreat of the Reuss Glacier (Switzerland) at the end of the Last Glacial Maximum". In: *Swiss Journal of Geosciences* 107.2, 293. DOI: 10.1007/s00015-014-0169-5.

Reeh, N. (1991). "Parameterization of Melt Rate and Surface Temperature on the Greenland Ice Sheet". In: *Polarforschung* 59, 113.

Region Fribourg (2020). *Bloc erratique*. https://www.fribourgregion.ch/fr/P20906/bloc-erratique.

Reitner, J. (2005). "Quartärgeologie und Landschaftsentwicklung im Raum Kitzbühel-St. Johann i.T.-Hopfgarten (Nordtirol) vom Riss bis in das Würm-Spätglazial (MIS 6-2)". PhD thesis. Universität Wien.

Ried bei Kerzers (2020). *Abkömmling der Murtenlinde sowie Findlinge von Ried*. https://www.ried.ch/de/gemeinde/gemeindeinfrastruktur/AbkmmlingderMurtenlindesowieFindlingevonRied1.pdf.

Ritz, Catherine, Tamsin L. Edwards, Gaël Durand, Antony J. Payne, Vincent Peyaud, and Richard C. A. Hindmarsh (2015). "Potential sea-level rise from Antarctic ice-sheet instability constrained by observations". In: *Nature* 528, 115. DOI: 10.1038/nature16147.

Rogozhina, I. and D. Rau (2014). "Vital role of daily temperature variability in surface mass balance parameterizations of the Greenland Ice Sheet". In: *The Cryosphere* 8.2, 575. DOI: 10.5194/tc-8-575-2014.

Roy, Kevin and W.R. Peltier (2018). "Relative sea level in the Western Mediterranean basin: A regional test of the ICE-7G_NA (VM7) model and a constraint on late Holocene Antarctic deglaciation". In: *Quaternary Science Reviews* 183, 76. DOI: https://doi.org/10.1016/j.quascirev.2017.12.021.

Saussure, Horace-Bénédict de (1779). *Voyages dans les Alpes, précédés d'un essai sur l'histoire naturelle des environs de Genève*. Vol. 1. Neuchâtel: Fauche-Borel.

Schäfer, Martina and Emmanuel Le Meur (2007). "Improvement of a 2-D SIA ice-flow model: Application to Glacier de Saint-Sorlin, France". In: *Journal of Glaciology* 53, 713. DOI: 10.3189/002214307784409234.

Schmidt, L. S., G. Aðalgeirsdóttir, F. Pálsson, P. L. Langen, S. Guðmundsson, and H. Björnsson (2020). "Dynamic simulations of Vatnajökull ice cap from 1980 to 2300". In: *Journal of Glaciology* 66.255, 97. DOI: 10.1017/jog.2019.90.

Schoof, C. (2003). "The effect of basal topography on ice sheet dynamics". In: *Continuum Mechanics and Thermodynamics* 15.3, 295. DOI: 10.1007/s00161-003-0119-3.

Seddik, H., R. Greve, T. Zwinger, and S. Sugiyama (2017). "Regional modeling of the Shirase drainage basin, East Antarctica: full Stokes vs. shallow ice dynamics". In: *The Cryosphere* 11.5, 2213. DOI: 10.5194/tc-11-2213-2017.

Seguinot, J. (2013). "Spatial and seasonal effects of temperature variability in a positive degree-day glacier surface mass-balance model". In: *Journal of Glaciology* 59.218, 1202. DOI: 10.3189/2013JoG13J081.

Seguinot, J., C. Khroulev, I. Rogozhina, A. P. Stroeven, and Q. Zhang (2014). "The effect of climate forcing on numerical simulations of the Cordilleran ice sheet at the Last Glacial Maximum". In: *The Cryosphere* 8.3, 1087. DOI: 10.5194/tc-8-1087-2014.

Seguinot, J., S. Ivy-Ochs, G. Jouvet, M. Huss, M. Funk, and F. Preusser (2018). "Modelling last glacial cycle ice dynamics in the Alps". In: *The Cryosphere* 12.10, 3265. DOI: 10.5194/tc-12-3265-2018.

Seierstad, Inger K. et al. (2014). "Consistently dated records from the Greenland GRIP, GISP2 and NGRIP ice cores for the past 104 ka reveal regional millennial-scale $\delta^{18}$O gradients with possible Heinrich event imprint". In: *Quaternary Science Reviews* 106. Dating, Synthesis, and Interpretation of Palaeoclimatic Records and Model-data Integration: Advances of the INTIMATE project(INTegration of Ice core, Marine and TErrestrial records, COST Action ES0907), 29. DOI: https://doi.org/10.1016/j.quascirev.2014.10.032.

Skamarock, William C., Joseph B. Klemp, Jimy Dudhia, David O. Gill, Dale M. Barker, Michael G. Duda, Xiang-yu Huang, Wei Wang, and Jordan G. Powers (2008). "A description of the Advanced Research WRF version 3". In: *NCAR Tech. Note NCAR/TN-475+STR*, 113 pp. DOI: 10.5065/D68S4MVH.

Spring, Jérôme (2004). "Les blocs erratiques granitiques de l'ancien glacier du Rhône". MA thesis. Université de Neuchatel.

Squitieri, Brian J. and William A. Gallus (2020). "On the Forecast Sensitivity of MCS Cold Pools and Related Features to Horizontal Grid Spacing in Convection-Allowing WRF Simulations". In: *Weather and Forecasting* 35.2, 325. DOI: 10.1175/WAF-D-19-0016.1.

Sutter, J., H. Fischer, K. Grosfeld, N. B. Karlsson, T. Kleiner, B. Van Liefferinge, and O. Eisen (2019). "Modelling the Antarctic Ice Sheet across the mid-Pleistocene transition – implications for Oldest Ice". In: *The Cryosphere* 13.7, 2023. DOI: 10.5194/tc-13-2023-2019.

Tierney, Jessica E., Jiang Zhu, Jonathan King, Steven B. Malevich, Gregory J. Hakim, and Christopher J. Poulsen (2020). "Glacial cooling and climate sensitivity revisited". In: *Nature* 584, 569. DOI: https://doi.org/10.1038/s41586-020-2617-x.

Velasquez, P. and C. C. Raible (in prep). "Role of Ice-Sheet Topography on the Alpine Climate at Glacial Times". In: *TBA*.

Velasquez, P., M. Messmer, and C. C. Raible (2020). "A new bias-correction method for precipitation over complex terrain suitable for different climate states: a case study using WRF (version 3.8.1)". In: *Geoscientific Model Development* 13.10, 5007. DOI: 10.5194/gmd-13-5007-2020.

Velasquez, Patricio (in prep). "Regional Climate Modelling over Europe at Glacial Times". PhD thesis. Universität Bern.

Venetz, Ignace (1833). *Mémoire sur les variations de la température dans les Alpes de la Suisse*. Orell, Füssli. DOI: 10.3931/e-rara-24595.

Višnjević, Vjeran, Frédéric Herman, and Günther Prasicek (2020). "Climatic patterns over the European Alps during the LGM derived from inversion of the paleo-ice extent". In: *Earth and Planetary Science Letters* 538, 116185. DOI: https://doi.org/10.1016/j.epsl.2020.116185.

Walker, Mike et al. (2009). "Formal definition and dating of the GSSP (Global Stratotype Section and Point) for the base of the Holocene using the Greenland NGRIP ice core, and selected auxiliary records". In: *Journal of Quaternary Science* 24.1, 3. DOI: https://doi.org/10.1002/jqs.1227.

Wang, Y., Qiuhua Liang, Georges Kesserwani, and Jim Hall (2011). "A positivity-preserving zero-inertia model for flood simulation". In: *Computers & Fluids - COMPUT FLUIDS* 46, 505. DOI: 10.1016/j.compfluid.2011.01.026.

Weis, M., R. Greve, and K. Hutter (1999). "Theory of shallow ice shelves". In: *Continuum Mechanics and Thermodynamics* 11.1, 15.

Wilton, David J., Amy Jowett, Edward Hanna, Grant R. Bigg, Michiel R. van den Broeke, Xavier Fettweis, and Philippe Huybrechts (2017). "High resolution (1 km) positive degree-day modelling of Greenland ice sheet surface mass balance, 1870–2012 using reanalysis data". In: *Journal of Glaciology* 63.237, 176–193. DOI: 10.1017/jog.2016.133.

Windham, William and Peter Martel (1744). *An account of the glacieres or ice alps in Savoy, in two letters, one from an English gentleman to his friend at Geneva; the other from Peter Martel, engineer, to the said English gentleman*. as laid before the Royal Society, London, printed for Peter Martel.

Winkelmann, R., M. A. Martin, M. Haseloff, T. Albrecht, E. Bueler, C. Khroulev, and A. Levermann (2011). "The Potsdam Parallel Ice Sheet Model (PISM-PIK) – Part 1: Model description". In: *The Cryosphere* 5.3, 715.

Wirsig, Christian, Jerzy Zasadni, Marcus Christl, Naki Akçar, and Susan Ivy-Ochs (2016). "Dating the onset of LGM ice surface lowering in the High Alps". In: *Quaternary Science Reviews* 143, 37. DOI: https://doi.org/10.1016/j.quascirev.2016.05.001.

Woollings, Tim (2016). "Storm tracks, blocking, and climate change: a review". In: *Dynamics and Predictability of Large-Scale, High-Impact Weather and Climate Events*. Ed. by Jianping Li, Richard Swinbank, Richard Grotjahn, and HansEditors Volkert. Special Publications of the International Union of Geodesy and Geophysics. Cambridge University Press, 113–121. DOI: 10.1017/CBO9781107775541.009.

Wu, H. B., J. L. Guiot, S. Brewer, and Z. T.: Guo (2007). "Climatic changes in Eurasia and Africa at the Last Glacial Maximum and mid-Holocene: reconstruction from pollen data using inverse vegetation modelling". In: *Clim. Dynam.* 29, 211.

Yan, Qing, Lewis A. Owen, Huijun Wang, and Zhongshi Zhang (2018). "Climate Constraints on Glaciation Over High-Mountain Asia During the Last Glacial Maximum". In: *Geophysical Research Letters* 45.17, 9024. DOI: 10.1029/2018GL079168.

Zekollari, H., M. Huss, and D. Farinotti (2019). "Modelling the future evolution of glaciers in the European Alps under the EURO-CORDEX RCM ensemble". In: *The Cryosphere* 13.4, 1125. DOI: 10.5194/tc-13-1125-2019.

Zekollari, Harry, Matthias Huss, and Daniel Farinotti (2020). "On the Imbalance and Response Time of Glaciers in the European Alps". In: *Geophysical Research Letters* 47.2. e2019GL085578 2019GL085578, e2019GL085578. DOI: 10.1029/2019GL085578.

Ziemen, F. A., R. Hock, A. Aschwanden, C. Khroulev, C. Kienholz, A. Melkonian, and J. Zhang (2016). "Modeling the evolution of the Juneau Icefield between 1971 and 2100 using the Parallel Ice Sheet Model (PISM)". In: *Journal of Glaciology* 62.231, 199. DOI: 10.1017/jog.2016.13.

# ACKNOWLEDGEMENTS

Here, I would like to express my gratitude to the many people that helped or accompanied me throughout this PhD. In particular I would like to thank...

... **Guillaume Jouvet** for offering me the position and the opportunity to write this thesis at VAW on a fascinating topic that kept me engaged throughout the entire course of the PhD. I will always be in debt to you for the guidance you provided in navigating throughout the challenges in the academic world and proceed towards the completion of this PhD. I am in particular grateful for your continuous help for structuring and writing scientific texts and also giving me the room to pursue some of my own ideas. Your door was always open for me to discuss any problem, which I greatly appreciated.

... **Martin Funk**, who was my "Doktorvater" during the first three years. During the course of this thesis, I greatly benefited from your wisdom and connections accumulated as a professor in glaciology. I am in particular thankful for your steadfast support and encouragement you provided me. And last but not least, I would like to thank you for your interest and commitment to the project well beyond your retirement.

... **Fabian Walter** for taking over the lead of my PhD after Martin Funk's retirement. You always provided swift and helpful feedback despite your tight agenda, which I am grateful for. I would also like to thank you for the very constructive and insightful comments that significantly enhanced the quality of my thesis, especially during the later stages of the PhD.

... **Julien Seguinot** for sharing with me his comprehensive PISM know-how and his broad expertise on past glaciations. I am deeply grateful for your countless contributions during inspiring discussions and I always treasured your calm nature and enthusiasm. Also a big merci for motivating and cheering me up when I was hit by big throwbacks, you helped me a lot in these situations.

... our collaborators **Patrico Velasquez and Christoph Raible** from University of Bern for their cooperation and help with their regional climate data.

... **Susan Ivy-Ochs, Sarah Kamleitner, Christian Schlüchter, and Natacha Gribenski** for sharing your vast expertise on geomorphology and geology with me. I very much enjoyed the lively discussions with you which proved to be very helpful to me.

... **Andy Aschwanden and Ed Bueler** for their support with PISM.

... **Andreas Born** for your support and taking over the lead to publish my master thesis. I was also very happy to visit you in Bergen and meet your lovely family.

... **Amandine, Amaury, Baudi, Christophe, Claudia, Cristina, Daniel, Dominik, Eef, Elias, Fini, Harry, Ian, Jane, Johannes, Fabian, Frederic, Kolumban, Loris, Luisa, Lukas, Ludovic, Matthias, Mauro, Michi, Romeo, Simon, Tobias, Vanessa, Yvo, Zhen and many others** from VAW. You all made VAW a very pleasant place that I was happy to work at. I really enjoyed the interesting discussions, joking, and laughing with you or having a casual beer together.

... **Frédéric Dreher and Daniel Henseler** for being excellent teachers in Taekwondo and Russian respectively. I really enjoyed attending your lessons, they always provided a welcome distraction to glaciers and digits.

... my fellow tank commanders **Märcu and Simu**. Unlike us, the evenings were never wasted.

... **Frank, Etienne, and Stibe** for our traditional Chäsbrotparties.

... **Yves, Marc, Chrige, Sämi, Kevin, Chrigu, Zappa, and Samira** for providing excellent distraction from work with nasty jokes, hiking, and relaxed ski weekends.

... **Ste and Nathalie** for the asylum you provided me when I needed a break from Zürich.

... **Martina** for your encouragement and support to apply for this PhD position. Not to forget the beers and ice cream ;)

... **Carlo Pedersoli and Mario Girotti** for always believing in me and providing steady backup with slaps, beans, onions, and garlic.

... **Lena, Elsa, Marcel, Daniel, and Manuel** for the casual lunches and coffee breaks at ETH or elsewhere in Zürich.

... **my family**, in particular my parents. I would like to express my deepest gratitude for your continuous encouragement and support – emotionally and financially – during the last four years and the time before.

This project was funded by the Swiss National Science Foundation (project 200021-162444).